Microwave-initiated Synthesis of Metal Chalcogenides on Graphene Support for Sustainable Energy Applications

by

Shatila Sarwar

A dissertation submitted to the Graduate Faculty of
Auburn University
in partial fulfillment of the
requirements for the Degree of
Doctor of Philosophy

Auburn, Alabama
August 7, 2021

Keywords: microwave synthesis, metal chalcogenides, graphene, hydrogen evolution reaction, energy storage

Approved by

Xinyu Zhang, Professor, Chemical Engineering
Tae-Sik Oh, Assistant Professor, Chemical Engineering
Andrew J Adamczyk, Assistant Professor, Chemical Engineering
Russell Mailen, Assistant Professor, Aerospace Engineering
Asha-Dee Celestine, Visiting Assistant Professor, Aerospace Engineering

Abstract

To meet the increasing demand on energy, new types of renewable resources along with advanced energy conversion and storage systems are being developed. Nanotechnology plays a vital role to solve the existing energy issues. Nanomaterials, such as carbon materials, metal oxides, metal chalcogenides, carbides, phosphides, polymers, etc. possess superior mechanical, thermal and electrical properties, leading to broad applications in composite materials, smart structures, chemical sensors, energy storage and nano-electronic devices. However, the high cost and difficulty in getting large scale, high quality nanomaterials remain challenges. This research proposes to demonstrate an ultrafast, facile, and reliable microwave-initiated synthesis approach for the direct growth of metal chalcogenides (MCs) on graphene support. In this regard, a series of suitable combinations of metals and chalcogens have been selected, such as molybdenum disulfide (MoS_2), molybdenum ditelluride ($MoTe_2$), molybdenum sulftotelluride (MoSTe), cobalt doped MoS_2 (Co-MoS_2) and other hybrids. To confirm the successful synthesis of desired products, the scanning electron microscope (SEM), energy dispersive spectroscopy (EDS), EDS mapping, transmission electron microscope (TEM), Raman spectroscopy, x-ray diffraction (XRD), and x-ray photoelectron spectroscopy (XPS) analyses have been performed. Moreover, electrochemical characterizations i.e., cyclic voltammogram (CV), linear sweep voltammogram (LSV), galvanostatic charge-discharge (GCD), electrochemical impedance spectroscopy (EIS), and other tests reveal that the as-produced nanocomposites can be used for hydrogen evolution reaction (HER) to generate useful hydrogen fuel and for electrical energy storage (EES) such as hybrid-capacitor applications. This research also intends to optimize the reaction parameters to improve the electrocatalytic and energy storage behaviors of MC/graphene nanocomposites. This single-step microwave approach can be universally employed to produce other useful MCs and their

hybrids, that will catalyze substantial development in more widespread uses of MC-based nanocomposites for successful energy applications.

The first chapter (Chapter 1) discussed the background, state-of-arts, and motivations for this research work. Current energy issues have been described and the potential solution for these issues through electrocatalysis and energy-storage systems were proposed, where the mechanisms were thoroughly reviewed. Further, the microwave-initiated synthesis of advanced energy materials, such as metal chalcogenides (MCs), were compared with other conventional methods. As well, the physicochemical and electrochemical characterization techniques were explained. The last section of this chapter emphasized on the motivation and objectives of this research.

The second chapter (Chapter 2) focuses on the microwave-initiated synthesis of molybdenum disulfide (MoS_2) on graphene and their characterizations for employing as electrocatalysts for hydrogen evolution reaction (HER). The microwave reaction conditions and the electrocatalytic performances were optimized. Additionally, the issues were addressed that occurred from using the platinum (Pt) counter electrode. Hence, for other projects described in the following chapters, the Pt electrode was replaced with graphite rod electrode.

The third chapter (Chapter 3) described the results obtained for electrocatalytic activities of microwave synthesized $MoTe_2$/graphene nanocomposites. Along with the experimental findings, a collaborative computational study was performed to understand the HER mechanisms and to identify the catalytic active sites in $MoTe_2$/graphene catalyst.

The fourth chapter (Chapter 4) portrayed a comprehensive study on the HER activities of different combinations of metal chalcogenides and their hybrids. Three major parameters (overpotential, Tafel slope, exchange current density) were compared for as-produced nanocomposites.

The fifth chapter (Chapter 5) discussed the synthesis methods and the effects of metal-rich hybrid MCs ($MoS_{0.46}Te_{0.58}$/graphene) on the improvement of HER activities. Based on the combined experimental and computational studies, this work revealed that the excess amount of molybdenum (Mo) in comparison to stoichiometry enhanced the number of active sites in the as-produced nanocomposites, which further improved their HER performances.

The sixth chapter (Chapter 6) focused on studying the impact of cobalt (Co) doping effect on the HER performance of MoS_2/graphene nanocomposite. The doping amount was optimized and revealed the enhancement on electrocatalytic behavior of Co-doped MoS_2/graphene comparing to the undoped counterpart.

The seventh chapter (Chapter 7) depicted the energy storage behaviors of $MoTe_2$/graphene nanocomposite. Based on this study, it was shown that, besides utilizing as electrocatalysts, the as-produced MCs and their hybrids possess promising charge storage abilities, which revealed their potential applications on developing supercapacitors, batteries, and hybrid-capacitors.

Finally, the eighth chapter (Chapter 8) summarized the results and outcomes from all the studied projects. It also described the possible future works to advance this current research.

Acknowledgements

Graduate school is a challenging experience in many ways. I would not have been able to complete this dissertation without help and support from many wonderful mentors, colleagues, friends, and family members. Firstly, I would like to express gratitude to my advisor Dr. Xinyu Zhang for his continuous support towards my doctoral study, for his patience, motivation, and immense knowledge. His guidance and suggestions helped me all along of my Ph.D. research.

I would also like to acknowledge the insightful comments and encouragement provided by my committee members, Dr. Tae-Sik Oh, Dr. Andrew J Adamczyk, Dr. Russell Mailen and Dr. Asha-Dee Celestine in writing this dissertation.

I would like to thank Dr. Ruigang Wang for helping us with material characterization tests. I am thankful to Dr. Andrew J Adamczyk and his student, Ashraf Ali for collaborating with us, who provided an opportunity to explore our research in different ways, most notably by way of atomistic modeling and analysis. Special thanks to Department of Chemical Engineering and to AU-Intramural Grants Program, without their precious support it would not be possible to conduct this research. I thank my fellow group members for the challenging discussions which inspired me to widen my research from various perspectives. I am grateful to Dr. Amit Nautiyal for training me to learn the electrochemical characterization techniques and providing the insights to solve many challenges.

At last, I would like to express my sincere gratitude to my family members and my friends who supported me throughout the years. My husband, Hasnat Hamim who stood by my side through all my struggles, my fits of antipathy and always supported me in the moments when there was no one to answer my queries.

Publications

1. **S. Sarwar**, A. Ali, Y. Wang, M. R. Ahasan, R. Wang, A. J. Adamczyk, X. Zhang, "Enhancement of Hydrogen Evolution Reaction Activity using Metal−rich Molybdenum Sulfotelluride with Graphene Support: A Combined Experimental and Computational Study". (under preparation)
2. **S. Sarwar**, M. Lin, M. R. Ahasan, Y. Wang, R. Wang*, X. Zhang*, "Direct Growth of Co-MoS_2/Graphene Hybrids through Microwave Irradiation with Enhanced Electrocatalytic Properties for Hydrogen Generation". (under review)
3. **S. Sarwar**, A. Ali, Z. Liu, J. Li, S. Uprety, H. Lee, R. Wang, M. Park, M. J. Bozack, A. J. Adamczyk*, X. Zhang*, "Towards Thermoneutral Hydrogen Evolution Reaction Using Noble Metal Free $MoTe_2$/Graphene Nanocomposites", *Journal of Colloid and Interface Science*, 581B, 2021, 847-859.
4. **S. Sarwar**, Z. Liu, J. Li, R. Wang*, X. Zhang*, "High performance hybrid-capacitor based on $MoTe_2$/graphene through ultra-fast, facile microwave-initiated synthesis", *Journal of Alloys and Compounds,* 846, 2020, 155886.
5. **S. Sarwar**, A. Nautiyal, J. Cook, Y. Yuan, J. Li, S. Uprety, R. S. Yassar, R. Wang, M. Park, M. J. Bozack, X. Zhang*, "Facile Microwave Approach towards High Performance MoS_2/Graphene Nanocomposite for Hydrogen Evolution Reaction", *SCIENCE CHINA Materials*, 63(1), 62-74, 2020.
6. G. Li, **S. Sarwar**, X. Zhang, C. Yang, X. Guo, X. Zhang*, D. Wu*, "Surface energetics of carbon nanotubes–based nanocomposites fabricated by microwave-assisted approach", *Journal of Materials Research* (2019), Pages 1-7.

7. J. Wang, **S. Sarwar**, J. Song, L. Du, Q. Guo, T. Li, Y. Zhang, B. Li, J. Luo*, X. Zhang*, "Self-supported CoSe2@NiSe2 nanoflowers on 3D nickel foam for high performance supercapacitors by microwave method". (submitted)
8. S. Liu, **S. Sarwar**, H. Zhang, T. Li, Q. Guo, J. Luo*, X. Zhang*, "The microwave synthesis of porous $CoSe_2$ nanosheets for super cycling performance supercapacitors*", J. Mater. Chem. C*, 2021, 9, 228-237.
9. Y. Tian, H. Du, **S. Sarwar**, W. Dong, Y. Zheng, S. Wang, Q. Guo, J. Luo*, X. Zhang*, "High-performance supercapacitors based on Ni_2P@CNT nanocomposites prepared using an ultrafast microwave approach", *Front. Chem. Sci. Eng.* (2020), Pages 1-12.
10. S. Liu, **S. Sarwar**, H. Zhang, Q. Guo, J. Luo*, X. Zhang*, "One-step microwave-controlled synthesis of $CoV_2O_6.2H_2O$ nanosheet for super long cycle-life battery-type supercapacitor", *Electrochimica Acta, 364,* 2020, 137320**.**
11. Y. Zheng, Y. Tian, **S. Sarwar**, J. Luo*, X. Zhang*, "Carbon nanotubes decorated $NiSe_2$ nanosheets for high-performance supercapacitors", *Journal of Power Sources 452, 2020, 227793.*
12. Y. Tian, **S. Sarwar**, Y. Zheng, Q. Guo, J. Luo*, X. Zhang*, "Ultrafast microwave manufacturing of MoP/MoO_2/carbon nanotube arrays for high-performance supercapacitors", *Journal of Solid State Electrochemistry*, 2020.
13. X. Yang, Y. Tian, **S. Sarwar**, M. Zhang, H. Zhang, J. Luo*, X. Zhang*, "Comparative evaluation of PPyNF/CoO_x and PPyNT/CoO_x nanocomposites as battery-type supercapacitor materials via a facile and low-cost microwave synthesis approach", *Electrochimica Acta*, Volume 311, Pages 230-243.

14. S. Li, C. Yang, **S. Sarwar**, A. Nautiyal, P. Zhang, H. Du, N Liu, J. Yin, K. Deng*, X. Zhang*, "Facile synthesis of nanostructured polyaniline in ionic liquids for high solubility and enhanced electrochemical properties", *Advanced Composites and Hybrid Materials,* 2:279–288.

Table of Contents

List of Figures

List of Tables

List of Abbreviations

EIA	Energy Information Administration	EChem	Electrochemical
ppm	Parts per million	CV	Cyclic voltammogram
EES	Energy storage system	LSV	Linear sweep voltammogram
HER	Hydrogen evolution reaction	EIS	EChem impedance spectroscopy
OER	Oxygen evolution reaction	AC	Alternative current
DFT	Density functional theory	CPE	Constant phase element
MC	Metal chalcogenide	TOF	Turnover frequency
TMD	Transition metal dichalcogenide	GCD	Galvanostatic charge-discharge
rGO	Reduced graphene oxide	Pt	Platinum
EDLC	Electrochemical double-layer capacitor	SAED	Selected area electron diffraction
EC	Electrochemical capacitors	GCE	Glassy carbon electrode
CNT	Carbon nanotube	PVDF	Poly vinylidene fluoride
GO	Graphene oxide	DMF	N, N-Dimethylformamide
CVD	Chemical vapor deposition	ECSA	Electrochemical surface area
vdW	Van der Waals	RHE	Reversible hydrogen electrode
ECS	Energy conversion and storage	TMC	Transition metal chalcogenide
IR	Infrared	PTFE	Polytetrafluoroethylene
RF	Radio frequency	SC	Supercapacitor
MIM	Microwave-initiated manufacturing	CP	Conducting polymer
SEM	Scanning electron microscopy	CC	Carbon cloth
EDS	Energy-dispersive X-ray spectroscopy	ORR	Oxygen reduction reaction
TEM	Transmission electron microscopy	GF	Graphene foam
XRD	X-ray powder diffraction	DNA	Deoxyribonucleic acid
XPS	X-ray photoelectron spectroscopy	RNA	Ribonucleic acid
BET	Brunauer–Emmett–Teller	FET	Field effect transistor

Chapter 1

Introduction

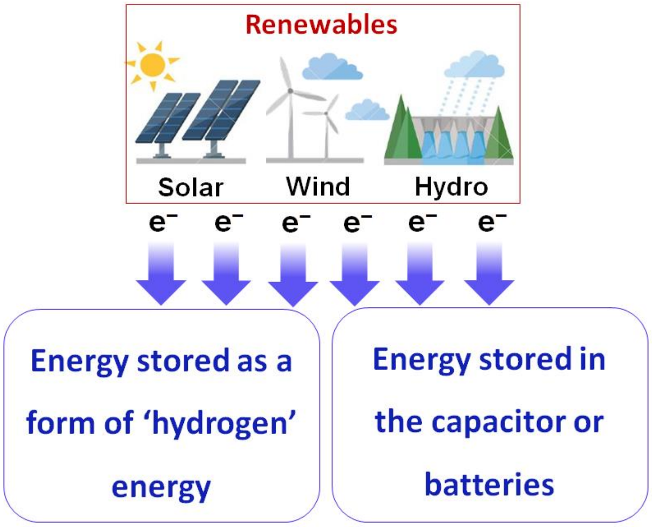

This chapter describes the background, state-of-arts, and motivations for this research work.

1.1. Global energy crisis and renewable energy issues

Based on current global trends, U. S. Energy Information Administration (EIA) projects nearly 50% increase in global energy consumption by the year 2050.[1] Rapid development of technology and the rising world population are the two major driving forces for this steady increase in global energy consumption. It creates the urgent global challenge of current century to fulfill the energy requirements for sustainable development of present and future generations. However, our near-exclusive dependence on fossil fuels is unsustainable, causing the environmental, economic, and safety concerns. In particular, the atmospheric carbon dioxide concentration is already the highest at present comparing to the amount it has been in the last 800,000 years.[2] The present concentration of carbon dioxide in earth's atmosphere is currently at nearly 417 parts per million (ppm) and continuously rising, which signifies an increase of more than 50% than the pre-industrial levels.[3] In this regard, a prompt shift to alternative, sustainable, and carbon-free green energy source has become essential to maintain the earth's ecosystem in balance.

To resolve these global energy crisis and climate issues, recently the renewable energy resources have come forward promisingly. Many infrastructures have already been well-established to supply useful energies from solar, wind, biomass, or hydro energy resources and according to U.S. EIA, the renewable energy will be the leading source of primary energy consumption by 2050, which can be depicted from the data in Figure 1.1a.[1] Moreover, it has been predicted that nearly 40% of the global electricity will be generated from renewables by 2050 (Figure 1.1b).[4] While renewable energy is considered as a promising alternative to traditional fossil fuel, many of these sources still face difficulties in being deployed at a large scale including, but not limited to, technological barriers, high start-up capital costs, and most importantly, the intermittency challenges.[5] Intermittency means the fact that the renewables like solar, hydro or wind can only produce energies when only the nature cooperates. Intermittent energy sources are predictable but cannot be transmitted to meet the demand of an electric power system. Therefore, to resolve this issue, a general approach is that a renewable energy system must have a well-established energy storage system to complement it and reduce the impact of intermittent generation, by storing excess energy for use on demand.

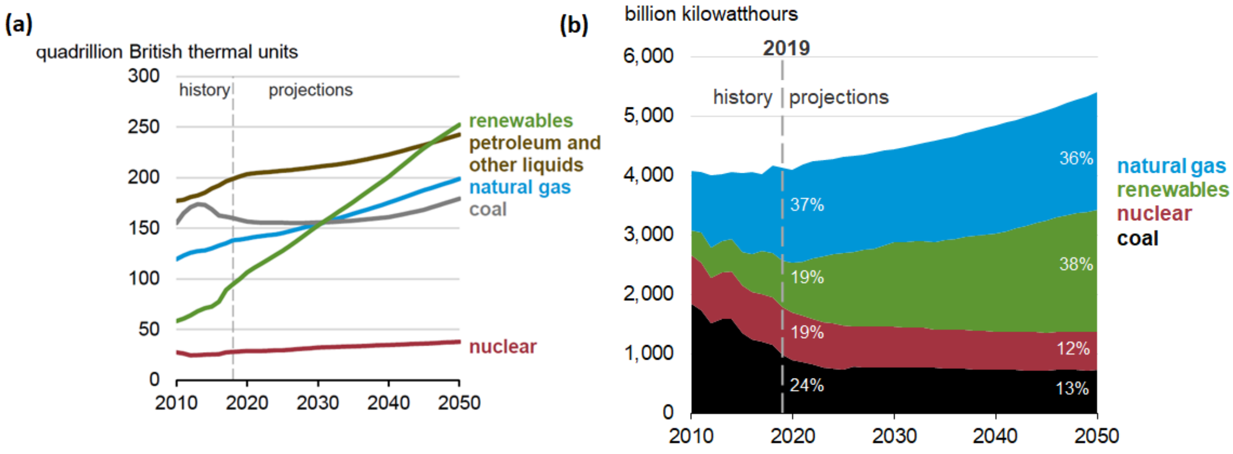

Figure 1.1. (a) Global primary energy consumption by energy sources (2010−2050). (b) Electricity generation from selected fuels. (Source: U.S. Energy Information Administration, International Energy Outlook 2019 and 2020).[1,2]

1.2. Solution to the intermittency challenges

To resolve the intermittent nature of renewable energy, storing the excess renewable power to use when electricity demand exceeds supply is a promising way. While energy storage comes in many forms, hydrogen energy and supercapacitor energy storage are the two solutions emerged promisingly in recent years to resolve the renewables' intermittency problems.

1.2.1. As a form of ‘hydrogen’ energy

Hydrogen is considered as a promising energy carrier for the intermittent renewable resources, which contains an energy density of 143 MJ kg^{-1}, nearly three times higher than the liquid hydrocarbon-based fuels.[6,7] Moreover, as hydrogen remains usually bonded with other materials, mainly with carbon and oxygen, this energy is not available as a naturally separated material in consumable scale in nature. As shown in Figure 1.2, hydrogen can be generated through water electrolysis process using the electricity generated from renewable energy resources (solar, wind or hydro). Later, hydrogen energy is stored, transported, and utilized in fuel cell or combustion engines. During the consumption, hydrogen combines with oxygen and generates useful energy, as well as by-product water is formed. Therefore, hydrogen from water electrolysis is popularly known as ‘green energy’, which does not produce any greenhouse gases.

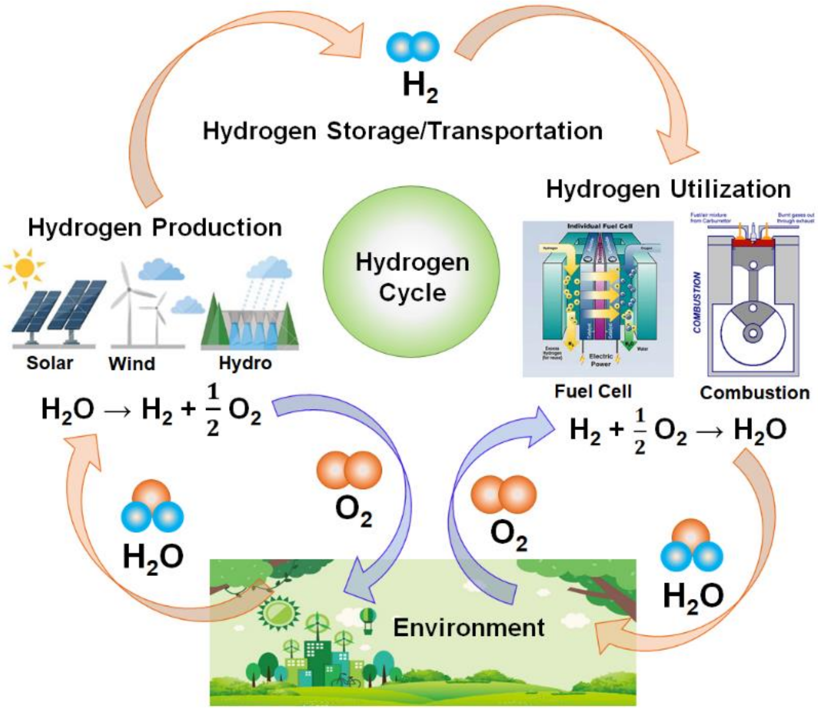

Figure 1.2. Hydrogen energy cycle from production to utilization steps.

1.2.2. Energy stored in capacitors/batteries

In addition to generating hydrogen, the electricity from renewables can also be stored in different energy storage systems (EES). Among them, the capacitor and battery storage systems are the most popular ways (Figure 1.3), where the energy can be stored directly in electric field for capacitors or as chemical energy in batteries during charging that converts to electrical energy during discharging.

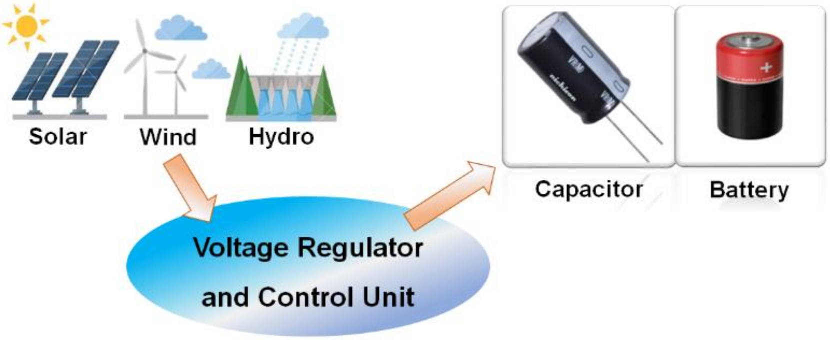

Figure 1.3. Energy stored systems (EES): capacitor and battery.

Benefiting from the high-power density of capacitor and high-energy density of battery, a new concept of supercapacitor has widely been emerged that combines both storage mechanisms to provide high energy and power density behaviors, which is known as 'hybrid supercapacitor' system.[8,9]

1.3. 'Hydrogen' as energy carrier

Unlike fossil fuels, hydrogen is an 'energy carrier' rather than a primary energy source,[10] meaning it is capable of transferring energy from one form to another. However, hydrogen must first be extracted from compounds such as hydrocarbons or water.

1.3.1. Hydrogen production methods

Hydrogen can be produced from different resources, including fossil fuels, such as natural gas and coal, nuclear energy, and other renewable energy sources, such as biomass, wind, solar, geothermal, and hydro-electric power, using a wide range of processes. A summary of the major ways to produce hydrogen is explained in Table 1.1.[11] Unfortunately, fossil-based fuels are still the main resource for industrial mass scale hydrogen production due to their low costs and easy usage in machines that designed for fossil fuels. This fact is absolutely in contradiction with policies towards a green and sustainable energy cycle.

Table 1.1. Major hydrogen production methods.

Method	**Process**	**Implementation**
Steam reforming of methane gas	$CH_4(g) + H_2O(l) \xrightarrow{\text{Ni, } 700-1100^{0}\text{C}} CO(g) + 3H_2(g)$ $CO(g) + H_2O(l) \xrightarrow{\text{low temperature}} CO_2(g) + H_2(g)$	Current major source of hydrogen
Coal gasification	$\text{Coal} + H_2O(l) + O_2(g) \xrightarrow{\text{high T \& P}} \text{Syngas}$ Syngas = $H_2 + CO + CO_2 + CH_4$	Current method of mass hydrogen production
Electrolysis or Photo-electrolysis	$2H_2O(l) \xrightarrow{\text{electricity or sunlight}} 2H_2(g) + O_2(g)$	Not in widespread use due to high cost

Nowadays, steam reforming of methane gas is known as the most economical method and has the largest share in global hydrogen production of nearly 48% (Figure 1.4).[6,12] Coal and oil have the second and third place in this ranking with 30% and 18% relative shares, respectively. Hydrogen production by the means of water electrolysis has the smallest share of

4% among the available methods of large scale hydrogen production.[6] Although the first two are the most popular methods to produce hydrogen, usually emit CO or CO_2 and other greenhouse gasses. Moreover, the resources are not renewable. In this regard, the electrolysis process is solely the green and sustainable approach.

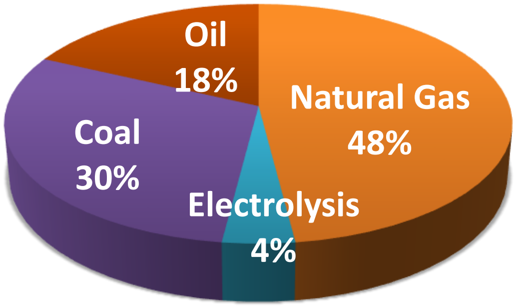

Figure 1.4. Relative shares of hydrogen production from different sources.

High production costs due to low conversion efficiency and electrical power expenses are the main drawbacks of electrochemical hydrogen production through water electrolysis. A typical electrolyzer consumes up to 50 kWh kg^{-1}. Therefore, many efforts are made to increase the efficiency of water electrolysis.[13,14] Higher efficiencies are obtained in extreme pressure and temperature conditions. At the same time, increased investment is required to build more complex and sophisticated electrolyzers which perform under intense conditions. In these cases, higher production efficiency comes with dramatically increased corrosion, operation and maintenance costs and reduced life span. Despite the mentioned cost disadvantages, water electrolysis has some unique qualities. The only requirements of this production are electricity and water. Moreover, this method can produce absolutely sustainable and clean hydrogen. This goal can be achieved if and only if the required electricity is obtained from an emission-free method such as wind, solar, geothermal systems, ocean wave or other renewable and green sources. Therefore, the idea of utilizing electricity from renewable energies can be the most promising way to produce sustainable hydrogen energy, along with solving the intermittency issues of renewable energy resources.

1.3.2. Hydrogen evolution reaction (HER) in water electrolysis

In 1789, water electrolysis was first reported by Troostwijk and Deiman who observed the decomposition of water into its constituent elements by an electric discharge.[15] Water electrolysis is therefore defined as the splitting of water into hydrogen and oxygen using electricity by performing the hydrogen evolution and oxygen evolution reactions. As shown in Figure 1.5, water splitting consists of two half-cell reactions, where oxidation takes place on anode generating oxygen (O_2) gas and reduction takes place on cathode generating hydrogen (H_2) gas, following the reactions below (Equation 1.1 and 1.2). Equation 1.3 represents the overall reaction of water electrolysis (at pH = 0).[6]

Oxidation: $2H_2O \rightarrow 4H^+ + 4e^- + O_2$, $E° = 1.23$ V vs. RHE ……………..………….……….. (1.1)

Reduction: $4H^+ + 4e^- \rightarrow 2H_2$, $E° = 0.00$ V vs. RHE ……….……………………………...... (1.2)

Overall: $2H_2O \rightarrow 2H_2 + O_2$, $E°_{cell} = -1.23$ V vs RHE…………………………………….... (1.3)

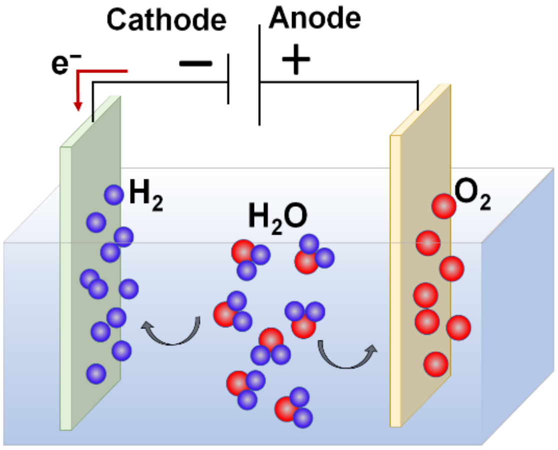

Figure 1.5. Electrochemical water electrolysis cell showing hydrogen and oxygen evolutions on cathode and anode, respectively.

The Equation 1.2 is known as hydrogen evolution reaction (HER), which is the reduction of protons or water to hydrogen molecules (H_2) on applying external potential or electrochemical energy. To split water into hydrogen and oxygen, the lowest limit of potential 1.23 V is required. However, this voltage is calculated thermodynamically which is a theoretical value. Based on kinetics in practical electrochemical cell, higher voltage is required depending on the electrode materials. This required energy barrier is called the overpotential (η). Therefore, a suitable catalyst is generally required to minimize the activation energy by reducing the overpotential of the system for efficient hydrogen production through water electrolysis process.

1.3.2.1. Thermodynamics

Water electrolysis is a non-spontaneous process, which requires a positive Gibbs free energy of $\Delta G^o = +237.23$ kJ mol^{-1} at room temperature, as calculated by Equation 1.4.[16]

$$\Delta G^o = \Delta H^o - T\Delta S^o = -nFE^o_{cell} \quad (1.4)$$

Where, ΔG^o is the change in Gibbs free energy, ΔH^o is the change in enthalpy (285.8 kJ mol^{-1}), ΔS^o is the change in entropy (163 J K^{-1} mol^{-1}), T is the temperature (K), n is stoichiometric number of moles of electrons involved in the reaction (here, $n = 2$), F is the Faraday constant (96485 C mol^{-1}) and E^o_{cell} is the cell potential (V). The minimum potential required for the overall water splitting reaction is governed by the conditions within the electrolyzer, *e.g.* temperature, pressure, and *pH* value. For example, at 0 K, E^o_{cell} is equal to 1.48 V, while at room temperature (298.15 K) energy acquires from the surroundings in the form of heat, and the minimum potential is lowered to 1.23 V. Therefore, the splitting of water becomes easier with increasing temperature. Similarly, *pH* has a profound effect on the required potential. In accordance with moving away from the standard conditions, the Nernst equation can be written as shown in Equation 1.5**.** Subsequently, the potential under non-standard conditions is defined by the Equation 1.6.[17]

$$\Delta G = \Delta G^o + RT\ln Q \qquad (1.5)$$

$$E = E^o - \frac{RT}{nF}\ln Q \qquad (1.6)$$

Where, R is the gas constant, T is the absolute temperature and Q is the reaction quotient. Q is defined as the ratio of activities of the oxidant and reductant species. Therefore, the effect of pH can be investigated by setting Q equal to the concentration of protons [H^+] and converting the natural log to $\log_{10}$. At standard temperature, Equation 1.6 can be rearranged into the following equation (Equation 1.7):

$$E = E^o - \frac{0.059}{n}\log[H^+] = E^o - \frac{0.059}{n}pH \qquad (1.7)$$

Accordingly, for every 1 pH unit change, the potential shifts by 0.059 V. The potentials required for the oxygen evolution reaction (OER) and hydrogen evolution reaction (HER) at varying pH values can therefore be written as Equation 1.8 and 1.9, respectively.

$$E_{OER} = 1.23 - 0.059\,pH \qquad (1.8)$$

$$E_{HER} = 0.00 - 0.059\,pH \qquad (1.9)$$

Since, in acidic conditions, both OER and HER are proton dependent, both reaction potentials shift by the same magnitude, meaning a constant cell potential of 1.23 V is required for the overall reaction, regardless of pH.

1.3.2.2. Overpotential, η

Although, the theoretical potential required for water electrolysis is 1.23 V, an excess of this value is required in practical applications, which is known as the *overpotential* (η). The overpotential is the difference between the thermodynamically required potential and the experimentally observed potential. If a cell has a defined equilibrium potential (E_{eq}), that potential is an important reference point for that system. The change of the electrode potential (or cell potential) from the equilibrium value upon passage of faradaic current is termed as *polarization.* The extent of polarization is measured by the *overpotential,* $\eta = E - E_{eq}$.[18] This overpotential arises due to several resistances within the system. Equation 1.10 highlights that the increase in energy inputs arises from the overpotentials associated with the anode and cathode, and the internal resistance of the water electrolysis cell (iR). Overpotentials arise due to energy being lost within the system, therefore, in order to drive the reaction, a higher voltage than theoretically calculated voltage is required.[19]

$$E_{total} = 1.23 + \eta_{anode} + \eta_{cathode} + iR \quad \ldots\ldots\ldots\ldots\ldots\ldots\ldots\ldots\ldots\ldots\ldots\ldots \quad (1.10)$$

The resistance (R) associated with the solvent is related to the conductivity of the electrolyte solution. This can be minimized by decreasing the *pH* of the electrolyte, since protons possess the highest ionic conductivity. Hence, conductivity increases with decreasing *pH,* which lowers the resistance. In addition, the electrodes play important roles in the setup of an electrochemical cell. The greater the distance between anode and cathode, the greater the resistance. Therefore, the positioning of the electrodes within the cell is of utmost importance. Further, overpotentials arise due to electron transfer between electrolyte and electrode surface (η_{anode} and $\eta_{cathode}$). These overpotentials can be minimized by applying an electrocatalyst to the electrode, which is currently an area of extensive research (see Section 1.4).

1.3.2.3. HER kinetics

The rate of HER is tested by the current through the circuit based on the following *current-overpotential relation*:[18]

$$i = i_0 \left[\frac{C_0 e^{-\alpha f \eta}}{C_0^{*}} - \frac{C_R e^{(1-\alpha) f \eta}}{C_R^{*}}\right] \quad \cdots\cdots\cdots\cdots\cdots\cdots\cdots\cdots\cdots\cdots\cdots\cdots \quad (1.11)$$

Where, C_0 and C_R represent surface concentrations, C_0^* and C_R^* are the bulk concentrations, i_0 is the exchange current density, α is the transfer coefficient (varies from 0 to 1), f represents the relation of $\frac{nF}{RT}$ (here, n = no. of electrons transferred during the cell reaction, F = Faraday constant, R = universal gas constant, T = absolute temperature), and η represents the overpotential. In this equation, the first term describes the cathodic current at any potential, and the second gives the anodic contribution. The behavior of the Equation 1.11 is predicted by depicting in Figure 1.6.

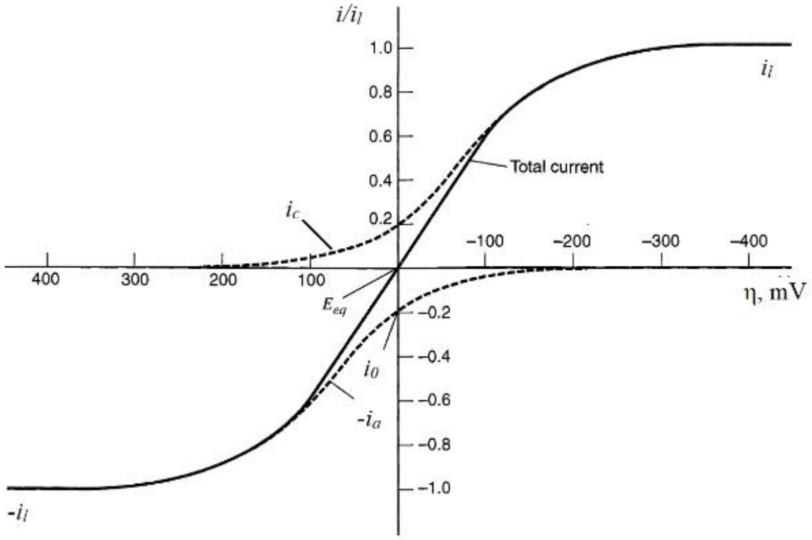

Figure 1.6. Current-overpotential curve for one step, one electron process; with $\alpha = 0.5$ (rates of anodic and cathodic reactions are equal), and $T = 298.15$ K (room temperature).[18]

The solid curve shows the actual total current, which is the sum of the components i_c (cathodic current) and i_a (anodic current), shown as dashed traces. For large negative overpotentials, the anodic component is negligible, hence the total current curve merges with that for i_c. At large positive overpotentials, the cathodic component is negligible, and the total current is essentially the same as i_a. In going either direction from equilibrium potential (E_{eq}), the magnitude of the current rises rapidly, because the exponential factors dominate behavior, but at extreme η, the current levels off. In these level regions, the current is limited by mass transfer rather than heterogeneous kinetics. The exponential factors in Equation 1.11 are then moderated by the factors $\frac{C_0}{{C_0}^*}$ and $\frac{C_R}{{C_R}^*}$, which manifest the reactant supply.^{18} If the electrolyte solution is well stirred in a system, or currents are kept so low that the surface concentrations do not differ appreciably from the bulk values, then the Equation 1.11 becomes:

$i = i_0\ [e^{-\alpha f\eta} - e^{(1-\alpha)f\eta}]$ ……………………………..…………………………...……… (1.12)

Which is historically known as the *Butler-Volmer equation.* For large values of η (either negative or positive) one of the terms (anodic or cathodic) becomes negligible. For example, is case of HER, at large negative overpotentials, it shows $e^{-\alpha f\eta} >> e^{(1-\alpha)f\eta}$. Thus, the following equation can be derived from Equation 1.12:

$i = i_0\ [e^{-\alpha f\eta}]$ …...…………………………………………………………..…..……...… (1.13)

Therefore, $ln\ (\frac{i}{i_0}) = -\frac{\alpha nF}{RT}\eta$ as, $f = \frac{nF}{RT}$

Taking $n = 1$, $\eta = \frac{RT}{\alpha F} ln\ (i_0) - \frac{RT}{\alpha F} ln\ (i)$ ………………...………………………..……. (1.14)

Thus, the kinetic relation outlined above yields an equation that the current increases exponentially with overpotential (η), which provides the *Tafel equation* (Equation 1.15):

$\eta = a + b \log(i)$ ……………..…………………………..………………….…….. (1.15)

Where, $a = \frac{2.3RT}{\alpha F} log\ (i_0)$ and $b = \frac{-2.3RT}{\alpha F}$.

If the electrode kinetics are facile, the system will approach the mass-transfer-limited current by the time such an extreme overpotential is established. Tafel relationships cannot be observed for such cases because they require the absence of mass-transfer effects on the current. When electrode kinetics are sluggish and significant activation overpotentials are required, good Tafel relationships can be seen. This point underscores the fact that Tafel behavior is an indicator of totally irreversible kinetics. Systems in that category allow no significant current flow except at high overpotentials, where the faradaic process is effectively unidirectional and, therefore, chemically irreversible.

A plot of 'log *i* vs η' known as a *Tafel plot,* is a useful tool for evaluating kinetic parameters.[18] Tafel plots represented in Figure 1.7 can be divided into three parts theoretically. Diffusion zone locates at high potential region, Tafel zone at middle region, and polarization zone at low potential area. In general, there is an anodic branch with slope $\frac{(1-\alpha)F}{2.3RT}$ and a cathodic branch with slope $\frac{-\alpha F}{2.3RT}$. Here, both linear segments extrapolate to an intercept of log i_0. The plots deviate sharply from linear behavior as η approaches zero, because the back reactions can no longer be regarded as negligible.[18] From this behavior, two important parameters are extracted, exchange current density (i_0) and Tafel slope (b), which are considered as major criterions for the electrocatalytic activity of HER catalysts.

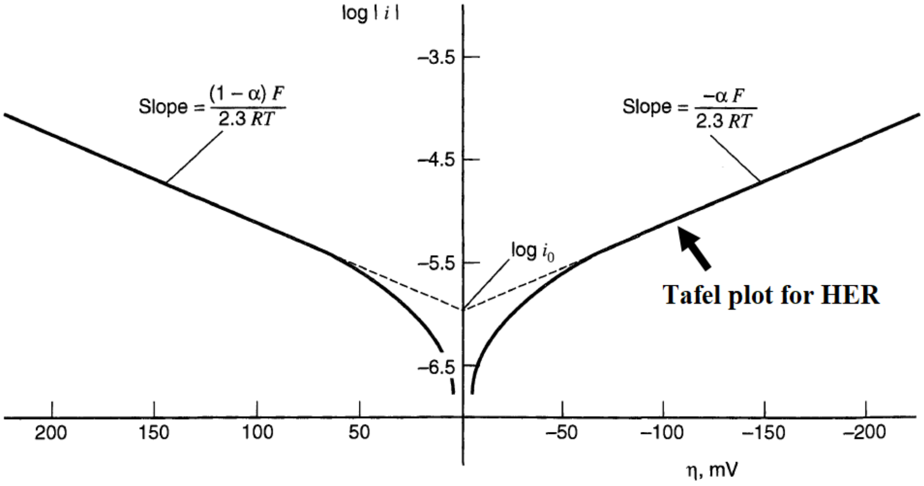

Figure 1.7. Tafel plots for anodic and cathodic reactions of the current-overpotential curve; with $\alpha = 0.5$, $T = 298$ K, and $i_0 = 10^{-6}$ A/cm^2.[18]

The constant b, defined as Tafel slope, an inherent property of the catalysts, is related to the reaction mechanism of a catalyst and is determined by the rate-limiting step of the HER. On the other hand, the exchange current density (i_0) suggests the catalytic activity. The value of i_0 depends on several factors, including the reaction pathway, concentration ratio of oxidized (C_o) and reduced (C_R) species, temperature, and the adsorption conditions of the active site.

1.4. HER electrocatalysts

1.4.1. Background

As discussed in Section 1.3.2.2, an excess of energy known as the overpotential (η) is required in order to drive the water splitting reaction. To reduce this overpotential as close to the thermodynamically required energy input as possible (0 V vs. RHE), electrocatalyst is applied to the electrode. The choice of the HER electrocatalysts employed at the cathode can have a profound influence on the cost, lifetime, and efficiency of the electrolyzers. So far, the HER is catalyzed most effectively by platinum (Pt) and Pt-group metals in acidic medium due to their optimum hydrogen binding free energy (ΔG^{0}_{H*}) and low activation energy for H desorption from Pt-surface. However, the large-scale application of Pt catalysts is limited by their high cost and scarcity. Therefore, the limited world-wide supply of Pt makes its use a barrier to mass production of H_2 by water electrolysis. The replacement of Pt with other noble metals such as palladium (Pd), rhodium (Rh), ruthenium (Ru) etc. demands a compromise in activity, and these Pt-group metals are equally as scarce.[20] In terms of the viability of fuel cell technologies, the only option is to replace Pt with an earth abundant alternative. Despite compromising on the activity, i.e. greater overpotentials being required, the development of cheap and earth abundant electrocatalysts for the HER has been a dominating field of research in recent years. Non-noble metals, namely molybdenum and nickel-based compounds have been increasing in interest as a potential replacement for platinum. To develop an efficient electrocatalyst, it is important to understand the mechanism how this catalyst assists to enhance the HER performance.

1.4.2. HER mechanisms

For hydrogen to be evolved, the hydrogen atoms must adsorb on to the surface of electrocatalyst for the reaction to take place, and subsequently desorb, allowing for the release of the gaseous product. The underlying electrochemical processes which described the mechanism of hydrogen evolution are illustrated in Figure 1.8.[21,22]

The mechanism of the HER is supposed to go *via* either the ‘Volmer–Heyrovsky’ mechanism or ‘Volmer-Tafel’ mechanism.[23–25] Both mechanisms involve the Volmer step (Equation 1.16), otherwise known as the discharge step. This involves the initial adsorption of protons form the acidic electrolyte on to the catalyst surface to form adsorbed H (H_{ads}). The

Volmer step is usually considered to be fast, with the rate determining step being either of the two subsequent steps.[24] These two possible routes are the Tafel step (Equation 1.17) or the Heyrovsky step (Equation 1.18).[22,26]

Volmer: $H^+ + e^- \rightarrow H_{ads}$ …………………………………….……………...………….. (1.16)

Tafel: $2H_{ads} \rightarrow H_2$ ……………………………………………………………….……..… (1.17)

Heyrovsky: $H_{ads} + H^+ + e^- \rightarrow H_2$ ………………………………………………...…….. (1.18)

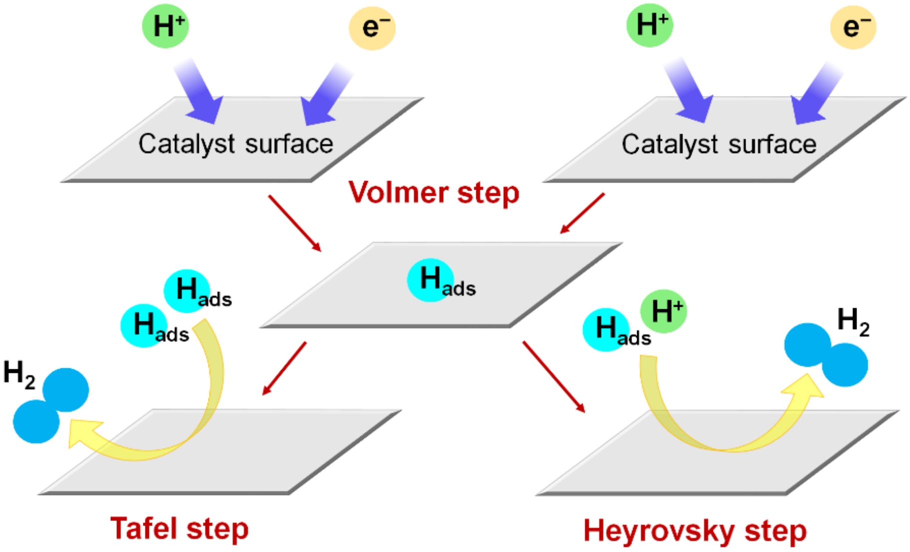

Figure 1.8. The HER mechanisms (Volmer to Tafel or Heyrovsky pathways) on the catalyst surface in acidic electrolyte.

Platinum is known to occur via the Volmer-Tafel mechanism, with Tafel step, also known as the recombination step, being rate-limiting step. This step involves the combination of two adsorbed H-atoms and can be predicted to occur when a Tafel slope of ~30 mV dec^{-1} is obtained. Alternatively, the Heyrovsky step involves ion-atom recombination during which a proton reacts with the adsorbed H-atom on the catalyst surface and produces the hydrogen gas.

Provided the Volmer reaction is fast, the Tafel slope for Volmer-Heyrovsky reaction mechanism is ~40 mV dec^{-1}. In some instances, the Volmer step may be rate-limiting, in which case the Tafel slope is expected to be ~120 mV dec^{-1}.[27]

1.4.3. Volcano plot

From Sabatier's principle, it follows that the energy of hydrogen adsorption should neither be too high nor too low.[28] At excessively endothermic (high) energies, adsorption of hydrogen on the catalyst substrate is slow, at particularly exothermic (low) energies, desorption is slow, thus the overall rate is limited in both cases. In other words, hydrogen must bind strongly enough to the catalyst surface for the reaction to take place, but if the binding energy is too strong, then the product cannot desorb. On the other hand, if the binding energy is too weak, then the hydrogen will be unable to bind to the catalyst surface, and no reaction will take place. For HER, the maximum efficiency is achieved at the equilibrium potential when the free energy of hydrogen adsorption is close to zero.[29] Therefore, metal-hydrogen binding energy has been considered for HER activity, which is known as *Gibbs free energy* of adsorbed atomic hydrogen (ΔG^0_{H*}).

A trend which led to the identification of possible electrocatalysts for the HER was first identified by Trasatti in 1971,[30] who coined the *Volcano plot* correlation of exchange current density of various metals with their chemisorption energy of hydrogen. In general, the exchange current density is unanimous with the reaction rate at the equilibrium potential, and is extrapolated from the Tafel slope at $\eta = 0$ V. The *Volcano plot* is very useful to summarize the HER activities of various metal catalysts, which is based on density functional theory (DFT) calculations. As shown in Figure 1.9,[31] the exchange current density (i_0, mA cm^{-2}) for different catalysts in acids are plotted as a function of the *Gibbs free energy* ($\Delta G^0_{H^*}$, eV).[31]

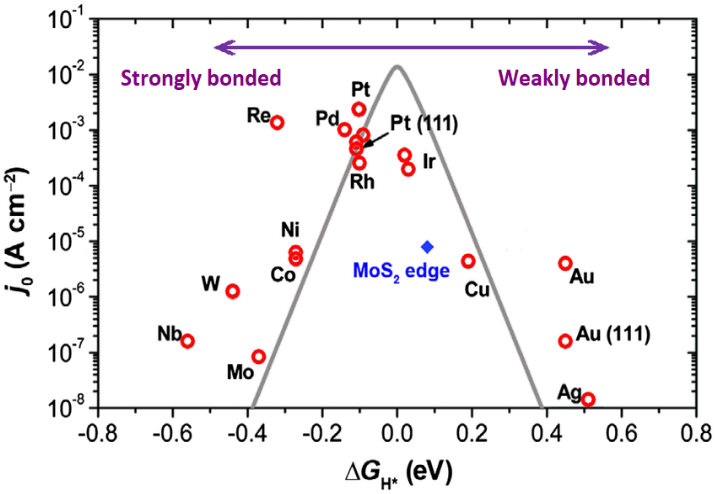

Figure 1.9. Volcano plot of different metal-catalysts for hydrogen evolution reaction (HER).

This DFT calculation helps to determine the thermochemistry (which is independent of the desorption step, Heyrovsky or Tafel) of the reaction. By calculating the free energy of atomic hydrogen bonding to the catalyst, different metal surfaces are compared as HER catalysts. It is obvious that for a chemical process to proceed at or around room temperature, no reaction step can be associated with large changes in the free energy, $\Delta G^0_{H^*}$. This immediately excludes the metals that form strong bonds to atomic hydrogen (Mo, W, etc. in Figure 1.9) as good catalysts because the adsorbed H atoms block the active sites, thus the hydrogen release step becomes slow. Metals that bind atomic hydrogen too weakly (Au, Ag, etc. in Figure 1.9) are also excluded because, they fail to stabilize the intermediate state, thus the proton/electron-transfer step becomes thermodynamically very slow. An optimal HER catalyst should provide catalytic surfaces that exhibit a Gibbs free energy of adsorbed hydrogen close to zero (e.g., $\Delta G^0_{H^*} \approx 0$ eV). Thus, the promising catalyst lies at the top of the curve (Pt, Pd, etc. in Figure 1.9), which is neither binding the intermediate H* too weakly nor too strongly. In recent studies, an alternative interpretation of Sabatier's principle has emerged suggesting that the adsorption free energy evaluated at an applied overpotential should be thermoneutral particularly for very active electrocatalysts,[32,33] where as in the established interpretation the thermoneutrality of the free energy value at zero applied overpotential ($\eta = 0$) is considered as the preferable indicator for the electrocatalytic activity.[34] This is the reason Pt is a commonly chosen catalyst for the HER. Importantly, by comparison of the exchange current densities of the common metals at their corresponding ΔG^0_{H*}, the value for molybdenum disulfide (MoS_2) just lies below those of the noble Pt group metals (Figure 1.9), suggesting the great potential of MoS_2-based materials as an alternative to Pt for the HER.

1.4.4. Metal chalcogenides (MCs) as HER electrocatalysts

Since graphene was discovered in 2004, two-dimensional (2D) inorganic nanomaterials, such as metal chalcogenides (MCs) have received extensive consideration, on account of their attractive structures and properties.[35] MCs are the chemical compounds consisting of at least one chalcogen (e.g. sulfur, selenium or tellurium) and at least one electropositive (e.g. metal) element. Different possible combinations of metals and chalcogens are shown in Figure 1.10.

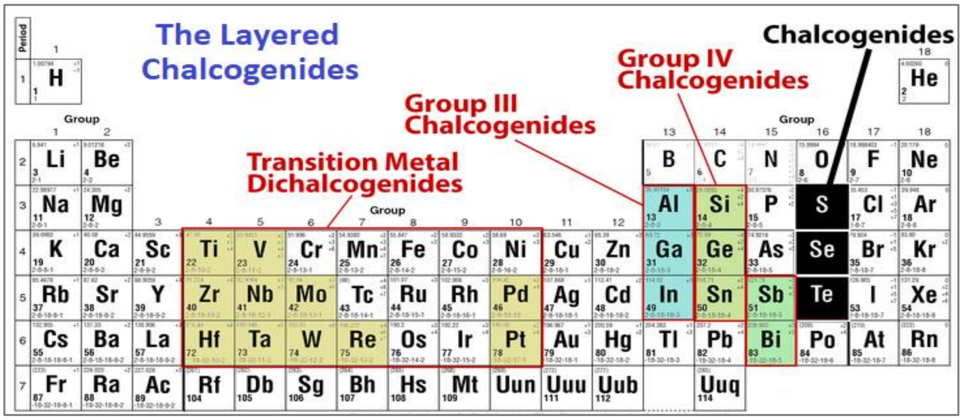

Figure 1.10. The periodic table highlighting the Chalcogenide families of elements. *[Image: Joshua Robinson / Penn State; https://news.psu.edu/photo/466006/2017/05/01/2d-stenciling]*

Among them, the layered structures of transition metal dichalcogenides (TMDs) are the excellent candidates for electrocatalysis, that consist of stacked planes of covalently bonded chalcogen and metal atoms, and the adjacent layers are connected by van der Waals interactions. They often crystallize to form atomically smooth thin films, nanotubes, and platelet or fullerene-like nanoparticles due to the anisotropic bonding. In addition, MCs tend to be more electrochemically reversible as compared to metal oxide counterparts due to their faster charge transfer kinetics, which is beneficial for their electrochemical applications.[36,37]

Molybdenum disulfide (MoS_2) is the most studied acid stable earth abundant HER catalyst. According to DFT calculations, hydrogen evolution on MoS_2 is expected to take place predominantly at the Mo-edge ($\Delta G^0_{H^*}$ = 0.08 eV) rather than the S-edge ($\Delta G^0_{H^*}$ = 0.18 eV).[38] Only the edges of MoS_2 are interesting in this context, as the basal plane of MoS_2 is catalytically inactive due to its unfavorable $\Delta G^0_{H^*}$ of 2 eV. This prediction was further confirmed experimentally on MoS_2 nanoparticles by systematically varying terrace and edge site densities, where a linear correlation between the exchange current density and MoS_2 edge length was established.[39] That is the reason why bulk MoS_2 is not an active catalyst for HER because not enough edge sites are exposed. As a result, efforts have been focused on exposing the catalytic edge sites by engineering the morphology of MoS_2. In this context various strategies have been explored through the development of various nanostructures in the form of ordered architectures, vertically aligned nanosheets, flowerlike nanosheets, micro-boxes and nanoparticles. Hinnemann et al. theoretically proved that unstable edges of layered MoS_2 nanocrystals are the catalytically active sites for HER.[40] Once the nature of the active site on MoS_2 had been identified, researchers have focused on finding ways to increase the number of active edge sites of MoS_2 to make excellent electrocatalysts. The first approach was simply to create more active sites on either a per mass basis or per area basis. Structures that predominately expose edges of the layers exhibit high surface energy and are often considered unstable. Kong, et al. have successfully synthesized the metastable MoS_2 and $MoSe_2$ films with vertically aligned layers (Figure 1.11) through a kinetically controlled rapid growth method that preferentially exposes the edge sites over terrace sites and exhibit remarkable HER activity.[41]

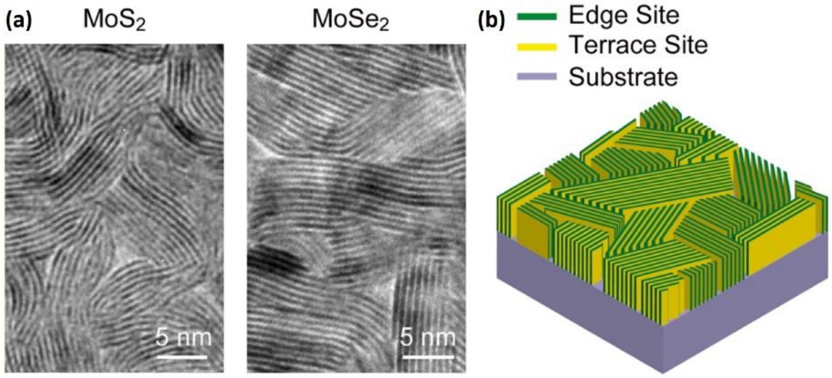

Figure 1.11. (a) Lattice fringes of MoS_2 and $MoSe_2$ films, showing exposed edges. (b) Idealized structure of MC-based electrocatalyst.

To improve the efficiency of TMDs as HER catalysts, the identification of their active sites is vital. Differing HER catalytic activities have been reported for TMDs of various structures; hence, it is essential to relate the HER activity to the TMD structure. Three main factors govern the HER performance of the TMDs: (i) HER active sites; (ii) the intrinsic catalytic activity of TMDs; and (iii) their conductivity.[42] Though initially MoS_2 was known to be an active HER catalyst because of its active edge sites, Nørskov et al. first reported the activation and optimization of the basal plane for the enhancement of HER activity by creating sulfur vacancies and strain on the basal plane of MoS_2.[43] Theoretical and experimental studies also support the fact that by creating pores and strain, new catalytic sites can be generated in the basal plane of

MoS_2, where hydrogen can bind directly to the exposed Mo atoms. Another approach to increase performance is to deposit small MoS_2 particles on a conducting, high surface area substrate. Although the initial work by Hinneman et al. was done on carbon paper,[40] the Dai et al. integrated MoS_2 with reduced graphene oxide (RGO) sheets and achieved better result towards HER activity.[25] Hydrothermally synthesized graphene-MoS_2 composites also showed much better HER activity and a low onset potential compared to MoS_2, where graphene provided better electrical coupling to the electrode.[25] Incorporation of small wt.% of graphene in the composites increases the activity with the graphene acting as an electron collector and enhancing the charge separation. Also, the addition of a small amount of dopants, such as cobalt (Co), niobium (Nb), manganese (Mn), etc. to the MoS_2 can increase the exposure of active sites, which increases the electrocatalytic performance.[44] Moreover, the MC-heterostructures (such as $MoS_2/MoSe_2$, $MoS_2/MoTe_2$, etc.) can show great potential as active materials for HER.[45–48] Considering all these factors to enhance electrocatalytic performance, present study focuses on exploring different metal chalcogenides on graphene substrate, as well the effect of substitutional doping on their catalytic activity of hydrogen generation in acidic electrolyte.

1.4.5. Substitutional doping effects on HER electrocatalysts

Heteroatomic doping would occur when other atoms enter the crystal, which can be divided into two types: substitutional heteroatomic defects and interstitial heteroatomic defects. Whether a heteroatom can enter the crystal of the materials and further replace one of the atoms depends on the energy effect (including electrostatic interaction energy and bond energy between ions) and the corresponding volume effect. A heteroatom should go to a position that is analogous to its electronegativity. If the heteroatomic electronegativity of a crystal material is not different from each other, or if the electronegativity of heteroatom is between them, geometric factors such as the size of heteroatoms will be the main factors that determine whether the doping process can be carried out. In various intermetallic compounds or covalent compounds, elements with similar atomic radius can replace each other. According to the kind of inducing heteroatoms, heteroatomic defects can be divided into nonmetal heteroatomic doping and metal heteroatomic doping. More and more researchers are beginning to pay attention to the significant role of heteroatomic doping, which plays a vital role in increasing electrical conductivity and inducing more defects. Recently, a large number of experiments have suggested that many electrocatalysts show better activity after being doped with many common heteroatoms (nonmetal atoms: F, O, S, N, P, B, and metal atoms Fe, Co, Ni, Cu, Mn, Zn, etc.).[43]

1.5. Electrochemical energy storage applications

In order to achieve a sustainable and renewable energy future, it is important to develop efficient energy storage systems, especially to store the energy produced from intermittent sources such as hydro, solar and wind to utilize the energy as per necessity.

1.5.1. Energy storage mechanisms

Charge storage mechanisms can be divided into three major types: batteries, supercapacitors (EDLC and pseudo-capacitors) and a new type of intercalative pseudocapacitors or hybrid capacitors.[49–51] The capacity of current rechargeable batteries mainly depends on the intercalation/de-intercalation or diffusion of cations (H^+, Li^+ or Na^+) within the crystalline structures of electrode materials, coupled with the redox reactions of metal ions within the crystalline framework (Figure 1.12a). As example, the charge/discharge of conventional Li-ion batteries depends on Li^+ intercalation/de-intercalation. It should be noted that the mechanisms involved in all rechargeable batteries also involve ‘phase-transformation’ and/or alloying reactions, besides the intercalation reaction mentioned above. On the other hand, the capacitance of supercapacitors mainly arises from surface reactions of electrode materials, including electrochemical adsorption/desorption of cations and anions at the electrode/electrolyte interface (i.e., capacitive behavior, Figure 1.12b), and surface faradic redox reactions (i.e., pseudocapacitive behavior, Figure 1.12b). Accordingly, supercapacitors can be classified as electrochemical double-layer capacitors (EDLCs) and pseudocapacitors.[52–54] EDLCs store and release energy by electrostatic charge accumulation at the electrochemical interface between and electrode and electrolyte.[55] This is achieved by adsorption of anions and cations of electrolyte at the electrode/electrolyte surface. In recent years, porous carbon has been widely used as the electrode material for EDLCs.

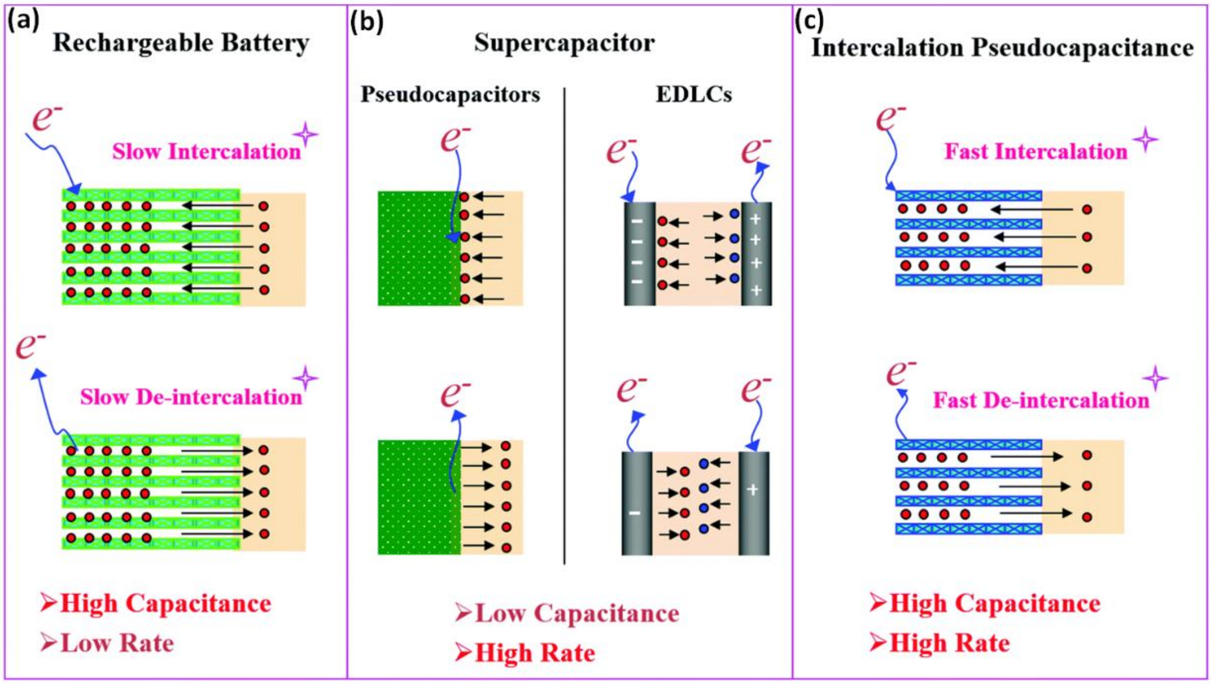

Figure 1.12. Schematic of different energy storage mechanisms: (a) Rechargeable battery, (b) Supercapacitor (pseudocapacitor and EDLC) and (c) Intercalation pseudocapacitor.[55]

Additionally, the pseudocapacitors store energy electrochemically by intercalation of electrolyte ions into the electrode and then by undergoing electron transfer reaction (Faradaic reaction) that occurs at the surface of the electrode. Transition metal oxides or conductive polymers exhibit typical pseudocapacitance and display much higher specific capacitance than carbon materials for EDLCs.[55] As mentioned above, both rechargeable batteries and pseudocapacitors store charges *via* a redox reaction of the metal ions in electrode-active materials. Their difference is that the former is limited by cation diffusion within the crystalline framework of active material, while the latter is not controlled by the diffusion process. As compared to batteries, electrochemical capacitors (ECs) have many essential characteristics, such as fast charging/discharging, large number of charge-discharge cycles, and wide operating temperatures.[56] Because of these characteristics, ECs are being employed in various applications, such as electric vehicles, hybrid vehicles, elevators, cranes, drones and forklifts.[56,57] Large-scale ECs can regulate the power supplied by the electrical grid, which can avoid the costly shutdown of industrial operations because of intermittent outages and power fluctuations. In addition, with the advancements of renewable energy like solar and wind, there will be a huge demand for complex energy storage systems that will necessitate the development of advanced ECs. Furthermore, as a new type of charge storage mechanism, intercalation pseudocapacitance (Figure 1.12c) depends on the intercalation/de-intercalation of cations (e.g. Li^+, Na^+, K^+, and H^+) in the bulk of active materials but is not limited by the diffusion of cations within the crystalline framework of active materials. In cation-intercalated pseudocapacitance, the advantage of batteries is united with the advantage of supercapacitors.[55]

The major advantages of electrochemical supercapacitors are high power density, lifetime, cycle efficiency, wide range of operating temperatures, environmental friendliness, and safety. However, the challenges to be focused on supercapacitor are (i) energy density: for practical application, high energy density electrochemical system is required. In view of this, the energy density of electrochemical supercapacitors is less than of batteries. (ii) cost efficiency: the commonly employed electrode materials such as high porous surface area carbon materials and RuO_2 are more expensive. Also, the costs of organic electrolytes are far from negligible. (iii) self-discharge rate: ECs have high in self discharge rate 10–40% per day.[58] In recent studies, these challenges of ECs are being addressed by developing the hybrid supercapacitors, which can achieve much higher energy and power density values in the basis of intercalation pseudocapacitor mechanism. A comparison of the energy and power densities for energy storage materials can be displayed in the *Ragone plot*, as displayed in Figure 1.13.[59] Hybrid supercapacitors offer the advantages of both high power-density of supercapacitors and high energy density of batteries with high life cycles. These hybrid capacitors can be applied in energy storage, energy management and power conversion systems for practical applications.

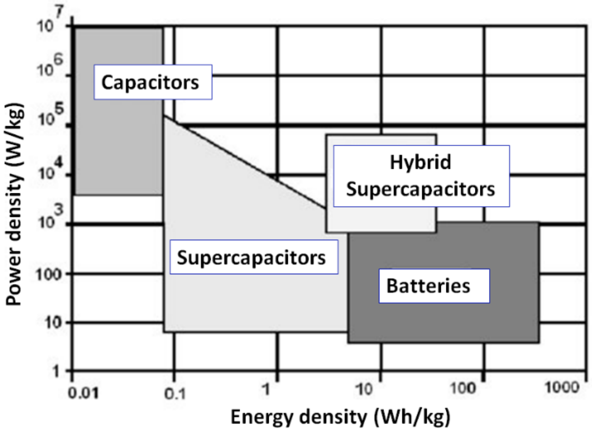

Figure 1.13. *Ragone plot* comparing the energy and power density ranges.[59]

1.5.2. Metal chalcogenides (MCs) as energy storage materials

Metal chalcogenides (MCs) have become a popular focus in the energy storage field because of their unique properties, such as: (i) improved life cycle; (ii) flexibility; (iii) additional reactive sites and catalytic activity; (iv) improving conductivity as well as reduction of inner resistance and ohmic loss; (v) short path lengths for electron transport; and (vi) displaying quantum-sized effects.[58] Due to their interesting intrinsic properties as well as good performance, some nanostructured MC-materials are receiving increasing attention as electrode materials for supercapacitors and batteries.[60–62] When the size of the MCs is reduced to the nanometer scale, new physical and chemical properties emerge owing to the well-known quantum size effect.[63] In addition, nanostructured MCs can provide a much higher specific surface area as compared with their bulk counterparts, which is beneficial to energy storage devices because the reaction/interaction between the devices and the interacting media can be significantly enhanced.[64,65] However, their high surface energy and van der Waals attraction easily cause serious stacking and restacking issue, leading to the generation of more inaccessible active sites with rapid capacity fading. The hybridization of 2D MCs with highly conductive materials, particularly, incorporating ultrasmall and few-layered MCs into carbon frameworks, can not only maximize the exposure of active sites but also effectively avoid their stacking and aggregation during the electrochemical reaction process.[66–68] Therefore, a satisfactory specific capacity can be achieved with a long cycle life. Carbon materials, especially activated carbon, carbon nanotubes (CNTs), graphene, and reduced graphene oxide (rGO) have been intensively studied as substrates to host various active nanomaterials for electrochemical storage applications because of their high conductivities and large surface areas. Notably, most progress has mainly focused on directly growing few layered MC-nanosheets on conductive carbon frameworks, to form hierarchical nanostructured hybrids.[69–71] Such nanohybrids usually have a large contact area between the MCs and electrolyte as well as rapid electrons transfer rate during the electrochemical process, and therefore, they exhibit enhanced electrochemical performance.

However, the MCs will detach from the carbon framework after a long charge/discharge process due to weak interface forces, resulting in the serious stacking and aggregation. The incorporation of nanostructures draws extensive attention for constructing high-performance and stable electrode materials that can effectively avoid phase separation and, meanwhile, retain the advantages of the hybrid configurations. Such impressive nanohybrids have high structural integrity and can support changes before and after cycling.[69]

Despite the above efforts, there is still a need to explore and develop the performance of MC materials by effective routes (e.g., forming MC-based composites) in order to achieve high-quality electrode materials for supercapacitor applications. While designing and constructing electrode materials, the researcher ought to take into consideration that they should be abundant, inexpensive, and eco-friendly for clean energy technology and potentially be of use in a broad selection of applications.[58,72]

1.6. Importance of graphene in electrochemical applications

Graphene is considered as an extraordinary nanomaterial with many potential applications. It is a one-atom-thick two-dimensional (2D) sheet composed of sp^2-hybridized carbon atoms that are densely packed in a honeycomb crystal lattice. The 2D planar structure of single layer graphene ensures high utilization of carbon atoms for the electron transfer, high surface area, and flexibility.[73] This 2D material has very high theoretical surface area (2630 m^2/g), excellent electrical conductivity (10^6–10^8 S/m) which is very stable over a wide temperature range.[74–76] Additionally, the extraordinary electron mobility and half-integer quantum Hall effect are yielded by zero-band gap characteristic of graphene.[77] It possesses the highest mechanical properties (Young’s modulus of 1 TPa, and strength of 130 GPa) known for

2D nanomaterials so far, and great thermal conductivity is also found for this nanomaterial.[78,79] Furthermore, another specific property of graphene is its functionalization ability with heteroatoms, molecules, or functional groups through covalence or non-covalence interactions. For example, plasma oxidation, chemical oxidation, and graphene oxide (GO) reduction can produce numerous oxygen-containing functional groups at its edges and surface. These groups can alter the electronic and chemical properties of graphene for better or worse.[80,81] Besides, graphene can be doped with some other heteroatoms, such as nitrogen, boron, sulfur, phosphorous, and fluorine, by substituting C atoms from the honeycomb lattice through CVD, arc discharge, hydrothermal or solvothermal approaches, which can offer p- or n-type behavior of graphene, and then its electrical properties could be remarkably modified to be suitable for specific application.[82,83] However, the weak van der Waals (vdW) attractions between individual graphene nanosheets tend to stack up the graphene layers and hence reduces its effectiveness.[84]

Furthermore, pristine graphene may not be able to offer required properties in some applications. Thus, composing the heterostructures of vertically stacked graphene and 2D TMDs can supply those desired properties due to the probability to govern and tailor band structure.[85] Additionally, the synergistic effect of the hybrid component can bring some new and unique characteristics to the heterostructure.[86–89] Graphene and graphene-based composites have been demonstrated to have enhanced performance in various energy storage and conversion systems (Figure 1.14), such as Li/Na-ion batteries, supercapacitors, electrocatalysis, and Li-S batteries.[73]

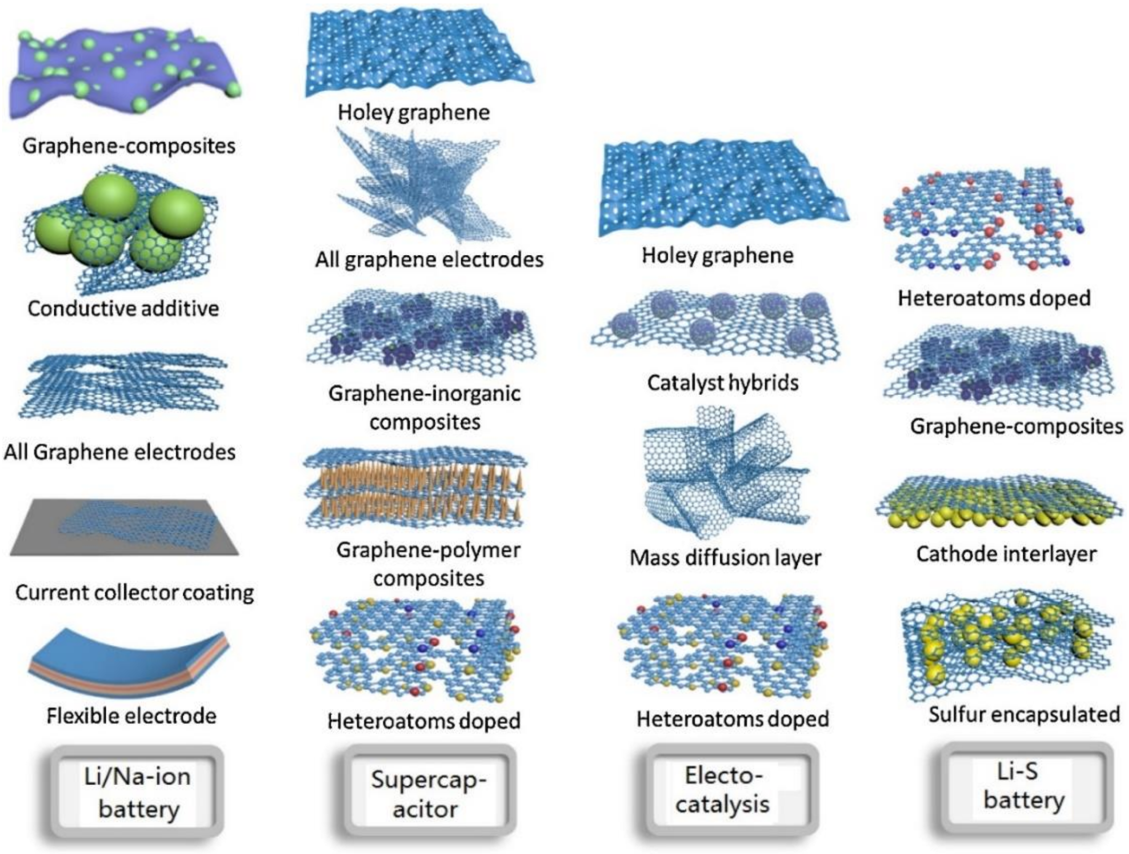

Figure 1.14. Schematic illustration of applications of graphene-based composites in Li/Na-ion battery, supercapacitor, electrocatalysis and Li-S battery.[73]

1.7. Microwave-initiated synthesis of MC/graphene nanocomposites

Synthesizing the efficient MC-based nano-compounds remains a challenge over times. In this regard, the microwave-assisted synthesis methods possess many of the advantages comparing to the most general synthesis approaches.

1.7.1. Conventional vs. microwave heating

Synthetic methods for MCs production mainly consist of (i) chemical methods such as solid-gas or gas-phase reactions,[90,91] thermal decomposition,[92,93], chemical vapor deposition

(CVD),[94,95] sono-chemical irradiation,[96] liquid exfoliation,[97] hydrothermal or solvothermal synthesis,[98–100] electrodeposition,[101] template synthesis,[102] etc. and (ii) other instant stimulation methods such as laser ablation,[103] arc discharge,[104] and electron beam irradiation.[105] Most of these approaches typically require energy-demanding preparation conditions (e.g., high temperature and ultrahigh vacuum) and relatively large quantities of reagents that may be detrimental to the environment. Innovative facile, energy efficient synthesis of MC nanomaterials on a large scale with controlled morphology, size, composition, and structure lie at the heart of their practical applications. To achieve this, conventional strategies are often unsatisfactory. Despite major progress, there are still several limitations and disadvantages associated with the existing fabrication techniques (summarized in Table 1.2). These challenges warrant the need to develop a method that can synthesize high purity, but low-cost products of MCs at industrial scales. Microwave-driven synthesis is an alternative approach which offers numerous opportunities to produce different metal chalcogenides for energy applications.

To meet the high requirement of modern energy conversion and storage (ECS) devices, innovative electrode/catalyst materials with new and enhanced performances are urgently needed. The ability to chemically modify an electrode/catalyst nanomaterial with other functional nanomaterials offers an intriguing route to engineer target materials with multifunctionalities or improved properties. In many studies, the loading of MC nanomaterials on the carbon materials (e.g. CNTs, graphene, graphite oxide, etc.) have been well demonstrated.[25,106–109]

Table 1.2. Conventional synthesis approaches and several issues to manufacture the metal chalcogenides and their composites.

Synthesis Methods		**Challenges**
Chemical	**Instant stimulation**	- Complicated processes, Complexity of equipment - Extreme reaction conditions (high temperature, argon protection) - Toxic and hazardous gases (e.g. H_2S) - Requirement of intense facilities (e.g., furnace, laser, arc discharge, and high voltage beams) - High energy consumption - Longer processing time (hours to days) - Safety, scalability, and cost issues
- Thermal decomposition - Chemical vapor deposition (CVD) - Chemical/mechanical exfoliation - Hydro-/solvo-thermal - Electrodeposition	- Laser ablation - Arc discharge - Electron beam irradiation	

Very recently, there has been a major surge in employing microwave-based ultrafast, energy-efficient, green, and facile approach for synthesizing multi-component nanostructures (e.g. metal oxides, carbon nanotube, carbon fiber, conducting polymer).[110] Microwave chemistry has been well expanded to synthesize inorganic MC nanomaterials due to its specific advantages such as high reaction rate, low processing costs, high yields, and side reaction depression.

1.7.2. Microwave heating chemistry

Microwaves are defined as electromagnetic waves with wavelengths ranging from 1 mm to 1 m, or frequencies between 0.3 and 300 GHz, i.e. between infrared (IR) and radio frequency (RF) in the electromagnetic range (Figure 1.15). Microwave heating has been widely recognized and used for industrial, scientific, and medical purposes, since it possesses higher energy efficiency comparing to conventional thermal heating. The most popular frequencies for microwave ovens are 0.915, 2.45, and 5.8 GHz, out of which 2.45 GHz (corresponds to a wavelength of 12.24 cm) is available worldwide, to avoid interference with wireless communications and cell phone frequencies.[110]

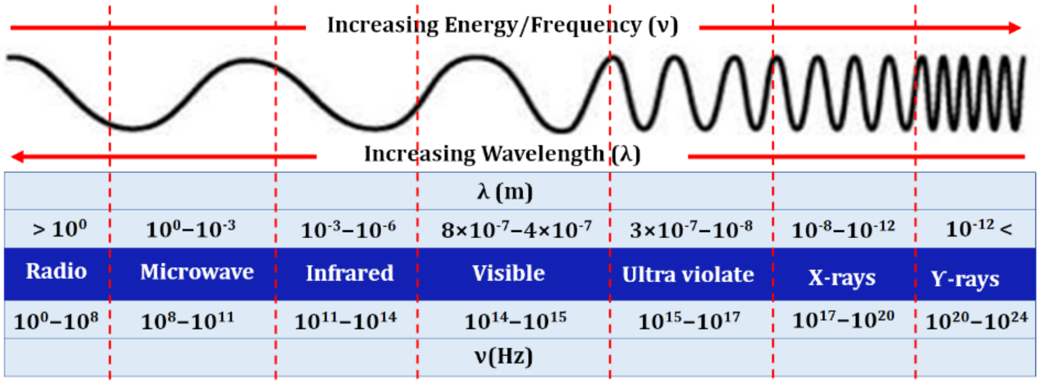

Figure 1.15. Electromagnetic waves representing their frequencies and wavelength ranges.

Microwave heating leads to the direct interaction between microwaves and conducting materials, which provides a uniform heating to the reaction materials in the entire reaction container, enabling rapid and consistent heat transfer. The main benefits of using microwave-assisted heating strategy are as follows:[110] (i) Facile operation: simple experimental setup with no requirement of any inert gas protection; (ii) Rapid heating: because of the reduction in activation energy barrier, reaction time is often considerably diminished from hours to minutes or even seconds; (iii) Energy and time-saving: heat is generated from inside the material, in contrast with conventional heating methods where heat is transferred from outside to inside. This internal heat allows a reduction of reaction time and energy cost; (iv) High selectivity: the desired reaction to generate specific product can be achieved by controlling the microwave power, temperature, heating time, etc.; (v) High product yield: shorter reaction time reduces the chance of undesirable side products, delivering high product yield. Compared to external heating, internal heating can also avoid the agglomeration phenomenon; (vi) High product purity: high purity products can be achieved through microwave synthesis methods as the formation of side products are not generally observed using microwave irradiation, and therefore the product is recovered in higher yield. As a result, the purification step is also faster and easier. (vii) Excellent reproducibility: the presence of uniform microwave field around the reaction mixture assures the high reproducibility. (viii) Lower processing costs: due to the simple setup, low energy utilization, and facile process, the cost of microwave-assisted synthesis is very low comparing to conventional approaches. (ix) Lower environmental impact: absence of toxic chemicals and gases can result very low environmental issues resulting from microwave heating.

Based on the previous studies by Zhang et. al on microwave-initiated manufacturing (MIM) technique, a facile and energy-efficient route for the microwave-assisted synthesis of metal disulfide (MS_2) nanoparticles has been proposed and preliminary results were collected.[111] This technique represents a clean, ultrafast (60 seconds) synthetic approach using microwave heating without any inert gas protection or use of intense facilities. Most importantly, this is a single-step metal chalcogenide (MC) formation process that is much faster and much more energy-efficient than all the other existing methods and can be universally employed to produce different kinds of MCs.

1.7.3. Role of 'graphene' on microwave heating

In general, the microwave heating takes place *via* dipolar polarization or ionic conduction mechanisms, where the ions or dipoles create collision to generate thermal energy.[110] However, in this research, graphene plays the major role to generate heat during microwave-initiated synthesis, where it exhibits strong interaction with microwaves making it an efficient susceptor to achieve heating rapidly and uniformly. As mentioned in Section 1.6, graphene is 2D sheet composed of sp^2-bonded carbon atoms, where one C-atom creates bonds with three other C-atoms leaving one delocalized electron in the structure (as shown in Figure 1.16). Because of the presence of these free electrons, graphene acts as conducting material and it has drawn significant attention due to its extraordinary electrical, thermal, mechanical properties and high specific surface area. These properties make graphene or graphene-based materials very promising in microwave heating, which is designed to absorb and dissipate incident electromagnetic waves by converting them to thermal energy.[112] Graphene sheets decorated with metals or metal compound nanoparticles by microwave-initiated approach have been reported in previous studies,[113,114] and it has been demonstrated that microwave-assisted method can be used for the highly efficient production of graphene-based composites. When graphene is exposed to microwave irradiation, electrons move freely on the surface and this flow of electrons can generate heat through a resistive heating mechanism. This interaction between microwave and conductive graphene is complicated. There are several parameters that affect the microwave heating process. Electronic conductivity is one of the most important factors in metallic and semiconducting materials. Experimental data demonstrated that the materials with moderate conductivity (10^{-5}~10 Ω·m) heat more efficiently than insulating or highly conducting materials. Besides conductivity, dimension of conducting material is another important factor. For a thick microwave susceptor, the microwave irradiation can be reflected in most of the cases due to the skin effects, while the

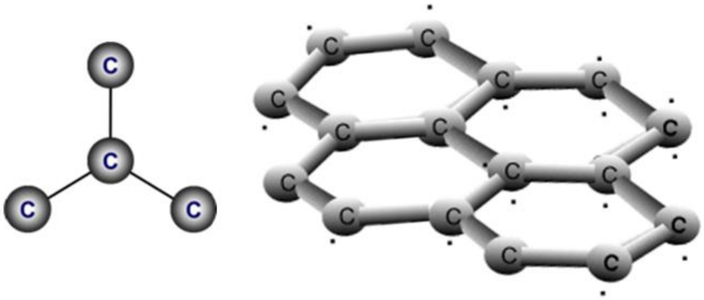

Figure 1.16. Graphene structure.

thin conductors have a lot less reflection than the thick ones, since the skin depth is larger than the dimension of the sample, thickness, or diameter etc. Therefore, the nanoscale structures of graphene sheets act as a promising microwave absorber, which can effectively and rapidly convert microwave energy to useful thermal energy.[112]

1.8. Characterization techniques

1.8.1. Physicochemical characterizations

In this study, the microwave synthesized nanocomposites are characterized *via* several analytical techniques. Scanning electron microscopy (SEM) is one of them, which is a type of electron microscopes that produces secondary electron images of a sample by scanning the surface with a focused beam of electrons. The electrons interact with atoms in the sample material, producing various signals that contain information about surface topography of the sample. Energy-dispersive X-ray spectroscopy, known as EDS, is another useful technique for the elemental analysis of a sample. It relies on an interaction between the source of X-ray excitation and a sample. Transmission electron microscopy (TEM) is one of the microscopy techniques in which a beam of electrons is transmitted through the sample to form an image. The image is then magnified and focused onto an imaging device. In TEM, the image can be magnified by more than 50 million times, while for the SEM, this is limited to 1–2 million times. However, the maximum field of view that SEMs can achieve is far larger than TEMs, meaning TEM can only focus on a very small part of the sample. X-ray powder diffraction (XRD) is the technique of determining the atomic and molecular structure of a crystal material, in which the crystalline structure causes a beam of incident X-rays to diffract towards many specific directions. By measuring the angles and intensities of these diffracted beams, one can produce a three-dimensional picture of the density of electrons. From this electron density, the mean positions of the atoms in the crystal can be determined, as well as their chemical bonds, their crystallographic order-disorder, lattice structures, and various other information. In addition, Raman spectroscopy is another spectroscopic technique usually applied to determine the vibrational modes of molecules in a sample. This technique is commonly used to provide a structural fingerprint by which molecules can be identified. Furthermore, the X-ray photoelectron spectroscopy (XPS) is a surface-sensitive quantitative spectroscopic technique based on the photoelectric effect that can identify the elements that exist within a material or are covering its surface, as well as their chemical state, the overall electronic structure, and density of the electronic states in the material. XPS is established on the radiation of a sample with X-Rays. If the incident X-Rays are absorbed by a core electron, the core electron can escape the sample as a photoelectron with a specific kinetic energy. Brunauer–Emmett–Teller (BET) is another helpful technique that aims to explain the physical adsorption of gas molecules on a solid surface and serves as the basis for an important analysis technique for the measurement of the specific surface area of materials.

1.8.2. Electrochemical characterizations

1.8.2.1. Electrochemical setup

In general, there are two different kinds of electrochemical setups: two- or three-electrode configurations. Although for practical applications, the two-electrode setup is popularly used, for laboratory research it is essential to use a three-electrode setup to understand the electrode kinetics taking place during the electrochemical tests.

Two-electrode configuration

This configuration consists of a working electrode (W) where the chemistry of interest occurs and a counter electrode (C) which acts as the other half of the cell (Figure 1.17a). The applied potential (V) is measured between the working and counter electrode and the resulting current (I) is measured in the working or counter electrode lead. The counter electrode in the two-electrode set-up serves two functions. It completes the circuit allowing charge to flow through the cell, and it also maintains a constant interfacial potential, regardless of current. In this system, it is very difficult to maintain a constant counter electrode potential while current is flowing. This fact, along with a lack of compensation for the voltage drop (iR drop) across the solution leads to poor control of the working electrode potential. The roles of passing current and maintaining a reference voltage are better served by two separate electrodes, which happens in the three-electrode setup.

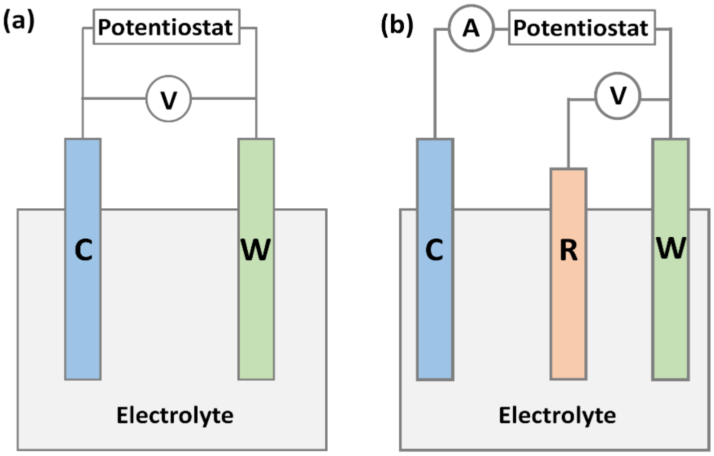

Figure 1.17. Two and three−electrode cell configurations (A−ammeter, V−voltmeter, and C−counter, W−working, and R−reference electrodes).

Three-electrode configuration

The three-electrode system remedies many of the issues of the two-electrode configuration. As shown in Figure 1.17b, the three-electrode system consists of a working electrode (W), counter electrode (C), and reference electrode (R). The reference electrode's role is to act as a reference in measuring and controlling working electrode potential, without passing any current. The reference electrode should have a constant electrochemical potential at low current density. Additionally, since the reference electrode passes negligible current, the iR drop between the reference and working electrode is often very small. Thus, with the three-electrode system, the reference potential is much more stable, and there is compensation for iR drop across the solution. This translates into superior control over working electrode potential. In this system, the only role of the counter electrode is to pass all the current needed to balance the current observed at the working electrode.

1.8.2.2. Characterization techniques

To perform the electrochemical (EChem) tests, the EChem cell is connected with a potentiostat, which is an electronic hardware that controls the EChem cell. There are several techniques applied in a potentiostat according to the experimental requirements, which are briefly described in this section.

Voltammetry

In voltammetry, information about an analyte can be obtained by measuring the current while the potential is varied. The analytical data for a voltammetric experiment comes in the form of a voltammogram which plots the current produced by the analyte versus the potential of the working electrode. In this project, two major types of voltammogram are employed: *cyclic voltammogram (CV)* and *linear sweep voltammogram (LSV)*. In a CV test, the working electrode potential is ramped linearly versus time as shown in Figure 1.18a. After the set potential is reached, the working electrode's potential is ramped in the opposite direction to return to the initial potential. These cycles of ramps in potential may be repeated as many times as needed. The rate of change of potential with time is referred to as the *scan rate* (V/s or mV/s). The current at the working electrode is plotted versus the applied voltage (Figure 1.18b) to give the cyclic voltammogram trace. Unlike CV, LSV (Figure 1.19) is a voltammetric method where the current at a working electrode is measured while the potential is swept linearly with time. Oxidation or reduction of species is registered as a peak or trough in the current signal at the potential at which the species begins to be oxidized or reduced. Therefore, basically LSV is the half portion of a whole CV curve.

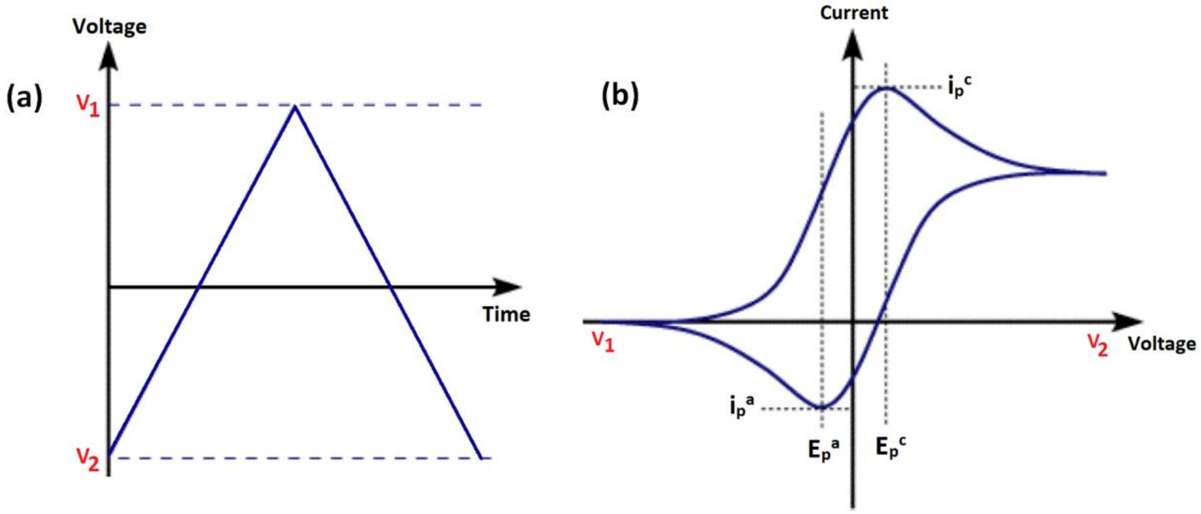

Figure 1.18. Cyclic voltammogram: (a) Voltage *vs.* time plot. (b) Current *vs.* voltage plot.[115]

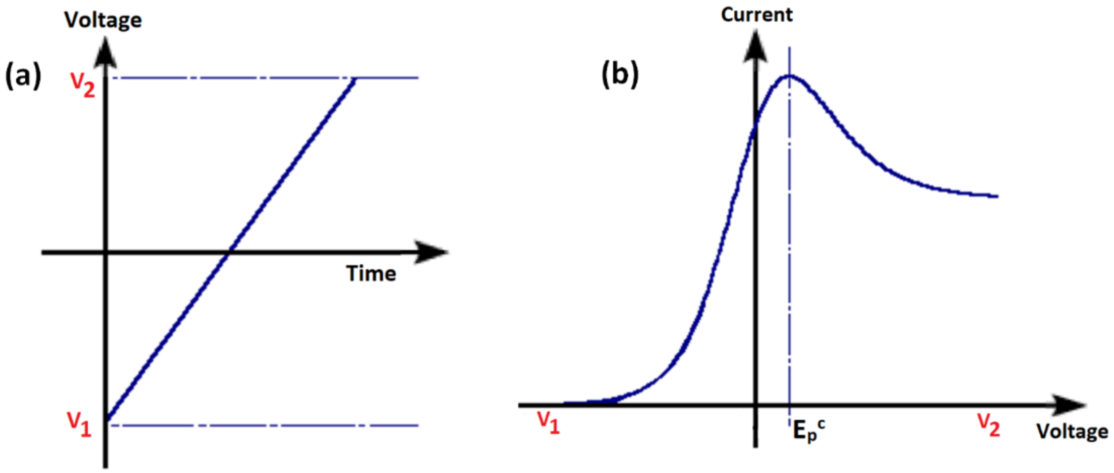

Figure 1.19. Linear sweep voltammogram: (a) Voltage *vs.* time plot. (b) Current *vs.* voltage plot.[115]

CV and LSV are powerful tools in the field of electrochemistry. They have been used extensively to characterize the performance of various electrical energy conversion and storage devices such as HER electrocatalysts, supercapacitors, sensors, transistors, etc.

Ohmic (iR) drop correction

The ohmic drop (*iR* drop) describes the overpotential due to the electron flow through a material and electrolyte. In electrochemistry, it often refers to the potential induced by the resistance of the electrolyte or any other interface such as surface films or connectors. The *iR*-correction of polarization curves can be performed according to the method mentioned in 'Potentiostat Fundamentals' by Gamry Instruments Inc.[116]

If a typical three-electrode EChem cell is configured as Figure 1.20, some reference points can be noted in the cell to which will be referred to develop the *iR*-corrected equation.

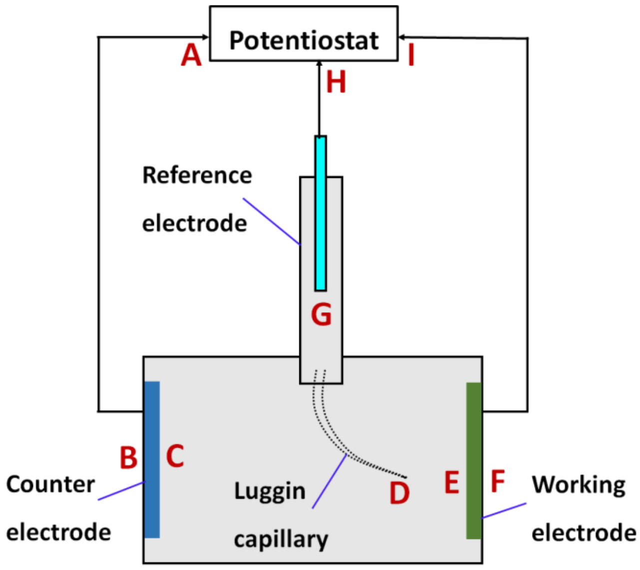

A: Counter electrode output at the potentiostat
B: Metal surface of counter electrode
C: Electrolyte surface of counter electrode
D: Electrolyte at the tip of the Luggin capillary
E: Electrolyte surface of the working electrode
F: Metal surface of the working electrode
G: Electrolyte surface of the reference electrode
H: Reference electrode input at the potentiostat
I: Working electrode output at the potentiostat

Figure 1.20. A typical three-electrode electrochemical setup to determine the *iR*-drop value.

Although any potentiostat can control and measure the voltage between points H & I, unfortunately, for an electrochemical analysis it is essential to control and measure the voltage between points E & F. This is the actual potential difference across the EChem interface which relates the main purpose of electrochemical study.

Therefore, $V_{important} = V_F - V_E$ ……………………………………………….……………… (1.19)

For purposes of this discussion, point I is equivalent to point F, point G is equivalent to H, except for a constant voltage offset caused by the difference in potential between working and reference electrodes, which is known as the open-circuit potential, V_{ocp}. And because there is no current flowing through the reference electrode, point G is equivalent to D. So, starting from the equation of $V_{measured} = V_I - V_H$, we can get:

$V_{measured} = V_F - V_D + V_{ocp}$ ………..…………………………………………………......... (1.20)

Also, point E is equivalent to point D except for that solution resistance, R_S.

By Ohm's law: $V_E - V_D = I_{cell} \times R_S$; So, substituting this in Equation 1.20 gives: $V_{measured} = V_F - V_E + I_{cell} \times R_S + \mathrm{V_{ocp}}$. Rearranging the result provides:

$$V_{important} = V_F - V_E = V_{measured} - I_{cell} \times R_S - V_{ocp} \quad \ldots\ldots \quad (1.21)$$

Here, the $V_{measured}$, I_{cell}, R_S, and V_{ocp} can be measured directly by potentiostat. The expression of $I_{cell} \times R_S$ represents the *iR*-drop for a typical electrochemical cell.

Electrochemical impedance spectroscopy (EIS)

EIS fundamentals are well explained by Gamry Instruments Inc.[117] Electrical resistance is a common term, which represents the ability of a circuit element to resist the flow of electrical current. Ohm's law (Equation 1.22) describes the resistance (*R*) in terms of the ratio between voltage (*E*) and current (*I*).

$$R = \frac{E}{I} \quad \ldots\ldots \quad (1.22)$$

While this is a well-known relationship, its use is limited to only one circuit element in the ideal resistor. However, the real circuit contains the elements that exhibit much more complex behavior. In this real system, instead of using the ‘resistance’, ‘impedance’ is a more general circuit parameter. Like resistance, impedance is a measure of the ability of a circuit to resist the flow of electrical current, but unlike resistance, it is not limited by the simple relationship shown above. Electrochemical impedance is usually measured by applying an AC potential to an EChem cell and then measuring the current through the cell. Assuming the potential excitation as a sinusoidal signal, the response to this potential is an AC current signal.

This current signal can be analyzed as a sum of sinusoidal functions. Usually, electrochemical impedance is measured using a small excitation signal with a pseudo-linear response. In a linear (or pseudo-linear) system, the current response to a sinusoidal potential will be a sinusoidal signal at the same frequency but shifted in phase as shown in Figure 1.21. Here, *E(t)* is time-dependent potential, E_0 is potential amplitude, ω is angular frequency, *t* is time, *i(t)* is time-dependent current, i_0 is current amplitude, and ∅ is phase angle.

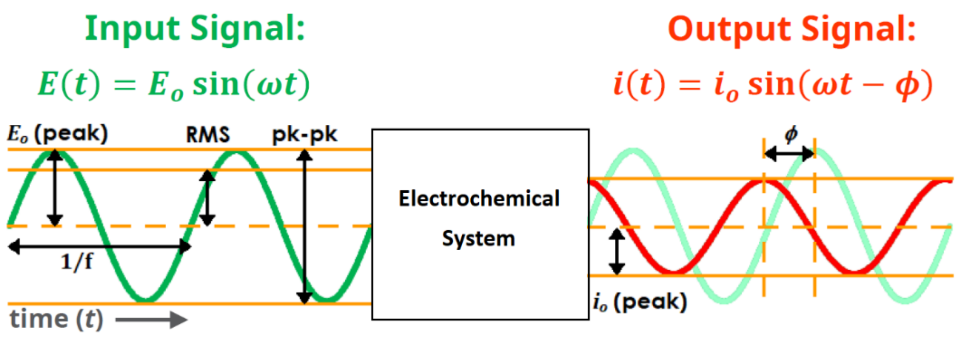

Figure 1.21. Input potential and output current as sinusoidal signals during EIS measurement. [*Courtesy: Pine Research Instrumentation, Inc.*]

An expression analogous to Ohm's Law is used to calculate the impedance of the system as:

$$Z = \frac{E_t}{I_t} = \frac{E_0 \sin(\omega t)}{I_0 \sin(\omega t - \emptyset)} = Z_0 \frac{\sin(\omega t)}{\sin\,(\omega t - \emptyset)} \quad \ldots\ldots\ldots\ldots\ldots\ldots\ldots\ldots\ldots\ldots\ldots\ldots \quad (1.23)$$

The impedance is therefore expressed in terms of a magnitude (Z_0), and a phase shift (∅). With Euler’s relationship [$\exp(j\emptyset) = cos\emptyset + jsin\emptyset$], it is possible to express the impedance as a complex function, $E_t = E_0 \exp(j\omega t)$ and the current response as, $I_t = I_0 \exp(j\omega t - \emptyset)$.

The impedance is then represented as a complex number,

$$Z(\omega) = \frac{E}{I} = Z_0 \exp(j\emptyset) = Z_0(cos\emptyset + jsin\emptyset) = Z_{Re} + Z_{Im} \quad \ldots\ldots\ldots\ldots\ldots\ldots\ldots\ldots\ldots\ldots \quad (1.24)$$

Here, the expression for $Z(\omega)$ is composed of a real (Z_{Re}) and an imaginary (Z_{Im}) parts.

In general, electrochemical cells can be modeled as a network of passive electrical circuit elements, known as *Randles equivalent circuit* as shown in Figure 1.22a. Most of the circuit elements in the model are common electrical elements such as resistors, capacitors, and inductors.

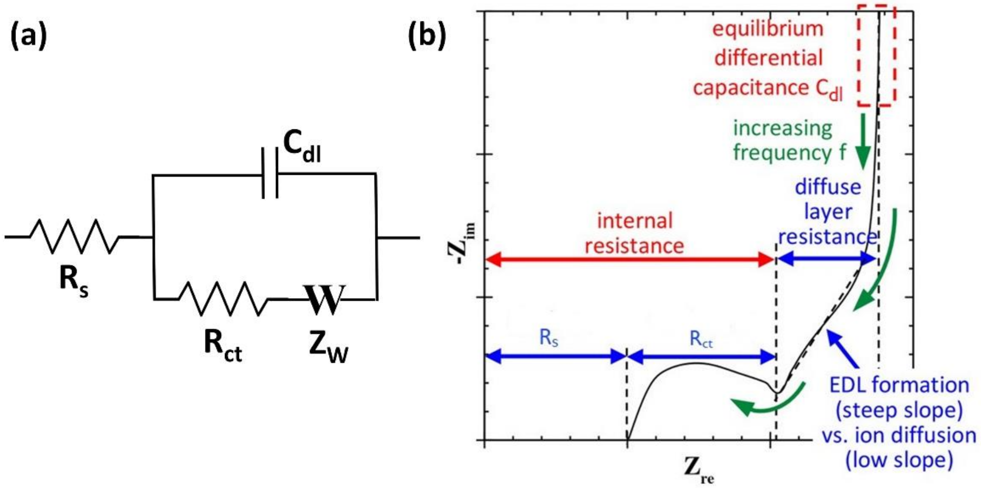

Figure 1.22. (a) A simple Randles equivalent circuit. (b) Nyquist plot.

The EIS response of this circuit can be calculated and compared to the actual EIS response of the electrochemical cell. In the circuit (Figure 1.22a), R_S represents the solution (or ohmic) resistance, C_{dl} is the double-layer capacitance, R_{ct} represents the charge transfer (or polarization) resistance and Z_W is the Warburg impedance of the system.[18] Warburg impedance is the diffusion circuit element, that models the unrestricted diffusion to an electrode. *Randles cell* is basically used in EIS for interpretation of impedance spectra, often with a constant phase element (*CPE*) replacing the C_{dl}. Moreover, if the real part (Z_{Re}) of Equation 1.24 is plotted on the X-axis and the imaginary part (Z_{Im}) is plotted on the Y-axis of a chart, *Nyquist plot* can be drawn as shown in Figure 1.22b. The HER kinetics occurring at the electrode/electrolyte interface can be studied by this plot under operating conditions. It shows both regions of mass-transfer and kinetic control at low and high frequencies, respectively.[18] However, both regions may not be well defined for any given system. The determining feature is the charge-transfer resistance, R_{ct} and its relation to Warburg impedance, Z_W. If the chemical system is kinetically slow, it will show a large R_{ct} and may display only a very limited frequency region where mass transfer is a significant factor and vice versa in fast system.

Turn over frequency (TOF)

The intrinsic per-site activity of a catalyst is also an important parameter necessary to consider for further improvement and to guide catalyst development, which is often measured by the *turnover frequency*, *TOF* (s^{-1}) for each active site. TOF is defined as the number of hydrogen molecules evolved on an active site in a time period (e.g. per 1 second). Assuming the cathodic current is entirely attributed to the HER, the TOF can be calculated from following Equation 1.25:[118,119]

$$\text{TOF} = \frac{\text{No. of total hydrogen turn overs/cm}^2\ \text{geometric area}}{\text{No. of active sites/cm}^2\ \text{geometric area}} \quad \ldots\ldots\ldots\ldots\ldots\ldots\ldots\ldots\ldots \text{(1.25)}$$

Because of the different nature of various HER electrocatalysts and their preparation methods, several approaches are used to determine the number of total hydrogens turn overs by calculating the current density values. TOF is closely related to the activity of each catalytic site of the catalysts. The difficulty in measuring a TOF is not only in determining the rate but also in counting the active sites. Besides, sites may not be all identical even for the same catalyst. Limitations of current experimental techniques make this task challenging. Most practical catalysts include many different types of surface sites, each with their own inherent activity, and there are few experimental techniques to probe individual sites. Different methods are required for different materials, measurements are often complicated by non-Faradaic current, catalyst instability, and/or transport limitations. The most common strategy for determining intrinsic per-site activity is to first measure the total electrode activity and then, through a separate measurement, to determine the total number of active sites and use these results to infer the average TOF. Therefore, in this research, the number of active sites and TOF of catalyst samples are calculated by an electrochemical approach through cyclic voltammetry (CV) measurements in phosphate buffer (pH = 7) solution at a scan rate of 10 mV s^{-1}, based on a general method mentioned by Dai et al.[120] The number of active sites (*n*) can be determined by following:

$$n = \frac{Q}{2F}\,;\ [Q = \frac{CV\ Area}{Scan\ rate}] \quad \text{……………………………………………………………} \quad (1.26)$$

Where, *n* is the number of active sites (mol g^{-1}) and *F* is the Faraday constant (96485 C mol^{-1}). The per-site TOF (s^{-1}) can be calculated from the following Equation 1.27:

$$\text{Turn over frequency, TOF} = \frac{I}{nF} \times \frac{1}{2} \quad \text{…………………………………………………………} \quad (1.27)$$

Where, the *I* is the current (A) at specific overpotential (η) during the linear sweep measurement in 0.5 M H_2SO_4. While less powerful than the ideal measurement, this strategy still enables the development of relationships between material properties and catalytic activity to drive further catalyst design efforts.

Stability tests

The stability of a HER electrocatalyst is another practical parameter to consider when designing long-term operations. A cyclic voltammetry (CV) test for 1000 to 5000 cycles can be performed to assess the electrochemical stability. Another way to determine the stability of HER electrocatalyst is *Amperometry* (constant potential) test, in which the current is measured at a fixed potential applied to the electrode, at different times since the start of polarization. Since the HER is a cathodic reaction, the negative current density is found and more negative this value indicates more of the hydrogen generation from the system.

Platinum electrode issue for HER tests

Even though great achievements have been obtained in the scientific community, very few reports concentrate on the influence of potential platinum (Pt) contamination on the HER performance when using Pt based counter electrodes during the experiment. Among the few of the studies, Wei et al. has shown a possible schematic illustration (Figure 1.23), which is presented for this Pt-electrode issue.[121]

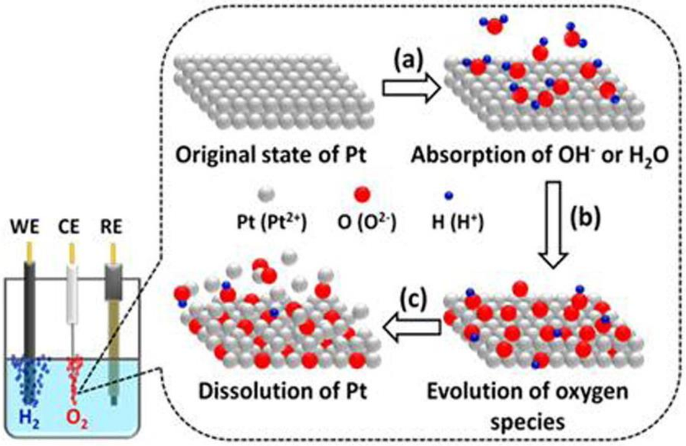

Figure 1.23. The possible schematic illustration for the transfer process of Pt from anode (counter electrode) to cathode (working electrode).[121]

Specifically, the dissolution of Pt is the result of the position exchange between oxygen and Pt atoms that substantially weakens the interaction between the surface Pt atoms and the interior bulk counterparts. All these results suggest that the improvement of HER performance during the long runs is generally caused by the Pt transfer and re-deposition onto the electrocatalysts of cathode, rather than the activation of the carbon materials themselves. Therefore, for HER, the use of Pt counter electrodes in sulfuric acid is susceptible to the generation of ‘false positives’ for electrocatalysis of the HER.

Chen and his co-workers[122] have studied thoroughly about the anodic dissolution of Pt counter electrode in both acidic and alkaline aqueous solutions. In consideration of their findings obtained, they finally gave several valuable suggestions: (i) purifying the electrolyte before HER process; (ii) replacing the Pt with other stable counter electrodes, such as graphite, carbon cloth, glassy carbon and Ti mesh; (iii) applying the ion exchange membrane to the setup preventing the Pt transfer across the working and counter electrodes. In this research, except the first project (Chapter 2), for all other HER projects the Pt counter electrode has been replaced by graphite rod electrode (specifically for the long tests). This replacement is shown in Figure 1.24, highlighting the change in electrochemical setup.

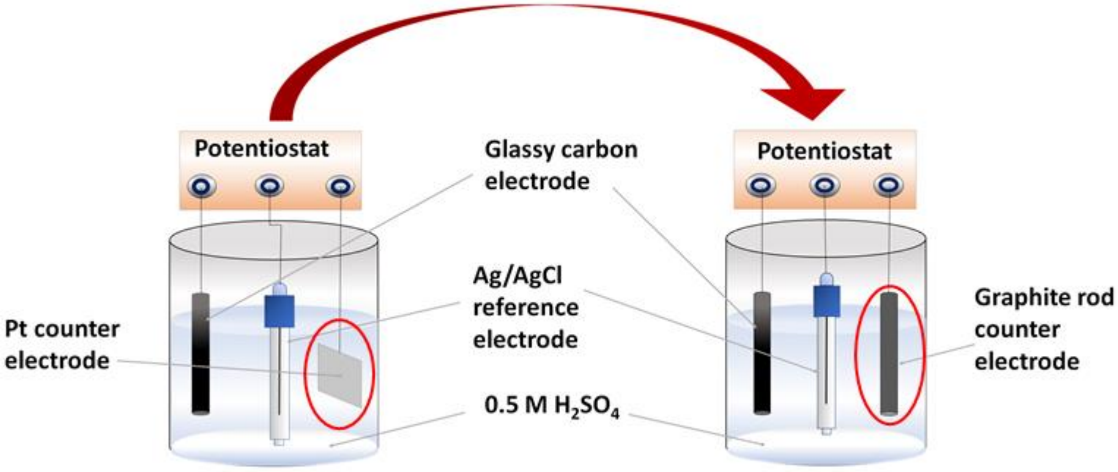

Figure 1.24. Replacing platinum (Pt) electrode by a graphite rod as counter electrode to avoid the possible Pt contamination during the stability tests in acidic medium (0.5 M H_2SO_4).

Galvanostatic charge-discharge (GCD)

Galvanostatic charge-discharge (GCD) is the standard technique used to test the performance and cycle-life of supercapacitors and batteries. A repetitive loop of charging and discharging is called cyclic *GCD*. Most often, charge and discharge are conducted at constant current until a set voltage is reached.[123] The *GCD* is a reliable method to evaluate the electrochemical capacitance of materials under controlled current conditions. This technique is very different from cyclic voltammetry (CV) because the current is controlled, and the voltage is measured. This is indeed one of the most widely used techniques in the field of supercapacitor because it can be extended from a laboratory scale to an industrial one. This method is also called as *Chronopotentiometry* and gives access to various parameters such as, capacitance, resistance, and cyclability of an energy storage material. In this method, a current pulse is applied to the working electrode and the resulting potential is measured against a reference electrode as a function of time. As shown in Figure 1.25a,[55] for non-linear *GCD* curve (pseudocapacitors or hybrid capacitors), the capacitance changes according to Equation 1.28.

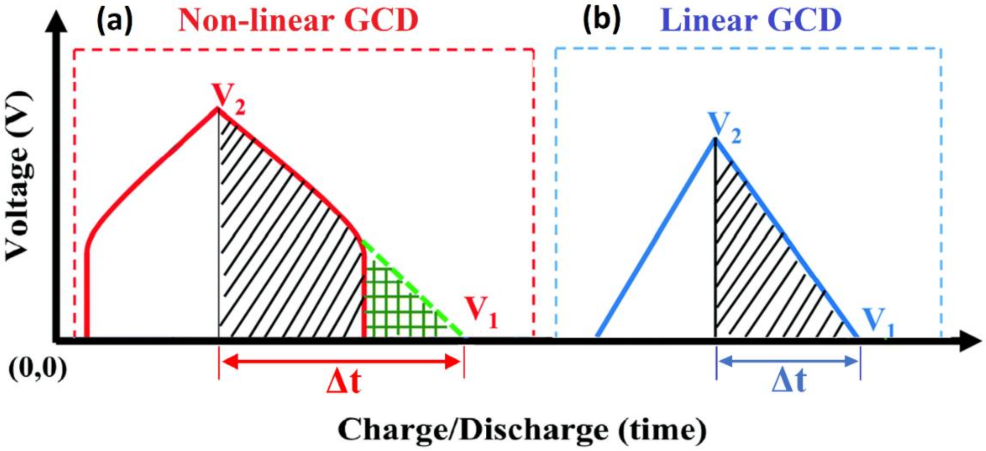

Figure 1.25. (a) Non-linear and (b) linear *GCD* plots.

$$C = \frac{\partial Q}{\partial V} = I\frac{\partial t}{\partial V} \qquad (1.28)$$

If current (I) remains constant, voltage will change from V_1 to V_2 over the time (t). Consequently, the average capacitance would be,

$$C = I\int\frac{\partial t}{\partial V} = I\frac{\int V\cdot\partial t}{\int_{V_1}^{V_2} V\cdot\partial V} = 2I\frac{\int V\partial t}{(\Delta V)^2} \qquad (1.29)$$

And, the specific capacitance would be, $C_s = \frac{C}{m} = 2I\frac{\int V\partial t}{m(\Delta V)^2}$ ……………………………… (1.30)

where, I is the set current, Δt is the discharge time and ΔV is the potential window.

For the linear *GCD* curve (electrical double layer capacitor, EDLC) as shown in Figure 1.25b,

$\int V\partial t = \frac{1}{2}\cdot\Delta V\cdot\Delta t$ (Applying the area of triangle equation).

Therefore, the specific capacitance would be,

$$C_s = 2I\frac{\int V\partial t}{m(\Delta V)^2} = 2I\frac{\frac{1}{2}\cdot\Delta V\cdot\Delta t}{m(\Delta V)^2} = \frac{I\Delta t}{m\Delta V} \qquad (1.31)$$

Equation 1.30 and 1.31 are two of the widely used equations to determine the specific capacitance (C_s, Fg^{-1}) of energy storage materials for non-linear and linear *GCD* curves, respectively. By repeating *GCD* measurements over large number of cycles, it is then also possible to determine the cyclic stability of supercapacitor cells.

1.9. Research motivation and objectives

In present days, developing the next generation HER electrocatalysts to replace the expensive platinum (Pt) remains as a challenge for many researchers. Most importantly, the manufacturing of new catalyst materials has always been a limiting factor. Similarly, the high-performance energy storage materials are emerging to solve the intermittency issue of renewable energies, as well as on high demand for portable miniaturized electronic devices. A breakthrough in manufacturing can pave the way for breakthroughs in the entire field. Nanomaterials, including organic polymers, inorganic metal oxides/sulfides, self-assembled super molecules, and many others, have demonstrated huge potential for employment in a myriad of applications due to their vastly improved mechanical, physical and chemical properties. In this regard, metal chalcogenides (MCs) represent one such group of nanomaterials that due to their excellent physicochemical, electrical and thermal performances have been widely employed in electronic devices, chemical sensors, energy storage devices, composite additives, etc.

The goal of this project is to develop high performance nanocomposite materials for energy storage and electrocatalysis applications through a fast and facile microwave-initiated heating approach. Major research objectives of this proposal are to (i) establish a general and optimized methodology for ultrafast and energy efficient synthesis of metal chalcogenide (MC)/graphene nanocomposites by using microwave-initiated heating approach; (ii) employ the as-produced nanocomposite materials in energy catalysis process, precisely as hydrogen evolution reaction (HER) electrocatalysts; (iii) explore the substitutionally doped MC-based nanocomposites following the microwave-initiated approach for HER applications. (iv) investigate the energy storage capability and understand the storage mechanism of resultant nanocomposites; (v) optimize the synthesis methods (reaction conditions, *i.e.* temperature, power, time, etc.), along with the optimization of physicochemical and electrochemical parameters for high-performance sustainable energy applications.

1.10. References

1 *U.S. Energy Inf. Adm.*, 2019, 1–3.

2 R. Lindsey and E. Dlugokencky, *Climate Change: Atmospheric Carbon Dioxide*, 2020.

3 R. Betts, *Carbon Br.*, 2021, 1–6.

4 *U.S. Energy Inf. Adm.*, 2019, 4–167.

5 J. P. Painuly, *Renew. Energy*, 2001, **24**, 73–89.

6 K. Mazloomi and C. Gomes, *Renew. Sustain. Energy Rev.*, 2012, **16**, 3024–3033.

7 M. Wietschel and M. Ball, *Int. J. Hydrogen Energy*, 2009, **34**, 613–639.

8 D. Majumdar, M. Mandal and S. K. Bhattacharya, *Journey from supercapacitors to supercapatteries: recent advancements in electrochemical energy storage systems*, 2020, vol. 3.

9 P. Forouzandeh, V. Kumaravel and S. C. Pillai, *Catalysts*, 2020, **10**, 1–73.

10 B. Sakintuna, F. Lamari-Darkrim and M. Hirscher, *Int. J. Hydrogen Energy*, 2007, **32**, 1121–1140.

11 R. Chamousis, *HYDROGEN : FUEL OF THE FUTURE*, .

12 *Int. Renew. Energy Agency*, 2018, 1–52.

13 J. Udagawa, P. Aguiar and N. P. Brandon, *J. Power Sources*, 2007, **166**, 127–136.

14 K. Onda, T. Kyakuno, K. Hattori and K. Ito, *J. Power Sources*, 2004, **132**, 64–70.

15 S. Trasatti, *J. Electroanal. Chem.*, 1999, **476**, 90–91.

16 T. Shinagawa and K. Takanabe, *ChemSusChem*, 2017, **10**, 1318–1336.

17 E. Dallatu, R. Sha'Ato, I. Eneji and A. Itodo, *Chem. Sci. Int. J.*, 2018, **22**, 1–16.

18 A. J. Bard, L. R. Faulkner, N. York, C. @bullet, W. Brisbane and S. E. Toronto, *ELECTROCHEMICAL METHODS Fundamentals and Applications*, 1944.

19 D. K. Bediako, *PhD Thesis*, 2015, 1–254.

20 C. J. Yang, *Energy Policy*, 2009, **37**, 1805–1808.

21 C. G. Morales-Guio, L. A. Stern and X. Hu, *Chem. Soc. Rev.*, 2014, **43**, 6555–6569.

22 J. Su, J. Zhou, L. Wang, C. Liu and Y. Chen, *Sci. Bull.*, 2017, **62**, 633–644.

23 A. B. Laursen, S. Kegnæs, S. Dahl and I. Chorkendorff, *Energy Environ. Sci.*, 2012, **5**, 5577–5591.

24 Q. Tang and D. E. Jiang, *ACS Catal.*, 2016, **6**, 4953–4961.

25 Y. Li, H. Wang, L. Xie, Y. Liang, G. Hong and H. Dai, *J. Am. Chem. Soc.*, 2011, **133**, 7296–7299.

26 E. Skúlason, G. S. Karlberg, J. Rossmeisl, T. Bligaard, J. Greeley, H. Jónsson and J. K. Nørskov, *Phys. Chem. Chem. Phys.*, 2007, **9**, 3241–3250.

27 N. M. Marković, B. N. Grgur and P. N. Ross, *J. Phys. Chem. B*, 1997, **101**, 5405–5413.

28 A. B. Laursen, A. S. Varela, F. Dionigi, H. Fanchiu, C. Miller, O. L. Trinhammer, J. Rossmeisl and S. Dahl, *J. Chem. Educ.*, 2012, **89**, 1595–1599.

29 P. Quaino, F. Juarez, E. Santos and W. Schmickler, *Beilstein J. Nanotechnol.*, 2014, **5**, 846–854.

30 S. Trasatti, *J. Electroanal. Chem.*, 1971, **33**, 351–378.

31 E. Pomerantseva, C. Resini, K. Kovnir and Y. V. Kolen'ko, *Adv. Phys. X*, 2017, **2**, 211–

253.

32 J. K. Nørskov, T. Bligaard, A. Logadottir, J. R. Kitchin, J. G. Chen, S. Pandelov and U. Stimming, *J. Electrochem. Soc.*, 2005, **152**, J23.

33 R. Parsons, *Trans. Faraday Soc.*, 1957, **53**, 1689–1699.

34 K. S. Exner, *ACS Catal.*, 2019, **9**, 5320–5329.

35 C. Tan, X. Cao, X. J. Wu, Q. He, J. Yang, X. Zhang, J. Chen, W. Zhao, S. Han, G. H. Nam, M. Sindoro and H. Zhang, *Chem. Rev.*, 2017, **117**, 6225–6331.

36 H. Fan, H. Yu, X. Wu, Y. Zhang, Z. Luo, H. Wang, Y. Guo, S. Madhavi and Q. Yan, *ACS Appl. Mater. Interfaces*, 2016, **8**, 25261–25267.

37 Y. Zhang, W. Sun, X. Rui, B. Li, H. T. Tan, G. Guo, S. Madhavi, Y. Zong and Q. Yan, *Small*, 2015, **11**, 3694–3702.

38 J. Bonde, P. G. Moses, T. F. Jaramillo, J. K. Norskov and I. Chorkendorff, *Faraday Discuss.*, 2008, **140**, 219–231.

39 T. F. Jaramillo, K. P. Jørgensen, J. Bonde, J. H. Nielsen, S. Horch and I. Chorkendorff, *Science (80-.).*, 2007, **317**, 100–102.

40 B. Hinnemann, P. G. Moses, J. Bonde, K. P. Jørgensen, J. H. Nielsen, S. Horch, I. Chorkendorff and J. K. Nørskov, *J. Am. Chem. Soc.*, 2005, **127**, 5308–5309.

41 D. Kong, H. Wang, J. J. Cha, M. Pasta, K. J. Koski, J. Yao and Y. Cui, *Nano Lett.*, 2013, **13**, 1341–1347.

42 X. Chia, A. Y. S. Eng, A. Ambrosi, S. M. Tan and M. Pumera, *Chem. Rev.*, 2015, **115**, 11941–11966.

43 H. Li, C. Tsai, A. L. Koh, L. Cai, A. W. Contryman, A. H. Fragapane, J. Zhao, H. S. Han, H. C. Manoharan, F. Abild-Pedersen, J. K. Nørskov and X. Zheng, *Nat. Mater.*, 2016, **15**, 48–53.

44 V. P. Pham and G. Y. Yeom, *Adv. Mater.*, 2016, **28**, 9024–9059.

45 S. Li, W. Zang, X. Liu, S. J. Pennycook, Z. Kou, C. Yang, C. Guan and J. Wang, *Chem. Eng. J.*, 2019, **359**, 1419–1426.

46 T. Kosmala, H. Coy Diaz, H. P. Komsa, Y. Ma, A. V. Krasheninnikov, M. Batzill and S. Agnoli, *Adv. Energy Mater.*, 2018, **8**, 1–8.

47 Q. Gong, L. Cheng, C. Liu, M. Zhang, Q. Feng, H. Ye, M. Zeng, L. Xie, Z. Liu and Y. Li, *ACS Catal.*, 2015, **5**, 2213–2219.

48 Y. Pan, F. Zheng, X. Wang, H. Qin, E. Liu, J. Sha, N. Zhao, P. Zhang and L. Ma, *J. Catal.*, 2020, **382**, 204–211.

49 M. S. Islam and C. A. J. Fisher, *Chem. Soc. Rev.*, 2014, **43**, 185–204.

50 N. S. Choi, Z. Chen, S. A. Freunberger, X. Ji, Y. K. Sun, K. Amine, G. Yushin, L. F. Nazar, J. Cho and P. G. Bruce, *Angew. Chemie - Int. Ed.*, 2012, **51**, 9994–10024.

51 M. Winter and R. J. Brodd, *Chem. Rev.*, 2004, **104**, 4245–4269.

52 B. E. Conway, *J. Electrochem. Soc.*, 1991, **138**, 1539.

53 R. Kotz and M. Carlen, *Electrochim. Acta*, 2000, **45**, 2483–2498.

54 X. Zhang, X. Cheng and Q. Zhang, *J. Energy Chem.*, 2016, **25**, 967–984.

55 Y. Wang, Y. Song and Y. Xia, *Chem. Soc. Rev.*, 2016, **45**, 5925–5950.

56 H. Zhou, S. Zhu, M. Hibino and I. Honma, *J. Power Sources*, 2003, **122**, 219–223.

57 H.-Q. Li, J.-Y. Luo, X.-F. Zhou, C.-Z. Yu and Y.-Y. Xia, *J. Electrochem. Soc.*, 2007, **154**, A731.

58 J. Theerthagiri, K. Karuppasamy, G. Durai, A. ul H. S. Rana, P. Arunachalam, K. Sangeetha, P. Kuppusami and H. S. Kim, *Nanomaterials*, , DOI:10.3390/nano8040256.

59 M. K. Ravikumar, E. Niranjana, A. Sundar Rajan, A. Banerjee, S. A. Gaffoor and A. K. Shukla, *J. Indian Inst. Sci.*, 2009, **89**, 455–463.

60 Q. Wang, L. Jiao, H. Du, J. Yang, Q. Huan, W. Peng, Y. Si, Y. Wang and H. Yuan, *CrystEngComm*, 2011, **13**, 6960–6963.

61 T. Zhu, B. Xia, L. Zhou and X. Wen Lou, *J. Mater. Chem.*, 2012, **22**, 7851–7855.

62 Z. Stević and M. Rajčić-Vujasinović, *J. Power Sources*, 2006, **160**, 1511–1517.

63 C. Burda, X. Chen, R. Narayanan and M. A. El-Sayed, *Chemistry and properties of nanocrystals of different shapes*, 2005, vol. 105.

64 C. H. Lai, M. Y. Lu and L. J. Chen, *J. Mater. Chem.*, 2012, **22**, 19–30.

65 R. Liu, J. Duay and S. B. Lee, *Chem. Commun.*, 2011, **47**, 1384–1404.

66 Y. Liu, X. He, D. Hanlon, A. Harvey, J. N. Coleman and Y. Li, *ACS Nano*, 2016, **10**, 8821–8828.

67 G. Li, D. Luo, X. Wang, M. H. Seo, S. Hemmati, A. Yu and Z. Chen, *Adv. Funct. Mater.*, 2017, **27**, 1–8.

68 Y. M. Chen, X. Y. Yu, Z. Li, U. Paik and X. W. Lou, *Sci. Adv.*, 2016, **2**, 1–9.

69 Z. Deng, H. Jiang and C. Li, *Small*, 2018, **14**, 1–9.

70 F. Zhou, S. Xin, H. W. Liang, L. T. Song and S. H. Yu, *Angew. Chemie - Int. Ed.*, 2014, **53**, 11552–11556.

71 B. Wang, S. Li, X. Wu, W. Tian, J. Liu and M. Yu, *J. Mater. Chem. A*, 2015, **3**, 13691–13698.

72 M. R. Gao, Y. F. Xu, J. Jiang and S. H. Yu, *Chem. Soc. Rev.*, 2013, **42**, 2986–3017.

73 B. Xu, S. Qi, M. Jin, X. Cai, L. Lai, Z. Sun, X. Han, Z. Lin, H. Shao, P. Peng, Z. Xiang, J. E. ten Elshof, R. Tan, C. Liu, Z. Zhang, X. Duan and J. Ma, *Chinese Chem. Lett.*, 2019,

30, 2053–2064.

74 Z. Li, M. Smeu, A. Rives, V. Maraval, R. Chauvin, M. A. Ratner and E. Borguet, *Nat. Commun.*, 2015, **6**, 6321.

75 D. A. C. Brownson and C. E. Banks, *Analyst*, 2010, **135**, 2768–2778.

76 S. K. Hong, K. Y. Kim, T. Y. Kim, J. H. Kim, S. W. Park, J. H. Kim and B. J. Cho, *Nanotechnology*, , DOI:10.1088/0957-4484/23/45/455704.

77 P. Avouris and C. Dimitrakopoulos, *Mater. Today*, 2012, **15**, 86–97.

78 C. Androulidakis, G. Tsoukleri, N. Koutroumanis, G. Gkikas, P. Pappas, J. Parthenios, K. Papagelis and C. Galiotis, *Carbon N. Y.*, 2015, **81**, 322–328.

79 A. A. Balandin, *Nat. Mater.*, 2011, **10**, 569–581.

80 T. Gokus, R. R. Nair, A. Bonetti, M. Böhmler, A. Lombardo, K. S. Novoselov, A. K. Geim, A. C. Ferrari and A. Hartschuh, *ACS Nano*, 2009, **3**, 3963–3968.

81 A. Nourbakhsh, M. Cantoro, T. Vosch, G. Pourtois, F. Clemente, M. H. Van Der Veen, J. Hofkens, M. M. Heyns, S. De Gendt and B. F. Sels, *Nanotechnology*, , DOI:10.1088/0957-4484/21/43/435203.

82 X. Wang and G. Shi, *Phys. Chem. Chem. Phys.*, 2015, **17**, 28484–28504.

83 T. D. Thanh, N. D. Chuong, H. Van Hien, T. Kshetri, L. H. Tuan, N. H. Kim and J. H. Lee, *Prog. Mater. Sci.*, 2018, **96**, 51–85.

84 J. Azadmanjiri, V. K. Srivastava, P. Kumar, M. Nikzad, J. Wang and A. Yu, *J. Mater. Chem. A*, 2018, **6**, 702–734.

85 A. Azizi, S. Eichfeld, G. Geschwind, K. Zhang, B. Jiang, D. Mukherjee, L. Hossain, A. F. Piasecki, B. Kabius, J. A. Robinson and N. Alem, *ACS Nano*, 2015, **9**, 4882–4890.

86 C. Li, Q. Cao, F. Wang, Y. Xiao, Y. Li, J. J. Delaunay and H. Zhu, *Chem. Soc. Rev.*, 2018, **47**, 4981–5037.

87 C. Zhao, X. Wang, J. Kong, J. M. Ang, P. S. Lee, Z. Liu and X. Lu, *ACS Appl. Mater. Interfaces*, 2016, **8**, 2372–2379.

88 Q. Liu, B. Cook, M. Gong, Y. Gong, D. Ewing, M. Casper, A. Stramel and J. Wu, *ACS Appl. Mater. Interfaces*, 2017, **9**, 12728–12733.

89 Z. Zhou, F. Xiu, T. Jiang, J. Xu, J. Chen, J. Liu and W. Huang, *J. Mater. Chem. C*, 2019, **7**, 10764–10768.

90 Z. Du, S. Yang, S. Li, J. Lou, S. Zhang, S. Wang, B. Li, Y. Gong, L. Song, X. Zou and P. M. Ajayan, *Nature*, 2020, **577**, 492–496.

91 A. Rothschild, J. Sloan and R. Tenne, *J. Am. Chem. Soc.*, 2000, **122**, 5169–5179.

92 J. Cui, L. Wang and X. Yu, *New J. Chem.*, 2019, **43**, 16007–16011.

93 M. Nath, A. Govindaraj and C. N. R. Rao, *Adv. Mater.*, 2001, **13**, 283–286.

94 M. A. Lukowski, A. S. Daniel, F. Meng, A. Forticaux, L. Li and S. Jin, *J. Am. Chem. Soc.*, 2013, **135**, 10274–10277.

95 S. Mao, Z. Wen, S. Ci, X. Guo, K. Ostrikov and J. Chen, *Small*, 2015, **11**, 414–419.

96 H. Liu, H. Cui, F. Han, X. Li, J. Wang and R. I. Boughton, *Cryst. Growth Des.*, 2005, **5**, 1711–1714.

97 T. A. Pomelova, T. Y. Podlipskaya, N. V. Kuratieva, A. G. Cherkov, N. A. Nebogatikova, M. R. Ryzhikov, A. Huguenot, R. Gautier and N. G. Naumov, *Inorg. Chem.*, 2018, **57**, 13594–13605.

98 H. Tian, C. Fan, G. Liu, S. Yuan, Y. Zhang, M. Wang and E. Li, *Appl. Surf. Sci.*, 2019, **487**, 1043–1048.

99 M. P. Thomas, A. Ullah, R. H. Pham, H. Djieutedjeu, J. P. Selegue and B. S. Guiton, *Cryst. Growth Des.*, 2020, **20**, 5728–5735.

100 L. Jiang and Y. J. Zhu, *Eur. J. Inorg. Chem.*, 2010, 1238–1243.

101 Y. Chen, C. Davoisne, J. M. Tarascon and C. Guéry, *J. Mater. Chem.*, 2012, **22**, 5295–5299.

102 H. Wang, S. Zhuo, Y. Liang, X. Han and B. Zhang, *Angew. Chemie*, 2016, **128**, 9201–9205.

103 C. Meng, M. C. Lin, X. W. Du and Y. Zhou, *ACS Sustain. Chem. Eng.*, 2019, **7**, 6999–7003.

104 A. Burnin, S. Poggio, J. King and J. J. BelBruno, *J. Mater. Sci.*, 2016, **51**, 9716–9722.

105 B. H. Kim, S. H. Kwon, H. H. Gu and Y. J. Yoon, *Phys. E Low-Dimensional Syst. Nanostructures*, 2019, **106**, 45–49.

106 P. Ge, M. D. Scanlon, P. Peljo, X. Bian, H. Vubrel, A. O'neill, J. N. Coleman, M. Cantoni, X. Hu, K. Kontturi, B. H. Liu and H. H. Girault, *Chem. Commun.*, 2012, **48**, 6484–6486.

107 L. Pu, D. Liu, K. Li, J. Wang, T. Yang, B. Ge and Z. Liu, *Int. J. Hydrogen Energy*, 2017, **42**, 14253–14263.

108 B. Bera and D. Banerjee, 2019, **21**, 19–30.

109 N. Kanda, Y. Nakanishi, D. Liu, Z. Liu, T. Inoue, Y. Miyata, D. Tománek and H. Shinohara, *Nanoscale*, 2020, **12**, 17185–17190.

110 A. Kumar, Y. Kuang, Z. Liang and X. Sun, *Mater. Today Nano*, 2020, **11**, 100076.

111 Z. Liu, L. Zhang, R. Wang, S. Poyraz, J. Cook, M. J. Bozack, S. Das, X. Zhang and L. Hu, *Sci. Rep.*, 2016, **6**, 1–8.

112 F. Meng, H. Wang, F. Huang, Y. Guo, Z. Wang, D. Hui and Z. Zhou, *Compos. Part B Eng.*, 2018, **137**, 260–277.

113 N. Liu, X. Wang, W. Xu, H. Hu, J. Liang and J. Qiu, *Fuel*, 2014, **119**, 163–169.

114 S. Anantharaj, J. Kennedy and S. Kundu, *ACS Appl. Mater. Interfaces*, 2017, **9**, 8714–

8728.

115 *Linear Sweep and Cyclic Voltametry : The Principles*, .

116 GAMRY, *Gamry Appl. Notes*, 2014, 1–19.

117 GAMRY, *Gamry Appl. Notes*, 1–33.

118 Z. Chen, D. Cummins, B. N. Reinecke, E. Clark, M. K. Sunkara and T. F. Jaramillo, *Nano Lett.*, 2011, **11**, 4168–4175.

119 J. Kibsgaard and T. F. Jaramillo, *Angew. Chemie - Int. Ed.*, 2014, **53**, 14433–14437.

120 X. Dai, K. Du, Z. Li, M. Liu, Y. Ma, H. Sun, X. Zhang and Y. Yang, *ACS Appl. Mater. Interfaces*, 2015, **7**, 27242–27253.

121 R. Wei, M. Fang, G. Dong and J. C. Ho, *Sci. Bull.*, 2017, **62**, 971–973.

122 R. Chen, C. Yang, W. Cai, H. Y. Wang, J. Miao, L. Zhang, S. Chen and B. Liu, *ACS Energy Lett.*, 2017, **2**, 1070–1075.

123 Gamry Instruments, *Gamry Appl. Notes*, 2012, 2–7.

Chapter 2

Facile Microwave Approach Towards High Performance MoS_2/graphene Nanocomposite for Hydrogen Evolution Reaction

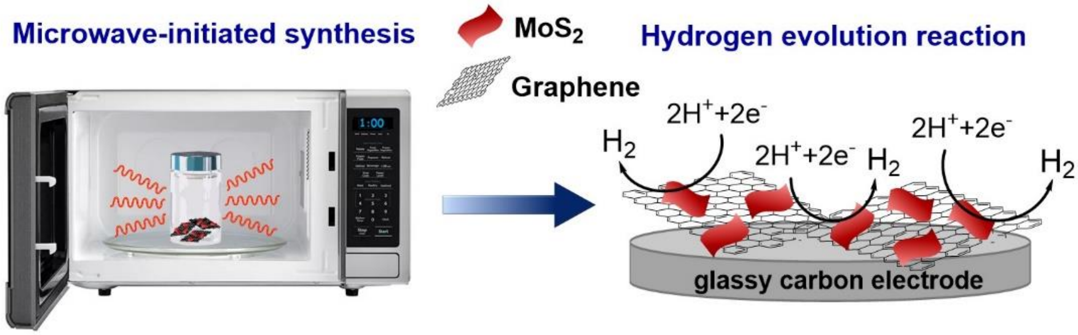

Part of this chapter has been published in Science China Materials 2020, 63(1): 62–74.

Abstract

Low-cost, highly efficient catalysts for hydrogen evolution reaction (HER) is very important to advance energy economy based on clean hydrogen gas. Intensive research on two-dimensional molybdenum disulfides (MoS_2) have been conducted due to their remarkable catalytic properties. However, most of the existing synthesis approaches are time consuming, complicated and less efficient. The present work successfully demonstrates the production of MoS_2/graphene catalyst through ultra-fast (60 seconds) microwave-initiated approach. High specific surface area and conductivity of graphene delivers a favorable conductive network for the growth of MoS_2 nanosheets, along with rapid charge transfer kinetics. As produced MoS_2/graphene nanocomposite exhibits superior electrocatalytic activity for the HER in acidic medium, with a low onset potential of 62 mV, high cathodic currents and a Tafel slope of 43.3 mV per decade. Beyond excellent catalytic activity, MoS_2/graphene reveals long cycling stability with a very high cathodic current density of around 1000 mA cm^{-2} at an overpotential of 250 mV. Moreover, the MoS_2/graphene-catalyst exhibits outstanding HER activities at a temperature range of 30 °C to 120 °C with low activation energy of 36.51 kJ mol^{-1}, providing the opportunity of practical scalable processing.

2.1. Introduction

Because of present climate issues and the deterioration of existing natural resources, the energy dependency on fossil fuels is becoming disputed in many ways. To resolve energy crisis, hydrogen is considered as a promising energy carrier for clean and sustainable energy technologies, especially for the intermittent renewable resources such as solar, hydro or wind energy.[1–3] Though water electrolysis is solely the green approach to generate hydrogen energy, large-scale hydrogen production through photo/electrolysis is still very challenging due to the lack of energy-efficient and cost-effective techniques. The electrolysis process requires advanced electrocatalyst to reduce the overpotential and to accelerate the kinetically rate-limiting steps involved within reductive half reaction of water splitting, known as the hydrogen evolution reaction (HER, i.e., $2H^+ + 2e^- \rightarrow H_2$).[1,4] To date, platinum (Pt) and its composites are known to be the most effective HER electrocatalysts in acidic media. However, the high cost and low earth abundance of these materials severely hinder their use for commercial applications. Nonprecious catalysts, which are made from earth-abundant elements are therefore emerging for a large-scale implementation as HER catalysts.[5,6] To develop the cost-effective alternatives to Pt, intense research is being conducted for hydrogen production through photo/electrocatalytic method. Such alternatives typically include nickel or nickel-based materials, which operate in alkaline electrolytes.[7–9] Nevertheless, HER generally requires acidic conditions and the long-term stability of low-cost catalysts needs to be improved in acidic electrolytes. Inspired by the HER mechanisms of natural catalysts such as hydrogenase and nitrogenase enzymes, metal chalcogenides (MCs) containing non-noble metals (Mo, W or Co) have been designed to catalyze the electrochemical production of hydrogen.[10,11] Among all the MCs, molybdenum disulfide (MoS_2) and its compounds have recently emerged as a very promising class of nonprecious, earth-abundant HER catalyst with high catalytic activity and good stability in acidic electrolytes.[12–15] In comparison to bulk MoS_2, nano-crystallized MoS_2 has been identified as a promising catalyst because of exposing more active edges in nanostructured forms. In past few years, extensive effort has been devoted to improve the HER catalytic activity of MoS_2 by identifying and exposing active sites,[16,17] as well as enhancing electron transport through nanostructuring, shape controlling, phase engineering, doping, intercalation, hybridization, and so on.[12,16,18–23] Besides morphology, the electrical conductivity is another key factor that influence electrocatalytic efficiency of HER catalysts. Taking these factors into account, carbon materials such as conducting polymers, graphene, reduced graphene oxide (r-GO), carbon nanotubes (CNTs), etc. are considered as ideal supports to improve the electrocatalytic activity because of their unique properties. The honeycomb graphene structure, which consists of extended two-dimensional sheets of sp^2-bonded carbon atoms shows superior properties such as fast mobility of charge carriers, high electrical conductivity and exceptionally large specific surface area.[24,25] Therefore, various forms of graphene have been investigated as a potential conducting support for MoS_2 catalyst to demonstrate high HER electrocatalytic activity.[18,26,27] To synthesize these hybrid materials, most of the approaches require complex equipment setups, long processing time, high energy consumption, along with safety, scalability and cost issues, which could limit the range of potential applications. Several examples involve the use of toxic gases along with calcination under H_2/Ar atmosphere,[28] long-time heating of precursor materials,[29] complex lyophilization dehydration process,[30] cumbersome electro-deposition which requires advanced care,[31] and so on. In this regard, microwave-initiated manufacturing can become a promising approach to develop efficient MoS_2/graphene-catalyst for HER. In present, the application of microwave approach in synthetic chemistry is a fast-growing research area, due to its advantages such as rapid volumetric heating, higher reaction rate, high selectivity, reducing reaction time, and increasing yields of products compared to conventional heating methods.[32–34] Successful synthesis of MCs by microwave-initiated approach have been reported and demonstrated that it can be used for the highly efficient production of different hybrid compounds.[35–38]

In this work, we demonstrated the direct growth of a nanocomposite of MoS_2 on graphene substrate via a facile, scalable and efficient microwave-initiated approach (Figure 2.1), following the previous study of our group to synthesize MCs on polypyrrole nanofiber substrate.[38]

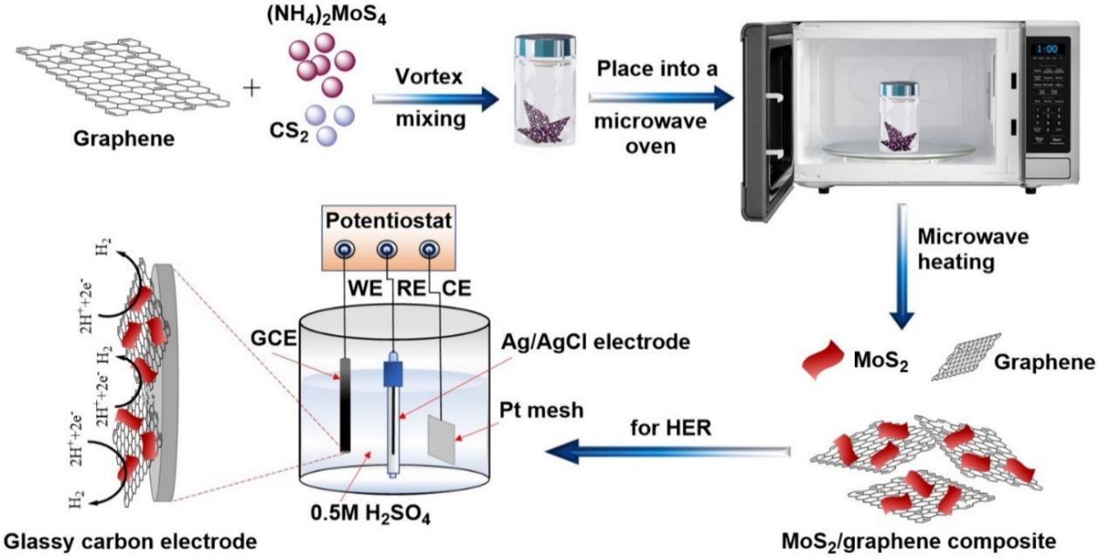

Figure 2.1. Illustration of the microwave-initiated synthesis of MoS_2/graphene composite, employing as an electrocatalyst for hydrogen evolution reaction.

This technique represents a clean, ultrafast (60 seconds) synthetic approach using microwave heating without any inert gas protection or use of intense facilities. More importantly, graphene exhibits strong interaction with microwaves making it an efficient susceptor to achieve microwave- heating rapidly and uniformly. During the reaction, the strong interaction between substrate material and microwave-irradiation takes place to achieve fast thermal decomposition of molybdenum-containing precursor to synthesize uniformly dispersed MoS_2/graphene nanocomposites. Benefiting from the synergistic effects of MoS_2 catalyst and graphene, this MoS_2/graphene nanocomposite has been demonstrated to be an active nonprecious metal-based catalyst for electrochemical hydrogen evolution reaction. As-produced MoS_2/graphene-catalyst exhibited low overpotential, small Tafel slope with a very high cathodic current density, along with fascinating cycling activation behavior and high stability under acidic condition, even at high operating temperatures (30−120°C).

2.2. Experimental details

2.2.1. Materials and reagents

Ammonium tetrathiomolybdate ($(NH_4)_2MoS_4$, 99.95%) was purchased from BeanTown Chemical, Inc. Carbon disulfide (CS_2, liquid, 99.9%), Molybdenum (IV) sulfide (MoS_2 ~325 mesh powder, 98%), and Poly (vinylidene fluoride) (PVDF powder, $(\text{-}CH_2CF_2\text{-})_n$) were purchased from Alfa Aesar. N, N-Dimethylformamide (DMF, $HCON(CH_3)_2$) was obtained from *Macron Fine Chemicals*™. Nitric acid (69-70%), and Acetone (CH_3COCH_3) were supplied by BDH Chemicals, VWR. Graphene substrate was obtained from Magnolia Ridge Inc. Sulfuric acid was purchased from Anachemia. All chemicals purchased were used without further treatment or purification. For electrochemical characterizations, platinum (Pt) gauze (100 mesh, 99.9% metal basis) was obtained from Alfa Aesar. Glassy carbon electrode (CHI 104, 3 mm in diameter) was purchased from CH Instruments, Inc. and silver/silver chloride (Ag/AgCl, 3 M KCl, E^o= +0.197 V vs. RHE) electrode was acquired from Hach.

2.2.2. Microwave-initiated synthesis of MoS_2/graphene nanocomposites

To prepare the MoS_2/graphene compound, certain amount of $(NH_4)_2MoS_4$ and graphene (weight ratio = 1:1 or 1:2 or 2:1) were taken in a glass vial and mixed homogeneously by a speed mixer at 2000 rpm. After a while, CS_2 solvent (200 μL) was added and mixed well by speed mixer at 2000 rpm. The solvent was evaporated after 10 mins of air drying. Next, the uniform mixture was subjected to microwave irradiation in a domestic microwave oven (frequency ≈ 2.45 GHz). Figure 2.2 shows a typical setup during microwave irradiation, placing the glass vial on top of a microwave kiln. Graphene served as a substrate to absorb the microwave energy and convert it to heat energy. During the process, microwave heating triggered the reduction of $(NH_4)_2MoS_4$ to MoO_2 and MoO_3, then converted to MoS_2 dispersed on graphene substrate, releasing other constituents in gaseous forms.

Figure 2.2. Microwave irradiation setup.

2.2.3. Physicochemical characterizations

The surface morphologies and chemical compositions of graphene and MoS_2/graphene were characterized by scanning electron microscope (SEM; JEOL 7000 FE), coupled with an energy dispersive X-ray spectrometer (EDS, Oxford Instruments) with an acceleration voltage of 20 kV. The transmission electron microscopy (TEM), high resolution TEM (HRTEM) and selected area electron diffraction (SAED) experiments were carried out using JEOL JEM-3010 TEM with a LaB6 electron gun operated under 300 kV. Micro-Raman spectroscopy was performed on the samples at room temperature by employing back-scattering geometry using the 442 nm line (80 mW) of a dual wavelength He-Cd laser (Kimmon Electric). The x-ray diffraction (XRD) pattern of MoS_2/graphene was analyzed by a Bruker D8 Advance x-ray powder diffractometer with Ni filtered CuK α radiation (wavelength, λ = 1.5406 Å).

Photoemission measurements were performed in a load-locked Kratos XSAM 800 surface analysis system and XPS spectra were recorded in the fixed analyzer transmission (FAT) mode with a pass energy of 80 eV. In addition, nitrogen adsorption isotherms were measured with the aid of Quantachrome's Nova 2200e instrument at 77 K. The Brunauer-Emmett-Teller (BET) method was used to calculate the specific surface area.

2.2.4. Electrochemical measurements

Before each electrochemical experiment, glassy carbon electrode (GCE) was polished with alumina powder (Al_2O_3, 0.05 μm) on a polishing mat to obtain a mirror-finished surface, followed by immersing in 6 M HNO_3 for 10 mins, rinsing with DI water and vacuum drying. To prepare the working electrode, MoS_2/graphene hybrid catalyst (2 mg) was mixed with PVDF powder (0.2 mg) and DMF (50 μL) to form a homogeneous black slurry. The catalyst slurry was drop-coated onto the clean surface of GCE (0.07 cm^2) with a mass loading of ~5 mg cm^{-2}, which was then dried in a vacuum dryer at 60 °C for 30 mins. For comparison, GCEs were also coated with pure MoS_2, pure graphene, and a physical mixture of MoS_2 and graphene (MoS_2+graphene) following the same steps. All electrochemical studies were performed using a CH Instrument (CHI 760D) potentiostat using 'Electrochemical Analyzer' software (version 15.03) in a standard three-electrode setup consisting of a glassy carbon working electrode, silver chloride electrode (Ag/AgCl, 3 M KCl) as the reference, and platinum (Pt) mesh as a counter electrode in 0.5 M H_2SO_4 electrolyte. To determine the HER activities of samples, the potentials were referred to the reversible hydrogen electrode (RHE) by using the equation: $V\,(vs.\ RHE) = V\,(vs.\ Ag/AgCl) + 0.197 + (0.059 \times pH)$. The electrocatalytic activity of MoS_2/graphene towards HER was examined by polarization curves using linear sweep voltammetry (LSV) at a scan rate of 1 mV s^{-1} in 0.5 M H_2SO_4 at room temperature. Before each LSV measurement, cyclic voltammetry (CV) was run for 50 cycles to achieve stable condition. CV was also performed to determine active surface area of catalyst samples. Prior to each measurement of LSV and CV, a resistance test was made and the *iR* compensation was applied using the CHI software. Electrochemical impedance spectroscopic (EIS) measurements were carried out in 0.5 M H_2SO_4 at various overpotentials from 50 mV to 300 mV (vs. RHE) in the frequency range of 10^{-2} to 10^{6} Hz with a single modulated AC potential of 5 mV. Afterward, the EIS spectra were fitted by the EC-Lab software.

2.3. Results and discussion

2.3.1. Observation during 60 seconds of microwave-initiated synthesis

Within almost 30 seconds of applying microwave irradiation, the reaction mixture sparks a fiery glow by forming a splendid plasma. As shown in Figure 2.3, the glowing spark continues to grow with time. After 60 seconds of microwave irradiation, the glass vial was taken out, opened and the products were collected and examined for further characterizations. In some cases, a thin film of material adhered to the surface of vial wall, which is also scratched out using a spatula.

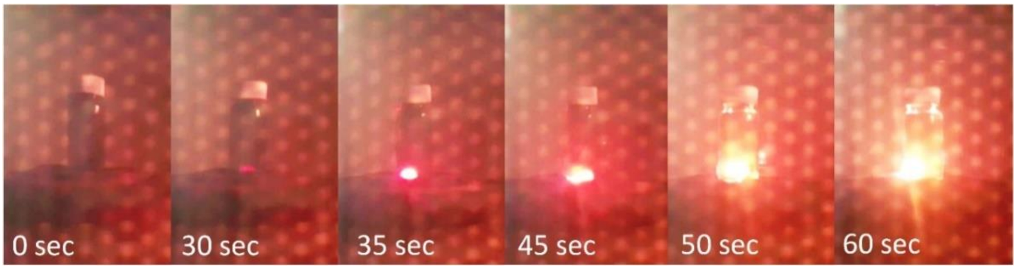

Figure 2.3. Observations during microwave irradiation for 60 seconds.

Although the exact nature of the interactions between microwaves and reaction precursors during microwave-initiated synthesis is somewhat unclear and speculative, the quality of products can be controlled *via* optimizing several reaction parameters.

2.3.2. Material characterizations

In this study, 7 different samples (sample C1, C2, C3, T1, T2, P1 and P2) of MoS_2/graphene compounds were prepared to optimize the microwave-assisted reaction parameters, such as, precursors quantity/ratios, irradiation time and irradiation power. The synthesis mechanism can be predicted by the following reaction steps (Equation 2.1, 2.2):

(i) $(NH_4)_2MoS_4 \rightarrow MoS_3 + 2\ NH_3 + H_2S;\ \ 155\ °C - 280\ °C$ .... (2.1)

(ii) $MoS_3 \rightarrow MoS_2 + S;\ \ 300\ °C - 820\ °C$ .... (2.2)

The elemental EDS analysis was performed to identify the synthesized samples, and the results are displayed in Figure 2.4 and 2.5. The sample C1, C2 and C3 contain different precursor ratios with 60 second of irradiation time and 1250 W of microwave power.

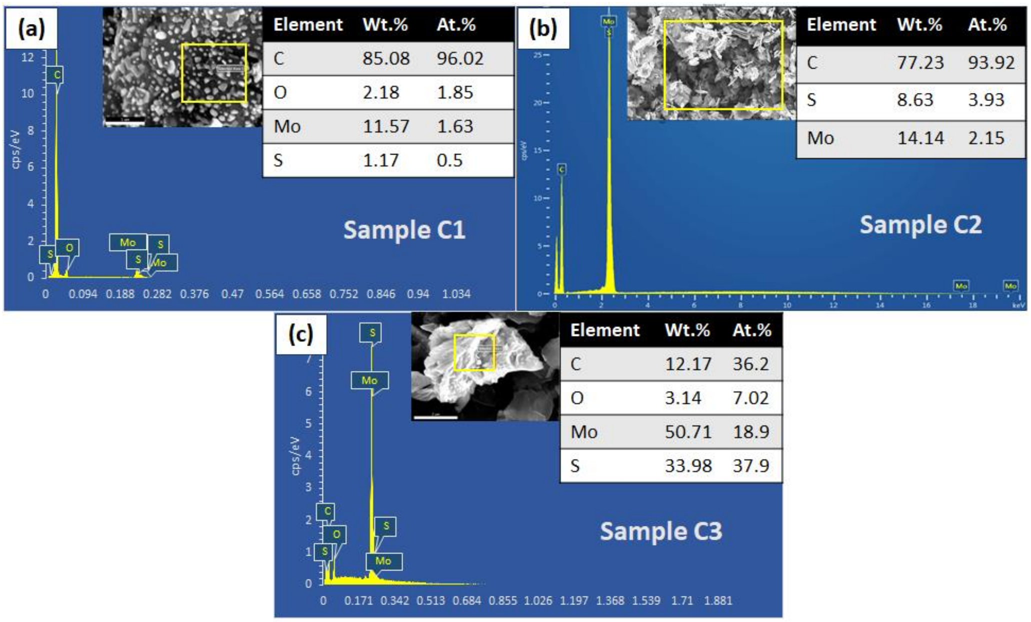

(a)

Element	Wt.%	At.%
C	85.08	96.02
O	2.18	1.85
Mo	11.57	1.63
S	1.17	0.5

(b)

Element	Wt.%	At.%
C	77.23	93.92
S	8.63	3.93
Mo	14.14	2.15

(c)

Element	Wt.%	At.%
C	12.17	36.2
O	3.14	7.02
Mo	50.71	18.9
S	33.98	37.9

Figure 2.4. EDS patterns of sample (a) C1, (b) C2 and (c) C3 [inset table: wt% and atomic% of carbon (C), Oxygen (O), Sulfur (S) and Molybdenum (Mo) elements].

Sample T1 and T2 were prepared with 30 and 120 seconds of irradiation times, respectively, and sample P1 and P2 were synthesized by applying 800 and 400 W of microwave powers, respectively. The EDS analysis revealed the best result for sample C2 (Figure 2.4b), which shows that the nanosheets were primarily composed of molybdenum (Mo) and sulfur (S). Additionally, a huge amount (~80 wt%) of carbon (C) content was found due to the presence of graphene substrate. The atomic ratio of Mo and S components was very close to 1:2, which satisfied the formula of MoS_2 (S-Mo-S), confirming the formation of MoS_2 in as-produced nanocomposites. The results are briefly described in Table 2.1 for each of the C1−P2 samples.

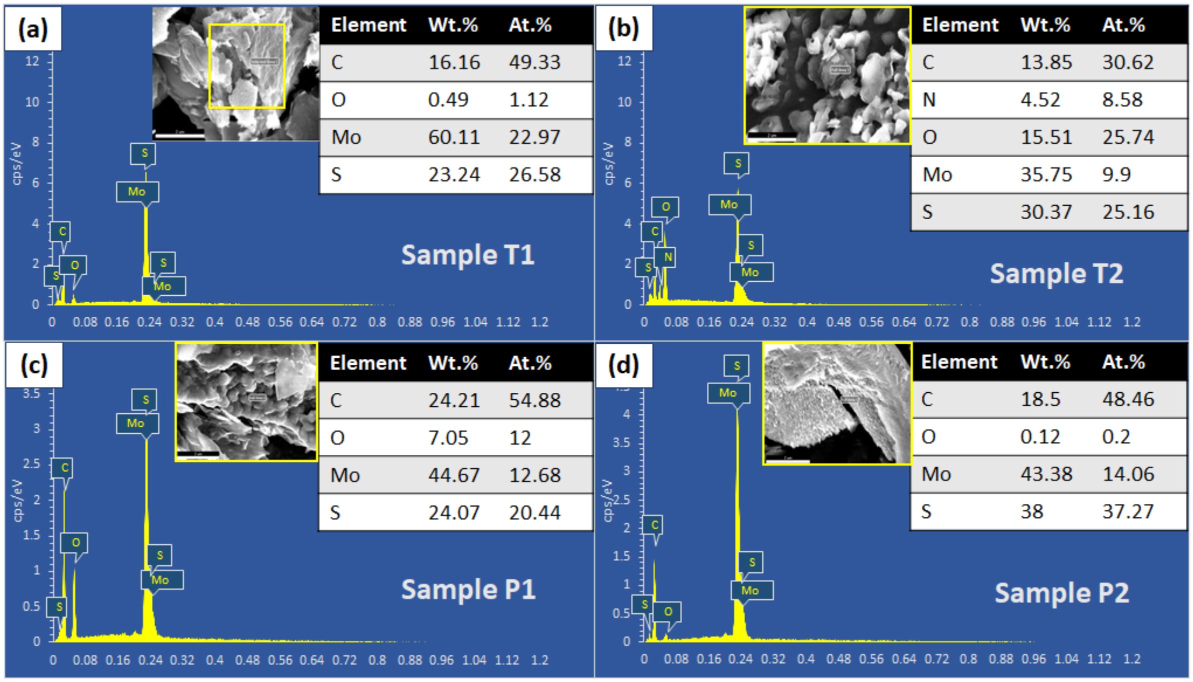

(a)

Element	Wt.%	At.%
C	16.16	49.33
O	0.49	1.12
Mo	60.11	22.97
S	23.24	26.58

(b)

Element	Wt.%	At.%
C	13.85	30.62
N	4.52	8.58
O	15.51	25.74
Mo	35.75	9.9
S	30.37	25.16

(c)

Element	Wt.%	At.%
C	24.21	54.88
O	7.05	12
Mo	44.67	12.68
S	24.07	20.44

(d)

Element	Wt.%	At.%
C	18.5	48.46
O	0.12	0.2
Mo	43.38	14.06
S	38	37.27

Figure 2.5. EDS patterns of samples T1, T2, P1 and P2 [inset table: wt% and atomic% of carbon (C), Nitrogen (N), Oxygen (O), Sulfur (S) and Molybdenum (Mo) elements].

Table 2.1. Optimization of reaction parameters (precursor ratios, microwave time, microwave power) for MoS_2/graphene sample.

Sample	**$(NH_4)_2MoS_4$ (mg)**	**Graphene (mg)**	**CS_2 (µL)**	**Microwave time (sec)**	**Microwave power (W)**	**Results (based on EDS analysis)**
C1	15	30	200	60	1250	Excess C
C2	15	15	200	60	1250	Mo:S ≈ 1:2
C3	30	15	200	60	1250	Excess MoS_x
T1	15	15	200	30	1250	Mo:S ≈ 1:1; insufficient reaction
T2	15	15	200	120	1250	Presence of high amount of O and N
P1	15	15	200	60	800	Temperature ↓; Mo:S ≈ 1:3
P2	15	15	200	60	400	Insufficient reaction

The surface morphologies of pure graphene and MoS_2/graphene were investigated by SEM analysis. As shown in Figure 2.6a and 2.6b, thick flake-like structures were observed for graphene. Whereas after microwave-initiated synthesis, the growth of MoS_2 layers (Figure 2.6c and 2.6d) was exhibited embedding with graphene flakes, substantiating the successful synthesis of MoS_2/graphene nanocomposite.

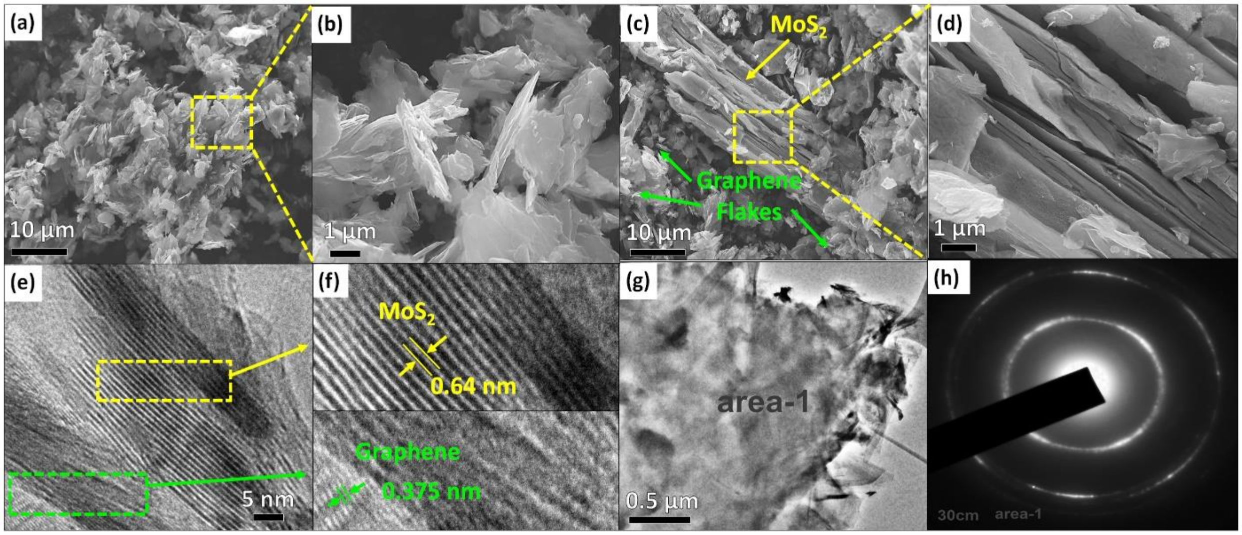

Figure 2.6. SEM images of (a, b) graphene flakes and (c, d) layered MoS_2 embedded on graphene, at low and high magnifications. (e) HRTEM image of MoS_2/graphene. (f) High-magnification HRTEM image of MoS_2 nanosheets and graphene. (g) Low-magnification TEM image of MoS_2/graphene nanocomposite. (h) SAED pattern of MoS_2 nanosheets.

High-resolution transmission electron microscopy (HRTEM) imaging was performed to examine the microstructure and crystallinity of MoS_2/graphene nanocomposite. Figure 2.6e exhibited the HRTEM image of MoS_2/graphene, while High-magnification HRTEM image (Figure 2.6f) prominently displayed the difference between graphene and MoS_2 nanosheets. The MoS_2 exhibited the few-layered structure with an interlayer distance of 6.4 Å, where the edge of the layers of 2D nanosheets were shown in white lines. MoS_2 nanosheets demonstrated the corrugated layers in the low-magnification TEM image, as shown in Figure 2.6g. In addition, the SAED patterns of corresponding area (marked as 'area 1' in Figure 2.6g and 2.6h) displayed broad and hazy diffraction rings, which indicates low crystallization of MoS_2 on crystal graphene surface.

Furthermore, Raman spectra of pure graphene and MoS_2/graphene were shown in Figure 2.7a and 2.7b. The characteristic Raman peaks for graphene (D, G and 2D bands) were clearly observed and from the MoS_2/graphene peaks it was revealed that the composite was crystalline 2H–MoS_2, which was confirmed by the Raman peaks located at 384.9 cm^{-1} (in-plane E^1_{2g} mode) and 409.3 cm^{-1} (out-of-plane A_{1g} mode).[39,40] Previously, it has been reported that the energy difference between two Raman peaks (Δ) can be used to detect the number of MoS_2 layers.[39,41] In this work, Δ is about 24.4 cm^{-1}, indicating the existence of the five to six layered MoS_2 nanosheets.

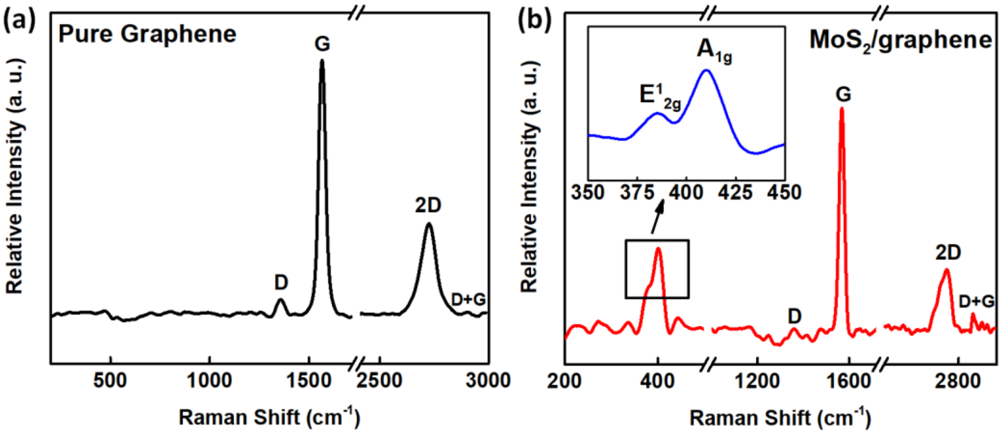

Figure 2.7. Raman spectra of (a) pure graphene and (b) MoS_2/graphene composite (inset shows the MoS_2 peaks).

In addition, the X-ray diffraction (XRD) and X-ray photoelectron spectroscopy (XPS) analyses were performed to identify the formation of crystalline MoS_2 nanosheets. The XRD pattern of the MoS_2 (Figure 2.8a) displays diffraction peaks in the range from 10° to 70°. The peaks appeared at 14.2°, 33.5°, 39.8°, 43.1°, 49.1° and 59.3° were corresponding to (002), (100), (103), (006), (105) and (110) planes, respectively. The patterns can be indexed to the standard hexagonal 2H–MoS_2 structure (JPCDS no. 37-1492),[42] indicating that after reacting under microwave irradiation Mo-precursor with CS_2 solution completely reduced to MoS_2. Since, graphene possessed almost 80 wt% in MoS_2/graphene composite, it displayed a peak at ~26° with high intensity as a reflection from carbon layers (002).[43] The peak around 18° could be corresponding to (003) plane, which suggested that some of the graphene was lying in the van der Waals gap of MoS_2 layers, leading to an expansion of the interplanar spacing.[44]

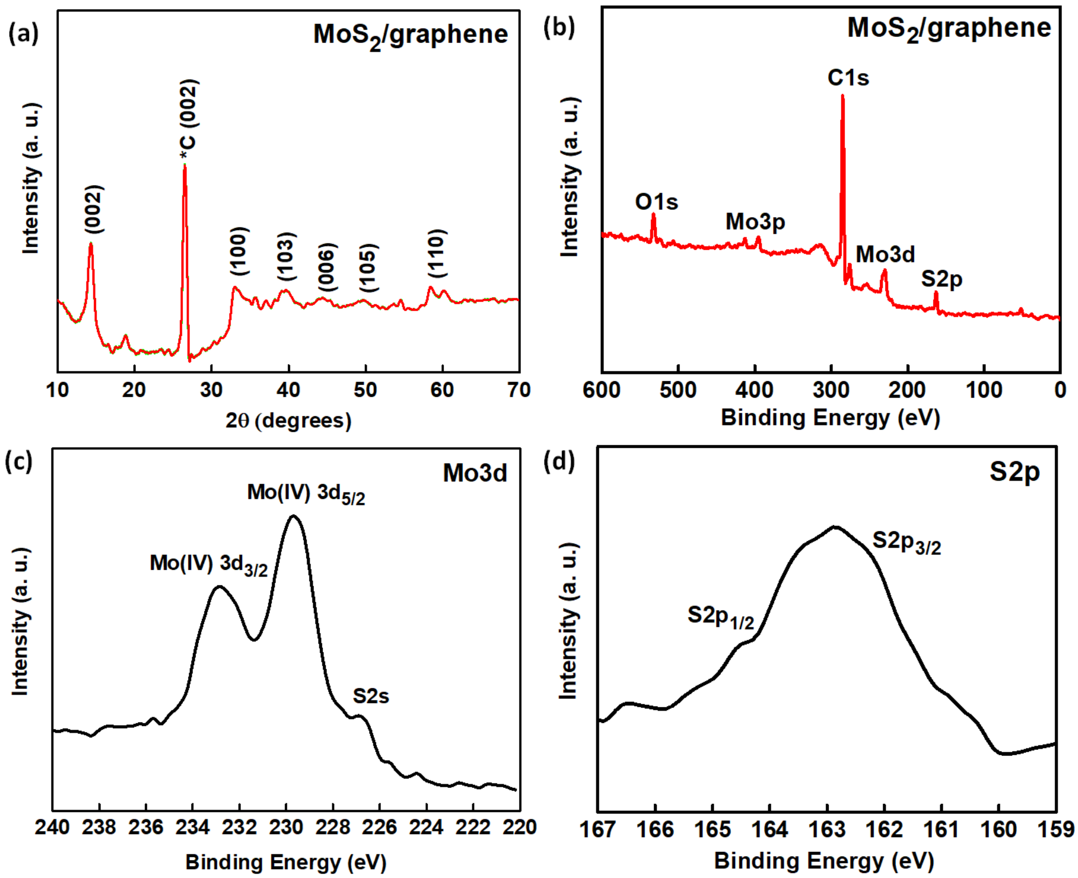

Figure 2.8. (a) XRD pattern, and (b) XPS spectrum of MoS_2/graphene composite. High resolution XPS spectra of (c) Mo 3d, and (d) S 2p regions of MoS_2/graphene.

X-ray photoelectron spectroscopy (XPS) was analyzed to further confirm the microwave reduction of Mo(VI) in $(NH_4)_2MoS_4$ precursor to Mo(IV) in MoS_2. The survey spectrum was represented in Figure 2.8b for MoS_2/graphene, and the peaks for C, Mo, S, and O elements were observed, indicating the presence of MoS_2 and graphene in the hybrid nanocomposite. The high-resolution XPS spectrum for Mo 3d (Figure 2.8c) showed the binding energies of Mo 3d5/2 and Mo 3d3/2 peaks at 229.4 and 232.7 eV, respectively, which were matched with typical values for Mo (IV) in MoS_2. The peaks at 162.1 eV and 164.2 eV in Figure 2.8d were attributed to 2p1/2 and 2p2/3 of S^{2-}. The binding energies observed from this study were close to the previously reported values for MoS_2,[27,30] which further signified the formation of MoS_2 in as-produced nanocomposite.

In addition, the Brunauer–Emmett–Teller (BET) analyses were performed to measure the specific surface areas of pure MoS_2, and MoS_2/graphene nanocomposite, which were found 3.35 and 28.30 m^2 g^{-1} (Figure 2.9a and 2.9b), respectively. From the BET values of pure MoS_2 and MoS_2/graphene nanocomposite, it was exhibited that graphene support clearly increased the surface area in nanocomposite form. Moreover, to get the better catalytic activities for hydrogen evolution reaction (HER), higher surface areas are preferred which can maximize the number of possible reaction sites while minimizing the total volume of the catalyst.

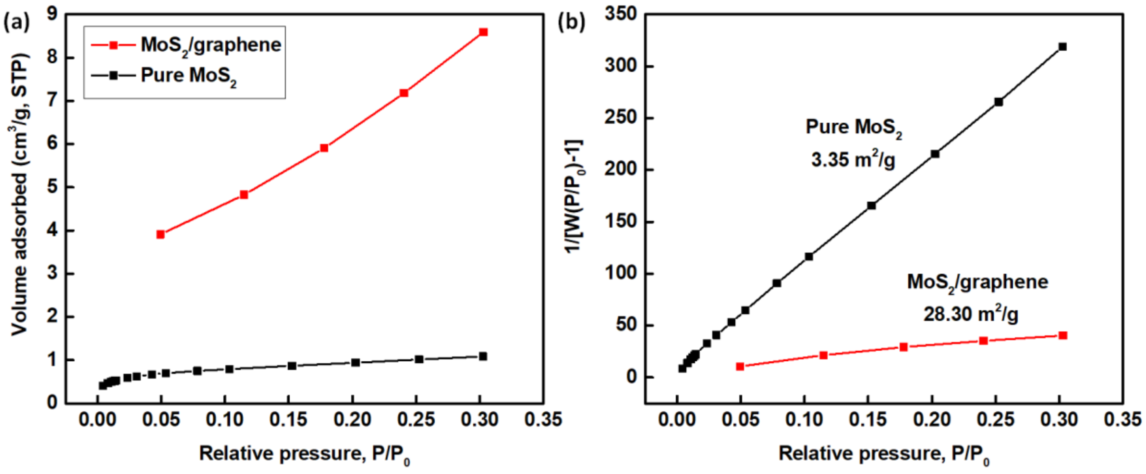

Figure 2.9. (a) Nitrogen adsorption isotherms and (b) BET surface area plots of pure MoS_2 and MoS_2/graphene composite.

2.3.3. Electrochemical characterizations

2.3.3.1. Optimization of reaction parameters

The electrocatalytic HER activities of MoS_2/graphene were investigated by Linear sweep voltammograms (LSVs) at room temperature, with a scan rate of 1 mV s^{-1} using a typical three-electrode setup. To optimize the electrolyte concentration, the LSV curves were obtained in various concentration of H_2SO_4 aqueous solution within a range of 0.1 to 1 M. As shown in Figure 2.10a the onset potentials (beyond which the cathodic current increased abruptly when the potential turns more negative) are not affected significantly by the electrolyte concentrations, rather only the current density increases with the increase in concentrations. It clearly indicates that the high amount of H^+ ions at higher concentration participates in H_2 generation, thus resulting greater current densities. Therefore, the widely used 0.5 M H_2SO_4 has been chosen for further characterizations to maintain the consistency with other literature works.

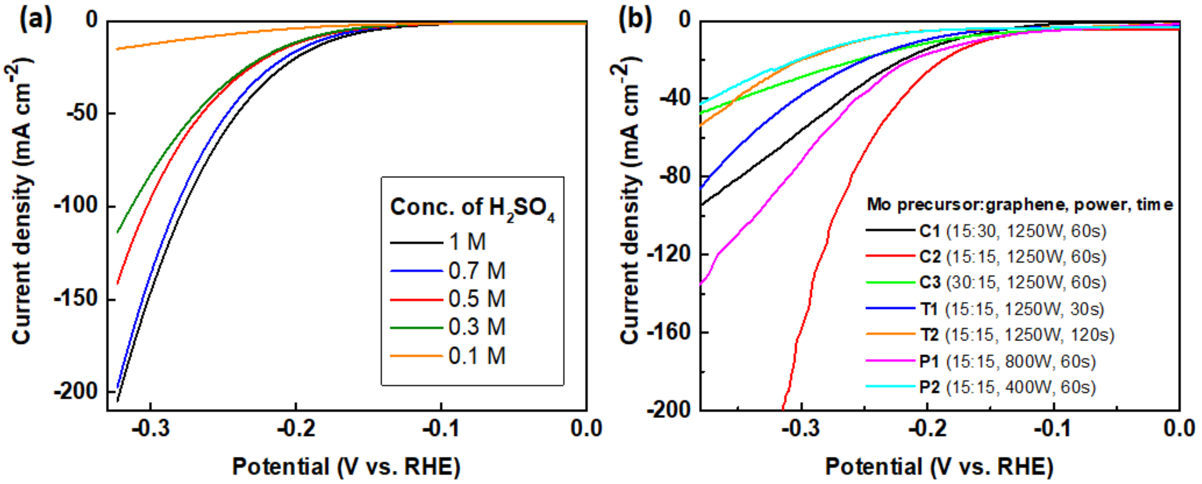

Figure 2.10. (a) LSVs of MoS_2/graphene catalyst in different concentration of H_2SO_4 electrolyte. (b) LSV profiles of C1−P2 samples in 0.5 M H_2SO_4.

To obtain the best catalyst sample, LSVs were performed on sample C1 to P2 (details on Table 2.1). C2 shows the most efficient HER activity than C1 and C3 (Figure 2.10b), which indicates the excess amount of graphene hinders catalytic activity of MoS_x (C1) and the excessive MoS_x anchored in the graphene framework (C3) may impede the electron transfer and thus increase the internal resistance in nanocomposite, which made the HER activity worse. In addition, the sample T1 and P2 undergo the insufficient microwave heating due to lack of time and microwave power, respectively. Moreover, the substantial agglomeration may occur in T2 due to excessive heating time, leading to a slight disorder in the synergetic effect. Sample P1 shows very similar result to sample C2 with lower current density due to formation of MoS_3, instead of MoS_2. Therefore, the optimized reaction condition would be 15:15 wt. ratio for Mo-precursor and graphene, with 60 seconds of microwave heating at 1250 W power.

2.3.3.2. Investigation of HER activities

The HER activities of MoS_2/graphene, pure MoS_2 particles, pure graphene, a physical mixture of MoS_2 and graphene (MoS_2+graphene), commercial Pt catalyst and bare GCE were studied under the same conditions for comparison. The GCE was coated with catalyst loading of around 5 mg cm^{-2} for each of the electrochemical test. The LSV (*iR* corrected) recorded on MoS_2/graphene shows a small onset potential of 100 mV (Figure 2.11a). All the major electrochemical parameters are shown in Table 2.2, which shows the overpotentials (η) for Pt and MoS_2/graphene to reach the current density of 10 mA cm^{-2} were 53 and 183 mV, respectively. In contrast, pure MoS_2 and MoS_2+graphene mixture displays trivial HER catalytic activities, while bare GCE and graphene shows no catalytic activity with the absence of MoS_2 catalyst (Figure 2.11a).

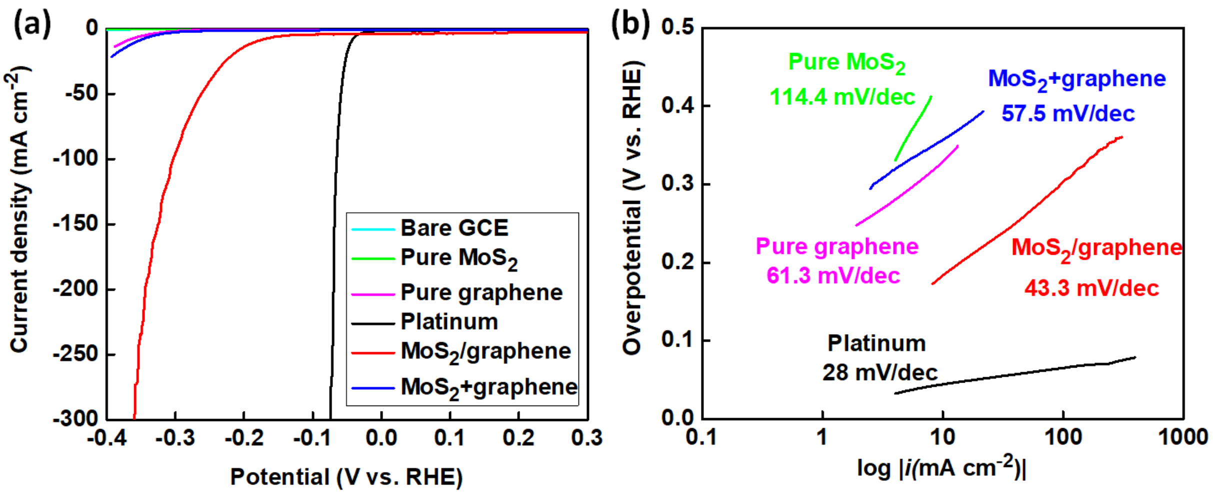

Figure 2.11. (a) LSVs of bare GCE, pure MoS_2, pure graphene, MoS_2+graphene mixture, MoS_2/graphene composite, and Pt catalyst. (b) Corresponding Tafel plots.

To further demonstrate the HER activities, Tafel plots are derived from LSVs by fitting the linear regions to Tafel equation ($\eta = b \log i + a$; where η is the overpotential, b is the Tafel slope, i is the current density and a is a constant). Tafel slope is an inherent property of the catalyst, related to the electrocatalytic reaction mechanism. Theoretically, there are three principal steps for HER in acidic electrolytes, which can elucidate electron transfer kinetics of the catalysts.[45,46] Three possible reactions are given in Equation 2.3 – 2.5:

Volmer: $H_3O^+(aq) + e^- + \rightleftharpoons H^* + H_2O(l)$ ………………………………………………….. (2.3)

Heyrovsky: $H^* + H_3O^+(aq) + e^- \rightleftharpoons H_2(g) + H_2O(l) + *$ ………………………...……....…. (2.4)

Tafel: $H^* + H^* \rightleftharpoons H_2(g) + 2^*$…………………………………………………...….…. (2.5)

In above equations, * indicates an empty active site and H* is a hydrogen atom bound to an active site of catalyst material. The overall HER reaction proceeds through a discharge step (Volmer reaction, Equation 2.3) with a Tafel slope around 120 mV per decade, followed by either a desorption step (Heyrovsky reaction, Equation 2.4) or recombination step (Tafel reaction, Equation 2.5), with the Tafel slopes around 40 and 30 mV per decade, respectively.[47] In this study, MoS_2/graphene exhibits the Tafel slope of 43.3 mV per decade (Figure 2.11b), indicating that the Volmer–Heyrovsky reaction mechanism dominates in the HER process of MoS_2/graphene catalyst and the electrochemical desorption is the rate determining step. This high performance of MoS_2/graphene demonstrates the advantage of synergistic effect between MoS_2 nanosheets and graphene, which generates more active sites for hydrogen evolution. Previous reports showed that the exchange current density (i_0) is proportional to the active surface area of catalyst materials, which can be obtained by an extrapolation method on the basis of Tafel equation.[48,49] The i_0 of MoS_2/graphene catalyst is calculated to be 2.512 mA cm^{-2}, which is very close to the i_0 of commercial Pt (3.981 mA cm^{-2}) (Table 2.2).

Table 2.2. Electrochemical parameters of MoS_2/graphene nanocomposite, comparing with commercial Pt, MoS_2+graphene mixture, pure MoS_2, and pure graphene samples.

Samples	**Onset potential, η_0 [mV vs. RHE]**	**Over potential, η_{10} [mV vs. RHE]**	**Tafel slope [mV/decade]**	**Exchange current density, i_0 [mA cm^{-2}]**
Platinum	45	53	28	3.981
MoS_2/graphene	100	183	43.3	2.512
MoS_2+graphene	201	365	57.5	1.007
Pure MoS_2	293	> 400	114.4	-
Pure graphene	204	374	61.3	-

2.3.3.3. Electrochemical double-layer capacitance (EDLC) measurements

The better electrocatalytic activity of MoS_2/graphene catalyst was further confirmed by the measurement of electrochemical double-layer capacitance (C_{dl}) at solid-liquid interface, another approach to estimate the electrochemically active surface area (ECSA). The ECSA gives an estimation of active reaction sites, which is proportional to C_{dl}.[48,50] To determine C_{dl} values, CV measurements were conducted for MoS_2/graphene catalyst within a potential range (0.3−0.4 V vs. RHE) with no apparent faradaic process (Figure 2.12a), where the currents are mainly attributed to the charging of the double layer.

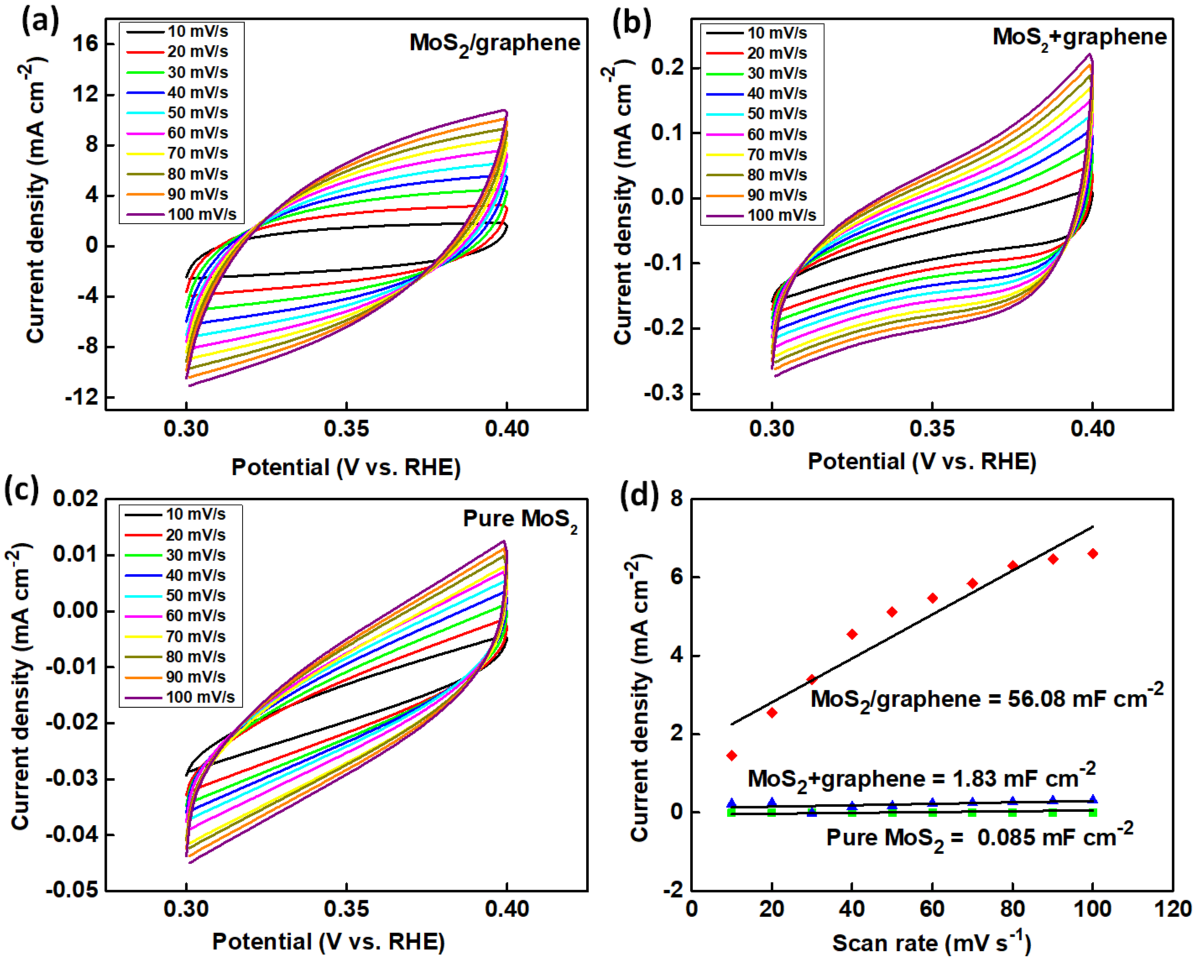

Figure 2.12. Cyclic voltammograms of (a) MoS_2/graphene (b) MoS_2+graphene mixture and (c) pure MoS_2 in a potential window without faradaic reaction. (d) Average capacitive current densities at different scan rates for the samples.

The double-layer charging current (i_c) is equal to the product of the scan rate (v) and double-layer capacitance (C_{dl}), which can be shown in the equation: charging current, $i_c = vC_{dl}$.[50] From this equation, C_{dl} can be measured from the slope by plotting a straight line of i_c vs. v. Representative plots for the determination of active surface areas of MoS_2/graphene, MoS_2+graphene mixture, and pure MoS_2 catalysts are shown in Figure 2.12a, 2.12b and 2.12c. As displayed in Figure 2.12d, capacitance of MoS_2/graphene is calculated to be 56.08 mF cm^{-2}, whereas those of MoS_2+graphene and MoS_2 are only 1.83 and 0.085 mF cm^{-2}, respectively. The measured capacitance (C_{dl}) of MoS_2/graphene composite is higher than the previously reported values for MoS_2 compounds, further resulting in high catalytic performance.[27,30]

2.3.3.4. Comparison with previous reports

Previously reported onset potentials (η_0) and Tafel slopes of molybdenum (Mo-) compounds were compared with the present data of MoS_2/graphene composite in Table 2.3. In contrast with ultrafast, facile microwave-initiated synthesis performed in this study, previously reported Mo- compounds were synthesized by different complex approaches. Moreover, it is obvious that the present material exhibits low onset potential and a small Tafel slope, that are comparable with other similar compounds. The improved electrocatalytic activity of MoS_2/graphene may be attributed to strong chemical and electronic coupling between MoS_2 nanosheets and graphene, resulting fast electronic kinetics between the catalyst and electrode surface.

Table 2.3. Comparison of electrochemical activities of microwave-synthesized MoS_2/graphene with previously reported MoS_2-based compounds.

Material	**Onset potential [mV vs. RHE]**	**Tafel slope [mV per decade]**	**Synthesis approach**	**Reference**
GA-MoS_2	100	41	hydrothermal	[30]
MoS_2/MGF	100	42	solvothermal	[51]
MoS_2/RGO	100	41	solvothermal	[18]
MoS_2/GO-CNT	35	38	wet-chemical	[43]
MoS_2/RGO_2	140	41	solvothermal	[52]
MoS_2/graphene	**100**	**43.3**	**microwave irradiation**	**present study**

2.3.3.5. Electrochemical impedance spectroscopy (EIS) measurements

This hypothesis was further confirmed by EIS measurements in 0.5 M H_2SO_4. The electrical equivalent circuit diagram in Figure 2.13a was used to model the solid liquid interface, where the constant phase element (CPE) was associated to electrical double layer formed at electrode/electrolyte interface of MoS_2/graphene catalyst. As shown in Figure 2.13b, the MoS_2/graphene displays much lower impedance than pure MoS_2 particles and MoS_2+graphene mixture. The charge transfer resistance R_{ct} is related to the kinetics of electrocatalysis, and a lower value resembles to a faster reaction rate. Because of the highly conductive surface and strong hydrogen adsorption capacity, MoS_2/graphene catalyst shows the R_{ct} of 1.50 kΩ at overpotential of 180 mV, while pure MoS_2 and MoS_2+graphene mixture presents very large R_{ct} of 37.7 and 246.4 kΩ, respectively (Figure 2.13b). The solution resistance (R_s) for MoS_2/graphene is 5 Ω, while pure MoS_2 and MoS_2+graphene shows higher values of 234.1 and 11.84 Ω, respectively. Hence, much faster electron transfer between the catalytic edge sites of

MoS_2/graphene and the electrode surface is one of the key factors contributing to the superior HER kinetics in acidic electrolyte.

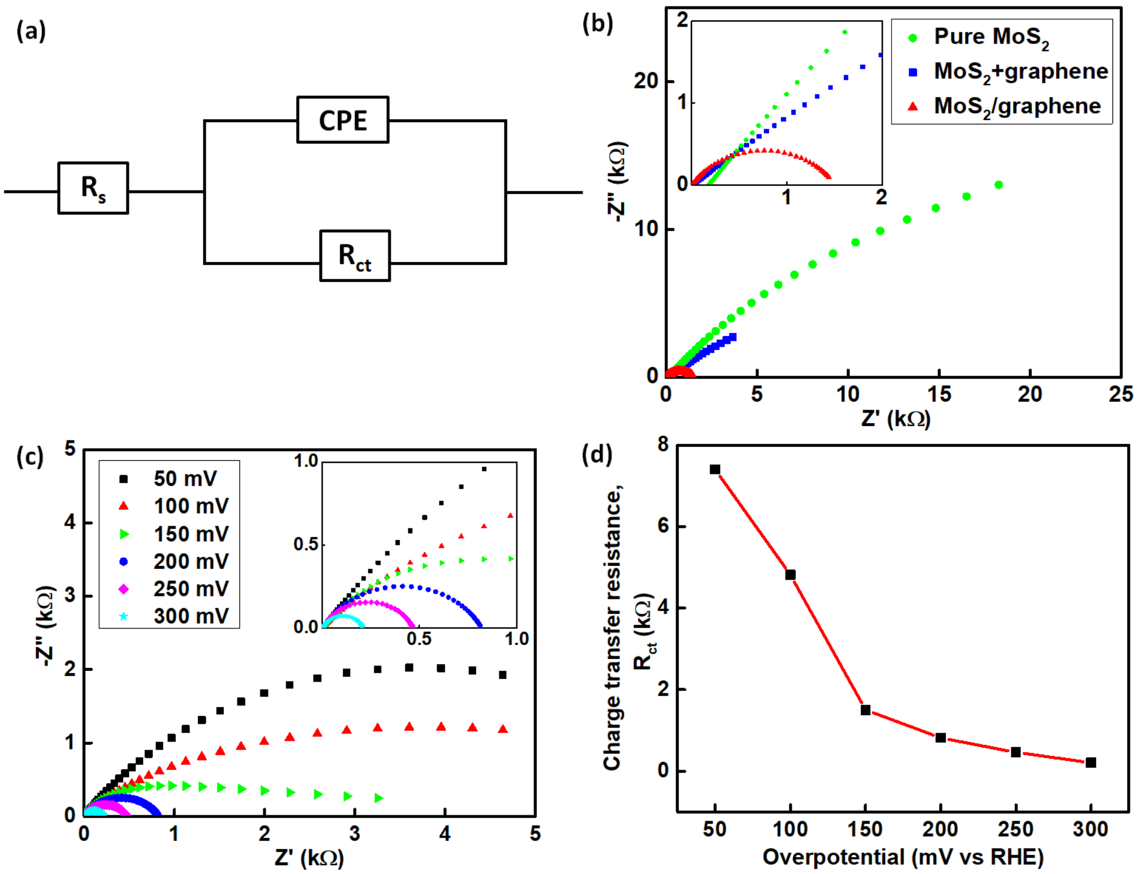

Figure 2.13. (a) Equivalent electrical circuit used to model the HER process on all catalyst samples. (b) Electrochemical impedance spectra of pure MoS_2, physical mixture of MoS_2+graphene, and MoS_2/graphene nanocomposite at an overpotential of 180 mV. (c) Nyquist plots showing the EIS responses of MoS_2/graphene at different overpotentials (50−300 mV) in 0.5 M H_2SO_4. (d) Charge transfer resistance (R_{ct}) as a function of HER overpotentials for MoS_2/graphene catalyst.

Additionally, Figure 2.13c represents the Nyquist plots of MoS_2/graphene catalyst at various overpotentials of 50−300 mV. In the high frequency zone, the MoS_2/graphene exhibits one capacitive semicircle, indicating that the reaction is kinetically controlled. In this system, R_{ct} decreases significantly with increasing overpotentials, from 7.4 kΩ at 50 mV to only 204.5 Ω at 300 mV (Figure 2.13d). Lower charge-transfer resistance (R_{ct}) illustrates the superior electrocatalytic activity at higher overpotential.

2.3.3.6. Stability tests

Besides high catalytic activities, good stability towards HER is also a key parameter for practical applications. To investigate the durability in an acidic environment, long-term stability of MoS_2/graphene was tested using the cyclic voltammetry (CV) technique from 0 to −350 mV vs. RHE scanning for 4000 cycles at a scan rate of 50 mV s^{-1} (Figure 2.14a). Very interestingly, the catalytic performance of MoS_2/graphene nanocomposite enhances with the potential cycling by reaching the overpotential value of only 62 mV after 4000 cycles (Figure 2.14b), which is very close to the overpotential (53 mV) of Pt catalyst. Similar improvement in the catalytic performance of MoS_2 by electrochemical cycling had been reported previously.[53,54] The improved catalytic performance during the potential cycling is due to catalytic activation by proton intercalation in MoS_2-layers. Another reason could be the self-optimizing morphological changes by perforation of H_2 bubbles, generating thinner and more porous catalyst materials. To compare the performances, cyclic stabilities of pure MoS_2 and the physical mixture of MoS_2+graphene have been conducted. As shown in Figure 2.14c, pure MoS_2 does not show any cyclic stability while, the physical mixture of MoS_2+graphene (Figure 2.14d) exhibits a slight activation, reaching the current density around -50 mA cm^{-2} with an overpotential of around 250 mV vs. RHE. These results clearly indicate that, the as-produced MoS_2/graphene-catalyst possesses the best catalytic behavior during cyclic stability.

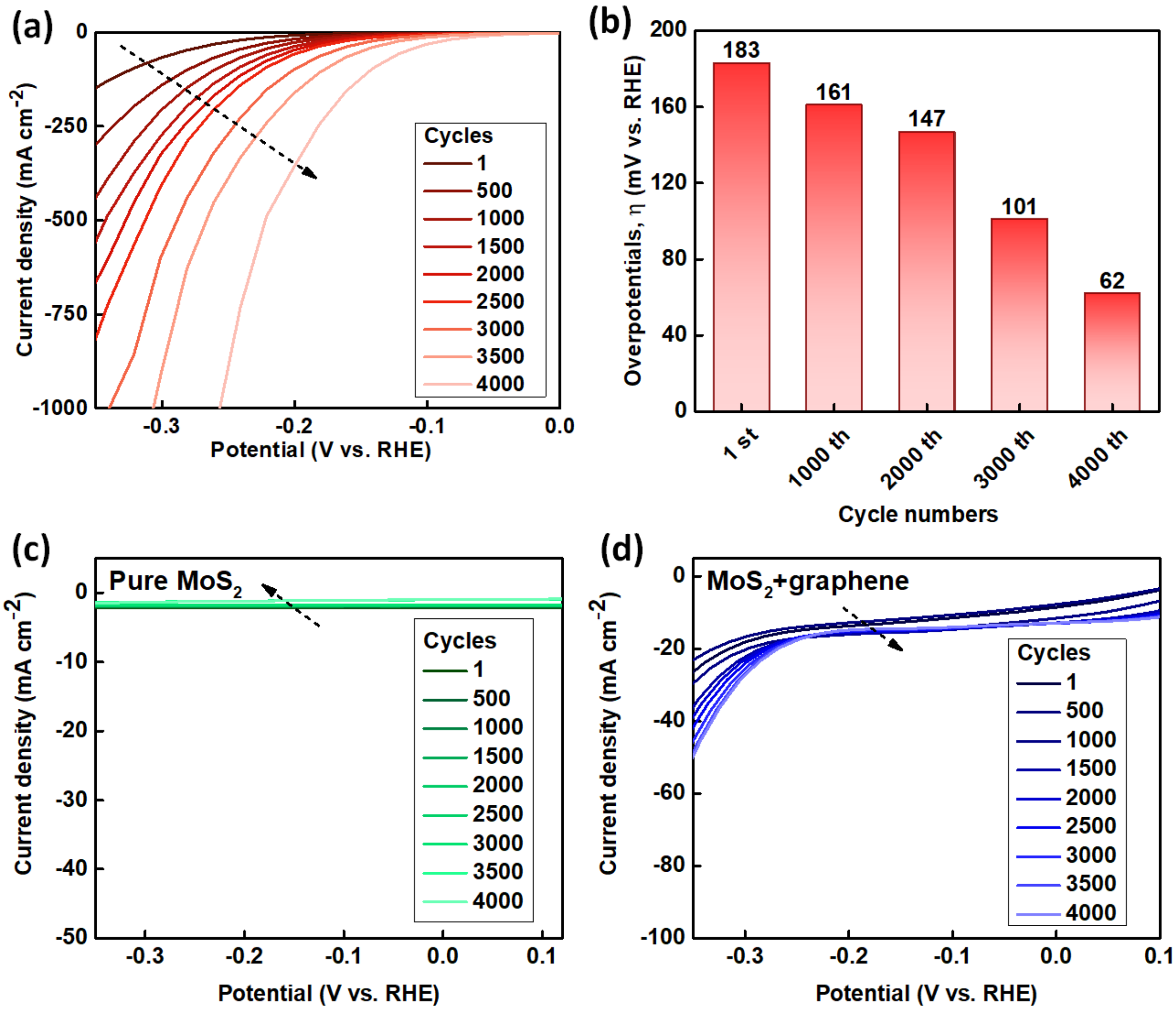

Figure 2.14. (a) Cycling stability of MoS_2/graphene from 0 to −350 mV vs. RHE at a scan rate of 50 mV s^{-1} in 0.5 M H_2SO_4, wherein the polarization curves from 1 to 4000 cycles are displayed. (b) Gradual decrease in overpotentials during cycling test. (c) and (d) Cycling stability tests for pure MoS_2 and MoS_2+graphene mixture for 4000 cycles, respectively.

The physical characterizations after running CV for 4000 cycles are shown in Figure 2.15, where the EDS and XRD results (Figure 2.15a and 2.15b, respectively) confirm the existence of MoS_2 nanosheets embedded on graphene network, maintaining the atomic ratio of molybdenum (Mo) and sulfur (S) equals to 1:2.

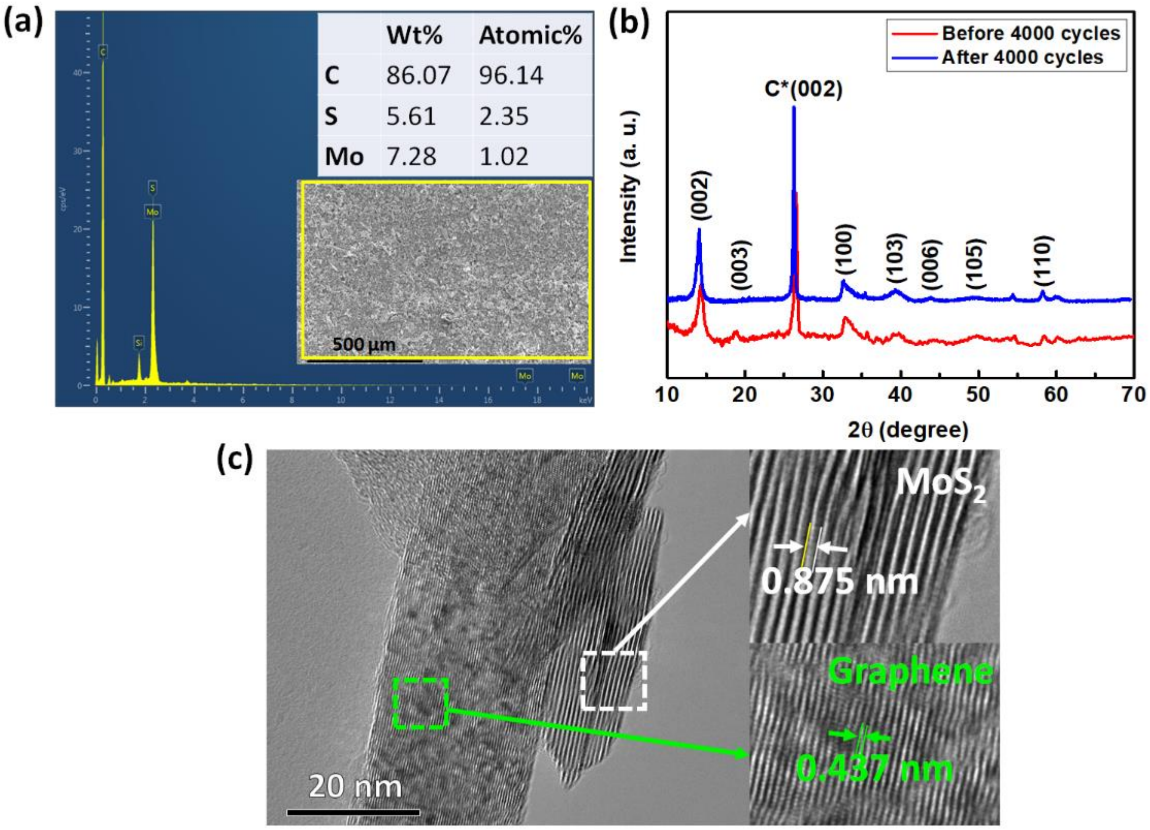

	Wt%	Atomic%
C	86.07	96.14
S	5.61	2.35
Mo	7.28	1.02

Figure 2.15. Physical characterizations after cyclic stability tests: (a) XRD pattern of MoS_2/graphene composite. (b) EDS pattern of MoS_2/graphene nanocomposite [inset table: wt% and atomic% of carbon (C), Sulfur (S), and Molybdenum (Mo) elements]. (c) High-magnification HRTEM image of MoS_2 nanosheets and graphene.

In addition, the dominating (002) planes of MoS_2 and graphene shift towards left (Figure 2.15b). According to Bragg's law ($d = \frac{\lambda}{2sin\theta}$, d = distance between layers, λ = wavelength and θ = diffraction angle), with an decrease in θ, interlayer distance (d) will increase. Therefore, this shift of (002) planes towards lower diffraction angles clearly indicates the increase in d. This phenomenon was further confirmed by TEM images (Figure 2.15c), which shows the higher interlayer spacings, 8.75 Å for MoS_2 and 4.37 Å for graphene nanosheets. This clearly supports the hypothesis of activation taking place in MoS_2/graphene catalyst by proton intercalation during the cyclic stability test.

Besides cycling stability, the practical operation of as-produced MoS_2/graphene catalyst was examined by electrolysis at constant potential over extended periods. As shown in Figure 2.16a, the MoS_2/graphene catalyst shows a stable increase in current density from −140 to −210 mA cm^{-2} for electrolysis over 90 hours at a constant overpotential of 180 mV. The increase in current density supports the hypothesis of catalytic activation observed during the cycling stability.

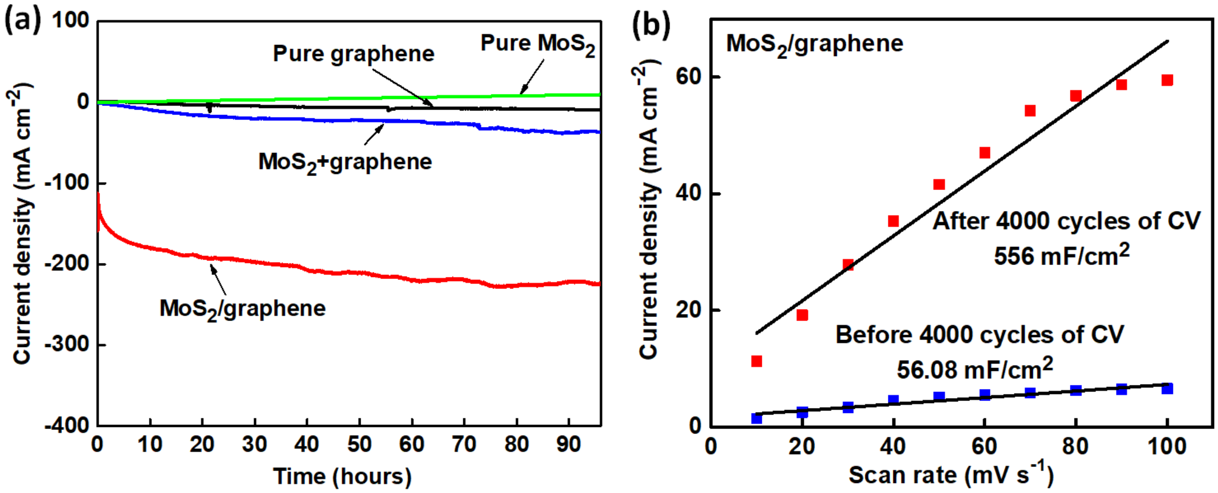

Figure 2.16. (a) Time dependence of cathodic current density on pure MoS_2, graphene, MoS_2+graphene mixture, and MoS_2/graphene composite during electrolysis over 90 hours at a constant overpotential of 180 mV. (b) Double layer capacitance measurements for MoS_2/graphene composite, before and after 4000 cycles of CV.

Furthermore, the double layer capacitance (C_{dl}) was calculated for MoS_2/graphene based on CV measurements after 4000 cycles. A remarkable increase is found in C_{dl}, from 56.08 to 556 mF cm^{-2} (Figure 2.16b), substantiating the increase in electrocatalytic active surface area of hybrid catalyst during the cycling activation process.

2.3.3.7. Platinum electrode issue

Although, platinum (Pt) has been widely employed as counter electrode to perform electrochemical tests, as mentioned in 1st chapter of Introduction (Section 1.8.2.2), Pt can influence the experimental results substantially owing to the electrochemical dissolution and re-deposition of Pt onto the active cathode materials. Therefore, the EDS tests were performed more carefully, and the characteristics Pt peaks were found as displayed in Figure 2.17, which confirms the deposition of Pt onto MoS_2/graphene electrocatalysts during the long test of 4000 CV cycles. Even though the amount of Pt is almost negligible (1.01 atomic%), it highly impacts the HER performance by catalytic activations, further enhancing the results by lowering overpotential and increasing current density values (Figure 2.14a).

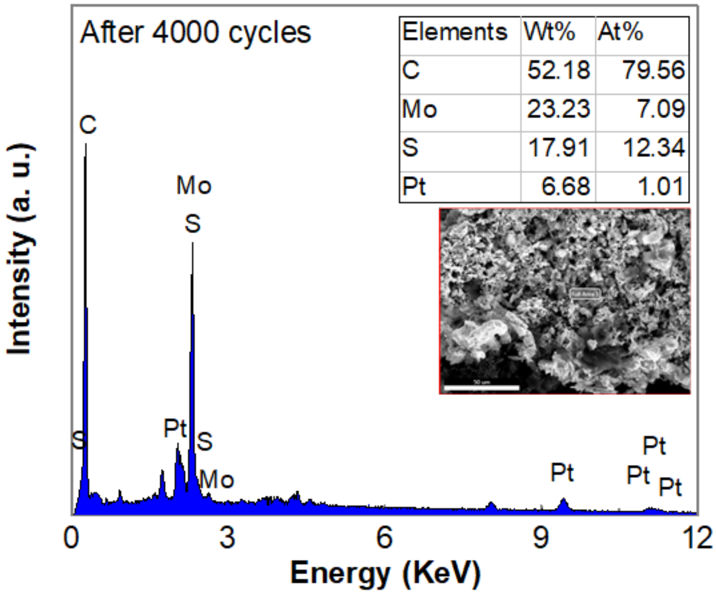

Figure 2.17. Presence of platinum (Pt) in active catalyst of MoS_2/graphene after 4000 cycles.

2.3.3.8. Activation energy calculations

In practical applications, water electrolysis cells may operate at relatively high temperatures about 50−70 °C. Therefore, the stability of as-produced MoS_2/graphene composite was measured by obtaining the LSVs at a temperature range from 30 °C to 120 °C (Figure 2.18a).

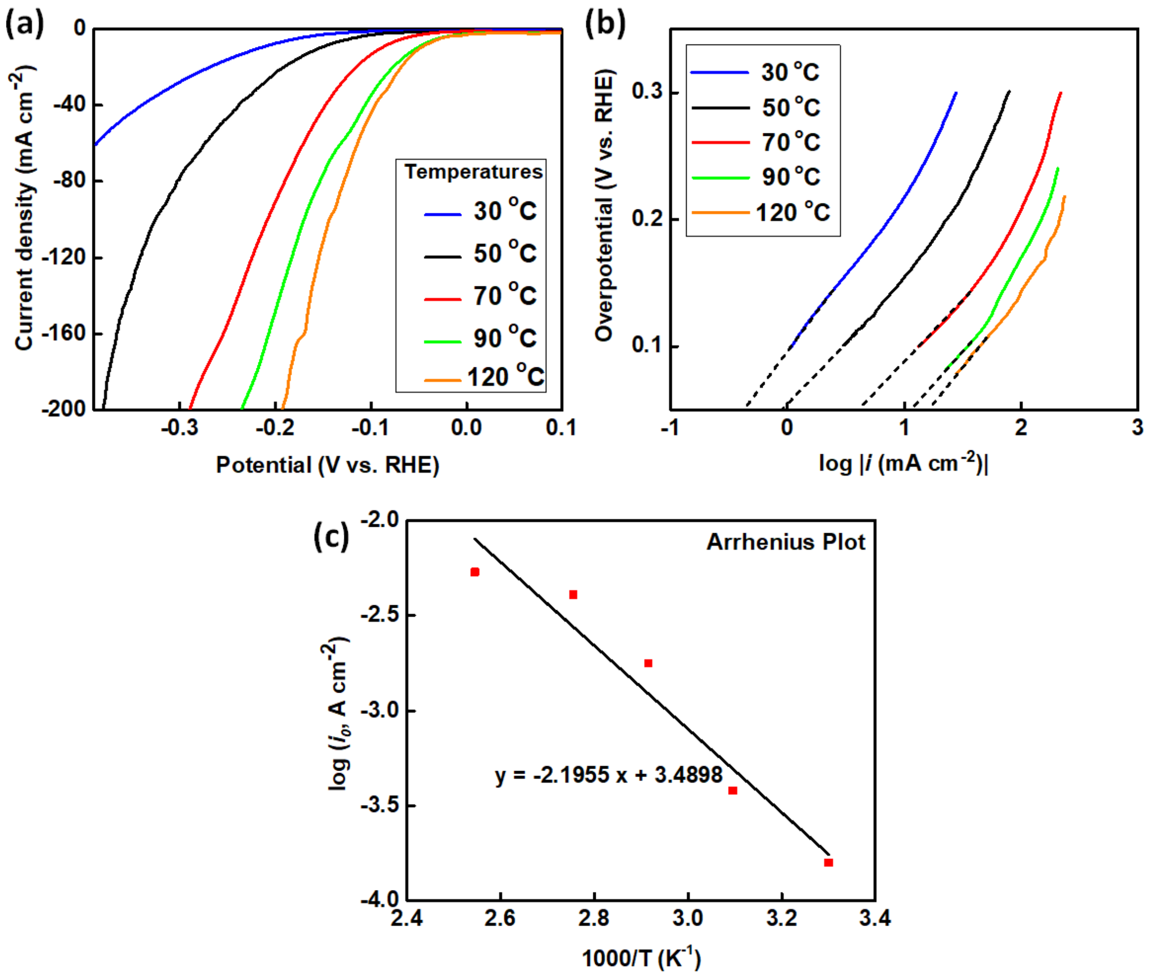

Figure 2.18. (a) LSVs of MoS_2/graphene at a temperature range of 30−120 °C in 0.5 M H_2SO_4, at a scan rate of 1 mV s^{-1}. (b) Corresponding Tafel plots. (c) Arrhenius plot for MoS_2/graphene.

In addition, the exchange current densities (i_0) were measured from corresponding Tafel slopes, which are shown in Figure 2.18b and the electrochemical parameters are tabulated in Table 2.4.

Table 2.4. HER parameters of MoS_2/graphene-catalyst at a temperature range of 30−120°C.

Temperature (°C)	**Onset potential (mV vs RHE)**	**Ex. current density, i_o (mA cm^{-2})**
30	100.2	0.158
50	85.4	0.380
70	73.2	1.778
90	68.7	4.074
120	57.2	5.370

The improvement in HER activities can be clearly observed with the increase in temperature by decreasing the onset potentials and increasing in exchange current densities. Even at high temperature of 120 °C, MoS_2/graphene shows good stability exhibiting a very low onset potential of 57.2 mV with a high current density. Moreover, activation energy (E_a) is another important parameter to measure the electrocatalytic performance of the HER catalyst. Based on the Arrhenius equation ($k = Ae^{\frac{-E_a}{RT}}$), E_a can be calculated by using the Equation 2.6. [55]

$$\log(i_0) = \log(A) - \frac{E_a}{2.3\,RT} \quad \ldots\ldots\ldots\ldots\ldots\ldots\ldots\ldots\ldots\ldots\ldots\ldots\ldots\ldots \text{(2.6)}$$

Where, A is the pre-exponential factor, R is universal gas constant and T is absolute temperature (in K). Plot of the log(i_0) as a function of $\frac{1000}{T}$ was shown in Figure 2.18c. From the slope of the Arrhenius plot, E_a is calculated to be 36.51 kJ mol^{-1} for MoS_2/graphene-catalyst. This lower activation energy can be comparable to Pt catalyst, which displays the E_a value in a range of 20−40 kJ mol^{-1}.[55,56] This enhanced catalytic activity and durability indicate that microwave-synthesized MoS_2/graphene nanocomposite is an efficient HER catalyst in acidic medium, even at the higher operating temperatures.

2.4. Summary

In conclusion, we have synthesized a highly active electrocatalyst of MoS_2 nanosheets dispersed over graphene by a fast, facile, energy efficient, environmentally friendly route involving reduction of Mo-precursor with presence of CS_2 and graphene under microwave irradiation. Along with being the microwave susceptor, graphene provides a stable conducting network and the large specific surface area for the growth of MoS_2 catalysts, facilitating both the electronic and ion transports between MoS_2/graphene compound and acidic electrolyte, further accelerating the catalytic reaction. As-produced MoS_2/graphene nanocomposite exhibited the enhanced HER activity with a low overpotential and large cathodic current. A small Tafel slope of 43.3 mV per decade suggested a Volmer-Heyrovsky mechanism for the HER. Besides, the catalyst material showed high cycling stability and a continuous hydrogen generation for 90 hours at constant potential operation. This non-noble, highly active and stable HER catalyst material is a promising candidate that could accelerate the efforts towards establishing a clean hydrogen-based energy economy. Even though the overpotential (η_{10}) for MoS_2/graphene is higher by 130 mV, it is substantially more preferred for commercial applications than the platinum material since MoS_2 is an earth abundant material and hence much cheaper than Pt. Above all, the microwave-initiated synthesis of MoS_2/graphene nanocomposite via an environmentally benign and simple method, capable for extending to large scale, economic production makes it an attractive catalyst for efficient hydrogen generation through water-electrolysis.

2.5. References

1 K. Mazloomi and C. Gomes, *Renew. Sustain. Energy Rev.*, 2012, **16**, 3024–3033.

2 J. A. Turner, *Science (80).*, 2004, **305**, 972–975.

3 M. Wietschel and M. Ball, *Int. J. Hydrogen Energy*, 2009, **34**, 613–639.

4 C. G. Morales-Guio, L.-A. Stern and X. Hu, *Chem. Soc. Rev.*, 2014, **43**, 6555.

5 V. S. Thoi, Y. Sun, J. R. Long and C. J. Chang, *Chem. Soc. Rev.*, 2013, **42**, 2388–2400.

6 X. Zou and Y. Zhang, *Chem. Soc. Rev.*, 2015, **44**, 5148–5180.

7 V. Marinović, J. Stevanović, B. Jugović and M. Maksimović, *J. Appl. Electrochem.*, 2006, **36**, 1005–1009.

8 N. V. Krstajić, V. D. Jović, L. Gajić-Krstajić, B. M. Jović, A. L. Antozzi and G. N. Martelli, *Int. J. Hydrogen Energy*, 2008, **33**, 3676–3687.

9 Q. Han, K. Liu, J. Chen and X. Wei, *Int. J. Hydrogen Energy*, 2003, **28**, 1345–1352.

10 D. J. Evans and C. J. Pickett, 2003, 268–275.

11 D. C. Rees and J. B. Howard, *Science (80).*, 2003, **300**, 929–931.

12 C. G. Morales-Guio and X. Hu, *Acc. Chem. Res.*, 2014, **47**, 2671–2681.

13 Y. Yan, B. Xia, Z. Xu and X. Wang, *ACS Catal.*, 2014, **4**, 1693–1705.

14 A. B. Laursen, S. Kegnæs, S. Dahl and I. Chorkendorff, *Energy Environ. Sci.*, 2012, **5**, 5577.

15 J. D. Benck, Z. Chen, L. Y. Kuritzky, A. J. Forman and T. F. Jaramillo, *ACS Catal.*, 2012, **2**, 1916–1923.

16 T. F. Jaramillo, K. P. Jørgensen, J. Bonde, J. H. Nielsen, S. Horch and I. Chorkendorff, *Science (80).*, 2007, **317**, 100–102.

17 D. Kong, H. Wang, J. J. Cha, M. Pasta, K. J. Koski, J. Yao and Y. Cui, *Nano Lett.*, 2013,

13, 1341–1347.

18 Y. Li, H. Wang, L. Xie, Y. Liang, G. Hong and H. Dai, *J. Am. Chem. Soc.*, 2011, **133**, 7296–7299.

19 Y. Yang, H. Fei, G. Ruan, C. Xiang and J. M. Tour, *Adv. Mater.*, 2014, **26**, 8163–8168.

20 D. Voiry, M. Salehi, R. Silva, T. Fujita, M. Chen, T. Asefa, V. B. Shenoy, G. Eda and M. Chhowalla, *Nano Lett.*, 2013, **13**, 6222–6227.

21 J. Deng, H. Li, J. Xiao, Y. Tu, D. Deng, H. Yang, H. Tian, J. Li, P. Ren and X. Bao, *Energy Environ. Sci.*, 2015, **8**, 1594–1601.

22 H. Wang, Z. Lu, S. Xu, D. Kong, J. J. Cha, G. Zheng, P.-C. Hsu, K. Yan, D. Bradshaw, F. B. Prinz and Y. Cui, *Proc. Natl. Acad. Sci.*, 2013, **110**, 19701–19706.

23 M. R. Gao, J. X. Liang, Y. R. Zheng, Y. F. Xu, J. Jiang, Q. Gao, J. Li and S. H. Yu, *Nat. Commun.*, 2015, **6**, 1–7.

24 Y. Zhu, S. Murali, W. Cai, X. Li, J. W. Suk, J. R. Potts and R. S. Ruoff, *Adv. Mater.*, 2010, **22**, 3906–3924.

25 Q. Xiang, J. Yu and M. Jaroniec, *Chem. Soc. Rev.*, 2012, **41**, 782–796.

26 E. G. S. Firmiano, M. A. L. Cordeiro, A. C. Rabelo, C. J. Dalmaschio, A. N. Pinheiro, E. C. Pereira and E. R. Leite, *Chem. Commun.*, 2012, **48**, 7687.

27 Y. J. Tang, Y. Wang, X. L. Wang, S. L. Li, W. Huang, L. Z. Dong, C. H. Liu, Y. F. Li and Y. Q. Lan, *Adv. Energy Mater.*, 2016, **6**, 1–7.

28 Y. Sun, X. Hu, W. Luo and Y. Huang, *ACS Nano*, 2011, **5**, 7100–7107.

29 A. Bhaskar, M. Deepa, T. N. Rao and U. V. Varadaraju, *J. Power Sources*, 2012, **216**, 169–178.

30 Y. Zhao, X. Xie, J. Zhang, H. Liu, H. J. Ahn, K. Sun and G. Wang, *Chem. - A Eur. J.*, 2015, **21**, 15908–15913.

31 S. Murugesan, P. Kearns and K. J. Stevenson, *Langmuir*, 2012, **28**, 5513–5517.

32 Y. Jiang and Y.-J. Zhu, *J. Phys. Chem. B*, 2005, **109**, 4361–4364.

33 X. Zhang and Z. Liu, *Nanoscale*, 2012, **4**, 707–714.

34 Z. Liu, L. Zhang, S. Poyraz, J. Smith, V. Kushvaha, H. Tippur and X. Zhang, *RSC Adv.*, 2014, **4**, 9308.

35 S. Anantharaj, J. Kennedy and S. Kundu, *ACS Appl. Mater. Interfaces*, 2017, **9**, 8714–8728.

36 G.-H. Dong, Y.-J. Zhu and L.-D. Chen, *J. Mater. Chem.*, 2010, **20**, 1976.

37 Y. Zhang, Z.-P. Qiao and X.-M. Chen, *J. Mater. Chem.*, 2002, **12**, 2747–2748.

38 Z. Liu, L. Zhang, R. Wang, S. Poyraz, J. Cook, M. J. Bozack, S. Das, X. Zhang and L. Hu, *Sci. Rep.*, 2016, **6**, 1–8.

39 H. Li, Q. Zhang, C. C. R. Yap, B. K. Tay, T. H. T. Edwin, A. Olivier and D. Baillargeat, *Adv. Funct. Mater.*, 2012, **22**, 1385–1390.

40 X. Zhang, F. Meng, S. Mao, Q. Ding, M. J. Shearer, M. S. Faber, J. Chen, R. J. Hamers and S. Jin, *Energy Environ. Sci.*, 2015, **8**, 862–868.

41 F. Mos, C. Lee, H. Yan, L. E. Brus, T. F. Heinz, Ḱ. J. Hone and S. Ryu, 2010, **4**, 2695–2700.

42 M. Mandal, D. Ghosh, S. S. Kalra and C. K. Das, *Int. J. Latest Res. Technol.*, 2014, **3**, 65–69.

43 M. Khan, A. Bin Yousaf, M. Chen, C. Wei, X. Wu, N. Huang, Z. Qi and L. Li, *Nano Res.*, 2016, **9**, 837–848.

44 Y. Liu, Y. Zhao, L. Jiao and J. Chen, *J. Mater. Chem. A*, 2014, **2**, 13109–13115.

45 W. Sheng, H. A. Gasteiger and Y. Shao-Horn, *J. Electrochem. Soc.*, 2010, **157**, B1529.

46 Thomas, J. G. N., *Trans. Faraday Soc.*, 1961, **57**, 1603–1611.

47 Z. Huang, W. Luo, L. Ma, M. Yu, X. Ren, M. He, S. Polen, K. Click, B. Garrett, J. Lu, K. Amine, C. Hadad, W. Chen, A. Asthagiri and Y. Wu, *Angew. Chemie - Int. Ed.*, 2015, **54**, 15181–15185.

48 D. Kong, H. Wang, Z. Lu and Y. Cui, *J. Am. Chem. Soc.*, 2014, **136**, 4897–4900.

49 Y. J. Tang, M. R. Gao, C. H. Liu, S. L. Li, H. L. Jiang, Y. Q. Lan, M. Han and S. H. Yu, *Angew. Chemie - Int. Ed.*, 2015, **54**, 12928–12932.

50 C. C. L. McCrory, S. Jung, I. M. Ferrer, S. M. Chatman, J. C. Peters and T. F. Jaramillo, *J. Am. Chem. Soc.*, 2015, **137**, 4347–4357.

51 L. Liao, J. Zhu, X. Bian, L. Zhu, M. D. Scanlon, H. H. Girault and B. Liu, *Adv. Funct. Mater.*, 2013, **23**, 5326–5333.

52 X. Zheng, J. Xu, K. Yan, H. Wang, Z. Wang and S. Yang, *Chem. Mater.*, 2014, **26**, 2344–2353.

53 G. Li, D. Zhang, Y. Yu, S. Huang, W. Yang and L. Cao, *J. Am. Chem. Soc.*, 2017, **139**, 16194–16200.

54 Y. Liu, J. Wu, K. P. Hackenberg, J. Zhang, Y. M. Wang, K. Keyshar, J. Gu, T. Ogitsu, R. Vajtai, J. Lou, M. Pulickel, B. C. Wood and B. I. Yakobson, *Nature Energy,* volume **2**, Article number: 17127 (2017).

55 D. M. F. Santos, C. A. C. Sequeira, D. Macciò, A. Saccone and J. L. Figueiredo, *Int. J. Hydrogen Energy*, 2013, **38**, 3137–3145.

56 J. Durst, C. Simon, F. Hasché and H. A. Gasteiger, *J. Electrochem. Soc.*, 2014, **162**, F190–F203.

Chapter 3

Towards thermoneutral hydrogen evolution reaction using noble metal free molybdenum ditelluride/graphene nanocomposites

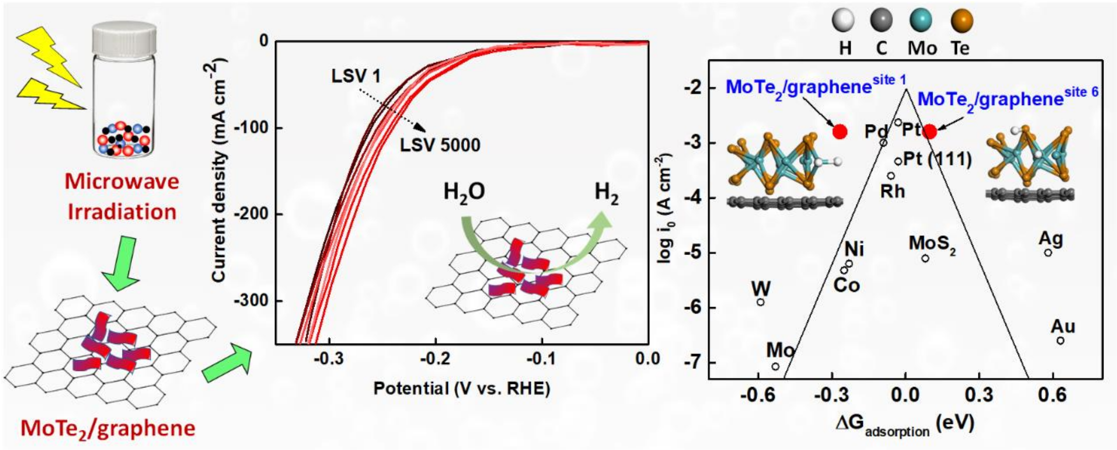

Part of this chapter has been published in Journal of Colloid and Interface Science, 581B, 2021, 847-859.

Abstract

The development of efficient electrocatalysts for hydrogen generation is an essential task to meet future energy demand. In recent years, molybdenum ditelluride ($MoTe_2$) has triggered incredible research interests due to intrinsic nontrivial band gap with promising semi-metallic behaviors. In this work, 2D $MoTe_2$ nanosheets have been synthesized uniformly on graphene substrate through ultra-fast microwave-initiated approach, that shows a superior hydrogen evolution in acidic medium with low overpotential (~150 mV), low activation energy (8.4362 ± 1.5413 kJ mol^{-1}), along with a Tafel slope of 94.5 mV/decade. Interestingly, $MoTe_2$/graphene exhibits the enhanced electrocatalytic stability during the long cycling test, resulting an increase in specific surface area of catalyst materials. Moreover, the results from periodic plane-wave density functional theory (DFT) indicates that, the best active sites are the corner of a Mo-atom and a critical bifunctional site comprised of adjacent Mo and Te edge atoms. Furthermore, the corresponding volcano plot reveals the near thermoneutral catalytic activity of $MoTe_2$/graphene for hydrogen generation.

3.1. Introduction

To solve the world energy crisis along with increased environmental pollution, it is high time to replace the traditional fossil fuels by renewable energy resources. According to the U.S. Energy Information Administration[1], 38% of world electricity will be generated from renewables by 2050. However, intermittency issues of renewable resources such as solar, hydro or wind energy still remain very challenging to be resolved and incidentally, hydrogen is believed to be a reliable energy carrier for these renewables.[2] The key idea is to generate H_2 through water electrolysis by utilizing the electricity generated from renewable resources.[3–5] Nevertheless, in water electrolysis process, hydrogen evolution reaction (HER, $2H^+ + 2e^- \rightarrow H_2$) requires electrocatalyst material as cathode. Although, the real bottleneck of this process corresponds to the anodic oxygen evolution reaction (OER), the cathode catalyst still represents a considerable portion of the total system cost.[6] So far, the platinum (Pt) and Pt-based materials exhibit the best catalytic activities providing higher current densities at low overpotentials in acidic media.[7] However, the high cost and scarcity of these materials severely limit their commercial applications and therefore, researchers are looking for nonprecious, earth-abundant HER catalyst materials intensively as alternatives.[8,9]

Hydrogenase and nitrogenase metalloenzymes are highly efficient biocatalysts for the HER that contain much less noble transition metals (Fe, Ni, and Mo).[10,11] Encouraged by these natural catalysts, recently, the transition metal dichalcogenides (TMDs) have emerged as promising catalysts for hydrogen evolution in acidic media. Among them MoS_2 and $MoSe_2$ have come forward with remarkable HER catalytic activities, whereas very few reports have been published on $MoTe_2$ as electrocatalyst, even though they have higher electronic conductivity, better electrical properties along with semi-metallic nature.[12–15] Moreover, the controlled high-yield production of $MoTe_2$ nanosheets is more challenging than MoS_2 or $MoSe_2$ because of a small electronegativity difference between Mo and Te (0.3 eV) atoms. To date, several synthesis methods, such as chemical vapor deposition (CVD), top-down exfoliation and annealing technology have been proposed for the preparation of $MoTe_2$.[13,16–18] Whereas, these approaches generally require high-temperature, high-pressure, heat-treatment, high-energy and long reaction time. In present work, we have synthesized $MoTe_2$ nanosheets on graphene substrate through microwave-irradiation, which is a facile, ultra-fast, energy-efficient, and scalable approach. Similar method was applied to develop MoS_2/graphene-catalyst in our previous work.[19] During this process, graphene performs an important role by absorbing the microwave energy to convert it to heat energy, along with improving the electrical and mechanical properties of as-produced $MoTe_2$/graphene composite. For the first time, the application of microwave irradiation has been introduced to synthesize $MoTe_2$–based HER catalyst. Although the solution-based microwave synthesis approaches are more conventional, the present study has illustrated a facile solid-state synthesis approach, which requires no solvent recovery steps, in addition to providing the high yield, high purity of resultant products. The brief overview of this study is presented in Figure 3.1.

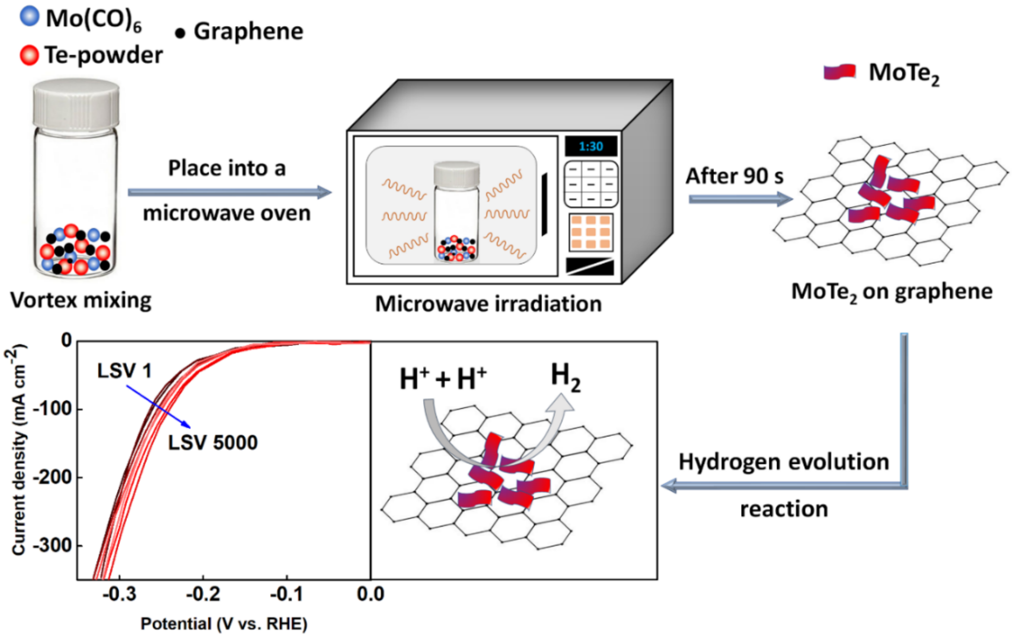

Figure 3.1. Schematic illustration of the microwave-initiated synthesis of $MoTe_2$/graphene composite, employing as an electrocatalyst for hydrogen evolution reaction.

In parallel with the experimental strategy, atomistic simulations have been carried out with periodic plane-wave DFT to probe the surface-electrochemistry of hydrogen adsorption. So far, several theoretical investigations with DFT method for hydrogen electrodes have been carried out, but to the best of our knowledge, no computational study has yet been performed to understand the HER activities of $MoTe_2$ catalyst with graphene support.[20–22] Based on Sabatier's principle, in present study, theoretically calculated adsorption free energies indicate the Mo edge and Mo corner as the most favorable sites of the $MoTe_2$/graphene composite for HER catalysis. The most prominent graphical representation of Sabatier's principle is the volcano plot,[23,24] which reveals the position of $MoTe_2$/graphene nanocomposite near the peak, almost at the similar height of Pt, and considerably above MoS_2. The combination of active $MoTe_2$-catalyst with extremely strong and conductive graphene support enhances the properties of the individual components and thereby exhibits higher performance for HER, which illustrates the future potential commercialization of $MoTe_2$/graphene for practical applications.

3.2. Experimental section

3.2.1. Materials and reagents

Molybdenum hexacarbonyl ($Mo(CO)_6$, 98%) was purchased from Strem Chemicals. Tellurium (Te) powder (~325 mesh) and poly-vinylidene fluoride (PVDF powder, $(-CH_2CF_2-)_n$) were obtained from Alfa Aesar. Graphene was acquired from Magnolia Ridge Inc. The N, N-dimethylformamide (DMF, $HCON(CH_3)_2$) was purchased from *Macron Fine Chemicals*™. Nitric acid (69-70%), and acetone (CH_3COCH_3) were provided by BDH Chemicals, VWR. Sulfuric acid was supplied by Anachemia. All chemicals were employed as received without further purification. For electrochemical tests, the platinum (Pt) gauze (100 mesh, 99.9% metal basis) and graphite rod (5 mm diameter, 99.997% metal basis) were acquired from Alfa Aesar to be used as counter electrode. The silver/silver chloride (Ag/AgCl, 3 M KCl, $E^0 = +0.197$ V vs. RHE) reference electrode was obtained from Hach and glassy carbon electrode (CHI 104, 3 mm diameter) was obtained from CH Instruments, Inc.

3.2.2. Microwave-initiated synthesis of $MoTe_2$/graphene composites

$MoTe_2$/graphene compound was prepared by reaction of molybdenum hexacarbonyl ($Mo(CO)_6$) and Te-powder on graphene substrate following the previously published synthesis approach[19]. At first, 20 mg of $Mo(CO)_6$, 40 mg of Te-powder and 20 mg of graphene (weight ratio = 1:2:1) were transferred in a glass vial and blended together consistently using a speed mixer at 2000 rpm. After that, the glass vial containing the solid mixture was placed inside a microwave oven (frequency 2.45 GHz, power 1250 W) and irradiate continuously for 90 seconds. During the process, graphene acted as microwave energy susceptor and provided the required heats to reduce $Mo(CO)_6$ to MoO_2 and MoO_3, then converted to $MoTe_2$ uniformly dispersed on graphene, releasing the other elements in gaseous forms (proposed pathways: (i) $Mo(CO)_6 \rightarrow MoO_2 + MoO_3$; (ii) $MoO_2 + Te \rightarrow MoTe_2$). Since tellurium cannot replace oxygen easily because of the large difference in ion radii of O and Te atoms, there is a possibility of remaining a mixture of MoO_2 and MoO_3 (MoO_x) present in as-produced nanocomposites of $MoTe_2$/graphene. Therefore, to compare the results of electrochemical characterizations, MoO_x/graphene compound was also prepared through microwave-initiated heating following the same steps except adding Te-powder. Thus, the synthesis of $MoTe_2$/graphene and MoO_x/graphene nanocomposites were taken place by 90 seconds of microwave irradiation.

3.2.3. Physicochemical characterizations

The morphological imaging and elemental analysis of $MoTe_2$/graphene was performed by scanning electron microscope (SEM; Apreo FE) connected with an energy dispersive X-ray spectrometer (EDS, EDAX Instruments) applying a 20 kV acceleration voltage. The transmission electron microscopy (TEM) and high resolution TEM (HRTEM) analyses were carried out using a FEI Tecnai F20 TEM, operated at 200 kV. To investigate the phase and crystal structures, the powder X-ray diffraction (XRD) patterns were collected on a Philips X'pert MPD diffractometer with Cu Kα radiation ($\lambda = 1.54056$ Å) at 45 kV and 40 mA. The scan speed of 0.06°/min over a 2θ range of 10-70° were used for all XRD data collection. In addition, the micro-Raman spectroscopy was carried out at room temperature by back-scattering geometry employing the 442 nm line (80 mW) of a dual wavelength He-Cd laser (Kimmon Electric). Photoemission measurements were performed in a load locked Kratos XSAM 800 surface analysis system and XPS spectra were collected in the fixed analyzer transmission (FAT) mode using a pass energy of 80 eV.

3.2.4. Electrochemical measurements

3.2.4.1. Electrochemical setup

All electrochemical experiments except the stability tests, were performed using a CH Instrument (CHI 760D) potentiostat with an 'Electrochemical Analyzer' software (version 15.03). The stability tests were performed on Arbin Instrument (version 4.21). The typical three-electrode setup was configured with a glassy carbon electrode as working electrode coated with catalyst material, silver/silver chloride (Ag/AgCl, 3 M KCl) as the reference electrode, and platinum (Pt) mesh as counter electrode in 0.5 M H_2SO_4 electrolyte at room temperature (~25°C). To avoid the Pt deposition on working electrode surface during HER tests, the new electrolyte was used for each electrochemical test. Also, for the same Pt deposition issue during long experiments, the graphite rod was used as counter electrode for the cyclic and constant potential stability tests. The measured potentials were presented with respect to reversible hydrogen electrode (RHE) by using the equation: $E \text{ (vs. RHE)} = E \text{ (vs. Ag/AgCl)} + E^0 \text{ (vs. Ag/AgCl)} + (0.059 \times \text{pH})$ [at 25 °C, E^0 (vs. Ag/AgCl) = 0.197].

3.2.4.2. Preparation of working electrode

Prior to coat with active catalyst, glassy carbon electrode (GCE) was polished on a polishing mat with alumina powder (Al_2O_3, 0.05 μm), rinsing with DI water and acetone, then vacuum drying for 1 hr at 60 °C. Then, a homogeneous paste was prepared by mixing $MoTe_2$/graphene catalyst (2 mg) with PVDF powder (0.2 mg) and DMF solvent (50 μL). The catalyst paste was drop-coated onto the GCE surface (0.07 cm^2) with an active material load of ~5 mg cm^{-2} and vacuum dried at 60 °C for 1 hr. To compare the performances, MoO_x/graphene and pure graphene were drop-coated on GCEs with consistent catalyst loading (~5 mg cm^{-2}).

3.2.4.3. Electrochemical tests

Cyclic voltammetry (CV) was performed to stabilize the system by running around 50 cycles. Then, the electrocatalytic activities of sample catalysts were analyzed by polarization curves using linear sweep voltammetry (LSV) with specific *iR* compensation. CV was also used to determine the double layer capacitance values, that determines the active surface area of catalyst samples. LSVs were interpreted at different temperatures (30 °C − 90 °C) to determine the activation energy. In addition, electrochemical impedance spectroscopic (EIS) measurements were carried out at various overpotentials from 100 − 300 mV vs. RHE in the frequency range of 10^{-1} to 10^6 Hz with a single modulated AC potential of 5 mV. Later, the collected EIS spectra were fitted by EC-Lab software using specific Randle cell.

3.2.5. Computational methodology

The theoretical study has been performed utilizing periodic plane-wave density functional theory (DFT) calculations. As presented in Figure 3.2, the $MoTe_2$/graphene composite was created by constructing a supercell model of $MoTe_2$ with 3×3 in plane periodicity supported on a 7×7×1 graphene basal plane. The Mo_9Te_{18} nanoparticle used in the composite was previously geometry optimized in the solid state hexagonal $MoTe_2$ lattice. For the cleaved Mo_9Te_{18} nanoparticle, the $(01\bar{1}0)$ plane best represents the exposed Te edge, and similarly the $(10\bar{1}0)$ plane best represents the exposed Mo edge. Details of this method are described in Ref. 25.[25]

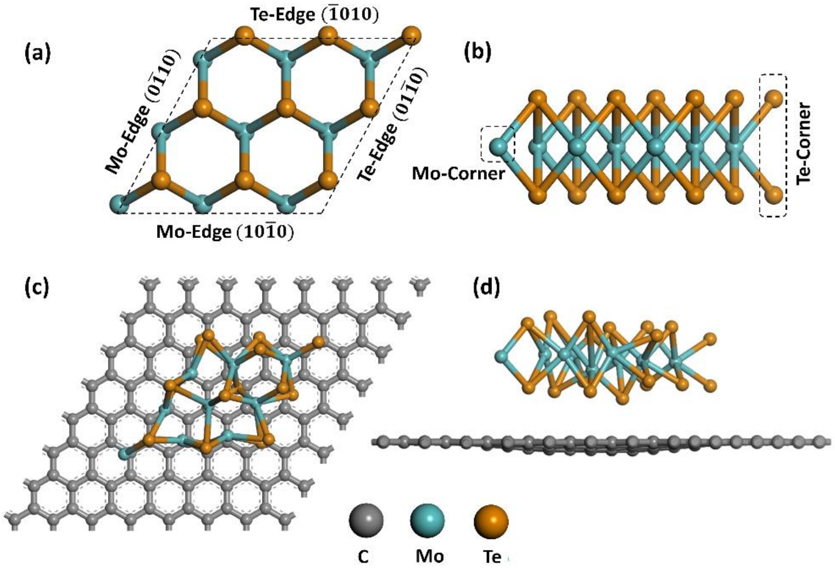

Figure 3.2. (a) Top and (b) side views of the Mo_9Te_{18} nanoparticle taken from a structurally optimized $MoTe_2$ crystal. (c) Top and (d) side views of the Mo_9Te_{18} nanoparticle over 7×7×1 graphene supercell with optimized geometries.

3.3. Results and discussion

3.3.1. Structural and compositional characterizations

The microscopic images of $MoTe_2$/graphene were studied by SEM and TEM analyses. Figure 3.3a and 3.3b exhibit the growth of $MoTe_2$ nanosheets embedded in graphene flakes. These morphological studies reveal the coalescing or overlapping of the graphene sheets, forming an interconnected conducting network, which is essential for the less-conducting $MoTe_2$ to facilitate the rapid electronic transport. Moreover, the entangled graphene network can provide enough mechanical strength to as-produced nanocomposite.

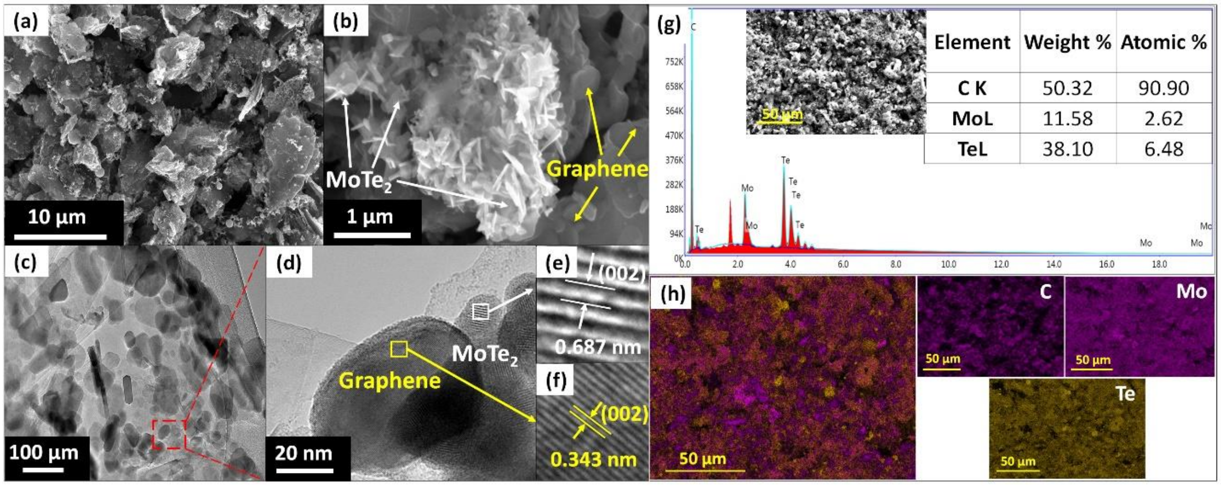

Element	Weight %	Atomic %
C K	50.32	90.90
MoL	11.58	2.62
TeL	38.10	6.48

Figure 3.3. (a, b) SEM images of $MoTe_2$/graphene nanocomposite. (c) TEM and (d) HR-TEM images of $MoTe_2$/graphene nanocomposite. (e, f) Interlayer spacings of $MoTe_2$ and graphene nanosheets. (g) EDS pattern of $MoTe_2$/graphene nanocomposite (inset table shows wt% and atomic% of carbon (C), molybdenum (Mo), and tellurium (Te) elements. (h) EDS elemental mapping of $MoTe_2$/graphene. *The violet, pink, and yellow colors represent carbon (C), molybdenum (Mo), and tellurium (Te), respectively*.

In addition, $MoTe_2$ demonstrates the corrugated sheets in the low-magnification TEM image, as shown in Figure 3.3c, while high-magnification HR- TEM image (Figure 3.3d) prominently displays the difference between graphene and $MoTe_2$ nanosheets by their well-resolved lattice fringes with separate interplanar spacings. The $MoTe_2$ exhibits the dominant 002 plane with an interlayer distance of 6.87 Å (Figure 3.3e), where the graphene displays distinctive interlayer spacing of 3.43 Å (Figure 3.3f). Moreover, the EDS results (Figure 3.3g) satisfy the formula of $MoTe_2$ (Te-Mo-Te) by revealing that, the atomic ratio of Mo and Te components is very close to stoichiometry (1:2). Furthermore, EDS mapping (Figure 3.3h) was performed that shows the uniform distribution of Mo and Te elements on graphene surface with slight agglomeration, which is beneficial for improving the electrical and ionic conductivity and enhancing the stability of $MoTe_2$ nanoparticles during the hydrogen evolution.

Moreover, the XRD analysis was performed to detect the formation of $MoTe_2$ nanosheets in the resultant nanocomposite**.** Figure 3.4a displays the diffraction peaks in a range from 10^o to 70^o, where the peaks appeared at 13.28^o, 27^o, 38.73^o, 53.94^o are corresponding to (002), (004), (006), (008) planes of $MoTe_2$, that can be indexed to the standard hexagonal 2H–$MoTe_2$ structure (JPCDS no. 15-0658).[26] As because, a large amount (90 at.%) of graphene is present in $MoTe_2$/graphene composite, it displays a graphitic peak (002) at ~26^o with high intensity.[27] Besides, The reflection positions in the XRD patterns at the angles of 23.51^o, 32.18^o, 32.9^o, 46.4^o, 50.1^o, 68.16^o, 38.73^o are appeared, which correspond to (110), (101), (111), (200), (002), and (202) planes of MoO_3.[28] Small diffraction peaks of MoO_2, such as (111), (211), (031), (402), and (204) are also emerged at 26.5^o, 36.1^o, 55.2^o, 61.3^o, 63.3^o, and 64.2^o [29], indicating that after reacting under microwave irradiation Mo-precursor with Te-powder partially reduced to $MoTe_2$ and there is a slight mixture of MoO_2 and MoO_3 (MoO_x) present in as-produced nanocomposite. In Figure 3.4a, there is a few of other insignificant peaks are shown that correspond to the unreacted Te-powder (JPCDS no. 65-3370).[26]

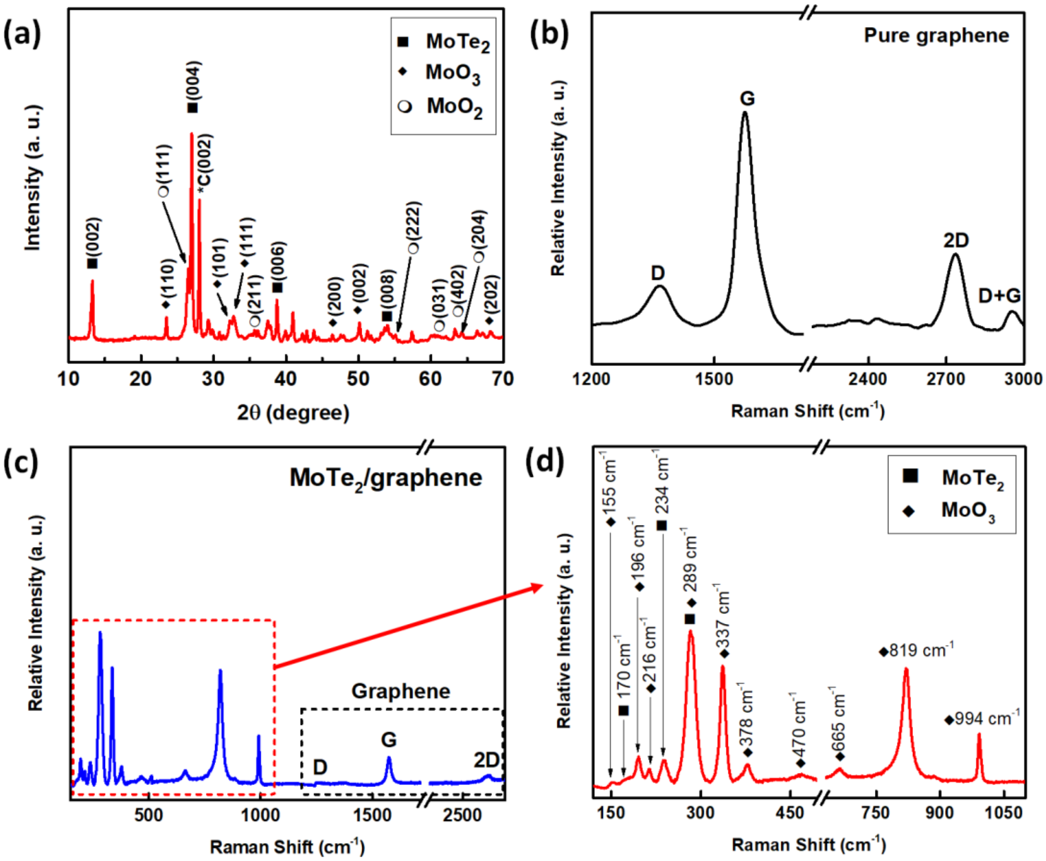

Figure 3.4. (a) XRD pattern of MoTe$_2$/graphene composite. Raman spectra of (b) pure graphene, and (c) MoTe$_2$/graphene composite. (d) Raman spectra within the range of 120−1100 cm^{-1} to focus on MoTe$_2$ and MoO$_x$ peaks.

To confirm the presence of both MoTe$_2$ and MoO$_x$ on graphene substrate, Raman analysis was performed. The Raman spectra of pure graphene and MoTe$_2$/graphene are shown in Figure 3.4b−3.4d. All the significant characteristic peaks for graphene (D, G and 2D bands) are clearly observed in both pure graphene (Figure 3.4b) and MoTe$_2$/graphene composite (Figure 3.4c). The characteristic phonon modes of MoTe$_2$, A_{1g} at 170 cm^{-1}, E^1_{2g} at 234 cm^{-1}, and B^1_{2g} at 289 cm^{-1} can be observed in Figure 3.4d, which confirms the successful formation of the crystalline 2H–MoTe$_2$.[30] Other peaks in Figure 3.4d at 155 cm^{-1}, 196 cm^{-1}, 216 cm^{-1}, 337 cm^{-1}, 378 cm^{-1}, and

470 cm^{-1} represent various modes of O–Mo–O and O=Mo=O bonds, which are in good agreement for MoO_3 crystalline phase. The peak at 665 cm^{-1}, 819 c m^{-1}, and 994 cm^{-1} can be assigned to the Mo_3–O, Mo_2–O, and terminal oxygen (Mo^{6+}=O) stretching modes, respectively.[31] Unfortunately, the overlapping of 289 cm^{-1} peak both from $MoTe_2$ and MoO_3 made it hard to identify the number of layers of $MoTe_2$ present in the nanocomposite. Although, high intensity of this peak can be an indication of the formation of few layers $MoTe_2$, while from the TEM images (Figure 3.3d) 7−8 layers can easily be observed. Although, XRD patterns show both the peaks of MoO_2 and MoO_3, Raman characterizes only the peaks for MoO_3, since MoO_2 could possibly be oxidized to MoO_3 in contact of air. These results clearly suggest the presence of molybdenum oxide (MoO_x) in $MoTe_2$/graphene composite, which is because of the larger atomic size of tellurium (Te) struggles to replace smaller oxygen (O) atoms from MoO_x during the microwave-initiated synthesis approach.

Furthermore, X-ray photoelectron spectroscopy (XPS) was investigated to further confirm the successful microwave reduction of Mo(VI) in $Mo(CO)_6$ precursor to Mo(IV) in $MoTe_2$. The survey spectrum is represented in Figure 3.5a for $MoTe_2$/graphene, and the peaks for carbon (C), molybdenum (Mo), tellurium (Te), and oxygen (O) elements are observed, indicating the presence of $MoTe_2$, MoO_x and graphene in the hybrid nanocomposite. Figure 3.5b displays the atomic compositions of each element, that are almost similar to the EDS results (Figure 3.3g) in addition of displaying the atomic% of O that confirms the presence of MoO_x. The high-resolution XPS spectrum for Mo 3d (Figure 3.5c) shows the binding energies of Mo $3d_{5/2}$ and Mo $3d_{3/2}$ peaks at 229.4 and 232.7 eV, respectively, which are matched with typical values for Mo (IV) in $MoTe_2$. For Te 3d spectrum, peaks are observed at 573.1 and 576.9 eV, as shown in Figure 3.5d, which can be assigned to Te $3d_{5/2}$ and Te(IV) 3d, respectively. Another characteristic peak of Te $3d_{3/2}$ at

583.6 eV is shown in survey spectrum (Figure 3.5a), which further signifies the formation of $MoTe_2$ in as-produced nanocomposite.[32,33]

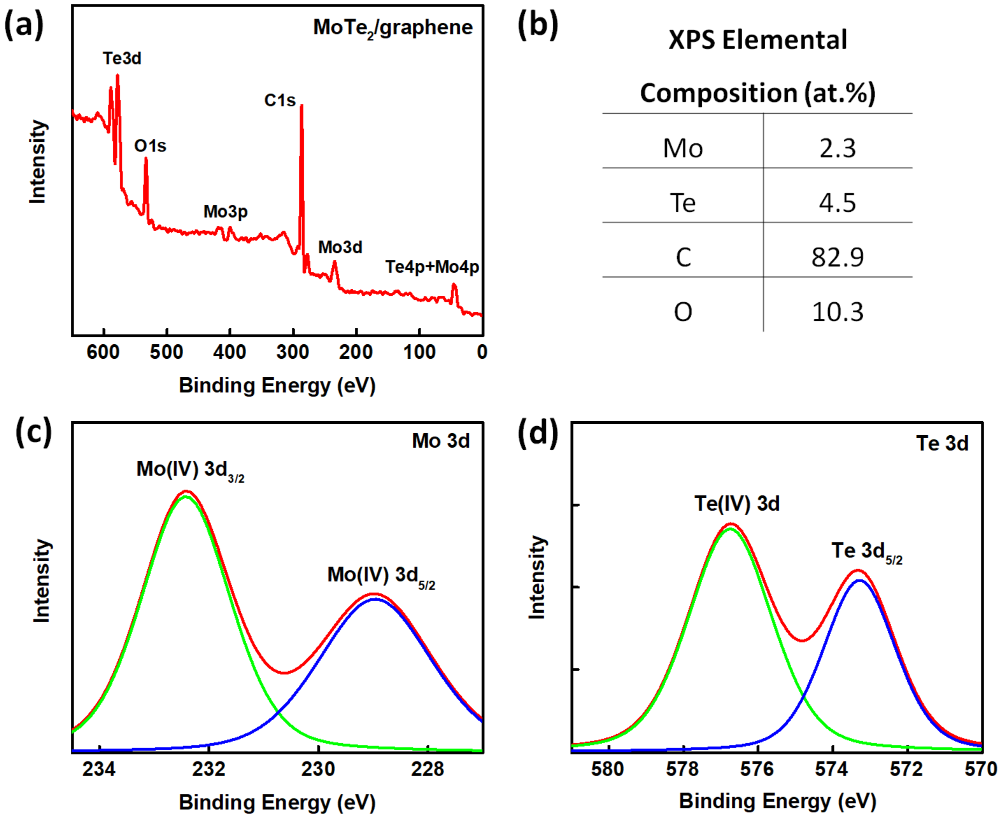

XPS Elemental Composition (at.%)

Mo	2.3
Te	4.5
C	82.9
O	10.3

Figure 3.5. (a) XPS survey spectrum of $MoTe_2$/graphene composite. (b) XPS elemental composition. High resolution XPS spectra of (c) Mo 3d, and (d) Te 3d regions of $MoTe_2$/graphene.

3.3.2. Electrocatalytic activities of $MoTe_2$/graphene towards HER

The HER activities of $MoTe_2$/graphene, bare GCE, pure graphene, MoO_x/graphene, and commercial Pt catalyst were determined in 0.5 M H_2SO_4 solution by linear sweep voltammetry (LSV) at room temperature, with a scan rate of 1 mV s^{-1}. The LSV (*iR* corrected) curve of $MoTe_2$/graphene displays a small onset potential of 100 mV (Figure 3.6a), beyond which the current starts increasing towards cathodic (negative) direction. The major parameters obtained from LSVs are shown in Figure 3.6b and Table 3.1, which reveals the overpotentials (η_{10}) for $MoTe_2$/graphene and Pt to attain the current density of 10 mA cm^{-2} are 150 and 53 mV, respectively. In disparity, MoO_x/graphene exhibits insignificant catalytic activities, while bare GCE and graphene possess no activity at all (Figure 3.6a). The LSV curve of MoO_x/graphene displays capacitive current (the offset from 0 mA cm^{-2}) due to the reduction of oxide layers. Similar trend is found for $MoTe_2$/graphene since, there is a small amount of MoO_x present in $MoTe_2$/graphene composite.

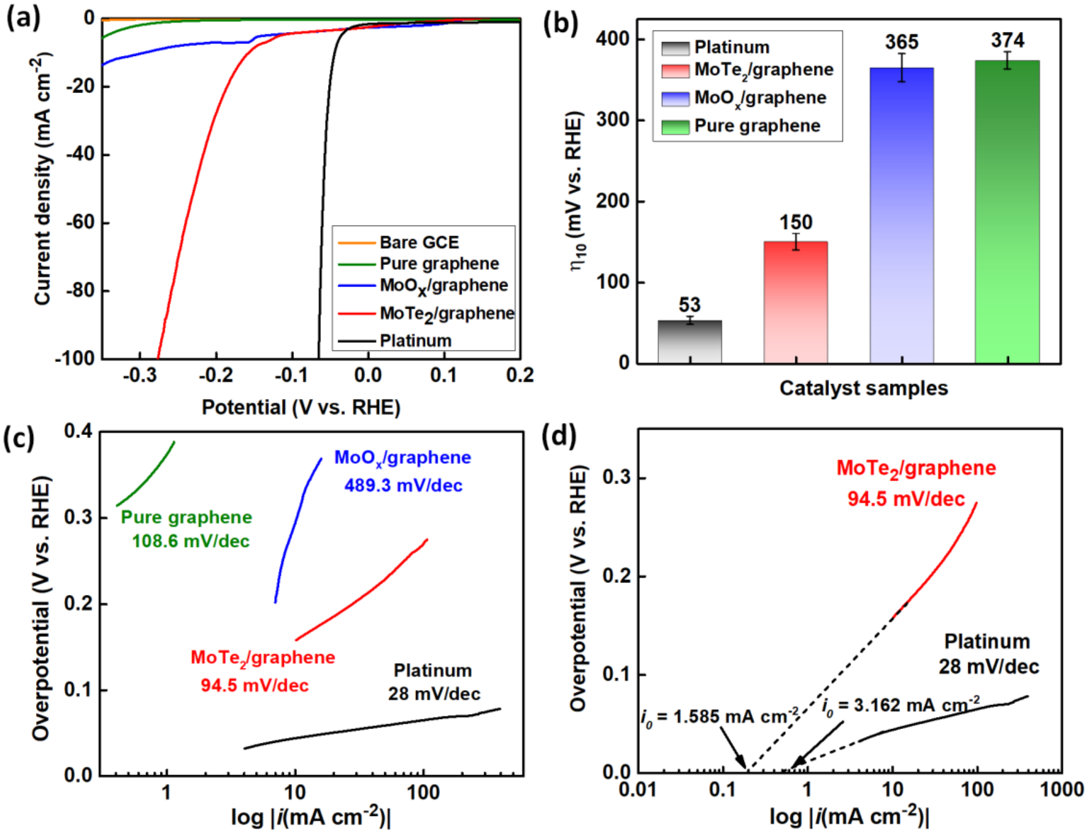

Figure 3.6. (a) Linear sweep voltammograms at a scan rate of 1 mV s^{-1} for bare GCE, pure graphene, MoO_x/graphene, $MoTe_2$/graphene, and Pt catalyst. (b) Corresponding overpotential values. (c) Corresponding Tafel plots. (d) Measurements of exchange current densities for platinum (Pt) and $MoTe_2$/graphene composite.

Table 3.1. Electrochemical parameters of $MoTe_2$/graphene nanocomposite, comparing with commercial platinum (Pt), MoO_x/graphene, and pure graphene samples.

Samples	***Onset potential, η_0 [mV vs. RHE]**	****Over potential, η_{10} [mV vs. RHE]**	**Tafel slope [mV/decade]**	**Exchange current density, i_0 (mA cm^{-2})**
Platinum	45	53	28.0	3.162
$MoTe_2$/graphene	100	150	94.5	1.585
MoO_x/graphene	201	365	489.3	-
Pure graphene	204	374	108.6	-

* Onset potential (η_0): Potential when current starts increasing towards cathodic direction

** Over potential (η_{10}): Potential when current density reaches 10 mA cm^{-2}

Furthermore, the Tafel plots were obtained from LSVs by fitting the linear regions to Tafel equation, $\eta = a + b \log i$. Where, η represents overpotential (V vs. RHE), a is a constant, b is the Tafel slope (mV/decade), and i is current density (mA cm^{-2}). Tafel slope can help to determine the electrocatalytic reaction mechanism of HER process. Theoretically, HER mechanism consists of three principal steps [Volmer reaction in which the adsorption and reduction of proton on electrode surface: $H_3O^+(aq) + e^- + \rightleftharpoons H^* + H_2O(l)$; Heyrovsky reaction where a proton is reduced while interacting with an adsorbed hydrogen atom, thus producing molecular hydrogen: $H^* + H_3O^+(aq) + e^- \rightleftharpoons H_2(g) + H_2O(l) + *$ and the Tafel reaction where two adsorbed hydrogen atoms undergo reversible recombination to produce molecular hydrogen: $H^* + H^* \rightleftharpoons H_2(g) + 2*$].[34,35] Here, * denotes the empty active site and H* is the adsorbed hydrogen atom on the active site of catalyst material. Assuming that the active surface refers to the underlying metal atom, and H* is not adsorbed yet, the overall HER reaction initiates with a discharge step (Volmer; b = 120 mV/decade), followed by either a desorption step (Heyrovsky; b = 40 mV/decade) or recombination step (Tafel; b = 30 mV/decade). While the value of the Tafel slope can be used to determine a governing mechanism, a low value favors HER. In this study, $MoTe_2$/graphene reveals the Tafel slope of 94.5 mV/decade (Figure 3.6c) in the overpotential range of 0.1−0.2 V vs. RHE. This result indicates that the Volmer–Heyrovsky reaction mechanism dominates in the HER process of $MoTe_2$/graphene catalyst and suggests that the Volmer is the rate determining step. In addition, previous studies mentioned that the exchange current density (i_0) is considered as proportional to the active surface area of the catalysts,[36,37] which can be attained by an extrapolation method, as shown in Figure 3.6d. According to the results in Table 3.1, the i_0 of $MoTe_2$/graphene is found of 1.585 mA cm^{-2}, which is very close to commercial Pt catalyst (3.162 mA cm^{-2}).

To date, only a few of the studies have been published on $MoTe_2$-based catalyst for HER, although there are many publications on MoS_2-based catalysts. Previously reported over potentials (η_{10}) and Tafel slopes of molybdenum (Mo)-based compounds have been compared with the present data of $MoTe_2$/graphene composite in Table 3.2. In contrast with simple microwave-initiated synthesis, previously reported synthesis approaches are complicated and time-consuming. Additionally, the present material exhibits good catalytic behavior, which is comparable with other Mo-based compounds. The improved electrocatalytic activity of $MoTe_2$/graphene was further verified by electrochemical impedance spectroscopy (EIS) measurements. Figure 3.7a displays the Nyquist plots of $MoTe_2$/graphene at different overpotentials from 100 to 300 mV. A single capacitive semicircle is found in the high frequency zone, suggesting that the reaction is kinetically controlled. In addition, the charge-transfer resistance (R_{ct}) decreases substantially with the increase in overpotentials, from 632.2 Ω at 100 mV to only 7.056 Ω at 300 mV (Figure 3.7b). Lower R_{ct} demonstrates better charge transfer capability, resulting the faster reaction taking place.

Table 3.2. Comparison of electrochemical activities of microwave-synthesized $MoTe_2$/graphene with previously reported similar Mo-based compounds.

Materials	**Synthesis approach**	**Electrolyte**	**Overpotential at 10 mAcm^{-2} [mV vs. RHE]**	**Tafel slope [mV per decade]**	**References**
$MoTe_2$-RGO/PI/Mo	Solvothermal, electrochemical-deposition	0.5 M PBS	200	128	[16]
1T'-$MoTe_2$	Annealing	1 M H_2SO_4	300	78	[18]
$MoTe_2$ nanosheets	Liquid exfoliation	0.5 M H_2SO_4	309	118.9	[38]
MoS_2/RGO	Solvothermal	0.5 M H_2SO_4	100	41	[39]
Porous $MoSe_2$	Liquid exfoliation	0.5 M H_2SO_4	75	80	[40]
$MoTe_2$/10%-SWNT	Liquid exfoliation	0.5 M H_2SO_4	~250	~86	[41]
1T' $MoTe_2$/CC	Chemical vapor deposition	1 M H_2SO_4	230.7	127.1	[42]
1T' $MoTe_2$	Flux method	0.5 M H_2SO_4	356	127	[43]
$MoSe_{0.17}Te_{1.83}$	Molecular beam epitaxy	0.5 M H_2SO_4	45	64	[44]
1T'-$MoTe_2$	Annealing	1 M H_2SO_4	178	68	[45]
$MoTe_2$ nanotubes	Hydrothermal	0.5 M H_2SO_4	283	102.06	[46]
$MoTe_2$/graphene	**Microwave irradiation**	**0.5 M H_2SO_4**	**150**	**94.5**	**present study**

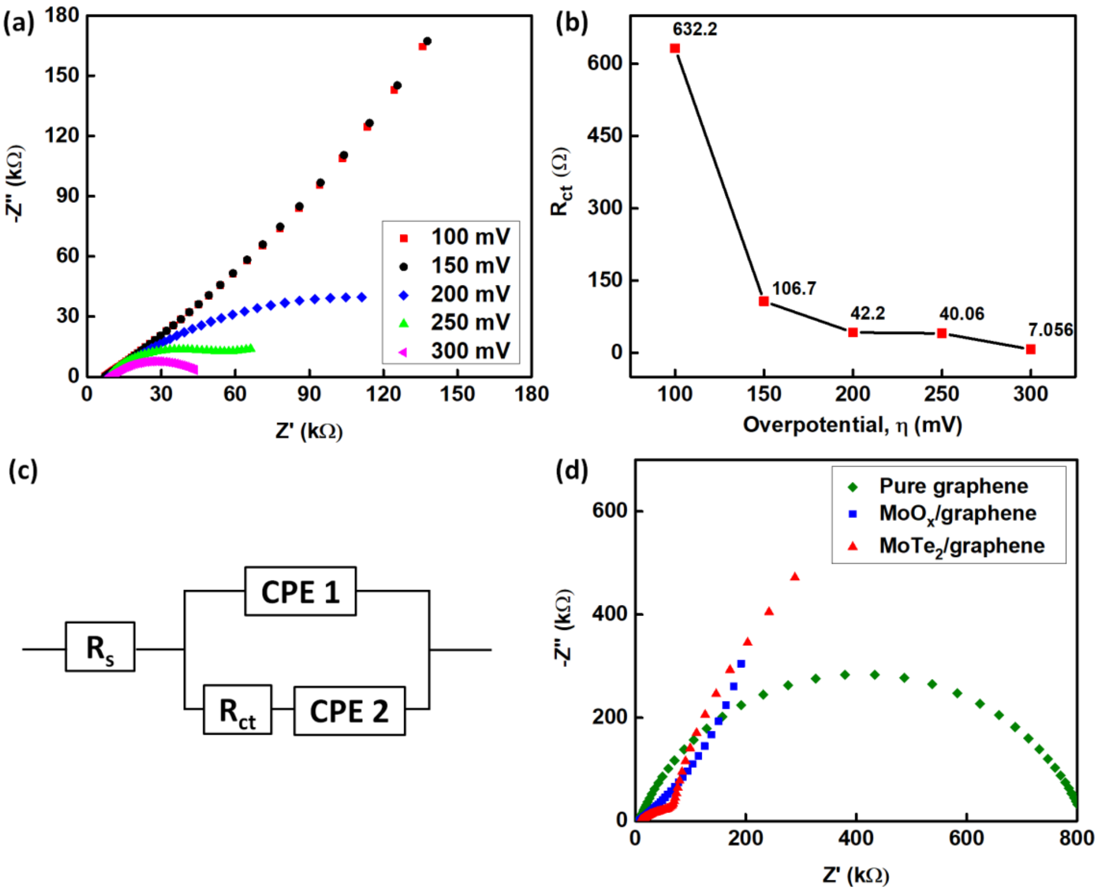

Figure 3.7. (a) Nyquist plots showing the EIS responses of MoTe$_2$/graphene at various overpotentials (100−300 mV). (b) Decrease in charge transfer resistance (R$_{ct}$) with increase in overpotentials (η) for MoTe$_2$/graphene. (c) Equivalent electrical circuit used to model the HER process. (d) Nyquist plots at the potential of 150 mV vs. RHE.

The Randles cell diagram shown in Figure 3.7c was chosen to model EIS data. The first constant phase element (CPE 1) is related to the electrical double layer formed at electrode/electrolyte interface and CPE 2 is corresponded to pseudocapacitance behavior of MoTe$_2$/graphene. The Nyquist plots were also determined to compare the impedance of catalyst samples at 150 mV (Figure 3.7d). Although the solution resistance (R_s) for all the samples are ~7 Ω, MoTe$_2$/graphene shows lower charge transfer resistance (R_{ct}) of 106.7 Ω than the values of

MoO_x/graphene and pure graphene samples. Thus, much faster electron transfer is one of the main factors impacting on the superior HER kinetics in $MoTe_2$/graphene catalyst. All the important EIS parameters are summarized in Table 3.3, which were obtained after z-fit analysis.

Table 3.3. Impedance parameters derived by fitting the EIS responses of $MoTe_2$/graphene, MoO_x/graphene and pure graphene samples at an overpotential of 150 mV.

Samples	**R_s (ohm)**	**R_{ct} (ohm)**	**CPE 1 (F s^{-1})**	**CPE 2 (F s^{-1})**
$MoTe_2$/graphene	6.94	106.7	1.836×10^{-3}	1.939×10^{-3}
MoO_x/graphene	7.02	266.6	1.08×10^{-2}	1.51×10^{-3}
Pure graphene	6.96	806.7	1.48×10^{6}	3.76×10^{-5}

Determination of electrochemical double-layer capacitance (C_{dl}) at the interface of electrode and electrolyte is another effective way to measure the electrochemically active surface area (ECSA), which helps to evaluate the active reaction sites.[47,48] Therefore, the CV measurements were performed within a potential range (0.3−0.4 V vs. RHE) with no apparent faradaic reaction taking place for $MoTe_2$/graphene catalyst (Figure 3.8a), where the currents are mainly assigned to the double-layer charging/discharging. Other CV measurements are shown in Figure 3.8b and 3.8c for MoO_x/graphene and pure graphene. Average capacitive current densities, $\frac{1}{2}(i_a - i_c)$ are plotted with respect to corresponding scan rates in Figure 3.8d for the catalyst samples of $MoTe_2$/graphene, MoO_x/graphene, and pure graphene. Here, i_a and i_c represent the anodic and cathodic peak current densities, respectively. The capacitance of $MoTe_2$/graphene is calculated 6.67 mF cm^{-2}, whereas those of MoO_x/graphene and pure graphene are only 2.84 and 0.037 mF cm^{-2}, respectively. This higher value of double-layer capacitance reveals more active sites present in $MoTe_2$/graphene catalyst, leading to the high catalytic performance.

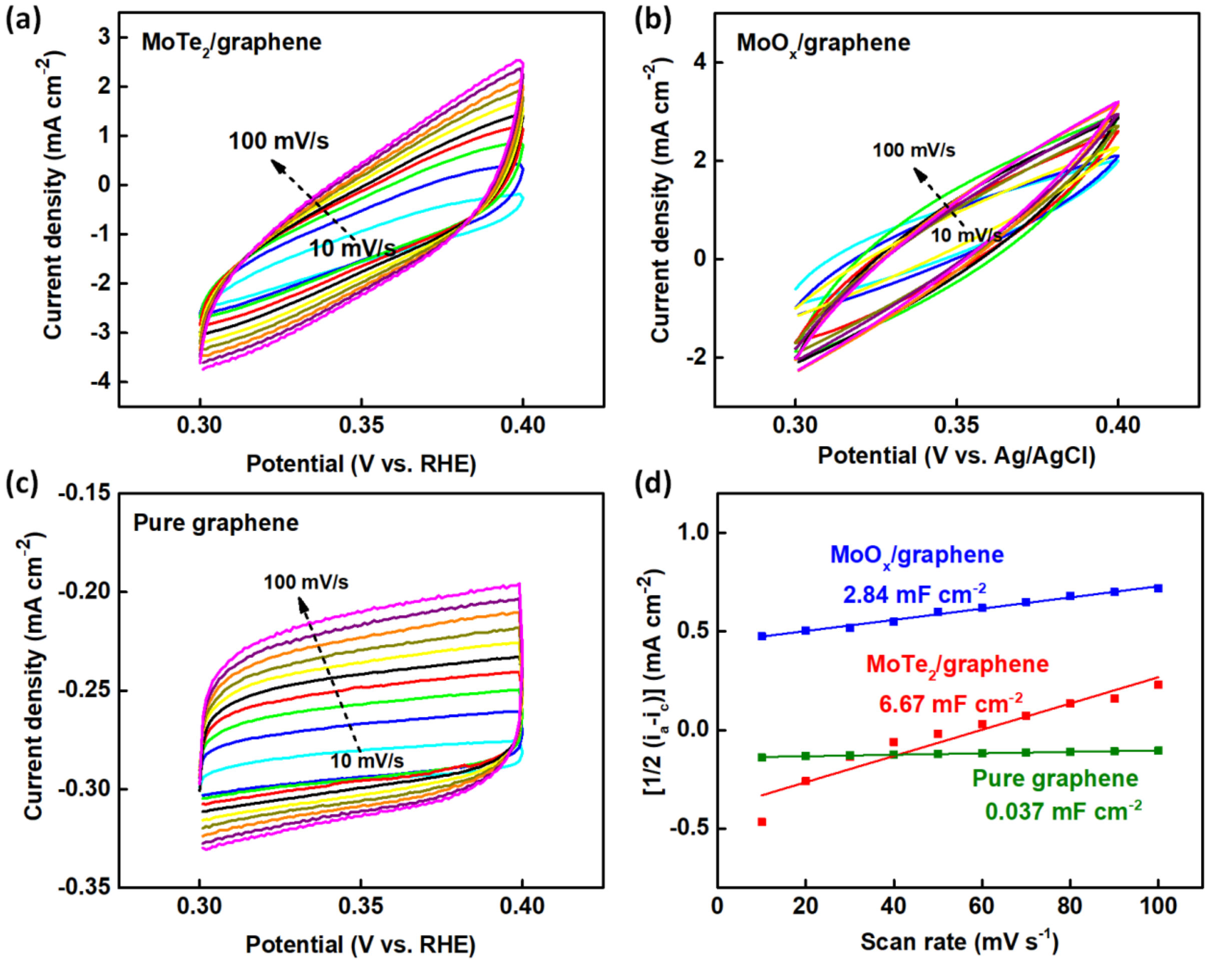

Figure 3.8. Cyclic voltammograms of (a) MoTe$_2$/graphene, (b) MoOx/graphene and (c) Pure graphene in a potential window without faradaic reaction at a scan rate of 10−100 mVs^{-1}. (d) Average capacitive current densities at different scan rates.

Besides high catalytic activities, for practical applications, another major factor is the good stability of materials towards HER. Therefore, the long-term stability of MoTe$_2$/graphene was tested using the CV from 0 to −350 mV vs. RHE for 5000 cycles at a scan rate of 50 mV s^{-1} (Figure 3.9a) in 0.5 M H_2SO_4. Remarkably, the catalytic performance of MoTe$_2$/graphene nanocomposite remains very stable while a slight shift of the LSV curve occurs toward lower Tafel slopes, enhancing the HER activity. This improved catalytic behavior during the potential cycling is possibly due to the catalytic activation by proton intercalation in both $MoTe_2$ and graphene layers. Another reason could be the generation of thinner and more porous catalyst surface by continuous perforation of H_2 bubbles.

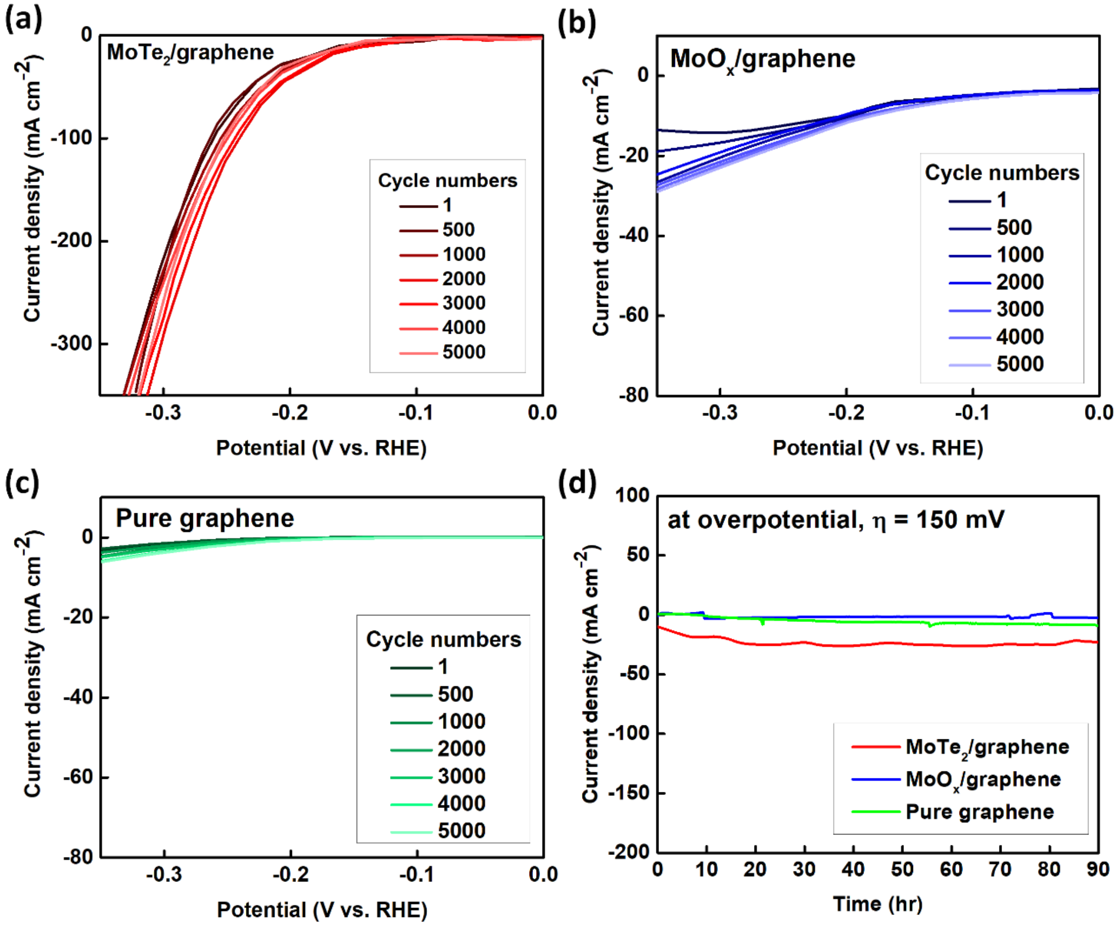

Figure 3.9. Cycling stability of (a) $MoTe_2$/graphene, (b) MoO_x/graphene and (c) Pure graphene from 0 to −350 mV at a scan rate of 50 mV s^{-1}, wherein the polarization curves from 1 to 5000 cycles are displayed. (d) Constant potential stability for 90 hours at an overpotential of 150 mV.

To compare this activation of catalyst samples, cycling stability tests were performed for MoO_x/graphene and pure graphene (Figure 3.9b and 3.9c). Pure graphene requires an overpotential in excess of 350 mV to reach the current density of 10 mA cm^{-2}, whether MoO_x/graphene exhibits slight activation with a high overpotential value of 196 mV, which indicate their insignificant catalytic activities towards HER. In addition to the cycling stability, the practical operation of $MoTe_2$/graphene catalyst was also observed by constant potential stability test. As shown in Figure 3.9d, the $MoTe_2$/graphene catalyst shows a slight increase in current density from −11 to −30 mA cm^{-2} from electrolysis for 90 hours at a constant overpotential of 150 mV vs. RHE. The increase in current density strengthens the hypothesis of catalytic activation detected during the cycling stability. Previous studies showed that, in the case of longtime HER tests, the Pt counter electrode would be oxidized to Pt^{2+} at the anode and deposited on the cathode.[45,49,50] To eliminate this Pt deposition probability on $MoTe_2$/graphene surface, the graphite rod has been used as counter electrode for both cycling and constant potential stability tests.

Moreover, the double layer capacitance (C_{dl}) was determined from CV measurements (Figure 3.10a−3.10c) after 5000 cycles. An increase is found in C_{dl}, from 6.67 to 11.58 mF cm^{-2}, substantiating the increase in electrocatalytic active surface area of $MoTe_2$/graphene during the cycling activation process. In comparison, while pure graphene shows slight increase in C_{dl} from 0.037 to 0.09 mF cm^{-2}, MoO_x/graphene displays a decrease in C_{dl} from 2.84 to 1.16 mF cm^{-2} (Figure 3.10d), indicating the superior catalytic activities of $MoTe_2$/graphene catalyst during stability tests.

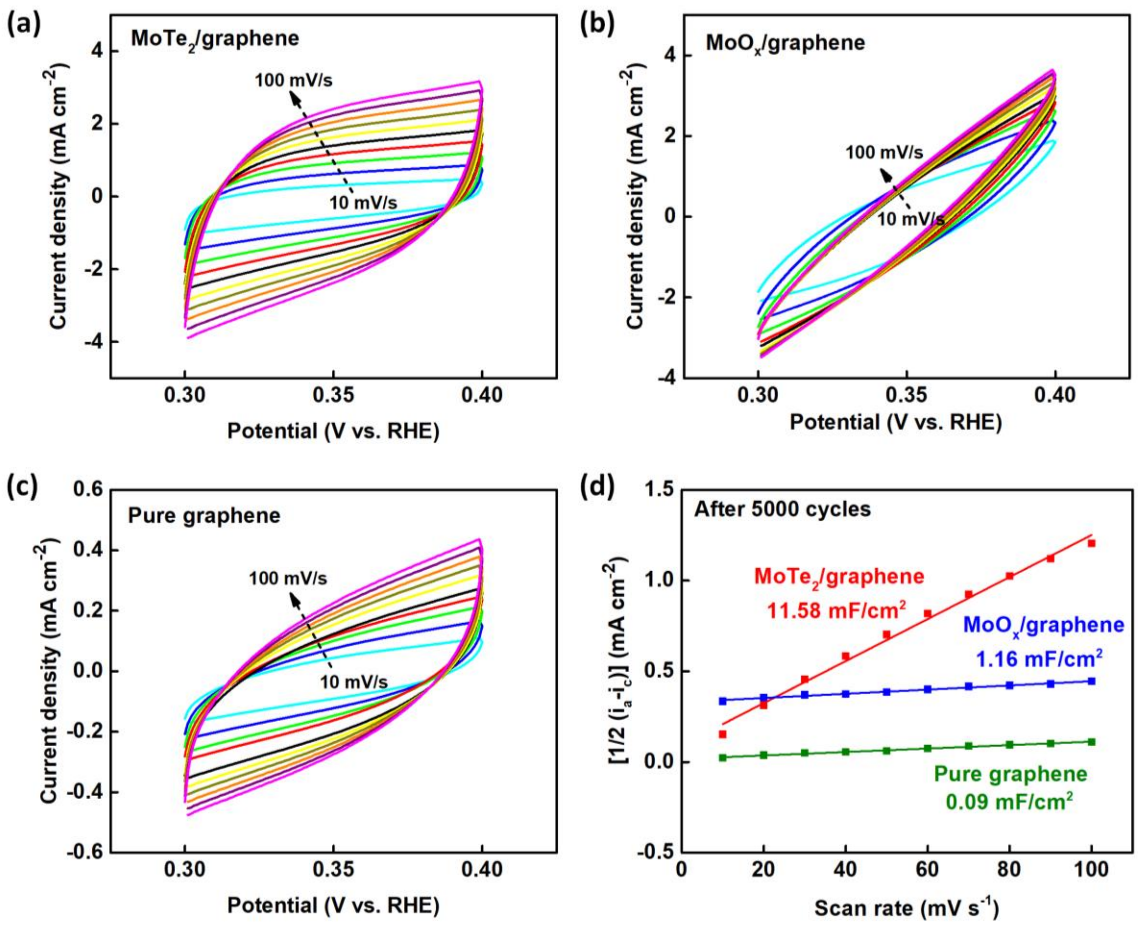

Figure 3.10. Cyclic voltammograms of (a) $MoTe_2$/graphene, (b) MoO_x/graphene and (c) Pure graphene to measure the ECSA after 5000 cycles, at a scan rate of 10−100 mVs^{-1}. (d) Double layer capacitance measurements after 5000 cycles.

The change in elemental compositions and morphologies of $MoTe_2$/graphene composite after 5000 CV cycles was examined by SEM, EDS, and TEM analyses (Figure 3.11), where the Figure 3.11a and 3.11b clearly show insignificant degradation of active material even after 5000 cycles, retaining the similar atomic ratio of Mo:Te ≈ 1:2. As displayed in Figure 3.11c, the nanosheet structures are well-preserved without any of significant collapses, which is because, the $MoTe_2$ nanosheets are uniformly embedded with graphene layers and graphene is highly stable material. Therefore, the presence of a large amount of graphene substrate sharply enhances the structural stability of $MoTe_2$ nanosheets during the HER. Better structural stability may be a direct response for the enhanced cycling stability. Moreover, from HR-TEM images (Figure 3.11d and 3.11e), there is an increase shown in the interlayer spacing of $MoTe_2$ and graphene nanosheets, from 6.87 Å to 7.01 Å and 3.43 Å to 3.75 Å, respectively. These phenomena strongly support the hypothesis of H^+ intercalation taking place during the cycling stability test, resulting a slight expansion between lattice fringes.

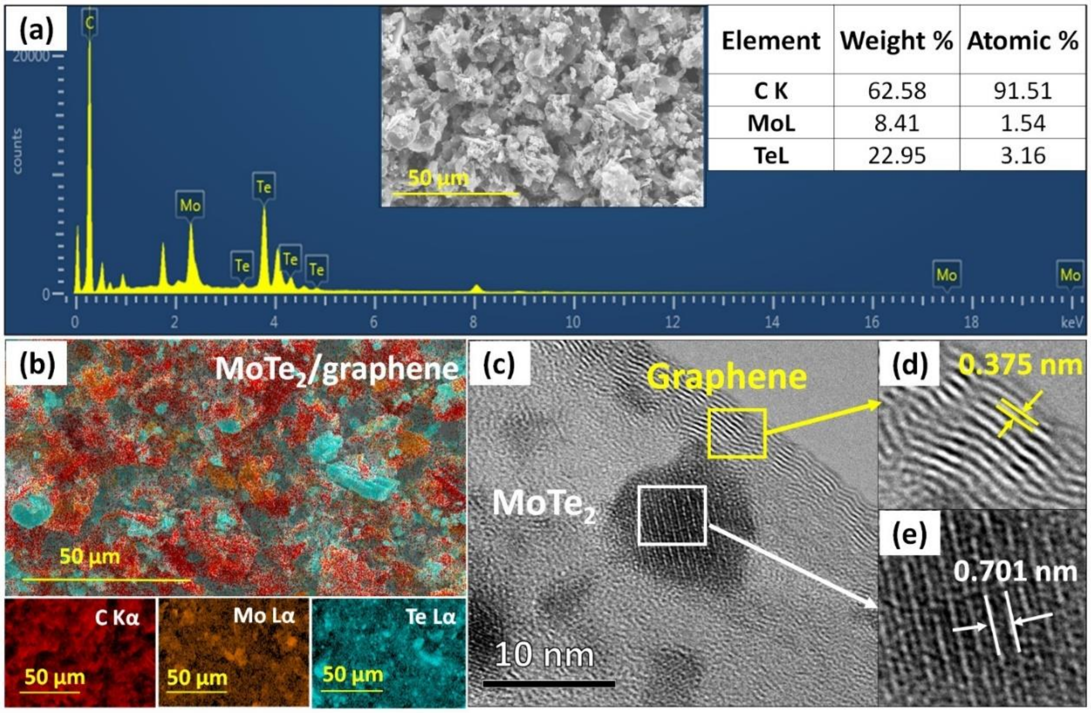

Element	Weight %	Atomic %
C K	62.58	91.51
MoL	8.41	1.54
TeL	22.95	3.16

Figure 3.11. (a) EDS pattern of $MoTe_2$/graphene nanocomposite (inset table shows wt% and atomic% of carbon (C), molybdenum (Mo), and tellurium (Te) elements; (b) EDS elemental mapping of $MoTe_2$/graphene. The red, orange, and cyan color represents carbon (C), molybdenum (Mo), and tellurium (Te), respectively. (c) HR-TEM images of $MoTe_2$/graphene nanocomposite. (d, e) Interlayer spacings.

Furthermore, besides operating for a long period of time, water electrolysis cells may operate at relatively high temperatures about 50−70°C in practical applications. Hence, the stability of $MoTe_2$/graphene catalyst was obtained from the LSVs at a temperature range of 30°C−90°C (Figure 3.12a). Moreover, the exchange current densities (i_0) were measured from corresponding Tafel slopes, which are represented in Figure 3.12b and the measured electrochemical parameters (η_0 and i_0) are tabulated in Table 3.4. It is clearly shown that, the onset potentials get decreased with increasing exchange current densities.

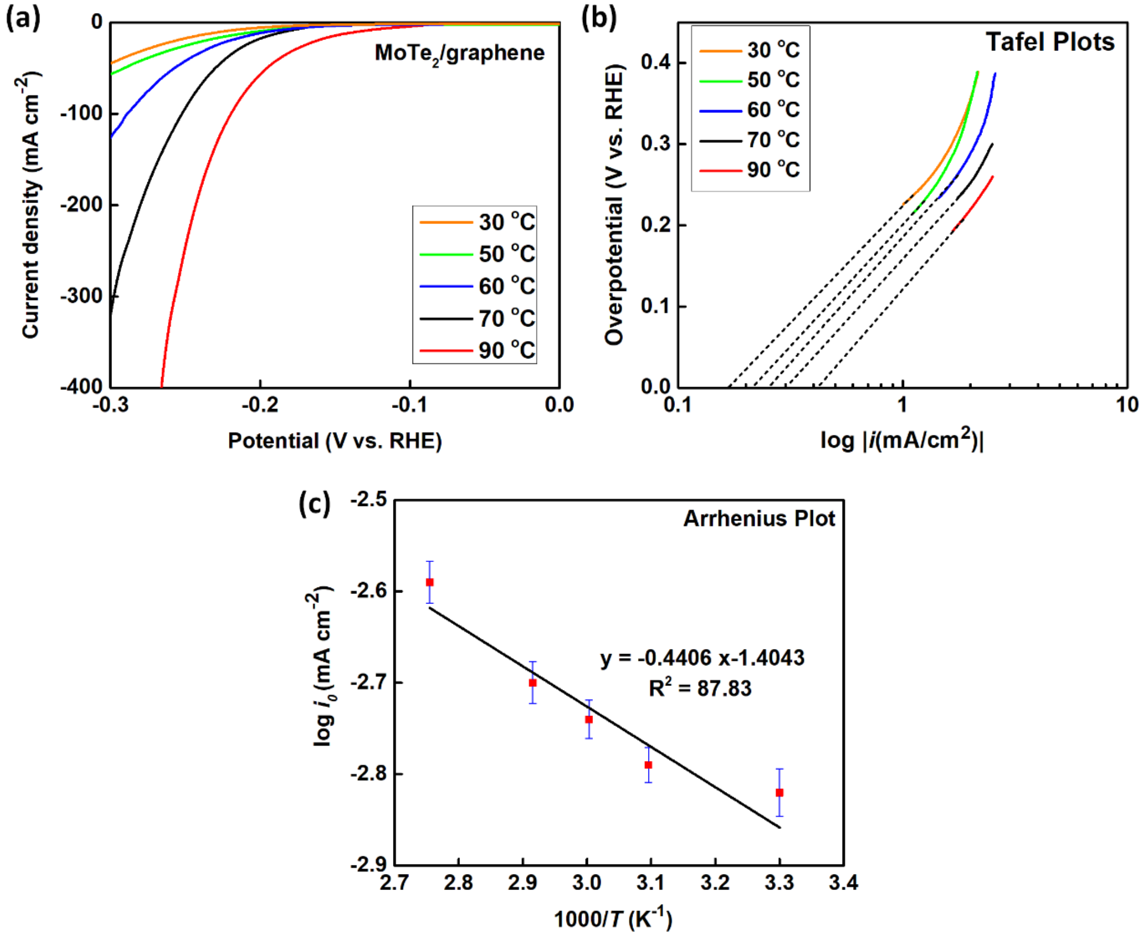

Figure 3.12. (a) LSVs of $MoTe_2$/graphene catalyst at a temperature range of 30−90 °C, at a scan rate of 1 mV s^{-1} in 0.5 M H_2SO_4. (b) Corresponding Tafel plots. (c) The Arrhenius plot.

Table 3.4. HER parameters of $MoTe_2$/graphene-catalyst at a temperature range of 30−90°C.

Temperature, T (°C)	**Onset potential, η_0 (mV vs RHE)**	**Exchange current density, i_0 (mA cm^{-2})**	**Activation energy, E_a (kJ mol^{-1})**
30	98.2	1.51356	8.4362 ± 1.5413
50	96.4	1.62181	
60	85.5	1.8197	
70	82.9	1.99526	
90	80.1	2.5704	

Moreover, based on this analysis, the activation energy (E_a) can be measured using the Arrhenius equation ($k = Ae^{\frac{-E_a}{RT}}$), where E_a can be calculated by the following Equation 3.1: [51]

$$\log(i_0) = \log(A) - \frac{E_a}{2.3\ RT} \quad \ldots\ldots\ldots\ldots\ldots\ldots\ldots\ldots (3.1)$$

Here, A represents pre-exponential factor, R is universal gas constant (8.314 J/mol·K) and T denotes the absolute temperature (K). Plot of the log i_0 *vs.* $\frac{1000}{T}$ is displayed in Figure 3.12c, from which E_a is calculated 8.4362 ± 1.5413 kJ mol^{-1} from the slope for $MoTe_2$/graphene catalyst, assuming the equilibrium potential (U = 0 V vs. RHE) remains unchanged with increasing the temperatures. This lower activation energy is even better than the Pt catalyst (20−40 kJ mol^{-1}) [51,52], which could be the result of higher active load (~ 5 mg cm^{-2}) of catalyst material. This apparent activation energy (E_a) only corresponds to the enthalpic part of the free-activation energy. Particularly in the HER, the entropic contribution to the free-activation energy is crucial, that exceeds the enthalpic contribution.[53] Therefore, although $MoTe_2$/graphene results lower E_a, but Pt is more active than $MoTe_2$/graphene catalyst. Nonetheless, in present study, $MoTe_2$/graphene has shown promising catalytic activity towards HER. This enhanced electrocatalytic activity and stability reveal that, the microwave-initiated synthesis is remarkably efficient to synthesize $MoTe_2$/graphene catalyst for hydrogen generation in acidic medium.

3.3.3. Computational study of HER activity on $MoTe_2$/graphene composite

For the computational study, multiple hydrogen adsorption sites on the Mo_9Te_{18} nanoparticle were investigated for the hydrogen adsorption process (Figure 3.2). The adsorption energy of a single H atom on the graphene supported Mo_9Te_{18} nanoparticle was calculated using the equation:

$$\Delta E_{adsorption} = \frac{1}{2}\left(E_{2H^*+MoTe_2/graphene} - E_{MoTe_2/graphene} - E_{H_2}\right) \ldots\ldots\ldots\ldots\ldots\ldots\ldots\ldots\ldots.. \quad (3.2)$$

Here, $E_{2H^*+MoTe_2/graphene}$ is the total electronic energy of the two hydrogen atoms bound to the Mo_9Te_{18} nanoparticle-graphene composite, $E_{MoTe_2/graphene}$ is the total electronic energy of Mo_9Te_{18} nanoparticle-graphene composite, and E_{H_2} is the electronic energy of hydrogen molecule. These adsorption energies were calculated to determine the best active catalytic sites on the $MoTe_2$/graphene nanocomposite catalyst responsible for HER activity. Furthermore, the binding free energy has been calculated using the generalized expression for HER catalysis developed by Nørskov and co-workers in the following equation[54]:

$$\Delta G_{adsorption} = \Delta E_{adsorption} + 0.24\ eV \ldots\ldots\ldots\ldots\ldots\ldots\ldots\ldots\ldots\ldots\ldots\ldots\ldots \quad (3.3)$$

Among the hydrogen adsorption sites considered, the exposed Mo corner (site 1) and the Mo edge adjacent to Te edge (site 6) on Mo_9Te_{18} nanoparticle exhibit the lowest $|\Delta G_{adsorption}|$ values, 0.267 and 0.097 eV, respectively. The $\Delta G_{adsorption}$ values are illustrated in an energy diagram (Figure 3.13a) to compare the results of the catalytically active $MoTe_2$/graphene composite sites (namely, site 1 and site 6) with other HER catalysts. Moreover, using the calculated binding free energy ($\Delta G_{adsorption}$) for these sites and the experimental value of exchange current density (i_0), the points for the $MoTe_2$/graphene nanocomposite on the volcano plot (Figure 3.13b) were found nearly thermoneutral, approaching the high-performing metals such as Pt.

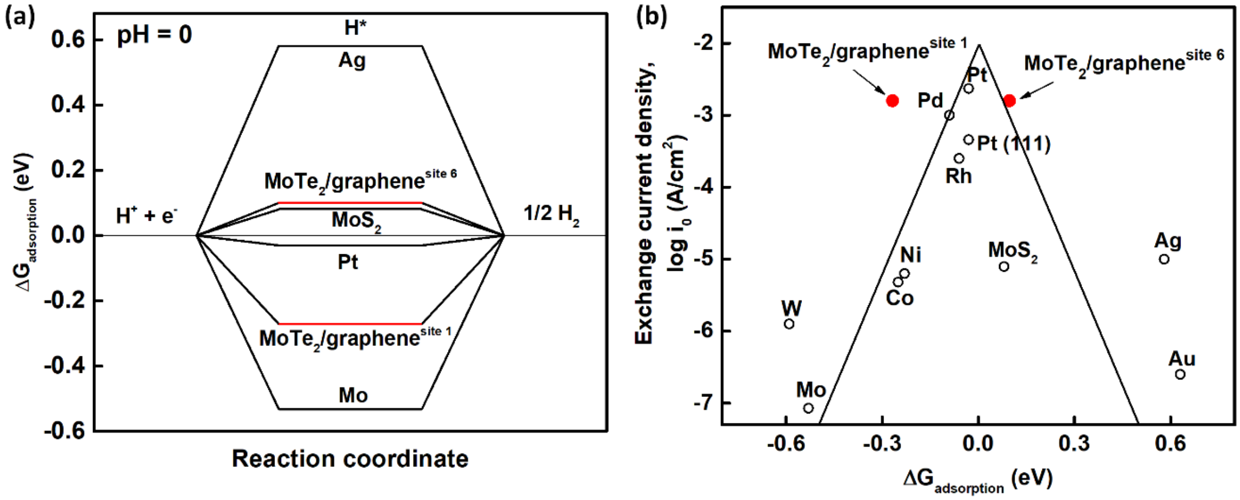

Figure 3.13. (a) Hydrogen adsorption free energy ($\Delta G_{adsorption}$) diagrams at equilibrium. (b) Volcano plot. [Note: Literature data for different metals and MoS_2-catalyst have been adapted from Nørskov et al.[54] and Jaramillo et al.[55], respectively. $MoTe_2$/graphene$^{site\ 1}$ and $MoTe_2$/graphene$^{site\ 6}$ represent Mo corner and Mo edge-Te edge adsorption sites from the current study, respectively.]

3.4. Summary

In summary, we have synthesized $MoTe_2$ nanosheets uniformly dispersed on graphene substrate by microwave-initiated heating method and have explored their practical application in hydrogen evolution reactions, along with theoretical studies to identify the most active sites of resultant $MoTe_2$/graphene nanocomposite. The physicochemical characterizations (i. e. SEM, EDS, XRD, etc.) verified that the as-produced $MoTe_2$ nanosheets were well anchored on graphene substrate, revealing the effectiveness of our ultra-fast (90 sec) synthesis method. The resultant

$MoTe_2$/graphene catalyst showed excellent electrocatalytic performance toward HER, with a small over potential of ~150 mV to obtain the current density of 10 mA cm^{-2}, large cathodic currents, and a Tafel slope of 94.5 mV per decade. More importantly, the hybrid composite demonstrated the enhanced catalytic stability for 5000 cycles, exhibiting the slight activation in catalyst materials. In addition, the $MoTe_2$/graphene composite showed remarkable stability even at high operating temperatures up to 90°C with a very low activation energy of 8.4362 ± 1.5413 kJ mol^{-1}. This enhanced catalytic activity of $MoTe_2$/graphene may be attributed to the strong chemical and electronic coupling between $MoTe_2$ nanosheets and graphene network, resulting fast electronic kinetics along with an additional mechanical support from graphene substrate. Moreover, the computational results clearly demonstrated the correlation between the hydrogen chemisorption free energies and the exchange current densities for HER, identifying most active sites on the synthesized catalyst structures. The volcano plot indicated that graphene supported $MoTe_2$ is a promising electrocatalyst as compared to other metals, because the hydrogen evolution reaction is near thermoneutral on $MoTe_2$/graphene and, similar to Pt at the equilibrium potential.

3.5. References

1 U.S. Energy Information Administration, *EIA energy outlook 2020*, 2020.

2 J. A. Turner, *Science (80).*, 2004, **305**, 972–975.

3 R. H. Lin, Y. Y. Zhao and B. D. Wu, *Int. J. Hydrogen Energy*, 2020, 1–12.

4 P. Moriarty and D. Honnery, *Int. J. Hydrogen Energy*, 2007, **32**, 1616–1624.

5 A. Chapman, K. Itaoka, K. Hirose, F. T. Davidson, K. Nagasawa, A. C. Lloyd, M. E. Webber, Z. Kurban, S. Managi, T. Tamaki, M. C. Lewis, R. E. Hebner and Y. Fujii, *Int. J. Hydrogen Energy*, 2019, **44**, 6371–6382.

6 M. Carmo, D. L. Fritz, J. Mergel and D. Stolten, *Int. J. Hydrogen Energy*, 2013, **38**, 4901–4934.

7 D. V Esposito, S. T. Hunt, A. L. Stottlemyer, K. D. Dobson, B. E. Mccandless, R. W. Birkmire and J. G. Chen, *Angew. Chemie - Int. Ed.*, 2010, 9859–9862.

8 E. Environ, M. Wang and L. Sun, *Energy Environ. Sci.*, 2012, **5**, 6763–6778.

9 X. Zou and Y. Zhang, *Chem. Soc. Rev.*, 2015, **44**, 5148–5180.

10 B. Hinnemann, P. G. Moses, J. Bonde, K. P. Jørgensen, J. H. Nielsen, S. Horch, I. Chorkendorff and J. K. Nørskov, *J. Am. Chem. Soc.*, 2005, **127**, 5308–5309.

11 W. Lubitz, H. Ogata, O. Rüdiger and E. Reijerse, *Chem. Rev.*, 2014, **114**, 4081–4148.

12 M. Liu, Z. Wang, J. Liu, G. Wei, J. Du, Y. Li, C. An and J. Zhang, *J. Mater. Chem. A*, 2017, **5**, 1035–1042.

13 Y. Lin, Y. Xu, S. Wang, S. Li and M. Yamamoto, *Adv. Mater.*, 2014, **26**, 3263–3269.

14 M. Dey, M. Dey, M. A. Matin and N. Amin, in *2016 4th International Conference on the Development in the in Renewable Energy Technology (ICDRET)*, IEEE, 2016, pp. 1–4.

15 D. Mao, B. Du, D. Yang, S. Zhang and Y. Wang, *Small*, 2016, **12**, 1489–1497.

16 Y. Zhou, L. Jia, Q. Feng, T. Wang, X. Li and C. Wang, *Electrochim. Acta*, 2017, **229**, 121–128.

17 L. Zhou, K. Xu, A. Zubair, A. D. Liao, W. Fang, F. Ouyang, Y. Lee, K. Ueno, R. Saito and M. S. Dresselhaus, *J. Am. Chem. Soc.*, 2015, **137**, 11892–11895.

18 J. C. Mcglynn, I. Cascallana-mat, J. P. Fraser, I. Roger, J. Mcallister, H. N. Miras, M. D. Symes and A. Y. Ganin, *Energy Technol.*, 2018, **6**, 345–350.

19 S. Sarwar, A. Nautiyal, J. Cook, Y. Yuan, J. Li, S. Uprety, R. Shahbazian-Yassar, R. Wang, M. Park, M. J. Bozack and X. Zhang, *Sci. China Mater.*, 2020, **63**, 62–74.

20 H. Oberhofer, *Electrocatalysis Beyond the Computational Hydrogen Electrode*, 2018.

21 D. R. Alfonso, D. N. Tafen and D. R. Kauffmann, First-principles modeling in heterogeneous electrocatalysis, *Catalysts* **8** (2018) 10.

22 J. Rossmeisl, E. Skúlason, M. E. Björketun, V. Tripkovic and J. K. Nørskov, *Chem. Phys. Lett.*, 2008, **466**, 68–71.

23 R. Parsons, *Trans. Faraday Soc.*, 1958, **54**, 1053–1063.

24 H. Gerischer, *Bull. Soc. Chim. Belg.*, 1958, **67**, 506–527.

25 S. Sarwar, A. Ali, Z. Liu, J. Li, S. Uprety, H. Lee, R. Wang, M. Park, M. J. Bozack, A. J. Adamczyk and X. Zhang, *J. Colloid Interface Sci.*, 2021, **581**, 847–859.

26 Z. Wang, W. Wang, Y. Yang, W. Li, L. Feng, J. Zhang, L. Wu and G. Zeng, *Int. J. Photoenergy*, 2014, 1–6.

27 M. Khan, A. Bin Yousaf, M. Chen, C. Wei, X. Wu, N. Huang, Z. Qi and L. Li, *Nano Res.*,

2016, **9**, 837–848.

28 M. Wang, X. Song, X. Cheng, X. Zhou, X. Zhang, Z. Cai, Y. Xu, S. Gao, H. Zhao and L. Huo, *RSC Adv.*, 2015, **5**, 85248–85255.

29 J. I. López-pérez, E. O. Ortiz-quiles, K. Habiba, M. Jiménez-rodríguez, B. R. Weiner and G. Morell, *ISRN Electrochem.*, 2014, 1–12.

30 C. Ruppert, O. B. Aslan and T. F. Heinz, *Nano Lett.*, 2014, **14**, 6231–6236.

31 V. Jadkar, A. Pawbake, R. Waykar and A. Jadhavar, *J. Mater. Sci. Mater. Electron.*, 2017, **28**, 15790–15796.

32 S. Hussain, S. A. Patil, D. Vikraman and N. Mengal, *Sci. Rep.*, 2018, 4–11.

33 N. Ma, X. Jiang, L. Zhang, X. Wang, Y. Cao and X.-Z. Zhang, *Small*, 2018, **14**, 1703680.

34 W. Sheng, H. A. Gasteiger and Y. Shao-Horn, *J. Electrochem. Soc.*, 2010, **157**, B1529.

35 C. Tang, Z. Pu, Q. Liu and A. M. Asiri, *Int. J. Hydrogen Energy*, 2015, **40**, 4727–4732.

36 D. Kong, H. Wang, Z. Lu and Y. Cui, *J. Am. Chem. Soc.*, 2014, **136**, 4897–4900.

37 Y. Tang, M. Gao, C. Liu, S. Li, H. Jiang, Y. Lan, M. Han and S. Yu, *Angew. Chemie - Int. Ed.*, 2015, **54**, 12928–12932.

38 H. Qiao, Z. Huang, S. Liu, Y. Liu, J. Li and X. Qi, *Ceram. Int.*, 2018, **44**, 21205–21209.

39 Y. Li, H. Wang, L. Xie, Y. Liang, G. Hong and H. Dai, *J. Am. Chem. Soc.*, 2011, **133**, 7296–7299.

40 Z. Lei, S. Xu and P. Wu, *Phys. Chem. Chem. Phys.*, 2016, **18**, 70–74.

41 Z. Gholamvand, D. McAteer, C. Backes, N. McEvoy, A. Harvey, N. C. Berner, D. Hanlon, C. Bradley, I. Godwin, A. Rovetta, M. E. G. Lyons and S. Duesberg, *Nanoscale*, 2016, **8**, 5737–5749.

42 D. Lu, X. Ren, L. Ren, W. Xue, S. Liu, Y. Liu, Q. Chen, X. Qi and J. Zhong, *ACS Appl. Energy Mater.*, 2019.

43 J. Seok, J. H. Lee, S. Cho, B. Ji, H. W. Kim, M. Kwon, D. Kim, Y. M. Kim, S. H. Oh, S. W. Kim, Y. H. Lee, Y. W. Son and H. Yang, *2D Mater.* **4** (2017)

44 T. Kosmala, H. Coy Diaz, H. P. Komsa, Y. Ma, A. V. Krasheninnikov, M. Batzill and S. Agnoli, *Adv. Energy Mater.*, 2018, **8**, 1–8.

45 J. C. McGlynn, T. Dankwort, L. Kienle, N. A. G. Bandeira, J. P. Fraser, E. K. Gibson, I. Cascallana-Matías, K. Kamarás, M. D. Symes, H. N. Miras and A. Y. Ganin, *Nat. Commun.*, *Nat. Commun.* **10** (2019)

46 K. S. Bhat and H. S. Nagaraja, *Int. J. Hydrogen Energy*, 2019, **44**, 17878–17886.

47 Y. Zhang, H. Sun, Y. Qiu, X. Ji, T. Ma, F. Gao, Z. Ma, B. Zhang and P. A. Hu, *Carbon N. Y.*, 2019, **144**, 370–381.

48 H. Sun, Z. Ma, Y. Qiu, H. Liu and G. gang Gao, *Small*, 2018, **14**, 1–12.

49 R. Wei, M. Fang, G. Dong and J. C. Ho, *Sci. Bull.*, 2017, **62**, 971–973.

50 G. Dong, M. Fang, H. Wang, S. Yip, H. Y. Cheung, F. Wang, C. Y. Wong, S. T. Chu and J. C. Ho, *J. Mater. Chem. A*, 2015, **3**, 13080–13086.

51 D. M. F. Santos, C. A. C. Sequeira, D. Macciò, A. Saccone and J. L. Figueiredo, *Int. J. Hydrogen Energy*, 2013, **38**, 3137–3145.

52 J. Durst, C. Simon, F. Hasché and H. A. Gasteiger, *J. Electrochem. Soc.*, 2014, **162**, F190–F203.

53 K. S. Exner, I. Sohrabnejad-Eskan and H. Over, *ACS Catal.*, 2018, **8**, 1864–1879.

54 J. K. Nørskov, T. Bligaard, A. Logadottir, J. R. Kitchin, J. G. Chen, S. Pandelov and U. Stimming, *J. Electrochem. Soc.*, 2005, **152**, 23–26.

55 T. F. Jaramillo, K. P. Jørgensen, J. Bonde, J. H. Nielsen, S. Horch and I. Chorkendorff, *Science (80)*, 2007, **317**, 100–102.

Chapter 4

A comprehensive study on HER activities of molybdenum chalcogenide/graphene and their hybrid-nanocomposites

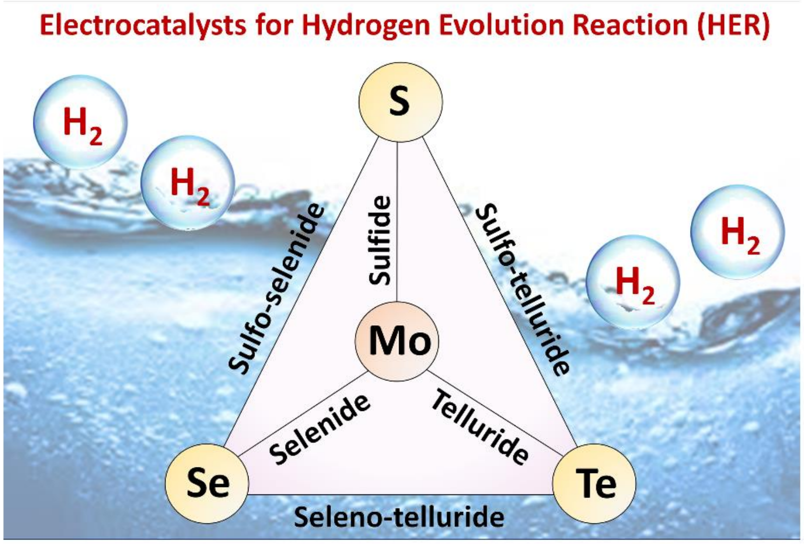

This chapter demonstrates the HER activities of molybdenum chalcogenides and their hybrids.

Abstract

In this work, the molybdenum dichalcogenides (MoX_2, X = S, Se, Te) and their hybrid nanocomposites (MoSSe, MoSeTe, MoSTe, and $Mo(SSeTe)_{0.67}$) were constructed on graphene network through the microwave-assisted heating approach. The as-synthesized materials were employed as working electrodes in a standard three electrode setup to investigate their electrocatalytic properties for hydrogen evolution reaction (HER). The electrochemical measurements revealed that all the materials are highly active and durable for HER with small overpotentials in the range of 127−217 mV and negligible activity loss for 96 hours of constant potential tests. Among all different molybdenum chalcogenide/graphene-nanocomposites, the materials containing tellurium (Te) exhibited better HER activities, which could be resulted due to the presence of metallic phase of $MoTe_2$ in the catalyst structures. Most importantly, hybrid nanocomposites, only except of $Mo(SSeTe)_{0.67}$ on graphene, exhibited improved performance in comparison to the MoX_2 compounds. We believe such improvements reflect the higher intrinsic activity of alloyed catalysts with the hydrogen adsorption free energy closer to thermoneutral.

4.1. Introduction

Transition metal dichalcogenides (TMD) have kindled a tremendous interest since the edges of MoS_2 nanoparticles exhibit a close resemblance to the catalytic center of the hydrogenase enzyme.[1] Especially the two-dimensional (2D) layered TMD compounds with a general formula of MX_2 (M= Mo, W, Cu, Ni, etc., X= S, Se, Te) have been demonstrated to be very promising HER catalysts.[2–6] Nonetheless in the bulk form, these materials provide poor performances because of the low density of active sites and scarce electrical conductivity. During the past several years, various techniques such as defect engineering, interface construction, phase engineering, hydrophilicity tuning, or integration with conductive materials (such as graphene, carbon nanotubes etc.) have been contributed to overcome the intrinsic shortcomings of bulk MX_2.[7–15] In addition to structural engineering, the HER activity of TMDs can be tuned through tailoring their chemical compositions. For example, sulfur in MoS_2 can be partially substituted by Se atom.[16–18] Similarly, any of the chalcogens (S, Se, or Te) can be substituted by any of the other chalcogens (S, Se, or Te), leading to a library of compounds that are promising for HER.[19–21] Inspired by the promising prospects of TMDs on carbon supports towards HER activities,[22–27] we have developed a direct growth strategy to synthesize MoX_2 compounds (MoS_2, $MoSe_2$ and $MoTe_2$) and their hybrid heterostructures (MoSSe, MoSeTe, MoSTe, and $Mo(SSeTe)_{0.67}$) on graphene supports through a simple microwave-assisted heating approach. Such nanocomposites can provide synergetic interactions between TMDs and graphene nanosheets in the kinetic process and electronic modulations. Indeed, the as-prepared compounds showed great potential as low-cost electrocatalysts for hydrogen evolution reaction (HER).

4.2. Experimental details

4.2.1. Materials and reagents

Ammonium tetrathiomolybdate, $(NH_4)_2MoS_4$ was purchased from BeanTown Chemical, Inc. Molybdenum hexacarbonyl, $Mo(CO)_6$ was purchased from Strem Chemicals. Carbon disulfide (CS_2), selenium (Se), tellurium (Te), and polyvinylidene fluoride (PVDF) were acquired from Alfa Aesar. N, N-Dimethylformamide (DMF) was purchased from *Macron Fine Chemicals*™. Graphene was supplied by Magnolia Ridge Inc., and 10 wt.% platinum on carbon (10 wt.% Pt/C) was obtained from Sigma-Aldrich. All chemicals purchased were used as received without further treatment or purification. For electrochemical characterizations, graphite rod (5 mm diameter) was provided by Alfa Aesar, glassy carbon electrode (3 mm diameter) was purchased from CH Instruments, Inc. and silver/silver chloride (Ag/AgCl, 3 M KCl, E^o= +0.197 V vs. RHE) reference electrode was acquired from Hach.

4.2.2. Microwave-initiated synthesis of catalyst samples

To prepare the molybdenum dichalcogenides and their hybrid catalysts on graphene supports, similar method was followed as mentioned in Chapter 2 and Chapter 3. First, the precursors were mixed homogeneously with graphene in a 20 mL scintillation vial using a speed mixer. The mass of the precursors for each of the nanocomposites are described in Table 4.1. Next, the vial containing uniform mixture was subjected to microwave irradiation at a constant power of 1250 W for 90 seconds for each of the mixtures. After the vial cooled down at room temperature, the product was collected from the vial and ground into fine powder.

Table 4.1. The mass of different precursors for the microwave-assisted synthesis of molybdenum dichalcogenides and their hybrids on graphene support.

Samples	**$(NH_4)_2MoS_4$**	**$Mo(CO)_6$**	**CS_2**	**Se powder**	**Te powder**	**Graphene**	**Microwave time**
MoS_2/Gr	20 mg	-	50 µL	-	-	20 mg	90 sec
$MoSe_2$/Gr	-	20 mg	-	35 mg	-		
$MoTe_2$/Gr	-	20 mg	-	-	55 mg		
MoSSe/Gr	20 mg	-	50 µL	17 mg	-		
MoSeTe/Gr	-	20 mg	-	17 mg	27 mg		
MoSTe/Gr	20 mg	-	50 µL	-	27 mg		
$Mo(SSeTe)_{0.67}$/Gr	20 mg	-	50 µL	11 mg	18 mg		

4.2.3. Preparation of working electrodes

To prepare the catalyst coating, a mixture of 100 mg composite and 10 mg PVDF powder were suspended in 5 mL DMF solvent, following by 20 min of probe sonication. The GCE surface (0.07 cm^2) was sequentially polished with 0.3- and 0.05-mm alumina slurries, then rinsed with DI water and acetone. Finally, 20 µL of the suspension was added to the GCE surface and dried in a vacuum dryer at 60°C, which results a mass loading of ~1 mg cm^{-2} for each catalyst sample.

4.2.4. Material characterization techniques

X-ray photoelectron spectroscopy (XPS) was investigated on a Kratos Axis Ultra DLD spectrometer using a monochromatic Al Kα radiation ($h\nu$ = 1486.6 eV) under UHV condition ($<8 \times 10^{-10}$ Torr), to determine the chemical state and surface composition of various elements in the nanocomposites. Moreover, to investigate the phase and crystal structures of as-synthesized materials, the powder X-ray diffraction (XRD) patterns were collected on a Philips X'pert MPD diffractometer with Cu Kα radiation ($\lambda = 1.54056$ Å) at 45 kV and 40 mA.

4.2.5. Electrochemical measurement techniques

Electrochemical experiments were performed with CH Instrument (CHI 760D) in a standard three-electrode system. This setup consists of an active material−coated glassy carbon electrode (GCE) as working electrode with a mass loading of ~1 mg cm^{-2}, Ag/AgCl as reference electrode, and graphite rod as a counter electrode in 0.5 M H_2SO_4 electrolyte. The observed potentials were translated to reversible hydrogen electrode (RHE) based on the equation: $V (vs. RHE) = V (vs. Ag/AgCl) + 0.197 + (0.059 \times pH)$ at room temperature (~ 25°C). The electrocatalytic activities and stability performances were determined by performing iR-corrected linear sweep voltammetry (LSV), Tafel analysis, and the constant potential tests.

4.3. Results and discussion

4.3.1. Materials characterizations

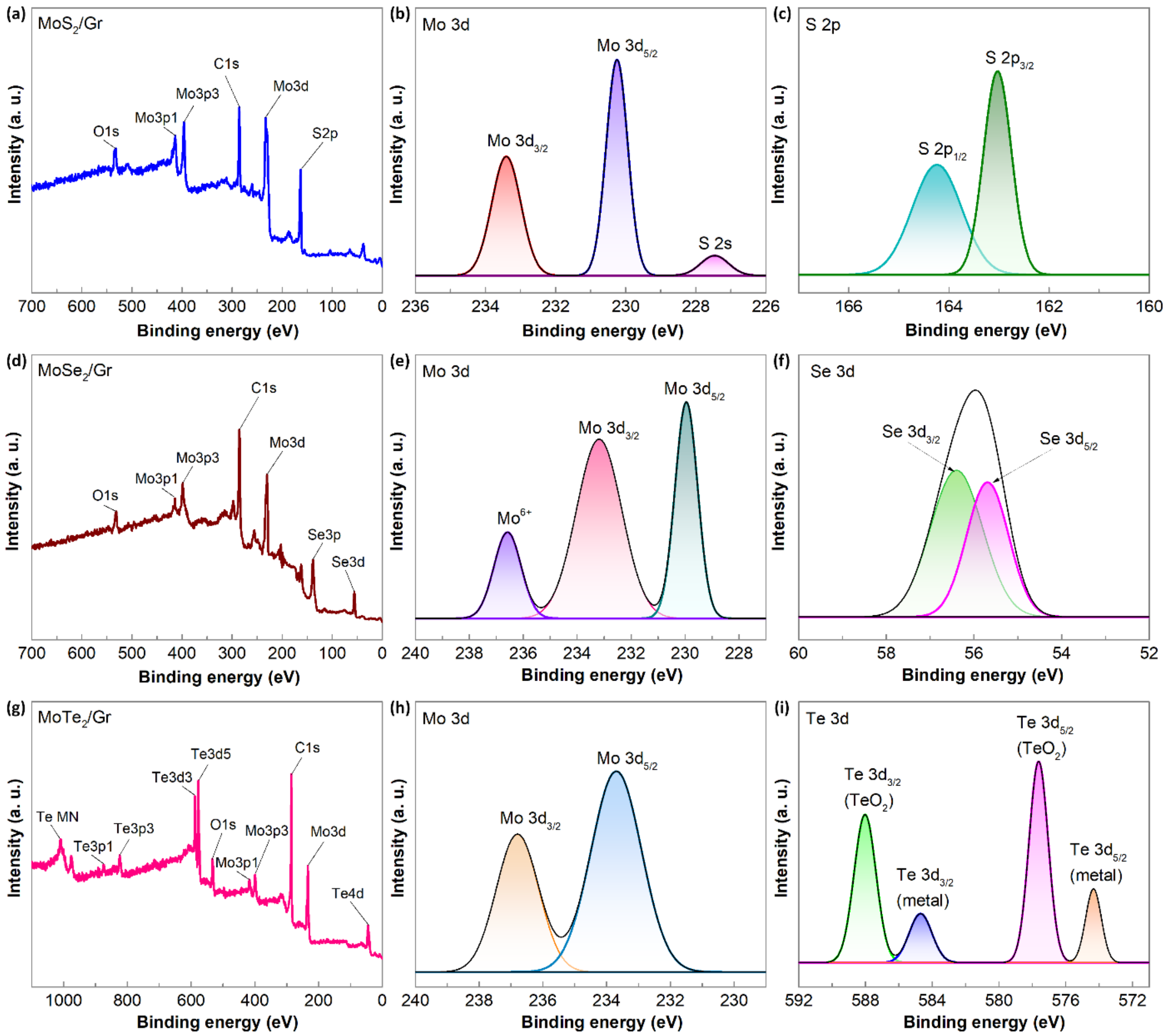

Figure 4.1. (a, d, g) XPS spectra of MoS$_2$/Gr, MoSe$_2$/Gr, and MoTe$_2$/Gr nanocomposites. High resolution XPS spectra of (b, e, h) Mo 3d, (c) S 2p, (f) Se 3d, and (i) Te 3d regions.

The elemental compositions and binding energies in as-produced samples were examined by XPS analysis. The survey spectra of MoS_2/Gr, $MoSe_2$/Gr, and $MoTe_2$/Gr (Figure 4.1a, 4.1d, and 4.1g) show the peaks due to Mo, C, and chalcogens (S or Se or Te), and the signal of O 1s due to air exposure. As displayed in Figure 4.1b, 4.1e, and 4.1h, the XPS spectra of Mo 3d regions are dominated by two peaks corresponding to the Mo $3d_{5/2}$ (~229.1 eV) and Mo $3d_{3/2}$ (~232.3 eV), implying Mo^{4+} features.[28]Additionally, a weak peak at ~226.2 eV is ascribed to S 2s orbital of MoS_2 (Figure 4.1b).[29] Another peak appears at ~235 eV in $MoSe_2$/Gr (Figure 4.1e), which corresponds to oxidized Mo^{6+} (likely MoO_3).[17] In Figure 4.1c, the peaks of S $2p_{3/2}$ and S $2p_{1/2}$ appear at ~162.7 and ~164.1 eV, which confirms the presence of S^{2-} for MoS_2.[30] The features at ~55.4 and ~56.2 eV (Figure 4.1f) correspond to Se $3d_{5/2}$ and Se $3d_{3/2}$ levels, respectively.[16] Furthermore, the XPS peaks at ~574.3 and ~584.6 eV (Figure 4.1i) are attributed to Te $3d_{5/2}$ and Te $3d_{3/2}$, respectively.[26] Two additional peaks at ~577.3 and ~588.0 eV are ascribed to TeO_2, owing to the partial oxidation due to the air exposure.[17] These XPS results clearly reveal that the ratio of Mo and chalcogen atoms (S, Se, and Te) perfectly match with the stoichiometry having a value of 1: 2 for Mo: S or Se or Te.

The survey spectrum of MoSSe/Gr sample is displayed in Figure 4.2a, which shows the XPS peaks for Mo, S, Se, C, and O. The binding energies of Mo $3d_{5/2}$ and Mo $3d_{3/2}$ are ~229.5 and ~232.7 eV (Figure 4.2b), which appears as a positive shift of about 0.4 eV relative to those of bare MoS_2 and $MoSe_2$. It suggests an efficient electron transfer in between MoS_2 and $MoSe_2$ under the unique heterojunction effect.[31,32] From Figure 4.2c, one can notice that the peaks of S $2p_{3/2}$ and S $2p_{1/2}$ appeared at ~162.3 and ~163.6 eV, confirming the presence of S^{2-}. Figure 4.2d shows the Se 3d spectrum, where the Se 3d peak can be resolved into two well-defined peaks at ~55.1 and ~56.0 eV. These peaks are associated with the $3d_{5/2}$ and $3d_{3/2}$ orbitals of the Se element, indicating the −2 valence of Se. There are slight shifts in S 2p and Se 3d peaks, which also support the charge transfer between MoS_2 and $MoSe_2$.[32,33]

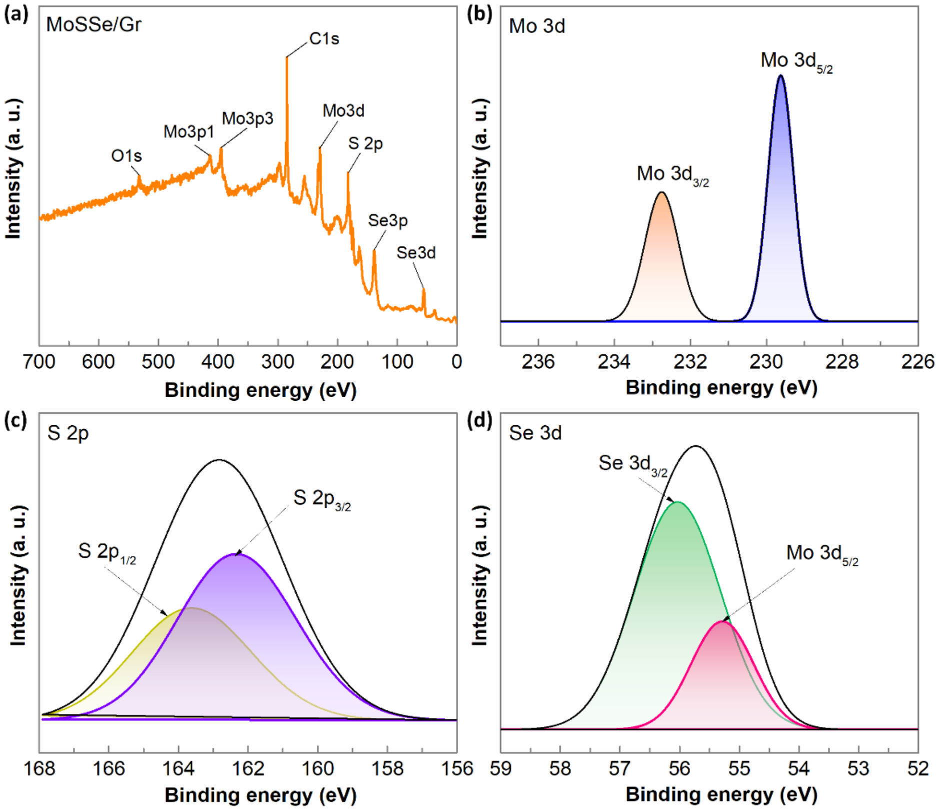

Figure 4.2. (a) XPS survey spectrum of MoSSe/Gr nanocomposite. High resolution XPS spectra of (b) Mo 3d, (c) S 2p, and (d) Se 3d regions.

Similarly, the XPS survey and the high resolution XPS (HRXPS) spectra were obtained for MoSeTe/Gr (Figure 4.3) and MoSTe/Gr (Figure 4.4) nanocomposites. The elemental compositions are summarized in Table 4.2, which clearly suggests the successful synthesis of molybdenum dichalcogenides and their nanohybrids with acceptable stoichiometry.

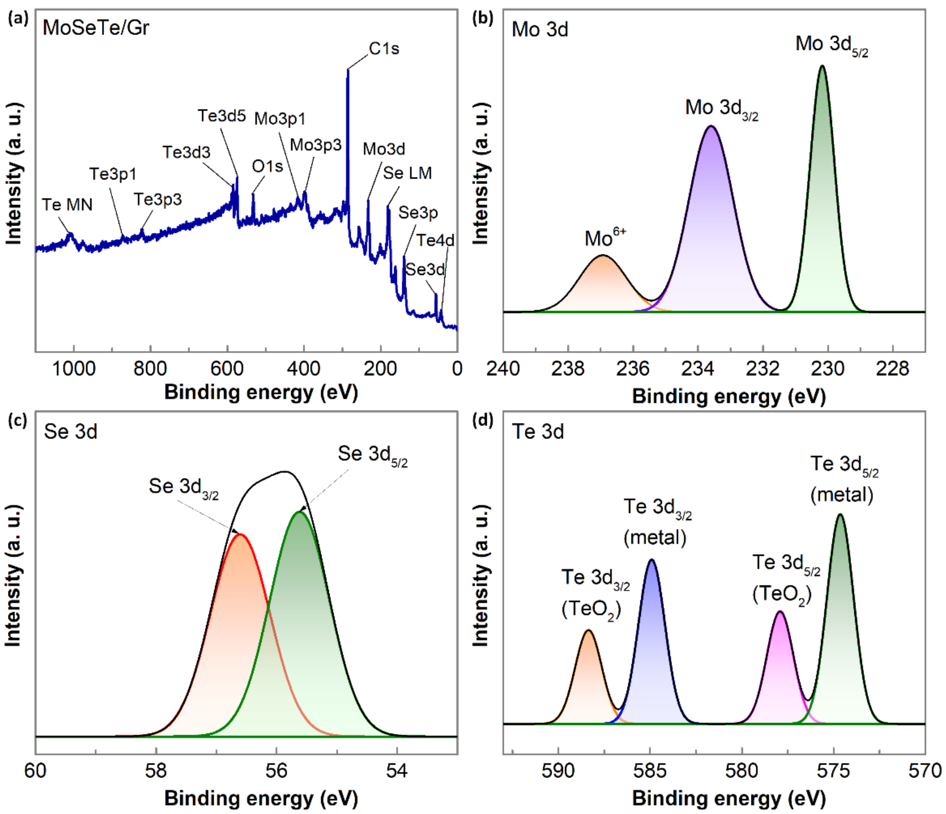

Figure 4.3. (a) XPS survey spectrum of MoSeTe/Gr nanocomposite. High resolution XPS spectra of (b) Mo 3d, (c) Se 3d, and (d) Te 3d regions.

Table 4.2. The weight % and atomic % of all elements (Mo, S, Se, Te, O, and C) in as-produced catalyst samples from the obtained XPS results.

Samples	**Mo**		**S**		**Se**		**Te**		**O**		**C**	
	Wt.%	**At.%**	**Wt.%**	**At.%**	**Wt.%**	**At.%**	**Wt.%**	**At.%**	**Wt.%**	**At.%**	**Wt.%**	**At.%**
MoS$_2$/Gr	49.42	16.76	30.78	31.24	-	-	-	-	2.75	5.6	17.05	46.24
MoSe$_2$/Gr	28.69	10.91	-	-	48.52	22.42	-	-	3.46	7.9	19.33	58.77
MoTe$_2$/Gr	23.41	10.75	-	-	-	-	56.73	19.59	3.57	9.82	16.30	59.84
MoSSe/Gr	28.8	8.04	10.13	8.46	27.44	9.31	-	-	1.57	2.62	32.06	71.57
MoSeTe/Gr	21.17	7.34	-	-	20.75	8.74	29.69	7.74	3.66	7.6	24.74	68.58
MoSTe/Gr	31.66	15.23	11.33	16.31	-	-	42.99	15.55	1.07	3.1	12.95	49.81
Mo(SSeTe)$_{0.67}$/Gr	30.65	12.59	7.30	8.97	16.45	8.21	26.16	8.08	2.07	5.09	17.37	57.06

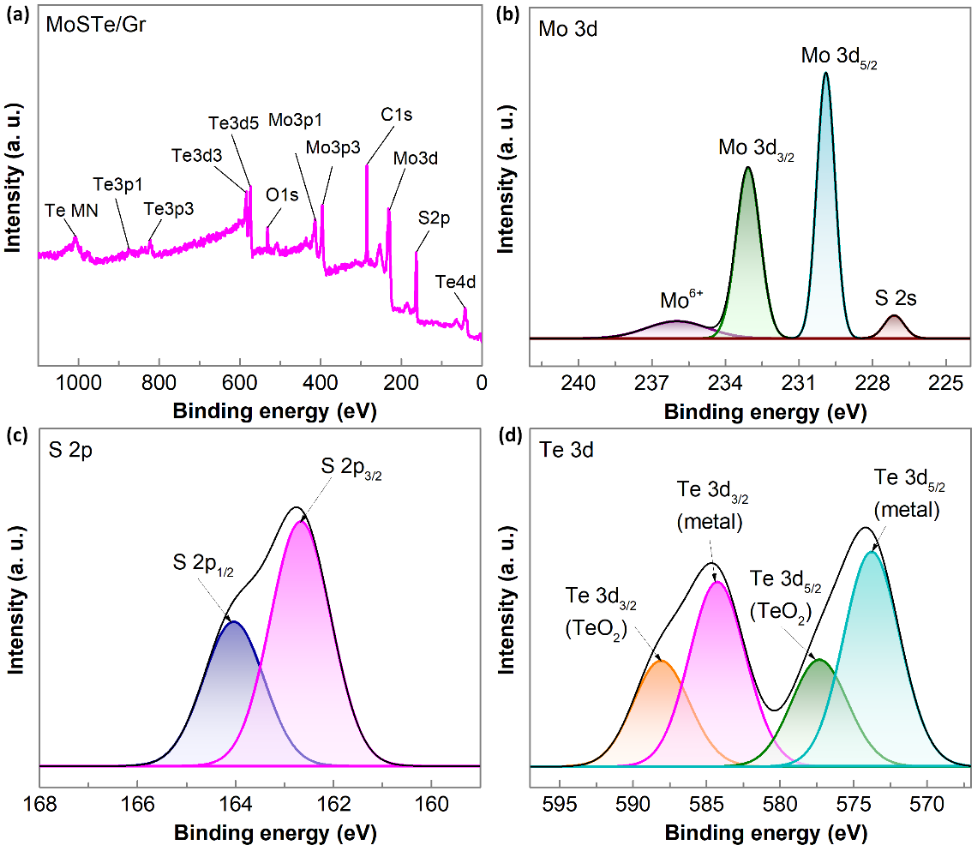

Figure 4.4. (a) XPS survey spectrum of MoSTe/Gr nanocomposite. High resolution XPS spectra of (b) Mo 3d, (c) S 2p, and (d) Te 3d regions.

In the case of hybrid $Mo(SSeTe)_{0.67}/Gr$, the survey spectrum (Figure 4.5a) identifies the characteristic XPS peaks for Mo, S, Se, Te, O, and C atoms. As shown in Figure 4.5b, two peaks corresponding to Mo $3d_{5/2}$ and Mo $3d_{3/2}$ levels are located at ~229.4 and ~232.6 eV, which are assigned to 2H-MoS_2, 2H-$MoSe_2$, and 2H-$MoTe_2$, further verifying the formation of 2H-phase.[34,35] Similar to the previous results, the HRXPS spectra of S 2p, Se 3d, and Te 3d regions show all the characteristic peaks for corresponding elements, thus confirming the successful synthesis of desired heterostructures of molybdenum dichalcogenides on graphene supports.

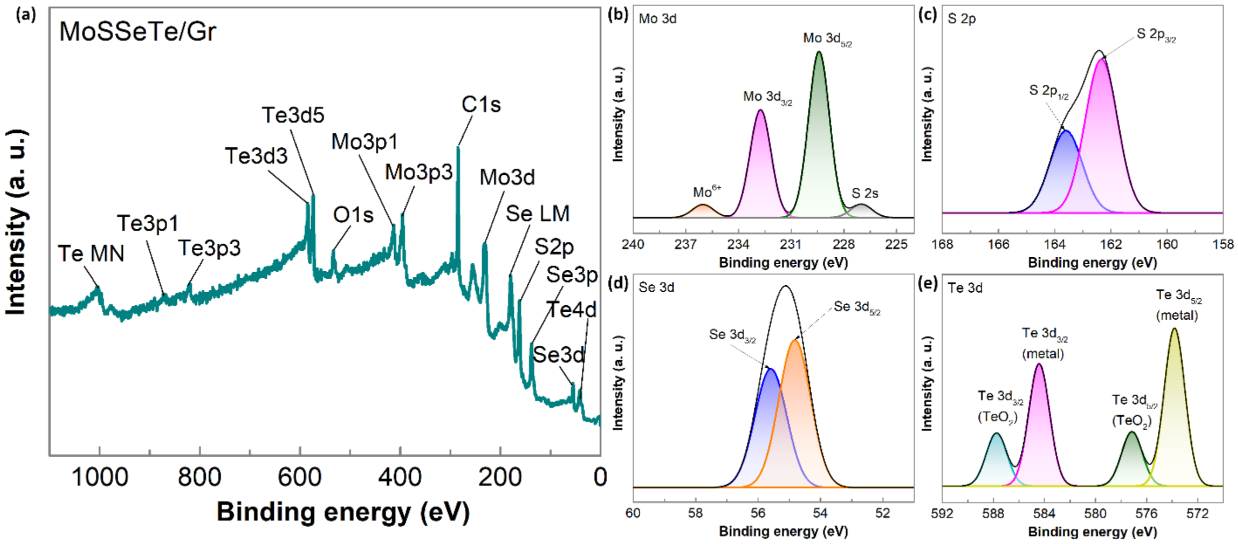

Figure 4.5. (a) XPS survey spectrum of Mo(SSeTe)$_{0.67}$/Gr nanocomposite. High resolution XPS spectra of (b) Mo 3d, (c) S 2p, (d) Se 3d, and (e) Te 3d regions.

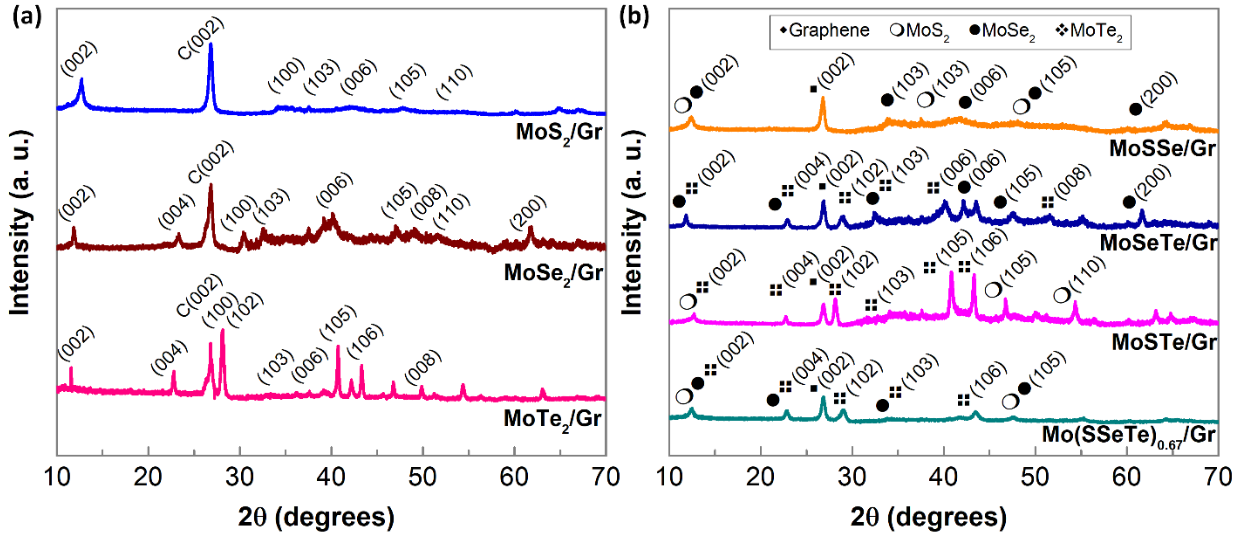

Figure 4.6. (a) XRD patterns of molybdenum dichalcogenides with graphene nanocomposites (i.e., MoS$_2$/Gr, MoSe$_2$/Gr, and MoTe$_2$/Gr). (b) XRD patterns of hybrid nanocomposites (i.e., MoSSe/Gr, MoSeTe/Gr, MoSTe/Gr, and Mo(SSeTe)$_{0.67}$/Gr).

The phase information of hybrid samples was characterized by XRD analysis. As shown in Figure 4.6, the signals from graphene are observed at ~26.0° in all catalyst samples for the plane of C(002).[30] The other diffraction peaks in Figure 4.6a correspond to hexagonal 2H–MoS_2 (JCPDS No. 37-1492),[36] 2H–$MoSe_2$ (JCPDS No. 29-0914),[37] and 2H–$MoTe_2$ (JCPDS No. 15-0658)[38] structures. Similarly, the XRD patterns of other hybrid nanocomposites (Figure 4.6b) reveal the successful synthesis of desired compounds through microwave-assisted heating.

Moreover, from the atomic% results (Table 4.2), it is found that the atomic ratio of MoX_2/Gr (X= S, Se, and Te) samples satisfy the stoichiometry of 1: 2 ratio. Besides, the hybrid nanocomposites of MoXY/Gr (X, Y= S and/or Se and/or Te) follow the stoichiometry of 1: 1: 1 ratio. Similarly, for the sample of $Mo(SSeTe)_{0.67}$/Gr the atomic ratio of Mo: S: Se: Te resulted as 1: 0.67: 0.67: 0.67, which also satisfies the stoichiometry (1:2) of the metal dichalcogenides.

4.3.2. Investigations of HER Activities

The electrocatalytic HER activities of as-synthesized catalyst samples were investigated by LSVs in 0.5 M H_2SO_4 electrolyte. The *iR* corrected−LSVs are displayed in Figure 4.7a, where $MoTe_2$/Gr displays the best catalytic behavior among all the MoX_2/Gr (X = S, Se, and Te) samples with the smallest overpotential (η) of 150.2 mV (Figure 4.7b) to reach the cathodic current density of 10 mA cm^{-2}. The order of HER activity based on η is found to be $MoTe_2$/Gr > MoS_2/Gr > $MoSe_2$/Gr. It clearly indicates, the higher electrical conductivity of $MoTe_2$ facilitates the faster electron transfer process. Furthermore, the Tafel diagrams were derived from LSVs by fitting the linear sections to the Tafel equation ($\eta = b \log i + a$), where η is overpotential, b is Tafel slope, i represents the cathodic current density, and a is a constant.[39] In general, the HER takes place through two consecutive steps: an adsorption step (Volmer, $H^+ + e^- \rightarrow H_{ads}$, 120 mV dec^{-1}), following by a reduction step (Heyrovsky, $H^+ + H_{ads} + e^- \rightarrow H_2$, 40 mV dec^{-1} or Tafel, $2H_{ads} \rightarrow H_2$, 30 mV dec^{-1}).[39] Tafel slope identifies the required overpotential to increase the reaction rate by factor of ten, therefore it is noticeable that the smaller Tafel slope favors HER activities. From Figure 4.7c, although $MoTe_2$/Gr shows the smallest overpotential, it shows higher Tafel slope of 49.8 mV dec^{-1} in comparison with other samples (38.5 mV dec^{-1} for MoS_2/Gr and 44.3 mV dec^{-1} for $MoSe_2$/Gr), which can be resulted due to the presence of TeO_2 in this catalyst sample.

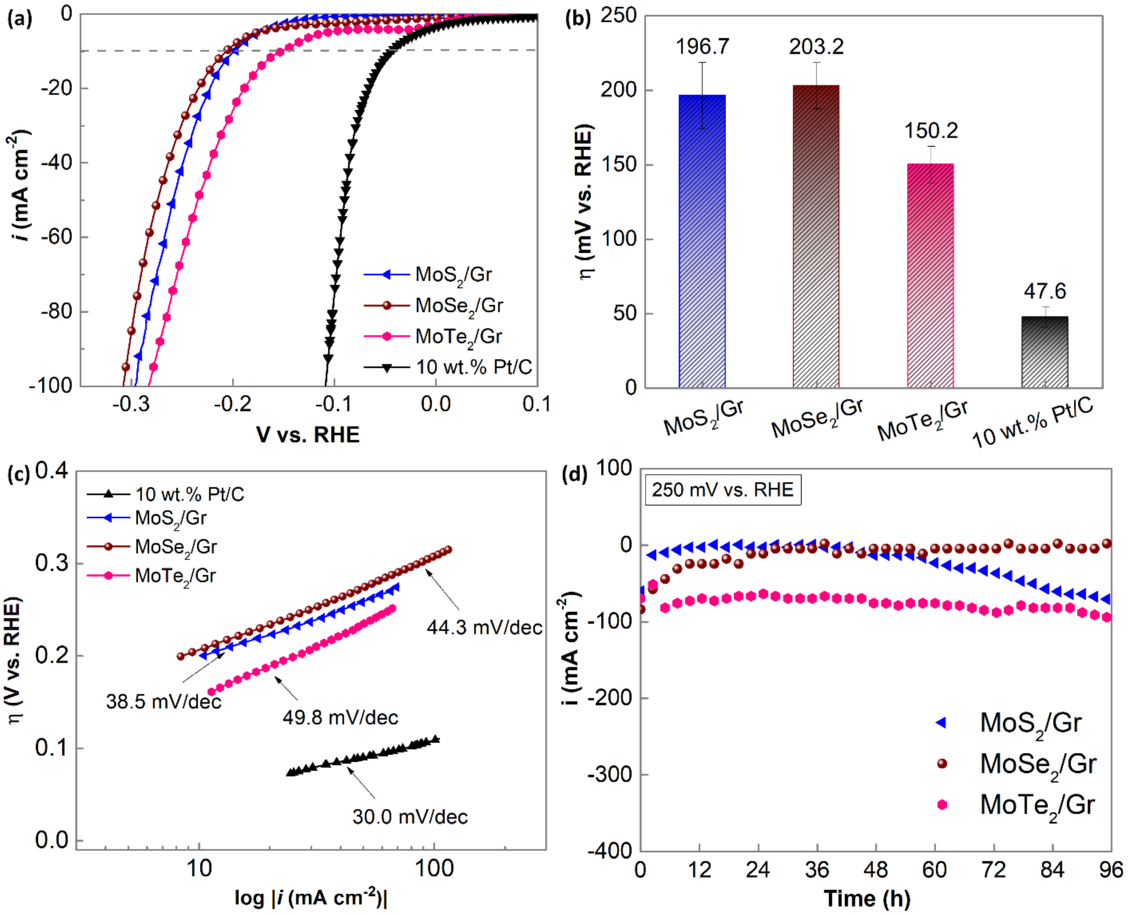

Figure 4.7. (a) LSVs at a scan rate of 2 mV s^{-1} for MoS_2/Gr, $MoSe_2$/Gr, $MoTe_2$/Gr, and 10 wt.% Pt/C catalysts. (b) Corresponding overpotential values. (c) Corresponding Tafel plots. (d) Constant potential stability tests for 96 hours at 250 mV *vs.* RHE.

Additionally, a chronoamperometric curve was obtained at the η of 250 mV, which is presented in Figure 4.7d. These constant potential tests reveal almost no degradation in the cathodic current density for 96 h of electrolysis. Moreover, $MoTe_2$/Gr shows the best stability results maintaining the highest current density of around −90 mA cm^{-2}. These remarkable stability results can be attributed to the compositional and structural stabilities of MoS_2/Gr, $MoSe_2$/Gr, and $MoTe_2$/Gr nanosheet structures supported by strong graphene network.

The HER activities of hybrid nanocomposites of MoXY/Gr (X, Y= S and/or Se and/or Te) and $Mo(SSeTe)_{0.67}$/Gr were further compared, as shown in Figure 4.8a. Based on the overpotential values (Figure 4.8b), the order of HER performance is revealed as MoSTe/Gr > MoSeTe/Gr > MoSSe/Gr > $Mo(SSeTe)_{0.67}$/Gr, which clearly indicates the presence of Te improves the electron transfer rate due to its higher electrical conductivity. For $Mo(SSeTe)_{0.67}$/Gr, although it consists of all the chalcogen atoms (S, Se, and Te), the HER performance is poor. Further studies are required to understand the reason behind this poor electrocatalytic performance. Based on the LSV curves, the Tafel analysis was performed. As shown in Figure 4.8c, MoSTe/Gr exhibited the lowest Tafel slope of 39.2 mV dec^{-1}, which is also very close to the value of commercial Pt/C catalyst (30.0 mV dec^{-1}). Moreover, all these hybrid catalysts revealed very good stability performance for 96 h of constant potential test at an overpotential of 250 mV, as displayed in Figure 4.8d. All the hybrid catalysts showed stable behaviors with slight decrease in HER performance by dropping the cathodic current density to lower value, where the MoSTe/Gr catalyst displayed the best performance with a slight decrease in current density from −160 to −100 mA cm^{-2}.

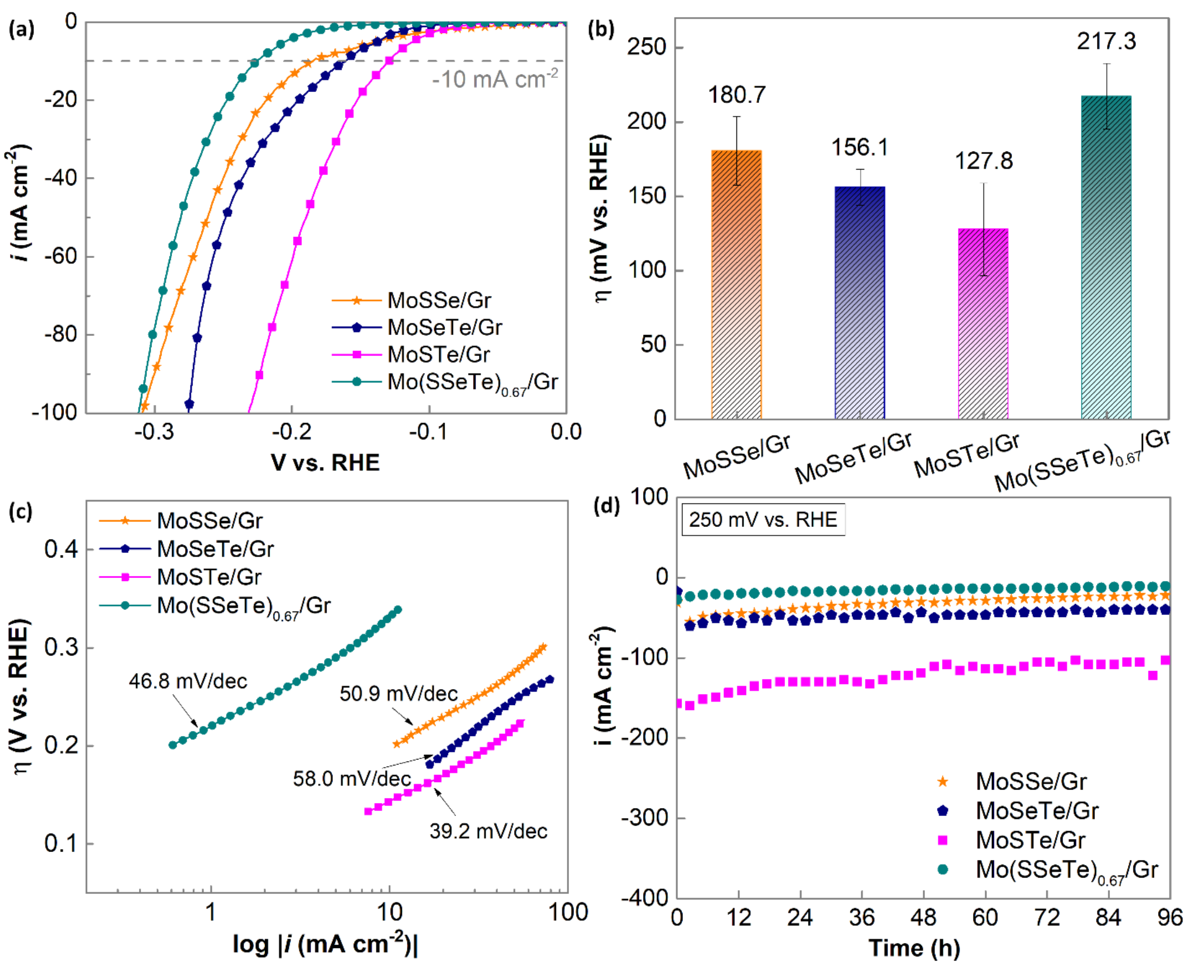

Figure 4.8. (a) LSVs at a scan rate of 2 mV s^{-1} for MoSSe/Gr, MoSeTe/Gr, MoSTe/Gr, and Mo(SSeTe)$_{0.67}$/Gr catalysts. (b) Corresponding overpotential values. (c) Corresponding Tafel plots. (d) Constant potential stability tests for 96 hours at 250 mV *vs.* RHE.

In addition, the exchange current densities (i_0) were measured following the Tafel slope extrapolation method,[39] as displayed in Figure 4.9. In comparison with 10 wt.% Pt/C catalyst, three of the molybdenum dichalcogenide/graphene nanocomposites with the highest i_0 values are MoSTe/Gr, MoSeTe/Gr, and $MoTe_2$/Gr. These results clearly indicate the better HER performance of as-synthesized catalyst samples that contain Te atoms.

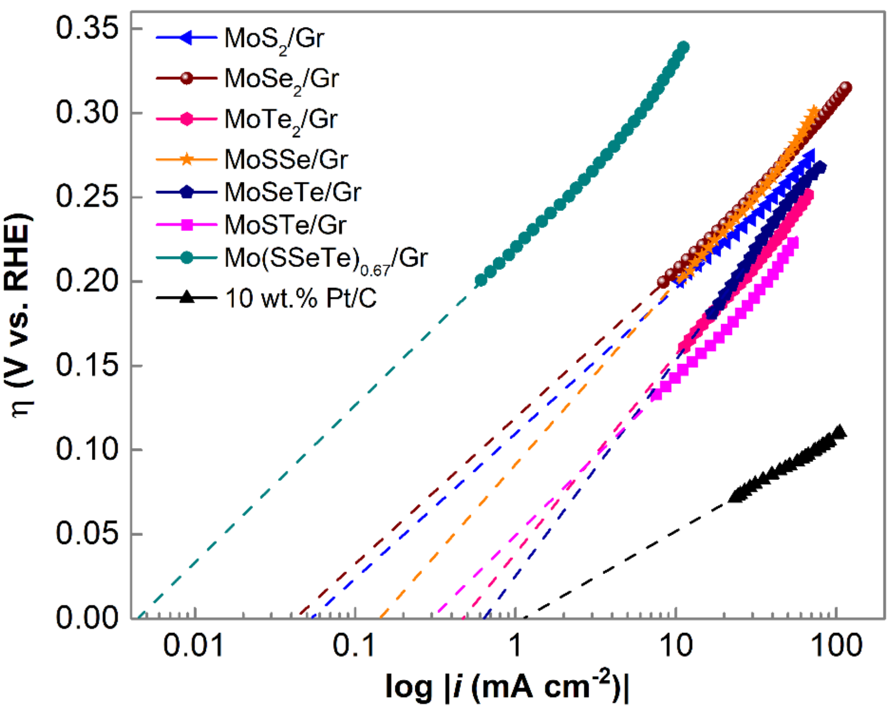

Figure 4.9. Measurements of exchange current densities for all different MC-based catalysts and for the 10 wt.% Pt/C catalyst.

Furthermore, all the major parameters (overpotential, Tafel slope, and exchange current density) for electrocatalytic performance of as-synthesized nanocomposites are summarized in Figure 4.10. Although, chemical formula appears to be similar for all the molybdenum dichalcogenides but structurally they are slightly different from each other. These structural differences give rise to variations in their electrical transport properties.[40] An important feature of tellurides that distinguishes it from the sulfides and selenides is the large atomic number of Te, which results exceptionality in its crystal structure, electronic configuration, and physicochemical properties.[40] Therefore, the catalyst samples containing Te, only except $Mo(SSeTe)_{0.67}/Gr$, showed very promising HER activities to generate hydrogen from water splitting.

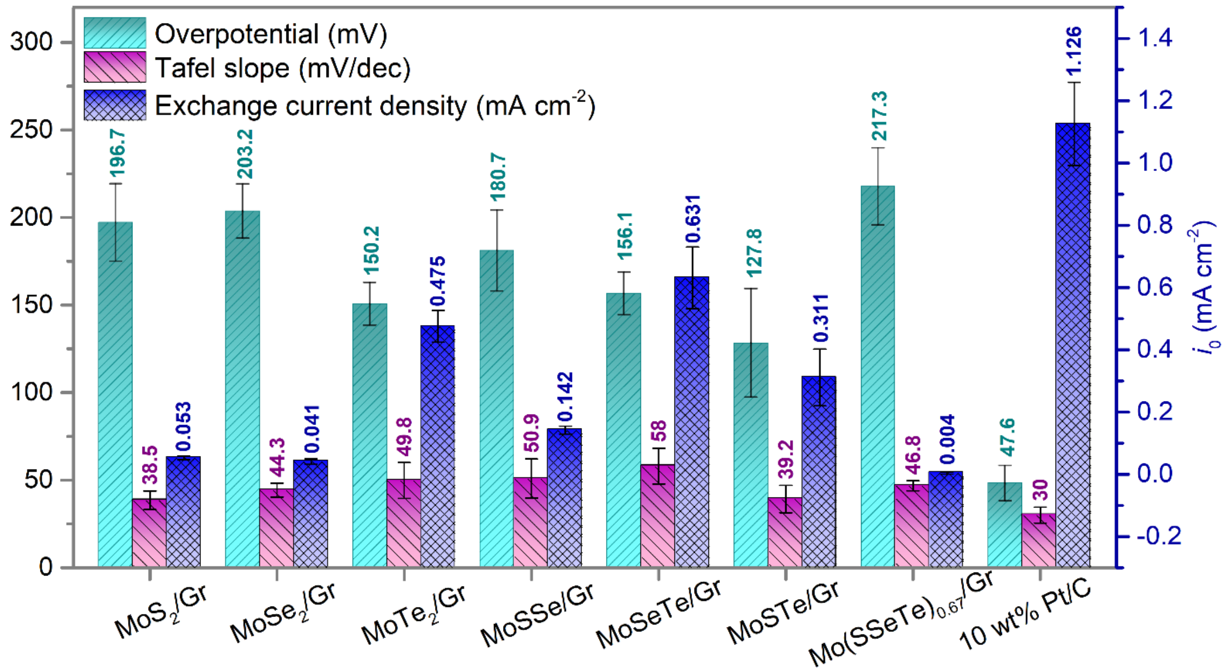

Figure 4.10. Bar graphs displaying the three major parameters (overpotential, Tafel slope, and exchange current density) of MC-based HER catalysts.

4.4. Summary

In this study, the compounds of three classes namely sulfides, selenides and tellurides of transition metal (Mo) were successfully synthesized on graphene supports with compositions of MoS_2/Gr, $MoSe_2$/Gr, $MoTe_2$/Gr, MoSSe/Gr, MoSeTe/Gr, MoTe/Gr, and $Mo(SSeTe)_{0.67}$/Gr through a simple, ultrafast (90 s), and energy-efficient microwave-assisted solid-state technique. The as-produced nanocomposites have high activity and durability for HER electrocatalysis with small overpotentials in the range of 127−217 mV and negligible activity loss for long-term hydrogen generation at constant potential of 250 mV. Among them, $MoTe_2$/Gr, MoSTe/Gr, and MoSeTe/Gr demonstrates the improved performance in comparison to other nanocomposites. We believe these results come from their higher intrinsic activities due to the existence of Te atoms. In future study, the influence of different chemical compositions of molybdenum dichalcogenides and their hybrids can be explored on HER activities.

4.5. References

1 B. Hinnemann, P. G. Moses, J. Bonde, K. P. Jørgensen, J. H. Nielsen, S. Horch, I. Chorkendorff and J. K. Nørskov, *J. Am. Chem. Soc.*, 2005, **127**, 5308–5309.

2 A. Eftekhari, *Int. J. Hydrogen Energy*, 2017, **42**, 11053–11077.

3 K. Zhang, Y. Li, S. Deng, S. Shen, Y. Zhang, G. Pan, Q. Xiong, Q. Liu, X. Xia, X. Wang and J. Tu, *ChemElectroChem*, 2019, **6**, 3530–3548.

4 Q. Ding, B. Song, P. Xu and S. Jin, *Chem*, 2016, **1**, 699–726.

5 J. C. McGlynn, T. Dankwort, L. Kienle, N. A. G. Bandeira, J. P. Fraser, E. K. Gibson, I. Cascallana-Matías, K. Kamarás, M. D. Symes, H. N. Miras and A. Y. Ganin, *Nat. Commun.*, **10**, 4916 (2019).

6 K. S. Bhat and H. S. Nagaraja, *Int. J. Hydrogen Energy*, 2019, **44**, 17878–17886.

7 J. Xie, H. Zhang, S. Li, R. Wang, X. Sun, M. Zhou, J. Zhou, X. W. Lou and Y. Xie, *Adv. Mater.*, 2013, **25**, 5807–5813.

8 C. Du, H. Huang, J. Jian, Y. Wu, M. Shang and W. Song, *Appl. Catal. A Gen.*, 2017, **538**, 1–8.

9 Y. Ouyang, C. Ling, Q. Chen, Z. Wang, L. Shi and J. Wang, *Chem. Mater.*, 2016, **28**, 4390–4396.

10 G. Ye, Y. Gong, J. Lin, B. Li, Y. He, S. T. Pantelides, W. Zhou, R. Vajtai and P. M. Ajayan, *Nano Lett.*, 2016, **16**, 1097–1103.

11 S. J. Deng, F. Yang, Q. H. Zhang, Y. Zhong, Y. X. Zeng, S. W. Lin, X. L. Wang, X. H. Lu, C. Z. Wang, L. Gu, X. H. Xia and J. P. Tu, *Adv. Mater.*, 2018, **30**, 1–9.

12 M. A. Lukowski, A. S. Daniel, F. Meng, A. Forticaux, L. Li and S. Jin, *J. Am. Chem. Soc.*, 2013, **135**, 10274–10277.

13 S. Deng, Y. Zhong, Y. Zeng, Y. Wang, Z. Yao, F. Yang, S. Lin, X. Wang, X. Lu, X. Xia and J. Tu, *Adv. Mater.*, 2017, **29**, 1700748.

14 H. Liang, Z. Cao, F. Ming, W. Zhang, D. H. Anjum, Y. Cui, L. Cavallo and H. N. Alshareef, *Nano Lett.*, 2019, **19**, 3199–3206.

15 F. Carraro, L. Calvillo, M. Cattelan, M. Favaro, M. Righetto, S. Nappini, I. Píš, V. Celorrio, D. J. Fermín, A. Martucci, S. Agnoli and G. Granozzi, *ACS Appl. Mater. Interfaces*, 2015, **7**, 25685–25692.

16 S. Li, W. Zang, X. Liu, S. J. Pennycook, Z. Kou, C. Yang, C. Guan and J. Wang, *Chem. Eng. J.*, 2019, **359**, 1419–1426.

17 T. Kosmala, H. Coy Diaz, H. P. Komsa, Y. Ma, A. V. Krasheninnikov, M. Batzill and S. Agnoli, *Adv. Energy Mater.*, 2018, **8**, 1–8.

18 Q. Gong, L. Cheng, C. Liu, M. Zhang, Q. Feng, H. Ye, M. Zeng, L. Xie, Z. Liu and Y. Li, *ACS Catal.*, 2015, **5**, 2213–2219.

19 Q. Wang, Y. Huang, L. Huang, Y. Wu and S. Ren, *J. Phys. Chem. C*, 2020, **124**, 26793–26800.

20 Y. Pan, F. Zheng, X. Wang, H. Qin, E. Liu, J. Sha, N. Zhao, P. Zhang and L. Ma, *J. Catal.*, 2020, **382**, 204–211.

21 D. Vikraman, S. Hussain, I. Rabani, A. Feroze, M. Ali, Y.-S. Seo, S.-H. Chun, J. Jung and H.-S. Kim, *Nano Energy*, 2021, **87**, 106161.

22 N. M. Julkapli and S. Bagheri, *Int. J. Hydrogen Energy*, 2015, **40**, 948–979.

23 Y. Guo, R. Wang, X. Xu, Y. Shang and B. Gao, *Electrochim. Acta*, 2018, **273**, 402–411.

24 X. Liu, J. Z. Zhang, K. J. Huang and P. Hao, *Chem. Eng. J.*, 2016, **302**, 437–445.

25 X. Wang, Y. Chen, B. Zheng, F. Qi, J. He, P. Li and W. Zhang, *Electrochim. Acta*, 2016,

222, 1293–1299.

26 S. Sarwar, A. Ali, Z. Liu, J. Li, S. Uprety, H. Lee, R. Wang, M. Park, M. J. Bozack, A. J. Adamczyk and X. Zhang, *J. Colloid Interface Sci.*, 2021, **581**, 847–859.

27 Y. Zhou, L. Jia, Q. Feng, T. Wang, X. Li and C. Wang, *Electrochim. Acta*, 2017, **229**, 121–128.

28 X. Zhao, J. Sui, F. Li, H. Fang, H. Wang, J. Li, W. Cai and G. Cao, *Nanoscale*, 2016, **8**, 17902–17910.

29 J. Si, H. Chen, C. Lei, Y. Suo, B. Yang, Z. Zhang, Z. Li, L. Lei, J. Chen and Y. Hou, *Nanoscale*, 2019, **11**, 16200–16207.

30 S. Sarwar, A. Nautiyal, J. Cook, Y. Yuan, J. Li, S. Uprety, R. Shahbazian-Yassar, R. Wang, M. Park, M. J. Bozack and X. Zhang, *Sci. China Mater.*, 2020, **63**, 62–74.

31 X. Zhou, Y. Liu, H. Ju, B. Pan, J. Zhu, T. Ding, C. Wang and Q. Yang, *Chem. Mater.*, 2016, **28**, 1838–1846.

32 J. Yang, J. Zhu, J. Xu, C. Zhang and T. Liu, *ACS Appl. Mater. Interfaces*, 2017, **9**, 44550–44559.

33 Y. Guo, L. Gan, C. Shang, E. Wang and J. Wang, *Adv. Funct. Mater.*, 2017, **27**, 1–7.

34 Q. D. Truong, M. Kempaiah Devaraju, Y. Nakayasu, N. Tamura, Y. Sasaki, T. Tomai and I. Honma, *ACS Omega*, 2017, **2**, 2360–2367.

35 S. Vishwanath, A. Sundar, X. Liu, A. Azcatl, E. Lochocki, A. R. Woll, S. Rouvimov, W. S. Hwang, N. Lu, X. Peng, H. H. Lien, J. Weisenberger, S. McDonnell, M. J. Kim, M. Dobrowolska, J. K. Furdyna, K. Shen, R. M. Wallace, D. Jena and H. G. Xing, *J. Cryst. Growth*, 2018, **482**, 61–69.

36 V. Shokhen, Y. Miroshnikov, G. Gershinsky, N. Gotlib, C. Stern, D. Naveh and D. Zitoun, *Sci. Rep.*, 2017, **7**, 1–11.

37 D. Gao, B. Xia, C. Zhu, Y. Du, P. Xi, D. Xue, J. Ding and J. Wang, *J. Mater. Chem. A*,

2018, **6**, 510–515.

38 Z. Wang, W. Wang, Y. Yang, W. Li, L. Feng, J. Zhang, L. Wu and G. Zeng, *Int. J. Photoenergy*, 2014, 956083.

39 A. P. Murthy, J. Theerthagiri and J. Madhavan, *J. Phys. Chem. C*, 2018, **122**, 23943–23949.

40 S. Altaf, A. Haider, S. Naz, A. Ul-Hamid, J. Haider, M. Imran, A. Shahzadi, M. Naz, H. Ajaz and M. Ikram, *Nanoscale Res. Lett.*, **15**, 144 (2020).

Chapter 5

Enhancement of hydrogen evolution reaction activity using metal−rich molybdenum sulfotelluride with graphene support

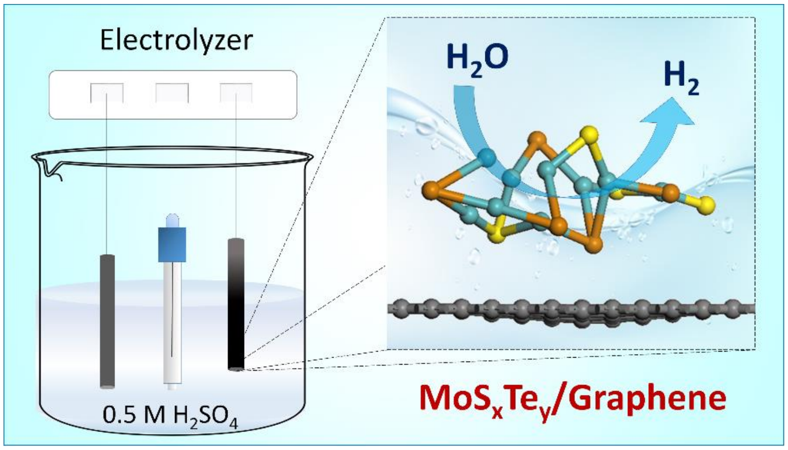

This chapter demonstrates the study of enhanced HER activities for metal-rich nanocomposites.

Abstract

‘Green hydrogen’ can be one of the promising energy technologies in near future. Therefore, the importance of discovering the efficient electrocatalysts for hydrogen generation can never be refuted. The present work demonstrates a facile, ultrafast (60 sec) microwave-assisted synthesis approach to develop an electrocatalyst of molybdenum sulfotelluride on graphene support, which is denoted as MoS_xTe_y/Gr. The abundant interfaces in hybrid nanostructure of MoS_xTe_y/Gr enable more exposed active sites for electrochemical reaction, facilitating the ion and charge transport activities. Among the resultant nanocomposites with different elemental ratios of Mo, S and Te, the $MoS_{0.46}Te_{0.58}$/Gr exhibits the best hydrogen evolution property with a lower overpotential of 62.2 mV at 10 mA cm^{-2}, a small Tafel slope of 61.1 mV dec^{-1}, and long−term stability in 0.5 M H_2SO_4 electrolyte. Moreover, using the tool of periodic plane-wave density functional theory (DFT) has been used to elucidate hydrogen binding energetics on various molybdenum sulfotelluride (stoichiometric and non-stoichiometric molybdenum-rich) and graphene nanocomposite systems. According to the computational results, high-performing catalytically active sites are found to be comprised of primarily exposed Mo atoms, thus showing Mo enrichment as a potential method for electrocatalyst engineering. Furthermore, in a volcano plot constructed with both computational and experimental values, the position of the $MoS_{0.46}Te_{0.58}$/Gr nanocomposite is found to be close to the apex with near thermoneutral catalytic activity.

5.1. Introduction

Hydrogen is an excellent storage solution for the intermittent renewable energy resources. One of the effective strategies is to utilize the electricity from renewable sources to split water into hydrogen and oxygen.[1–3] Thus, the extra electricity generated from renewables can be stored as a form of useful hydrogen energy and while required this hydrogen can be used in fuel cell or in chemical industries. During this water electrolysis, the negative electrode (also known as cathode) undergoes with the hydrogen evolution reaction (HER). However, the efficiency of water-splitting reaction is very low, mainly due to the high overpotential (the difference between theoretical potential and actual potential of an electrochemical reaction). In this regard, the electrocatalysts are critical as cathode materials to promoting the HER kinetics and make the process energy-efficient by reducing overpotential.[4,5] In convention, platinum (Pt) and Pt-group metals are well recognized as highly efficient HER catalysts. Nevertheless, their high cost and lack of resource prevent their widespread industrial applications.[6–8] In purpose to establish a cost-effective production of green hydrogen, there is no alternative than replacing the expensive Pt-electrodes. As a result, last couple of decades have witnessed a fast-paced expansion of noble-metal-free HER electrocatalysts, including transition-metal chalcogenides (TMCs)[9–12] phosphides[13,14], carbides[15,16], etc., considering their unique properties of driving good electrocatalytic performance with low cost and natural abundance. To achieve better catalytic activities of TMC-based catalysts, structural engineering has been robustly practiced by many researchers. Numerous techniques have already been developed, such as increasing the number of active sites by generating different nanostructured morphologies, by hybridizing with highly conductive materials such as graphene, reduced graphene oxide (rGO), carbon nanotubes (CNTs), or conducting polymers (polypyrrole, polyaniline, etc.), and by introducing dopants, defects, strains and vacancies through various surface modifications.[17–24] In addition, the HER activity of metal chalcogenides can be tuned by partially substituting one chalcogen (S, Se, or Te) with another chalcogen (S, Se or Te), leading to a new type of material with broken symmetry along the Z direction, thus improving the electrocatalytic performances in HER.[25–29] For instance, J. Zhang et al. has observed significantly improved HER performance in a single-layer SeMoS Janus structure compared to both MoS_2 and $MoSe_2$.[30] Similarly, in another study, T. Kosmala has demonstrated better HER results from molybdenum selenotellurides than $MoSe_2$ and $MoTe_2$.[28] Therefore, the doping at anion (chalcogen) sites of TMC compounds has the high potential for inventing new materials with enhanced electrocatalytic properties. Although, the coupling of metal chalcogenides with conducting supports (such as graphene, rGO, CNT, etc.) are essential to prevent the easy aggregation of TMC-layers, only a few of Janus-type Mo-S-Se compounds have been hybridized with conducting supports.[31–33] Moreover, the sulfides and selenides have been studied vigorously, while only a few of the recent papers have been focused on the remarkable properties and potential applications of telluride-based materials.[28,34–37] To the best of our knowledge, there has not been any work demonstrated electrocatalytic properties of molybdenum sulfotelluride compound for HER. In addition, hydrothermal,[27] solvothermal,[29,38] and chemical vapor deposition (CVD)[30,35,39] are the common methods applied to effectively prepare the TMC nanohybrids. Nevertheless, these methods requiring the complex synthesis approaches with high cost and high energy consumption indisputably restrict their large-scale applications. Therefore, it is still a great challenge to develop a simple and efficient method to prepare the TMC-based composites with improved HER performance. Herein, for the first time, we present a simple solid-state synthesis of molybdenum sulfotelluride compounds with graphene support (MoS_xTe_y/Gr) *via* a scalable, ultrafast (60 sec) and efficient microwave-assistant heating approach and further employ these composites as HER electrocatalysts in acidic medium. The research scheme is briefly displayed in Figure 5.1. Compared to conventional heating methods, microwave-assisted heating has several advantages, such as, rapid volumetric heating, higher reaction rate, high purity, high selectivity, reducing reaction time, and increasing yields of products, etc. Benefiting from the defects created in the crystal structures, the as-prepared MoS_xTe_y/Gr nanocomposite has been demonstrated to be an active nonprecious metal-based electrocatalyst for HER, resulting low overpotential, small Tafel slope with a high exchange current density, along with outstanding long-term stability under acidic condition, even at a high temperature range.

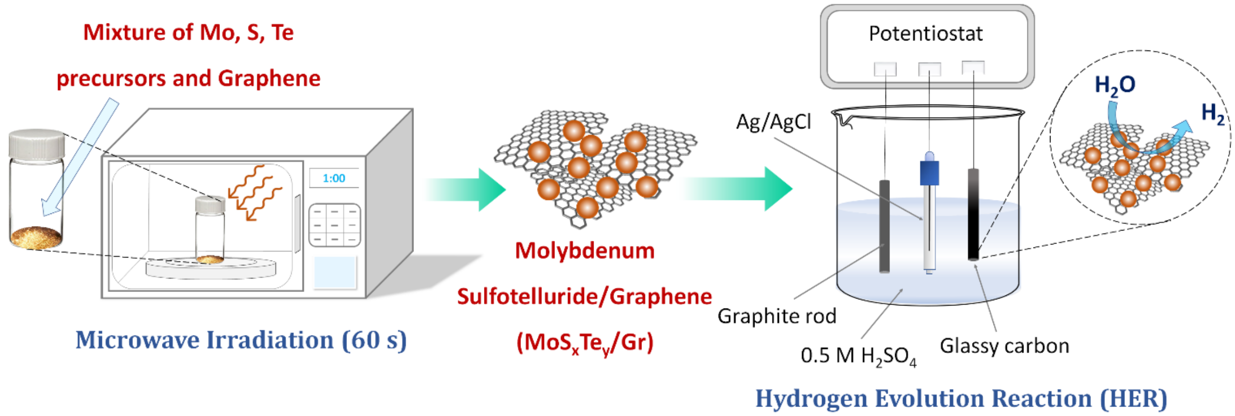

Figure 5.1. Illustration of the microwave−assisted synthesis of MoS_xTe_y/Gr hybrid, employing as an electrocatalyst for hydrogen evolution reaction (HER) in acidic medium.

Alongside with experimental investigation, molecular modeling studies have been performed with periodic plane-wave density functional theory (DFT) to delve into the surface-electrochemistry of hydrogen binding. The role of binding energy in catalysis is supported by Sabatier’s principle, stating that for ideal catalysis conditions the binding free energy should be near zero.[40] In this computational analysis, the conventional criterion of $\Delta G_{binding} \approx 0$ has been considered as the measure to establish the most suitable binding sites for HER catalysis. In literature, there are many studies for molybdenum chalcogenides with or without graphene support as hydrogen electrodes, but to the best of our knowledge no similar study has yet been carried out to understand HER activity of metal rich nanocomposite of molybdenum sulfotelluride and graphene as an electrocatalyst.[33,41–45] The most well-known graphical depiction of Sabatier's principle is the volcano plot, which in this study exhibits the position of metal-rich MoS_xTe_y/Gr hybrid near the apex of the volcano.[40,46] Our combined experimental and computational studies demonstrate the higher electrocatalytic ability of MoS_xTe_y/Gr composite comprised of a higher molybdenum-to-chalcogen ratio for HER, thus showing potential for practical application with prospective commercialization.

5.2. Methodology

5.2.1. Materials and reagents

Ammonium tetrathiomolybdate ($(NH_4)_2MoS_4$, 99.95%) precursor was purchased from BeanTown Chemical, Inc. Carbon disulfide (CS_2, liquid, 99.9%), Tellurium (Te) powder (~325 mesh), and Polyvinylidene fluoride (PVDF) were acquired from Alfa Aesar. N, N-Dimethylformamide (DMF) was purchased from *Macron Fine Chemicals*™. Graphene was supplied by Magnolia Ridge Inc., and 10 wt.% platinum on carbon (10 wt.% Pt/C) was obtained from Sigma-Aldrich. All chemicals purchased were used as received without further treatment or purification. For electrochemical characterizations, graphite rod (5 mm diameter) was provided by Alfa Aesar. Glassy carbon electrode (CHI 104, 3 mm diameter) was purchased from CH Instruments, Inc. and silver/silver chloride (Ag/AgCl, 3 M KCl, E^o= +0.197 V vs. RHE) electrode was acquired from Hach.

5.2.2. Preparation of catalyst samples and the modified GCE

To prepare the MoS_xTe_y/Gr hybrid, at first the Mo, S, and Te precursors were mixed homogeneously with graphene in a 20 mL scintillation vial using a speed mixer at 2000 rpm. The effects of different mass ratios of precursors were explored as described in Table 5.1. Then, the mixture was air dried for 10 mins inside a fume hood. Next, the vial containing uniform mixture was subjected to microwave irradiation at a constant power of 1250 W for 60 seconds for each mixture. During this process, the vial was loosely sealed by a PTFE cap to allow releasing of gaseous residues. A variety of MoS_xTe_y/Gr samples were prepared and denoted as MST-1 to MST-4 (Table 5.1). For comparison, MST-5 and MST-6 samples were prepared by physically mixing the microwave synthesized MoS_2/Gr and $MoTe_2$/Gr composites. The synthesis procedures of MoS_2/Gr and $MoTe_2$/Gr are explained in previous studies.[44,47]

Table 5.1. MoS_xTe_y/Gr nanocomposites with different precursor ratios.

MoS_xTe_y/Gr Samples	**$(NH_4)_2MoS_4$ (mg)**	**Te powder (mg)**	**CS_2 (µL)**	**Graphene (mg)**
MST-1	10	20	100	10
MST-2	10	10	100	10
MST-3	20	10	100	10
MST-4	10	5	100	10
MST-5	Physical mixture of MoS_2/Gr and $MoTe_2$/Gr (wt. ratio, 1:1)			
MST-6	Physical mixture of MoS_2/Gr and $MoTe_2$/Gr (wt. ratio, 2:1)			

To prepare the catalyst coating, a mixture of 100 mg composite and 10 mg PVDF powder were suspended in 5 mL DMF solvent, following 20 min of probe sonication. The GCE surface (0.07 cm^2) was sequentially polished with 0.3- and 0.05-mm alumina slurries, then rinsed with DI water and acetone for 1 min. Finally, 20 µL of the suspension was added to the GCE surface and dried in a vacuum dryer for 30 mins at 60°C, which results a mass loading of ~1 mg cm^{-2} for each catalyst sample.

5.2.3. Material characterizations techniques

X-ray photoelectron spectroscopy (XPS) was investigated on a Kratos Axis Ultra DLD spectrometer using a monochromatic Al Kα radiation ($h\nu$ = 1486.6 eV) under UHV condition ($<8 \times 10^{-10}$ Torr), to determine the chemical state and surface composition of various elements in MoS_xTe_y/Gr-composite. The morphology and chemical compositions were characterized by scanning electron microscope (SEM; Apreo FE) coupled with an energy dispersive X-ray spectrometer (EDS, EDAX Instruments) using an acceleration voltage of 20 kV. In addition, a FEI Tecnai F20 transmission electron microscope (TEM) was used for structural and chemical analysis of the powder samples, operated at 200 kV and equipped with an EDAX EDS detector and GIF (Gatan Image Filter) Tridiem 863 electron energy loss spectroscopy (EELS) system. Moreover, to investigate the phase and crystal structure of MoS_xTe_y/Gr-composite, the powder X-ray diffraction (XRD) patterns were collected on a Philips X'pert MPD diffractometer with Cu Kα radiation ($\lambda = 1.54056$ Å) at 45 kV and 40 mA.

5.2.4. Electrochemical measurements techniques

Electrochemical experiments were performed with CH Instrument (CHI 760D) and Arbin Instrument (version 4.21) in a typical three-electrode system. This setup consists of an active material−coated glassy carbon electrode (GCE) as working electrode with a mass loading of ~1 mg cm^{-2}, Ag/AgCl electrode as reference, and graphite rod as a counter electrode in 0.5 M H_2SO_4 electrolyte. In order to compare the HER activities, the potentials were converted to reversible hydrogen electrode (RHE) based on the equation: $V\ (vs.\ RHE) = V\ (vs.\ Ag/AgCl) + 0.197 + (0.059 \times pH)$ at room temperature (~ 25°C). The electrocatalytic activities and corresponding mechanisms were determined by performing linear sweep voltammetry (LSV), cyclic voltammetry (CV), electrochemical impedance spectroscopy (EIS), and constant potential tests. The EIS spectra were further fitted by the EC-Lab software.

5.2.5. Computational methodology

The computational study has been carried out using periodic plane-wave density functional theory (DFT) with the Cambridge Serial Total Energy Packages (CASTEP).[48–53] In this computational analysis, multiple types of molybdenum sulfotelluride/graphene nanocomposite systems have been studied, such as $Mo_9S_8Te_{10}$/Gr, $Mo_9S_6Te_7$/Gr, and two types of $Mo_9S_4Te_5$/Gr composites. The $Mo_9S_4Te_5$/Gr system was considered with a similar atomic ratio as experiments (Mo: S: Te ≈ 1: 0.46: 0.58 ≈ 9: 4: 5). In Type-1, all of the Mo atoms were kept on the upper layer with chalcogen atoms adjacent to the graphene. In Type-2, all of the chalcogen atoms were kept on the upper layer with the Mo atoms adjacent to the graphene.

5.3. Results and discussion

5.3.1. Material characterizations

The MST-2 sample has been chosen for material characterizations due to the best HER activities displayed by this sample (described in Section 5.3.2) among all the prepared hybrid samples. The compositions and binding energies of MST-2 hybrid were examined by XPS. The XPS full spectrum (Figure 5.2a) discloses the present of four principal elements of carbon (C), molybdenum (Mo), sulfur (S), and tellurium (Te), and a small peak of oxygen (O), with an atomic ratio of Mo: S: Te ≈ 1: 0.46: 0.58. Therefore, the MST-2 is signified as $MoS_{0.46}Te_{0.58}$/G composite for further characterizations. The XPS spectrum of Mo 3d (Figure 5.2b) is dominated by two peaks corresponding to the $3d_{5/2}$ (229.1 eV) and $3d_{3/2}$ (232.3 eV), implying Mo^{4+} characteristics.[47] Additionally, a weak peak at 226.2 eV is ascribed to S 2s orbital of MoS_2.[54] Another peak appears at ~235 eV, which corresponds to Mo^{6+} (likely MoO_3).[28] From Figure 5.2c, one can see that the peaks of S $2p_{3/2}$ and S $2p_{1/2}$ appeared at 161.9 and 163.1 eV, which confirms the presence of S^{2-} with a slight shift of typical binding energies (161.3 and 162.1 eV, respectively) for MoS_2.[47] This indicates the ratio of Mo and S atoms differs from typical 1:2 value. The XPS peaks at 572.9 and 583.3 eV (Figure 5.2d) are attributed to Te $3d_{5/2}$ and Te $3d_{3/2}$, respectively.[44] Two additional peaks at 576.2 and 586.6 eV are ascribed to TeO_2.[28] Moreover, the structural morphology of $MoS_{0.46}Te_{0.58}$/Gr hybrid was surveyed by SEM. The as-synthesized composite exhibits nanosheet-like architecture with uniform rough surfaces, and those nanosheets were grown on graphene network intertwined with each other (Figure 5.2e). Such unique heterostructure would increase the density of active sites and promote the electron/charge transfers. In addition, the TEM images displayed in Figure 5.2f and 5.2g confirm both $MoS_{0.46}Te_{0.58}$ and graphene have a thin and layered sheet structure, which are in agreement with SEM images. As illustrated in Figure 5.2g, the well-resolved lattice fringes reveal that the distinguished lattice spacings are around 0.34 nm and 0.67 nm, which are consistent with the (002) planes of graphene and $MoS_{0.46}Te_{0.58}$, respectively. In addition, the EDS mapping (Figure 5.2h) clearly suggests that C, Mo, S and Te elements coexist in the $MoS_{0.46}Te_{0.58}$/Gr nanosheet, and these elements distribute homogeneously throughout the whole nanosheet.

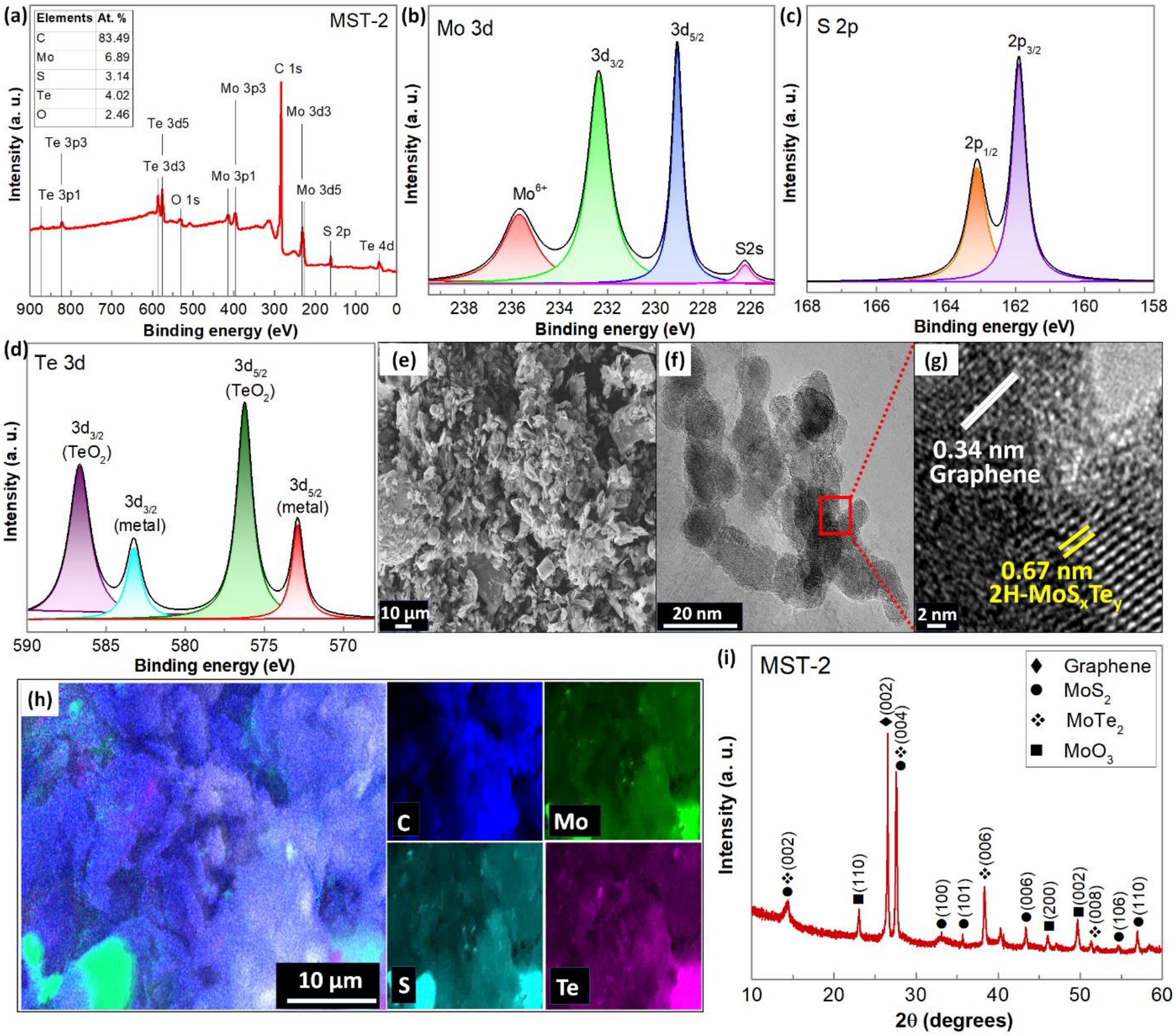

Figure 5.2. (a) XPS survey spectrum of MST-2 sample. (b-d) High resolution XPS spectra of Mo 3d, S 2p, and Te 3d regions, respectively. (e) EDS mapping of carbon (C), molybdenum (Mo), sulfur (S), and tellurium (Te) species. (f) SEM, (g) TEM, (h) HRTEM images, and (i) XRD pattern of $MoS_{0.46}Te_{0.58}$/Gr hybrid (MST-2).

Furthermore, the phase information of $MoS_{0.46}Te_{0.58}$/Gr hybrid was characterized by XRD. As shown in Figure 5.2i, the signal from graphene is observed at 26.0°.[47] The diffraction peaks at 2θ of 14.4°, 27.5°, 33.1°, 35.7°, 43.4°,54.6°, and 56.9° are ascribed respectively to the (002), (004), (100), (101), (006), (106) and (110) planes, respectively, corresponding to hexagonal 2H–MoS_2

structure (JPCDS No. 37-1492).[55] The diffraction peaks around 14.4°, 27.5°, 38.4°, and 52.7° are corresponding to (002), (004), (006), and (008) planes, which can be indexed to the standard hexagonal 2H–$MoTe_2$ structure (JPCDS no. 15-0658).[56] Besides, the reflection positions in the XRD patterns at the angles of 23.1°, 46.0°, and 49.7° are appeared, which correspond to (110), (200), and (002) planes of MoO_3, respectively.[44] These results indicate the presence of MoO_3 in as-synthesized $MoS_{0.46}Te_{0.58}$/Gr nanohybrid. A few of other insignificant peaks are also appeared in XRD pattern of MST-2 sample, which correspond to the unreacted particles of Mo and Te.[55,56] Moreover, the EDS results (Figure 5.3) reveal the elemental analysis of Mo, S and Te components for MST-1, MST-2, MST-3, and MST-4 samples. Noticeably, the atomic ratio of MST-2 is found as Mo: S: Te ≈ 1: 0.44: 0.45, which is very similar to the findings from XPS investigations.

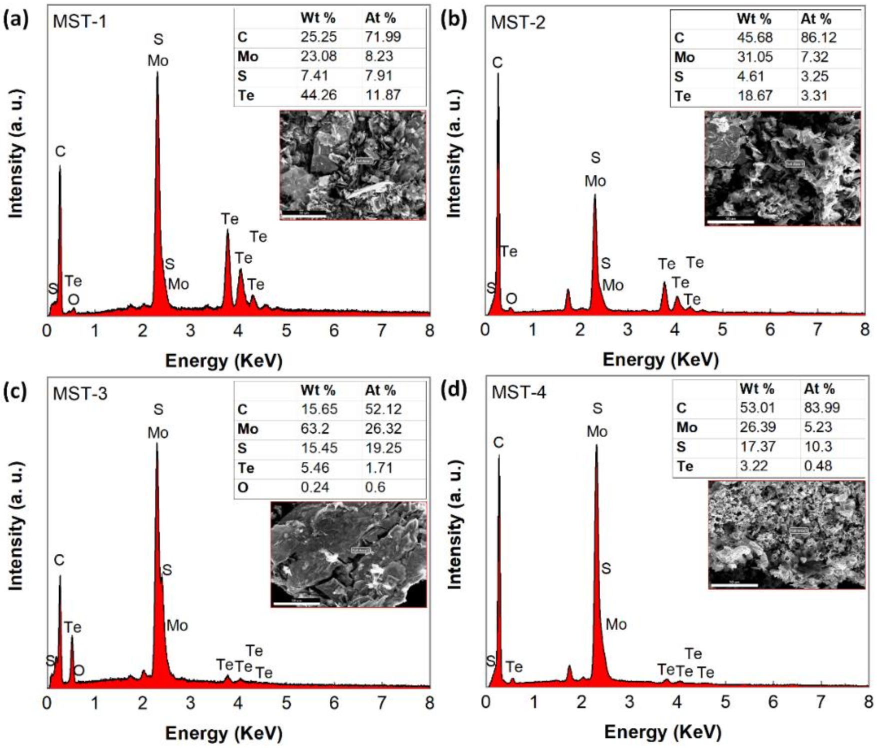

(a) MST-1

	Wt %	At %
C	25.25	71.99
Mo	23.08	8.23
S	7.41	7.91
Te	44.26	11.87

(b) MST-2

	Wt %	At %
C	45.68	86.12
Mo	31.05	7.32
S	4.61	3.25
Te	18.67	3.31

(c) MST-3

	Wt %	At %
C	15.65	52.12
Mo	63.2	26.32
S	15.45	19.25
Te	5.46	1.71
O	0.24	0.6

(d) MST-4

	Wt %	At %
C	53.01	83.99
Mo	26.39	5.23
S	17.37	10.3
Te	3.22	0.48

Figure 5.3. EDS patterns of MoS_xTe_y/Gr samples: (a) MST-1, (b) MST-2, (c) MST-3, (d) MST-4. [inset tables display the wt.% and at.% of carbon (C), molybdenum (Mo), sulfur (S), tellurium (Te) and oxygen (O) elements]

5.3.2. Investigations of HER performance

The electrocatalytic HER activities of samples MST-1 to MST-6 were investigated by linear sweep voltammograms (LSVs) in an acidic electrolyte of 0.5 M H_2SO_4. The *iR* corrected−LSVs are shown in Figure 5.4a, where MST-2 displays the best catalytic behavior with the smallest overpotential (η) of 62.2 mV *vs.* RHE to reach the cathodic current density of 10 mA cm^{-2}. As displayed in Figure 5.4b, the order of HER activity based on η is MST-2 > MST-1 > MST-5 > MST-6 > MST-3 > MST-4. It clearly indicates, the ratio of molybdenum sulfide to molybdenum telluride is crucial to the catalytic ability and it is found that too much of sulfur does not favor the hydrogen evolution (for MST-3 and MST-6, see Table 5.1 and Figure 5.3). On the other side, the best results are found from the samples containing almost equal ratio of S and Te (MST-2, MST-5) or sample with a little high amount of Te (MST-1). Among these samples, MST-1 may have contained some unreacted Te-powder, and the physical mixture of MST-5 may not have a fully interconnected network in crystal structure, which limit their catalytic performances. Besides, as shown in Figure 5.3d, MST-4 contains a very small amount of active catalyst comparing to the high amount of graphene present in the sample, thus does not show good HER activity. Consequently, MST-2 exhibits the best combination of molybdenum sulfide and molybdenum telluride ratio on graphene network and is further studied for electrocatalytic behaviors, which is renamed as '$MoS_{0.46}Te_{0.58}$/Gr' based on the XPS elemental results. The HER activity of $MoS_{0.46}Te_{0.58}$/Gr nanocomposite was compared with bare GCE, graphene, MoS_2/Gr, $MoTe_2$/Gr, and 10 wt.% Pt/C catalyst samples based on LSV curves (Figure 5.4c). The observed overpotentials (η) for these samples are displayed in Figure 5.4d and it clearly indicates that $MoS_{0.46}Te_{0.58}$/Gr catalyst emerges with a smaller overpotential than those of MoS_2/Gr and $MoTe_2$/Gr samples. The η of $MoS_{0.46}Te_{0.58}$/Gr is around only 62.2 mV at 10 mA cm^{-2}, and the cathodic current density rises promptly with an increase in η. In comparison, both MoS_2/Gr and $MoTe_2$/Gr exhibit higher overpotential, approximately 197.2 and 167.1 mV, respectively. In contrast, bare GCE and graphene does not show any catalytic activity. Furthermore, the Tafel diagrams were derived from LSVs by fitting the linear sections to the Tafel equation ($\eta = a + b \log i$), where η is overpotential, a is a constant, b is the Tafel slope and i represents the cathodic current density.[57] Tafel slope can reveal the rate determining step (RDS) during hydrogen generation. As a result of applying sufficient potential at specific reaction condition, the HER takes place through an adsorption step (Volmer, $H^+ + e^- \rightarrow H_{ads}$, 120 mV dec^{-1}), following by a reduction step (Heyrovsky, $H^+ + H_{ads} + e^- \rightarrow H_2$, 40 mV dec^{-1} or Tafel, $2H_{ads} \rightarrow H_2$, 30 mV dec^{-1}).[57] Tafel step is the fastest reaction in HER, therefore it is noticeable that the smaller Tafel slope favors HER activities. From the present results shown in Figure 5.4e, $MoS_{0.46}Te_{0.58}$/Gr exhibits a Tafel slope of 61.1 mV dec^{-1}, which combines both outcomes from MoS_2/Gr (54.2 mV dec^{-1}) and $MoTe_2$/Gr (99.4 mV dec^{-1}). Moreover, it suggests that the Volmer–Heyrovsky reaction mechanism dominates in the HER process of $MoS_{0.46}Te_{0.58}$/Gr. In addition, the exchange current densities (i_0) are also measured following the Tafel slope extrapolation method,[57] and all the key parameters of HER performance are displayed in Table 5.2. The kinetics of hydrogen evolution process was further investigated by electrochemical impedance spectroscopy (EIS) measurements. Figure 5.4f represents the Nyquist plots of bare GCE, graphene, MoS_2/Gr, $MoTe_2$/Gr and $MoS_{0.46}Te_{0.58}$/Gr at a given overpotential of 150 mV, and corresponding R_s and R_{ct} values are displayed in Table 5.2. Here, a small internal resistance (R_s) of 7.3 Ω for $MoS_{0.46}Te_{0.58}$/Gr indicates that the intrinsic resistance of electrode material and ionic resistance of electrolyte is much low for the hybrid $MoS_{0.46}Te_{0.58}$/Gr system. In the high−frequency zone, it exhibits one capacitive semicircle, indicating that the reaction is kinetically controlled. This semicircle represents the charge transfer process at the interface between the electrolyte and the catalytic electrode, which is composed of the charge transfer resistance (R_{ct}) and the double layer capacitance (C_{dl}). The lower value of R_{ct} represents faster charge transfers in the electrode, resulting rapid reaction in the electrocatalytic kinetics. The low−frequency inclined line signifies the Warburg impedance (Z_W) for the diffusion process of H^+ ions through active materials, which is prominently shown for only $MoS_{0.46}Te_{0.58}$/Gr hybrid. As exhibited in Figure 5.4f and Table 5.2, a small R_{ct} of 145.6 Ω can be found for $MoS_{0.46}Te_{0.58}$/Gr, which indicates a higher conductivity and faster electron transfer process, and further explains the higher HER activity of $MoS_{0.46}Te_{0.58}$/Gr catalyst.

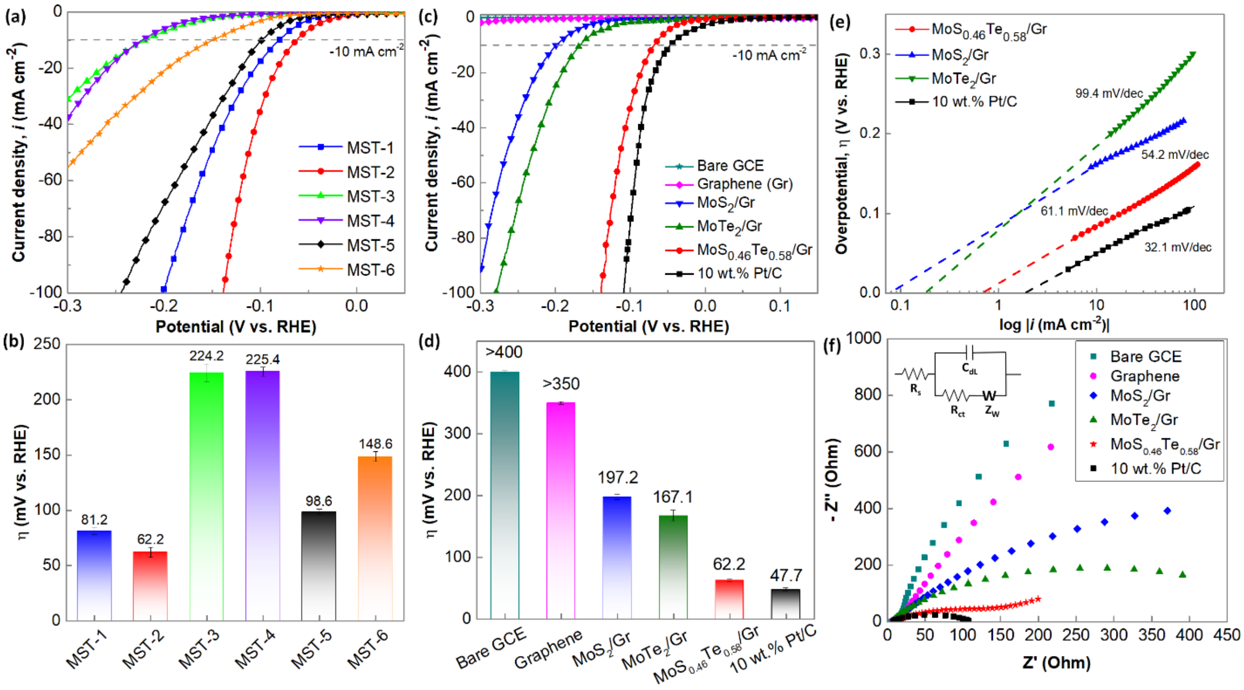

Figure 5.4. (a) LSVs at a scan rate of 2 mV s^{-1} for samples MST-1 to MST-6. (b) Corresponding overpotentials to reach the current density of 10 mA cm^{-2}. (c) LSVs of bare GCE, graphene, MoS_2/Gr, $MoTe_2$/Gr, $MoS_{0.46}Te_{0.58}$/Gr and Pt/C catalysts at a scan rate of 2 mV s^{-1}. (d) Corresponding overpotentials at the cathodic current density of 10 mA cm^{-2}. (e) Tafel slopes and (f) Nyquist plots of catalyst samples.

Table 5.2. The major HER parameters of all catalyst samples.

Samples	**Overpotential (mV vs. RHE)**	**Tafel slope (mV dec^{-1})**	i_0 **(A cm^{-2}) × 10^{-3}**	R_s **(Ohm)**	R_{ct} **(Ohm)**
Bare GCE	> 400	-	-	15.6	1124.1
Graphene	> 350	-	-	15.0	1006.3
MoS_2/Gr	197.2	54.2	0.075	8.5	811.5
$MoTe_2$/Gr	167.1	99.4	0.194	9.5	490.7
$MoS_{0.46}Te_{0.58}$/Gr	62.2	61.1	0.694	7.3	145.6
10 wt.% Pt/C	47.7	32.1	1.882	6.9	111.4

In addition, Figure 5.5a represents the Nyquist plots of $MoS_{0.46}Te_{0.58}$/Gr at various overpotentials (50−200 mV). The R_s and R_{ct} values are summarized in Table 5.3 as measured. As expected, the R_{ct} diminishes markedly with the increasing of η, resulting the acceleration of hydrogen evolution.

Table 5.3. R_s and R_{ct} values of $MoS_{0.46}Te_{0.58}$/Gr at the potential range of 50−200 mV.

η **(mV)**	R_s **(Ohm)**	R_{ct} **(Ohm)**
50	10.9	713.2
80	10.3	448.6
110	10.2	310.2
140	10.3	169.6
170	9.9	71.4
200	9.9	15.5

Next, the turnover frequency (TOF) was analyzed at the η of 10−200 mV. TOF is defined as the number of hydrogen molecules evolved on an active site per 1 second. Assuming the cathodic current is entirely attributed to the HER, the TOF can be calculated from the following equation:[58,59]

$$\mathrm{TOF} = \frac{\text{No. of total hydrogen turn overs/cm}^2\text{ geometric area}}{\text{No. of active sites/cm}^2\text{ geometric area}} \quad \ldots\ldots\ldots\ldots\ldots\ldots\ldots\ldots\ldots\ldots\ldots \text{(5.1)}$$

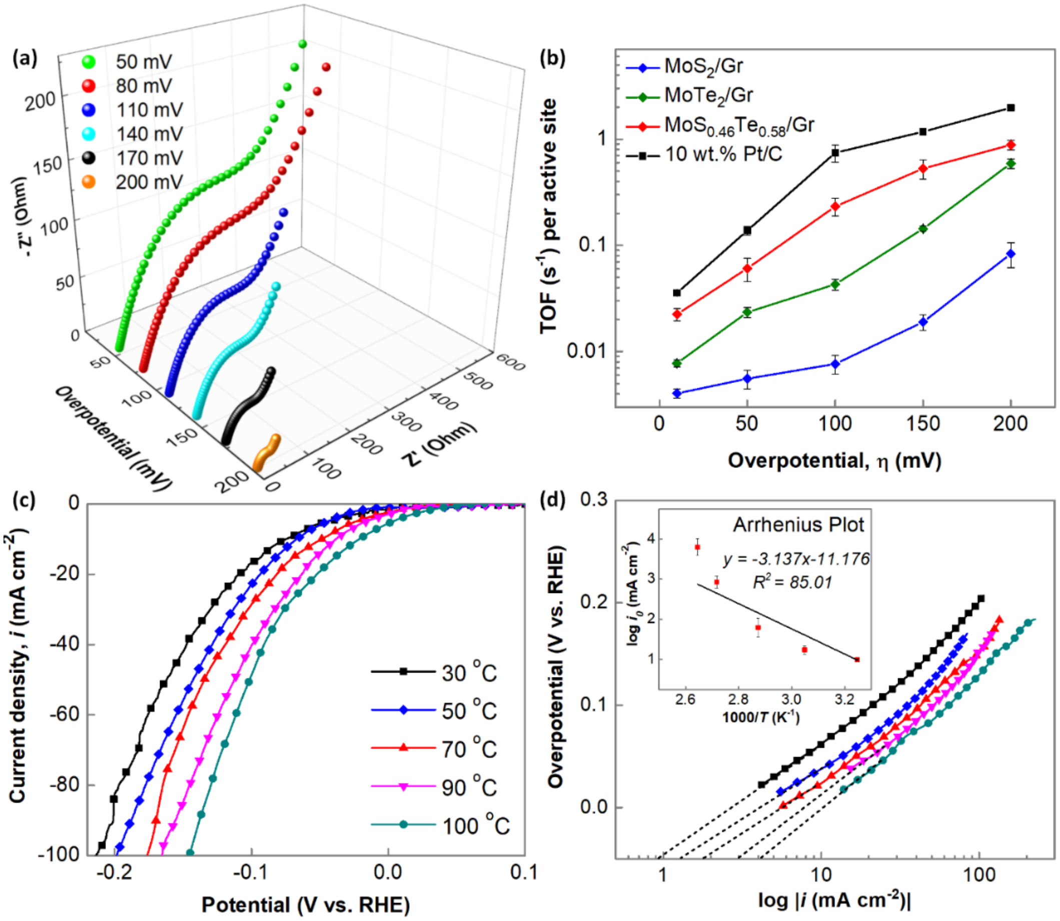

Figure 5.5. (a) Nyquist plots of $MoS_{0.46}Te_{0.58}$/Gr at various η of 50−200 mV. (b) Turnover frequency (TOF) estimations for catalyst samples at the η of 10−200 mV. (c) The LSVs of $MoS_{0.46}Te_{0.58}$/Gr within a temperature range of 30 ºC to 100 ºC. (d) Corresponding Tafel plots [Inset: Arrhenius plot to determine the activation energy].

In this study, the number of active sites and TOF of catalyst samples were calculated based on the electrochemical approach through CV measurements in phosphate buffer (pH = 7) at a scan rate of 10 mV s^{-1} (Figure 5.6), based on a general method mentioned by Dai et al.[60] As displayed in Figure 5.5b and Table 5.4, at η = 150 mV, The TOF of 10 wt.% Pt/C, $MoS_{0.46}Te_{0.58}$/Gr, MoS_2/Gr, and $MoTe_2$/Gr catalysts are estimated as 1.17, 0.53, 0.02, and 0.14 s^{-1}, respectively. These results clearly support the higher HER activity of as−produced $MoS_{0.46}Te_{0.58}$/Gr hybrid comparing to the single components (MoS_2/Gr and $MoTe_2$/Gr).

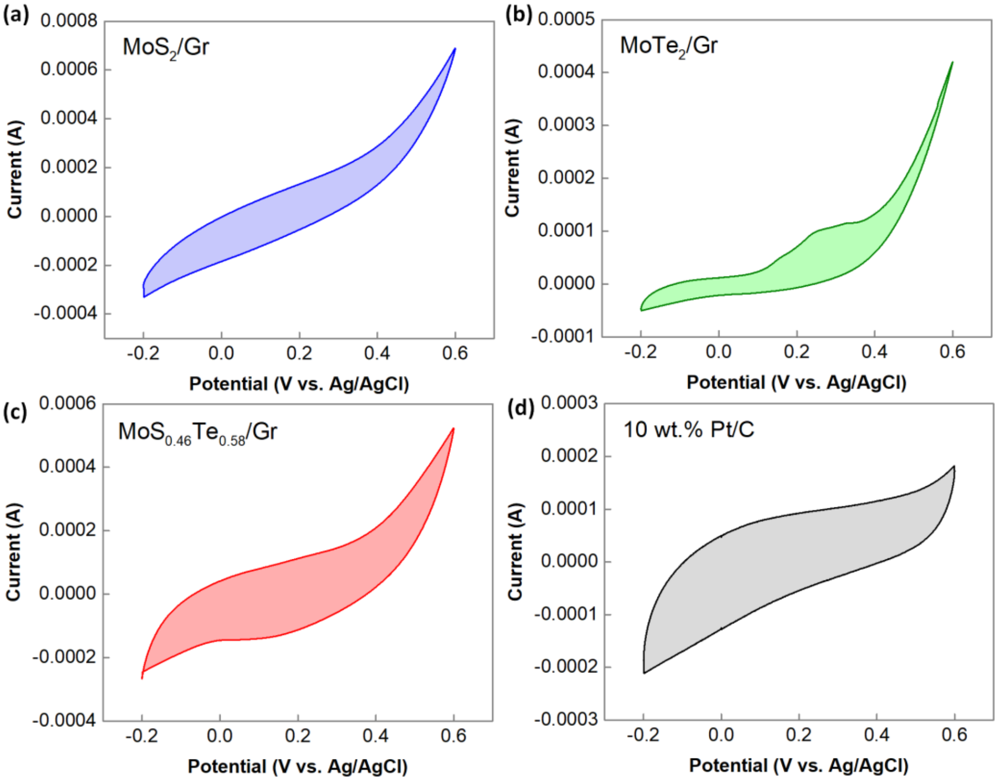

Figure 5.6. CV curves in phosphate buffer solution (pH = 7) for the catalyst samples of (a) MoS_2/Gr, (b) $MoTe_2$/Gr, (c) $MoS_{0.46}Te_{0.58}$/Gr and (d) 10 wt.% Pt/C.

To demonstrate the stability at high temperatures and to measure the apparent activation energy (E_a) of $MoS_{0.46}Te_{0.58}$/Gr, the LSV tests were performed at a wide range of temperature (Figure 5.5c) in 0.5 M H_2SO_4. As summarized in Table 5.5, the overpotentials gradually decrease from 66.2 mV to 25.3 mV with the increase in operating temperature from 30 to 100 °C, enabling faster ion and electron transfer at higher temperatures. Besides, the corresponding exchange current densities (i_0) were measured from the Tafel slopes (Figure 5.5d) and Table 5.5 summarizes the electrochemical parameters (η and i_0) at different temperatures. Based on these results, the E_a was measured by Arrhenius equation: $\log i_0 = logA - \frac{E_a}{2.3\ RT}$, which is one of the major key factors to determine the efficiency of HER electrocatalyst for H_2 production.[61,62] Here, A is the pre-exponential factor, R is the universal gas constant (8.314 J K^{-1} mol^{-1}) and T is absolute temperature (K). The Arrhenius plot of $\log(i_0)$ *vs.* $\frac{1000}{T}$ is displayed in inset of Figure 5.5d, from which E_a was calculated as 59.85 ± 12.33 kJ mol^{-1}. Such an energy barrier may be due to the combination effect of water splitting to H^+ and OH^- ions, H^+ adsorption and desorption on cathode, and cluster of H_2 bubbles formation.

Table 5.4. Turn over frequency (TOF, s^{-1}) values at different overpotentials.

Samples	**10 mV**	**50 mV**	**100 mV**	**150 mV**	**200 mV**
10 wt.% Pt/C	0.03578	0.13760	0.74305	1.17420	1.97597
$MoS_{0.46}Te_{0.58}$/Gr	0.02248	0.06063	0.23238	0.52820	0.88492
MoS_2/Gr	0.00404	0.00556	0.00765	0.01898	0.08341
$MoTe_2$/Gr	0.00777	0.02344	0.04294	0.14337	0.59067

Table 5.5. Electrochemical measurements of $MoS_{0.46}Te_{0.58}$/Gr catalyst at different temperatures.

Temperature (°C)	**Overpotential, η (mV) at −10 mA cm^{-2}**	**Exchange current density, i_0 (mA cm^{-2})**	**Activation energy, E_a (kJ mol^{-1})**
30	66.2	0.9	59.85 ± 12.33
50	62.3	1.2	
70	49.7	1.8	
90	38.2	2.9	
100	25.3	3.8	

Finally, a continuous cycling test was carried out for 5000 cycles at a scan rate of 50 mV s^{-1} to determine the long-term durability of $MoS_{0.46}Te_{0.58}$/Gr catalyst. Their polarization curves are displayed in Figure 5.7a within a potential range of 0 to −0.25 V *vs.* RHE. The polarization curves show slight changes after 5000 cycles, resulting an overpotential (η) shift of only 10 mV at high current density of −200 mA cm^{-2}. Additionally, a chronoamperometric curve was obtained at the η of 150 mV, which is presented in Figure 5.7b. This constant potential test exhibits almost no degradation in the cathodic current density (around −45 mA cm^{-2}) for over 90 h of electrolysis. It suggests the remarkable stability of $MoS_{0.46}Te_{0.58}$/Gr during the HER process, which can well be attributed to compositional and structural stability of $MoS_{0.46}Te_{0.58}$/Gr heterostructure supported by graphene network. Moreover, the electrochemical double-layer capacitance (C_{dl}) was measured to evaluate the electrochemically active surface area (ECSA) of $MoS_{0.46}Te_{0.58}$/Gr hybrid. The ECSA value is supposed to be linearly proportional to the value of C_{dl}, which can be derived by CV measurements.[63] Figure 5.7c and 5.7e exhibit the non-faradaic CV curves for $MoS_{0.46}Te_{0.58}$/Gr catalyst before and after the cycling stability tests for 5000 cycles, respectively. As shown in Figure 5.7d, the variation of average capacitive currents, $\frac{1}{2}(i_a - i_c)$ are displayed with respect to the scan rate for MoS_2/Gr, $MoTe_2$/Gr and $MoS_{0.46}Te_{0.58}$/Gr catalyst samples. Corresponding CV curves of MoS_2/Gr and $MoTe_2$/Gr are included in Figure 5.8. The value of C_{dl} is estimated from the slope of the plots, where $MoS_{0.46}Te_{0.58}$/Gr yields the highest C_{dl} of 17.73 mF cm^{-2} comparing with those of MoS_2/Gr (12.81 mF cm^{-2}) and $MoTe_2$/Gr (13.95 mF cm^{-2}), implying the highest exposure of efficient active sites for the enhanced HER performance. Additionally, as shown in Figure 5.7f, C_{dl} of $MoS_{0.46}Te_{0.58}$/Gr increases almost four times, resulting the value of 70.52 mF cm^{-2} after 5000 cycles of HER test. This phenomenon indicates an improvement in active sites of the material due to the H_2 bubbling from catalyst surface, creating more defects in nanosheets.

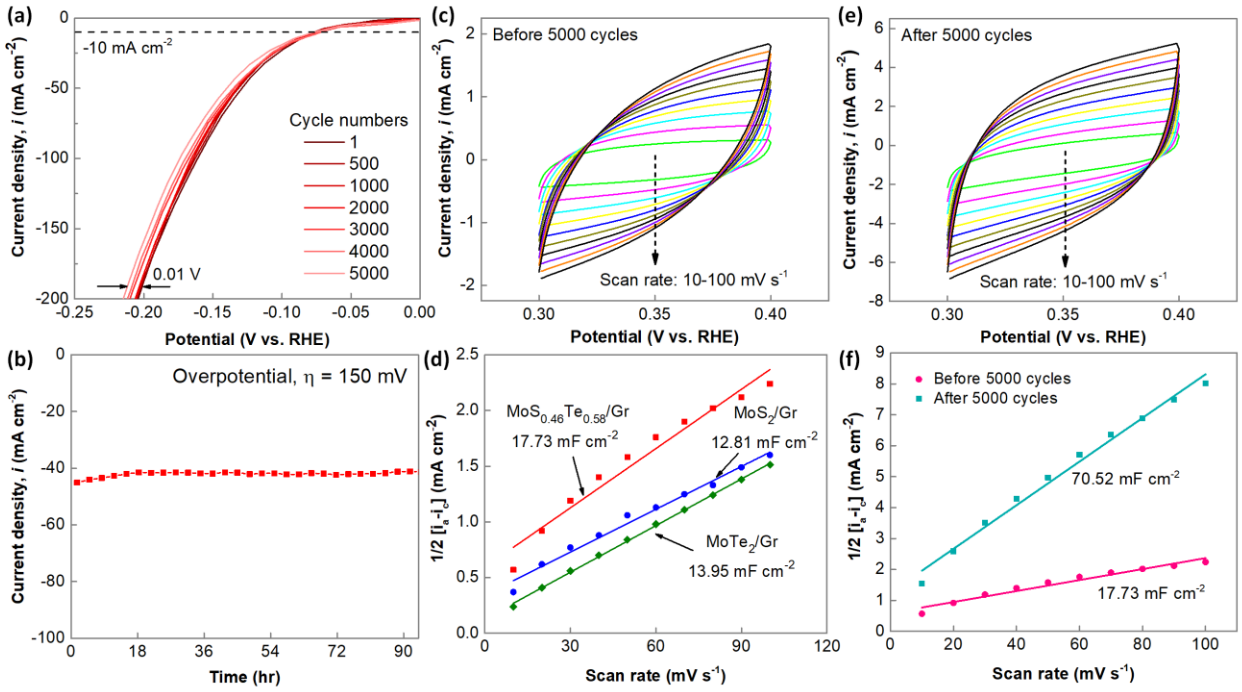

Figure 5.7. (a) Cycling stability of $MoS_{0.46}Te_{0.58}$/Gr at a scan rate of 50 mV s^{-1} (LSV curves from 1 to 5000 cycles are displayed). (b) Chronoamperometric curve during the electrolysis over 90 hours at a constant overpotential of 150 mV. (c) CVs of $MoS_{0.46}Te_{0.58}$/Gr in a non-faradaic potential window before 5000 cycles. (d) Measured EDLCs for MoS_2/Gr, $MoTe_2$/Gr and $MoS_{0.46}Te_{0.58}$/Gr. (e) CVs of $MoS_{0.46}Te_{0.58}$/Gr in a non-faradaic potential window after 5000 cycles. (f) Measured EDLCs for $MoS_{0.46}Te_{0.58}$/Gr before and after 5000 cycles.

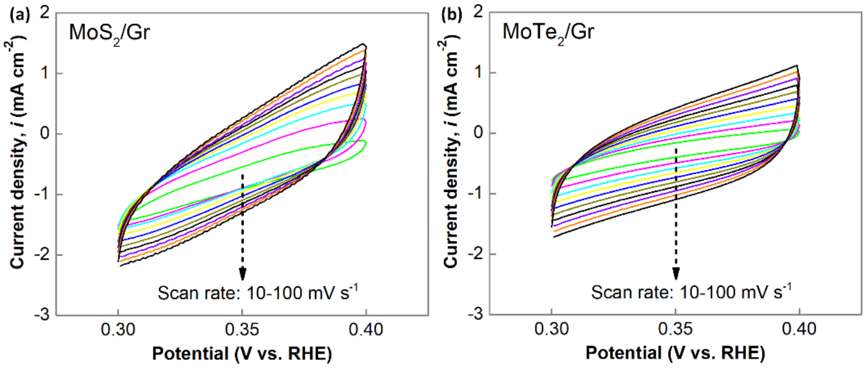

Figure 5.8. CVs of MoS_2/Gr and $MoTe_2$/Gr in a non-faradaic potential window of 0.3−0.4 V *vs.* RHE at scan rates of 10 to 100 mV s^{-1}.

The elemental and structural analyses of $MoS_{0.46}Te_{0.58}$/Gr were further examined after stability test (Figure 5.9), where the results clearly show insignificant degradation of active material after 5000 cycles. The atomic ratio retains almost similar as initial and $MoS_{0.46}Te_{0.58}$ nanosheets remain uniformly embedded in graphene network.

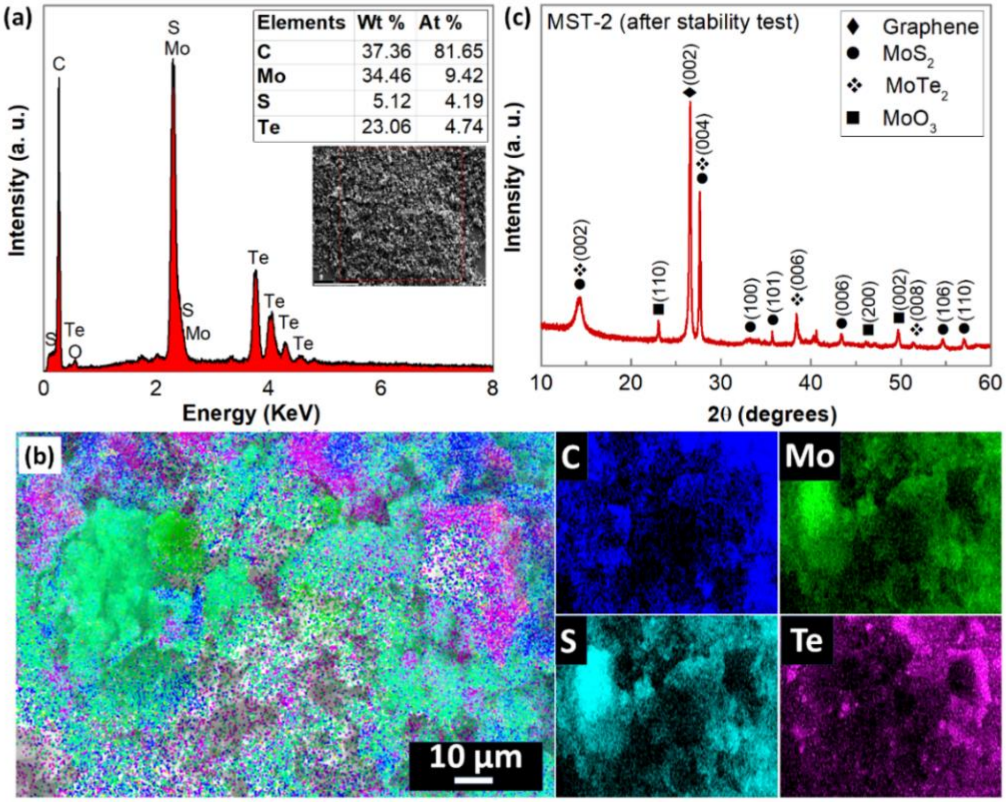

Elements	Wt %	At %
C	37.36	81.65
Mo	34.46	9.42
S	5.12	4.19
Te	23.06	4.74

Figure 5.9. (a) EDS analysis, (b) XRD pattern, and (c) EDS mapping of $MoS_{0.46}Te_{0.58}$/Gr nanocomposite after cycling stability test for 5000 CV cycles.

The above results unambiguously reveal that the $MoS_{0.46}Te_{0.58}$/Gr nanocomposite acquires improved HER activity in comparison to either MoS_2/Gr or $MoTe_2$/Gr. The superior HER performance can be considered from the combination of molybdenum sulfide and molybdenum telluride presents a synergistic effect on graphene network, assembling the intrinsic properties of the two components. Therefore, more active sites have been exposed due to the surface defects and shorten the electron transfer pathways. Additionally, the stable connection between $MoS_{0.46}Te_{0.58}$/Gr nanostructure and graphene can further remarkedly accelerate the electron transfer ability, favoring the much enhanced HER performance and stability for long-term tests. From this study, it has also been demonstrated that Mo-rich nanocomposites with the slight increase in Te fraction (or conversely reduction of S) in the hybrid nanostructure is associated with better catalytic performances.

5.3.3. Computational investigations to evaluate HER activities

For the computational study, multiple hydrogen adsorption sites on each of the MoS_xTe_y/Gr nanocomposites were investigated for binding energetics. For the $Mo_9S_8Te_{10}$/Gr structure, these binding sites consist of chalcogen and Mo atoms. For the $Mo_9S_6Te_7$/Gr and $Mo_9S_4Te_5$/Gr structures, the binding sites are primarily comprised of exposed Mo atoms, since the sites associated with Mo atoms possessed the lowest binding energies for the $Mo_9S_8Te_{10}$/Gr structure. In case of the $Mo_9S_4Te_5$/Gr structure, which was constructed to closely resemble the atomic ratio (Mo: S: Te ≈ 1: 0.46: 0.58 ≈ 9: 4: 5) of the experimentally determined best system (Figure 5.4a and 5.4b), only Mo-based hydrogen binding sites are considered based on learnings from the previous structure of stoichiometric ratio. In this metal-rich nanocomposite, several thermoneutral hydrogen binding energy values have been observed. Conventionally, the binding free energies for high-performing catalytically active sites are within the range of −0.2 and 0.2 eV. Notably, the two Mo-rich systems ($Mo_9S_6Te_7$/Gr and $Mo_9S_4Te_5$/Gr) have multiple catalytically active binding sites as compared to the composite system comprised of a nanoparticle of stoichiometric ratio ($Mo_9S_8Te_{10}$/Gr). Moreover, using the experimentally measured current density (i_0) along with the theoretically determined $\Delta G_{binding}$ value of the best performing nanocomposite, the relative position of this nanocomposite in the volcano plot (Figure 5.10) is found very close to the apex, approaching the high-performing noble metals Pt and Pd.

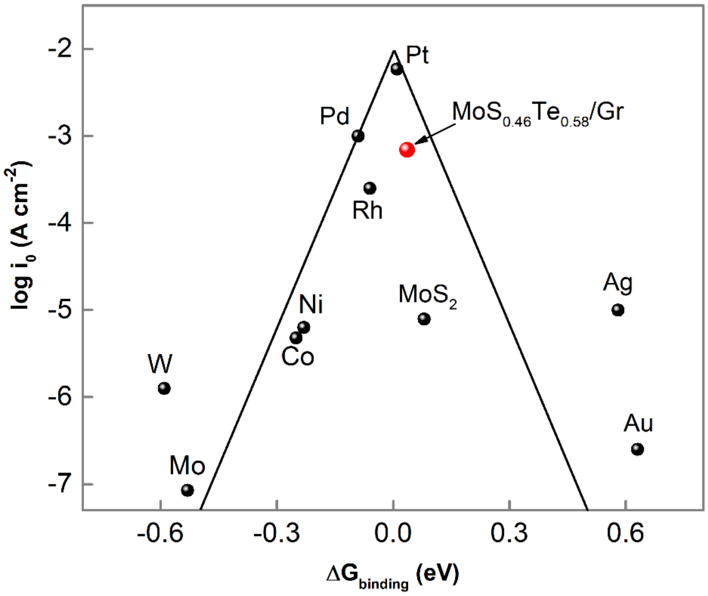

Figure 5.10. Volcano plot of experimentally measured current density (i_0) vs. DFT calculated Gibbs free energy of hydrogen binding ($\Delta G_{binding}$). With the exception of the $MoS_{0.46}Te_{0.58}/Gr$ system, all presented data values are from literature sources.[64–66] The computationally derived $\Delta G_{binding}$ value for the $MoS_{0.46}Te_{0.58}/Gr$ composite is from the $Mo_9S_4Te_5/Gr$ system with the most similar empirical formula.

Additionally, a comparison of previous results of HER activities on TMC-based ternary compounds with current results for $MoS_{0.46}Te_{0.58}/Gr$ is described in Table 5.6. In contrast with facile, ultra-fast (60 sec) microwave-assisted synthesis performed in this study, other compounds were synthesized by different complex approaches. Moreover, it is obvious that the present material exhibits better catalytic performance with lower overpotential and a small Tafel slope.

Table 5.6. Comparison of electrochemical activities of $MoS_{0.46}Te_{0.58}$/Gr catalyst with previously reported similar TMC−based hybrid compounds.

Materials	**Synthesis approach**	**Electrolyte**	**Over potential at 10 mA cm^{-2} [mV vs. RHE]**	**Tafel slope [mV per decade]**	**Ref.**
$MoSe_2/MoS_2$	Hydrothermal	0.5 M H_2SO_4	162	61	[27]
$MoSe_{0.17}Te_{1.83}$	Molecular beam epitaxy	0.5 M H_2SO_4	45	64	[28]
MoSSe	Solution method	0.5 M H_2SO_4	164	48	[38]
$MoS_{2x}Se_{2(1-x)}$	Hydrothermal	0.5 M H_2SO_4	136	50	[29]
SeMoS	CVD	0.5 M H_2SO_4	> 200	-	[30]
Te-doped WS_2	CVD	0.5 M H_2SO_4	213	94	[35]
$MoSe_xS_{2-x}$	Electrochemical exfoliation	1 M KOH	123	123	[54]
$Mo(S_{1-x}Se_x)_2$	Hydrothermal	0.5 M H_2SO_4	161	42.8	[67]
MoS_2/WTe_2	CVD, solvothermal	0.5 M H_2SO_4	140	40	[68]
$W(Se_xS_{1-x})_2$	EChem anodization, CVD	0.5 M H_2SO_4	45	59	[69]
$MoS_{0.46}Te_{0.58}$/Gr	Microwave irradiation	0.5 M H_2SO_4	62.2	61.1	This work

5.4. Summary

In summary, the hybrid molybdenum sulfotelluride (MoS_xTe_y) nanosheets were prepared intertwined with graphene network *via* a simple and rapid (60 sec) microwave−assisted heating approach. Applying this strategy, a remarkable reduction of processing time from hour−scale to minute−scale compared to the conventional approaches has been achieved. Various samples with different precursor ratios were explored and their electrocatalytic HER activities were examined in acidic medium. It is evidenced that the HER catalytic activity is noticeably modified with the ratio of Mo, S and Te elements. The best result was found from the $MoS_{0.46}Te_{0.58}$/Gr nanocomposite consisting slightly more Te than S atom and higher amount of Mo than the stoichiometry, which shows a small overpotential of only 62.2 mV to reach the cathodic current density of 10 mA cm^{-2}, a small Tafel slope of 61.1 mV dec^{-1}, high TOF of 0.53 s^{-1} at an overpotential of 150 mV and negligible degradation of activity from long−term stability tests. This excellent electrocatalytic behavior is derived from the coexistence of S and Te atoms which reduces the apparent activation energy by creating more active sites in defect−rich catalyst surface, accelerating both ion and electron transfer and the presence of graphene improves the electrical conductivity. In addition, the computational results clearly provide microscopic insight by way of effective hydrogen binding free energy values into the experimental catalytic performance for HER. Here, it has been deduced that the most active sites for catalysis of the molybdenum sulfotelluride/graphene nanocomposite are primarily comprised of exposed Mo atoms. This combined computational and experimental study shows the very high potential for the metal-rich molybdenum sulfotelluride nano-electrocatalyst with graphene support for hydrogen generation through water electrolysis. Moreover, in basis of the proposed microwave−assisted synthesis method, other hybrid metal chalcogenides can also be prepared in large−scale with low cost, high efficiency, and stability, which will boost the practical applications of metal chalcogenide−based heterostructures as high−performance HER electrocatalysts.

5.5. References

1 A. Ursua, P. Sanchis and L. M. Gandia, *Proc. IEEE*, 2012, **100**, 410–426.

2 J. Chi and H. Yu, *Cuihua Xuebao/Chinese J. Catal.*, 2018, **39**, 390–394.

3 S. Shiva Kumar and V. Himabindu, *Mater. Sci. Energy Technol.*, 2019, **2**, 442–454.

4 A. Li, Y. Sun, T. Yao and H. Han, *Chem. - A Eur. J.*, 2018, **24**, 18334–18355.

5 A. Eftekhari, *Int. J. Hydrogen Energy*, 2017, **42**, 11053–11077.

6 Y. Zheng, Y. Jiao, Y. Zhu, L. H. Li, Y. Han, Y. Chen, M. Jaroniec and S. Z. Qiao, *J. Am.*

Chem. Soc., 2016, **138**, 16174–16181.

7 M. Smiljanic, Z. Rakocevic, A. Maksic and S. Strbac, *Electrochim. Acta*, 2014, **117**, 336–343.

8 S. Trasatti, *J. Electroanal. Chem.*, 1972, **39**, 163–184.

9 G. Zhou, Y. Shan, L. Wang, Y. Hu, J. Guo, F. Hu, J. Shen, Y. Gu, J. Cui, L. Liu and X. Wu, *Nat. Commun.*, **10**, 399 (2019).

10 R. Wang, J. Han, X. Zhang and B. Song, *J. Mater. Chem. A*, 2018, **6**, 21847–21858.

11 K. C. Majhi and M. Yadav, *Int. J. Hydrogen Energy*, 2020, **45**, 24219–24231.

12 K. S. Bhat and H. S. Nagaraja, *Int. J. Hydrogen Energy*, 2019, **44**, 17878–17886.

13 H. Du, R. M. Kong, X. Guo, F. Qu and J. Li, *Nanoscale*, 2018, **10**, 21617–21624.

14 Y. Shi and B. Zhang, *Chem. Soc. Rev.*, 2016, **45**, 1529–1541.

15 S. Meyer, A. V. Nikiforov, I. M. Petrushina, K. Köhler, E. Christensen, J. O. Jensen and N. J. Bjerrum, *Int. J. Hydrogen Energy*, 2015, **40**, 2905–2911.

16 W. F. Chen, J. T. Muckerman and E. Fujita, *Chem. Commun.*, 2013, **49**, 8896–8909.

17 Y. Li, Y. Yu, Y. Huang, R. A. Nielsen, W. A. Goddard, Y. Li and L. Cao, *ACS Catal.*, 2015, **5**, 448–455.

18 S. K. Park, J. K. Kim and Y. C. Kang, *ACS Sustain. Chem. Eng.*, 2018, **6**, 12706–12715.

19 S. Xie, B. Sun, H. Sun, K. Zhan, B. Zhao, Y. Yan and B. Y. Xia, *Int. J. Hydrogen Energy*, 2019, **44**, 15009–15016.

20 C. Du, H. Huang, J. Jian, Y. Wu, M. Shang and W. Song, *Appl. Catal. A Gen.*, 2017, **538**, 1–8.

21 M. Ghorbani-Asl, S. Kretschmer, D. E. Spearot and A. V. Krasheninnikov, 2017 *2D Mater.* **4** 025078.

22 G. Zhao, K. Rui, S. X. Dou and W. Sun, *Adv. Funct. Mater.*, 2018, **28**, 1–26.

23 M. Li, M. Yu and X. Li, *Appl. Surf. Sci.*, 2018, **439**, 343–349.

24 G. Ou, P. Fan, X. Ke, Y. Xu, K. Huang, H. Wei, W. Yu, H. Zhang, M. Zhong, H. Wu and Y. Li, *Nano Res.*, 2018, **11**, 751–761.

25 W. Shi, G. Li and Z. Wang, *J. Phys. Chem. C*, 2019, **123**, 12261–12267.

26 J. Yuan, Y. Shan and T. Li, *J. Phys. D. Appl. Phys.*, 2020 *J. Phys. D: Appl. Phys.* **53** 125502.

27 S. Li, W. Zang, X. Liu, S. J. Pennycook, Z. Kou, C. Yang, C. Guan and J. Wang, *Chem.*

Eng. J., 2019, **359**, 1419–1426.

28 T. Kosmala, H. Coy Diaz, H. P. Komsa, Y. Ma, A. V. Krasheninnikov, M. Batzill and S. Agnoli, *Adv. Energy Mater.*, 2018, **8**, 1–8.

29 R. Wang, X. Li, T. Gao, T. Yao, S. Liu, X. Wang, J. Han, P. Zhang, X. Cao, X. Zhang, Y. Zhang and B. Song, *ChemCatChem*, 2019, **11**, 3200–3211.

30 J. Zhang, S. Jia, I. Kholmanov, L. Dong, D. Er, W. Chen, H. Guo, Z. Jin, V. B. Shenoy, L. Shi and J. Lou, *ACS Nano*, 2017, **11**, 8192–8198.

31 J. Yang, Y. Liu, C. Shi, J. Zhu, X. Yang, S. Liu, L. Li, Z. Xu, C. Zhang and T. Liu, *ACS Appl. Energy Mater.*, 2018, **1**, 7035–7045.

32 H. Yang, T. Zhang, H. Zhu, M. Zhang, W. W. Wu and M. L. Du, *Int. J. Hydrogen Energy*, 2017, **42**, 1912–1918.

33 B. Konkena, J. Masa, W. Xia, M. Muhler and W. Schuhmann, *Nano Energy*, 2016, **29**, 46–53.

34 S. Hussain, S. A. Patil, D. Vikraman, I. Rabani, A. A. Arbab, S. H. Jeong, H. S. Kim, H. Choi and J. Jung, *Appl. Surf. Sci.*, 2020, **504**, 144401.

35 Y. Pan, F. Zheng, X. Wang, H. Qin, E. Liu, J. Sha, N. Zhao, P. Zhang and L. Ma, *J. Catal.*, 2020, **382**, 204–211.

36 M. Yagmurcukardes, C. Sevik and F. M. Peeters, *Phys. Rev. B*, 2019, **100**, 1–8.

37 M. Idrees, H. U. Din, R. Ali, G. Rehman, T. Hussain, C. V. Nguyen, I. Ahmad and B. Amin, *Phys. Chem. Chem. Phys.*, 2019, **21**, 18612–18621.

38 Q. Gong, L. Cheng, C. Liu, M. Zhang, Q. Feng, H. Ye, M. Zeng, L. Xie, Z. Liu and Y. Li, *ACS Catal.*, 2015, **5**, 2213–2219.

39 Q. Feng, Y. Zhu, J. Hong, M. Zhang, W. Duan, N. Mao, J. Wu, H. Xu, F. Dong, F. Lin, C. Jin, C. Wang, J. Zhang and L. Xie, *Adv. Mater.*, 2014, **26**, 2648–2653.

40 R. Parsons, *Trans. Faraday Soc.*, 1958, **54**, 1053–1063.

41 B. Hinnemann, P. G. Moses, J. Bonde, K. P. Jørgensen, J. H. Nielsen, S. Horch, I. Chorkendorff and J. K. Nørskov, *J. Am. Chem. Soc.*, 2005, **127**, 5308–5309.

42 T. Liao, Z. Sun, C. Sun, S. X. Dou and D. J. Searles, *Sci. Rep.*, 2014, **4**, 1–7.

43 H. Tang, K. Dou, C. C. Kaun, Q. Kuang and S. Yang, *J. Mater. Chem. A*, 2014, **2**, 360–364.

44 S. Sarwar, A. Ali, Z. Liu, J. Li, S. Uprety, H. Lee, R. Wang, M. Park, M. J. Bozack, A. J.

Adamczyk and X. Zhang, *J. Colloid Interface Sci.*, 2021, **581**, 847–859.

45 D. B. Putungan, S. H. Lin and J. L. Kuo, *Phys. Chem. Chem. Phys.*, 2015, **17**, 21702–21708.

46 H. Gerischer, *Bull. Soc. Chim. Belg.*, 1958, **67**, 506–527.

47 S. Sarwar, A. Nautiyal, J. Cook, Y. Yuan, J. Li, S. Uprety, R. Shahbazian-Yassar, R. Wang, M. Park, M. J. Bozack and X. Zhang, *Sci. China Mater.*, 2020, **63**, 62–74.

48 W. Kohn and L. J. Sham, *Phys. Rev.*, 1965, **140**, 1133–1136.

49 G. P. Srivastava and D. Weaire, *Adv. Phys.*, 1987, **36**, 463–517.

50 S. J. Clark, M. D. Segall, C. J. Pickard, P. J. Hasnip, M. I. J. Probert, K. Refson and M. C. Payne, *Zeitschrift fur Krist. Mater.*, 2005, **220**, 567–570.

51 A. J. Adamczyk, *Surf. Sci.*, 2019, **682**, 84–98.

52 G. Lozano-Blanco and A. J. Adamczyk, *Surf. Sci.*, 2019, **688**, 31–44.

53 S. Wu, B. J. Tatarchuk and A. J. Adamczyk, *Surf. Sci.*, 2021, **708**, 121834.

54 J. Si, H. Chen, C. Lei, Y. Suo, B. Yang, Z. Zhang, Z. Li, L. Lei, J. Chen and Y. Hou, *Nanoscale*, 2019, **11**, 16200–16207.

55 V. Shokhen, Y. Miroshnikov, G. Gershinsky, N. Gotlib, C. Stern, D. Naveh and D. Zitoun, *Sci. Rep.*, 2017, **7**, 1–11.

56 Z. Wang, W. Wang, Y. Yang, W. Li, L. Feng, J. Zhang, L. Wu and G. Zeng, *Int. J. Photoenergy*, 2014, 956083.

57 A. P. Murthy, J. Theerthagiri and J. Madhavan, *J. Phys. Chem. C*, 2018, **122**, 23943–23949.

58 Z. Chen, D. Cummins, B. N. Reinecke, E. Clark, M. K. Sunkara and T. F. Jaramillo, *Nano Lett.*, 2011, **11**, 4168–4175.

59 J. Kibsgaard and T. F. Jaramillo, *Angew. Chemie - Int. Ed.*, 2014, **53**, 14433–14437.

60 X. Dai, K. Du, Z. Li, M. Liu, Y. Ma, H. Sun, X. Zhang and Y. Yang, *ACS Appl. Mater. Interfaces*, 2015, **7**, 27242–27253.

61 B. E. Conway and D. J. MacKinnon, *J. Electrochem. Soc.*, 1969, **116**, 1665.

62 Z. Da He, J. Wei, Y. X. Chen, E. Santos and W. Schmickler, *Electrochim. Acta*, 2017, **255**, 391–395.

63 H. Sun, Z. Ma, Y. Qiu, H. Liu and G. gang Gao, *Small*, 2018, **14**, 1–12.

64 T. F. Jaramillo, K. P. Jørgensen, J. Bonde, J. H. Nielsen, S. Horch and I. Chorkendorff,

Science (80)., 2007, **317**, 100–102.

65 S. Gudmundsdóttir, E. Skúlason, K. J. Weststrate, L. Juurlink and H. Jónsson, *Phys. Chem. Chem. Phys.*, 2013, **15**, 6323–6332.

66 J. K. Nørskov, T. Bligaard, A. Logadottir, J. R. Kitchin, J. G. Chen, S. Pandelov and U. Stimming, *J. Electrochem. Soc.*, 2005, **152**, 7–10.

67 Z. Lin, B. Lin, Z. Wang, S. Chen, C. Wang, M. Dong, Q. Gao, Q. Shao, T. Ding, H. Liu, S. Wu and Z. Guo, *ChemCatChem*, 2019, **11**, 2217–2222.

68 Y. Zhou, J. V. Pondick, J. L. Silva, J. M. Woods, D. J. Hynek, G. Matthews, X. Shen, Q. Feng, W. Liu, Z. Lu, Z. Liang, B. Brena, Z. Cai, M. Wu, L. Jiao, S. Hu, H. Wang, C. M. Araujo and J. J. Cha, *Small*, 2019, **15**, 1–11.

69 K. Liang, Y. Yan, L. Guo, K. Marcus, Z. Li, L. Zhou, Y. Li, R. Ye, N. Orlovskaya, Y. H. Sohn and Y. Yang, *ACS Energy Lett.*, 2017, **2**, 1315–1320.

Chapter 6

Direct growth of Co-MoS$_2$/graphene hybrids through microwave irradiation with enhanced electrocatalytic properties for hydrogen evolution reaction

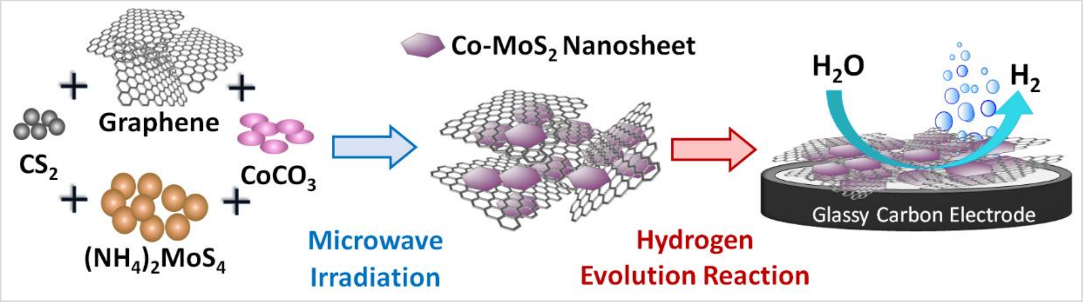

Part of this chapter has been submitted for peer-reviewed journal publication.

Abstract

Molybdenum disulfide (MoS_2) nanosheets are promising candidates as electrode materials for the efficient hydrogen production through water splitting. However, their activities are only governed by the edge sites and their charge transfer efficiencies are still unsatisfactory. Defects generation and hybridization are two very effective ways to tune the nanostructures of MoS_2 and enhance their electrocatalytic properties. Herein, cobalt-doped molybdenum disulfide (Co-MoS_2) nanosheets have been synthesized on graphene network by an ultrafast, facile, and reliable microwave irradiation technique. The structural, morphological, and compositional properties were characterized for these Co-MoS_2/G composites. The compositionally optimized catalyst of as-produced Co-MoS_2/G delivers excellent hydrogen evolution reaction (HER) performance in acidic medium with a low overpotential of 78.1 mV, a small Tafel slope of 40.0 mV per decade, and high exchange current density of 0.0917 mA cm^{-2}, which also exhibits excellent electrochemical stability for 5000 cycles with negligible loss of the cathodic current and long-term durability for 94 h. Co-doping greatly enhanced the intrinsic activity of MoS_2 nanosheet catalyst by creating abundant defects, and in addition, the integration of graphene notably promoted the electrical conductivity and mechanical properties of Co-MoS_2/G composite. This study would supply an ultrafast, simple, and efficient strategy for developing excellent metal-doped electrocatalysts for HER.

6.1. Introduction

In present days, hydrogen (H_2) is extensively being generated by steam and oil reforming processes. However, there is a growing interest in increasing the share of hydrogen production through water electrolysis in order to avoid the use of carbon-based sources.[1–3] Electrochemical water splitting offers an environmentally suitable and technologically promising approach to produce useful hydrogen fuel that can comply with future energy demand.[4,5] To achieve the optimal performance in water splitting, efficient cathode catalysts are required for hydrogen evolution reaction (HER). As known, platinum (Pt) and Pt-group metals are the most electroactive catalysts, but the rareness and high costs limit their large-scale commercial utilization. Therefore, many current researchers are focusing on developing highly effective HER catalysts based on the earth-abundant elements.[5–7] A combination of high surface area, high conductivity, fast charge transfer ability, excellent intrinsic activity, promising stability, material abundancy and low material cost is universally desired for potential HER catalysts. Noble metal-free compounds, such as transition-metal oxides, chalcogenides, carbides, nitrides, phosphides, etc. have been studied vigorously as electrocatalysts for hydrogen generation.[8–13] Recently, the transition-metal dichalcogenides (MX_2, M = Mo, W, Zn, Fe, etc. and X = S, Se, Te) have drawn much attention as efficient HER catalysts.[14–16] Among them, molybdenum disulfide (MoS_2) has received exceptional attention due to the low hydrogen adsorption free energy ($\Delta G_H* \approx 0$) on catalyst surface, which makes it a promising alternative to the Pt catalysts.[8,17,18] Nevertheless, low conductivity, inadequate active sites, restacking of MoS_2 sheets, and the inert S atoms in plane sites make it difficult to achieve high efficiency for hydrogen generation. To overcome these shortcomings, extensive studies have been set forth to develop several nanostructures of MoS_2-based compounds, such as, nanoparticles, nanosheets, nanoribbons, core-shells, etc.[19–24] In addition to the structural optimizations, defect incorporations have also been widely established and acclaimed to enhance the intrinsic activity of MoS_2, such as hybridization with carbon-based materials,[25–27] hybridization with other materials (cadmium sulfide, vanadium sulfide, etc.),[28–30] substitutional doping,[31–33] and 2H to 1T phase conversion,[34,35] etc. Among them, doping with metal elements (such as Co, Fe, Au, Ni, Pt, etc.) is a facile method to achieve structural and/or chemical modifications.[31,36–40] For instance, Dai et al. investigated Co-doping into the MoS_2 nanosheets, which can result MoS_2 with higher surface area, higher active sites, and substantially superior HER activity than pure MoS_2 counterparts.[41] Bose et al. demonstrated that the doping of Co atom on pristine MoS_2 can serve as additional active sites, further enhancing the HER performance.[42] Very recently, Ma et al. reported a hydrothermal method to generate bifunctional catalyst of Co-doped MoS_2 uniformly dispersed on reduced graphene oxide (rGO), both for HER and oxygen evolution reaction (OER).[43] The enhanced HER performance was attributed to the synergetic effects of Co, MoS_2 and rGO by high conductivity and interconnectivity, which formed abundant defects and accelerated the electron transfer. To overcome the poor charge transfer ability of transition-metal doped MoS_2, carbonaceous materials (such as graphene, carbon nanotubes, rGO, etc.) have been widely applied in the fabrication of HER catalysts due to their large specific surface area, superior electron conductivity, and good stability.[33,44–46] Despite of progress in recent works, large-scale fabrication of Co-doped MoS_2 catalysts with improved activity and durability properties still faces several practical challenges. Thus, based on our precent works,[11,47] we propose to fabricate cobalt-doped molybdenum sulfide nanosheets on graphene network (Co-MoS_2/G) by an ultra-fast, facile, reliable, and scalable microwave irradiation process. It is expected that the synergistic effect of Co, MoS_2, and graphene endows the composites with excellent HER activity, good charge transfer ability, along with long-term stability. Besides acting as an intertwined network for anchoring the Co-MoS_2 nanosheets, graphene plays a crucial role during microwave-initiated heating, acting as a microwave susceptor. Our results reveal that the Co-MoS_2/G through microwave irradiation exhibits enhanced electrocatalytic activity comparing to the undoped MoS_2/G with low overpotential, small Tafel slope, high exchange current density and excellent durability, which are superior to the most previously reported Co-doped MoS_2-based electrocatalysts.

6.2. Experimental details

6.2.1. Materials and reagents

Cobalt carbonate ($CoCO_3$) and ammonium tetrathiomolybdate ($(NH_4)_2MoS_4$) precursors were obtained from Alfa Aesar and BeanTown Chemical, Inc., respectively. Graphene was acquired from Magnolia Ridge Inc. 10 wt.% Pt/C catalyst was purchased from Sigma-Aldrich, Inc. For electrochemical characterizations, Ag/AgCl (3 M KCl) reference electrode was purchased from Hach, graphite rod (5 mm diameter) was obtained from Alfa Aesar, and glassy carbon electrode (3 mm diameter) was purchased from CH Instruments, Inc. All chemicals were of analytical grades and applied without further purification.

6.2.2. Preparation of catalyst samples

To prepare the Co-MoS_2/G compounds, commercial powders of $CoCO_3$, $(NH_4)_2MoS_4$, and graphene were mixed with CS_2 solvent homogeneously in a 20 mL scintillation vial based on the different ratio shown in Table 6.1. After that, the vial was air dried and positioned inside a microwave oven, then electromagnetically irradiated for 60 seconds at the power of 1250 W. During the process, graphene absorbs the microwave energy and generates thermal energy (~1000 ºC) by resistive heating, which triggers the vigorous reaction among precursors. Five different Co-MoS_2/G composites were prepared by tailoring the amount of Co−loading from 1 to 10 mg. Following the similar steps, CoS_2/G composite was prepared except adding $(NH_4)_2MoS_4$ precursor and MoS_2/G composite was synthesized except adding the $CoCO_3$ precursor (Table

6.1). In addition, to compare the HER performances, CoO_x/G composite was also synthesized through microwave irradiation.

Table 6.1. Different amounts of precursors to synthesize the hybrid catalysts.

Samples	**$CoCO_3$ (mg)**	**$(NH_4)_2MoS_4$ (mg)**	**CS_2 (μL)**	**Graphene (mg)**	**Microwave power (W)**	**Microwave time (sec)**
Co-MoS_2/G-1	1	15	50	15	1250	60
Co-MoS_2/G-3	3	15	50	15		
Co-MoS_2/G-5	5	15	50	15		
Co-MoS_2/G-8	8	15	50	15		
Co-MoS_2/G-10	10	15	50	15		
CoS_2/G	5	-	50	15		
MoS_2/G	-	15	50	15		
CoO_x/G	5	-	-	15		

6.2.3. Materials characterizations

The morphologies and chemical compositions of catalyst samples were determined by scanning electron microscope (SEM; Apreo FE) connected with an energy dispersive X-ray spectrometer (EDS, EDAX Instruments) applying the 20 kV acceleration voltage. Additionally, transmission electron microscope (TEM, FEI Tecnai F20) was used for further analysis at 200 kV. The crystal structures were investigated by the powder X-ray diffraction (XRD) on a Philips X'pert MPD diffractometer with Cu Kα radiation ($\lambda = 1.54056$ Å) at 45 kV and 40 mA.

Furthermore, to determine the chemical states and compositions of catalyst samples, X-ray photoelectron spectroscopy (XPS) analysis was performed on a Kratos Axis Ultra DLD spectrometer applying a monochromatic Al Kα radiation under UHV condition.

6.2.4. Electrochemical characterizations

To prepare a catalyst ink, 50 mg of active material was uniformly mixed with 5 mg of PVDF (polyvinylidene fluoride) and 2.5 mL of DMF (N, N-dimethylformamide) by 20 mins of sonication. Then, 20 μL of each catalyst ink was loaded onto the clean surface of glassy carbon electrode (GCE, 3 mm in diameter) maintaining a consistent mass loading of around 1 mg cm^{-2} for each sample and vacuum dried at 60 °C for 30 mins. A three-electrode setup was used to perform the tests consisting of a catalyst modified GCE as working electrode, Ag/AgCl (3 M KCl) as reference electrode, and a graphite rod as counter electrode in 0.5 M H_2SO_4 acidic electrolyte. Measured potentials were referred to the reversible hydrogen electrode (RHE) based on the equation, $V\ (vs.\ RHE) = V_{measured}\ (vs.\ Ag/AgCl) + 0.197 + (0.059 \times pH)$. Therefore, prior to each of the test, the *pH* value was measured using a benchtop pH meter.

6.3. Results and discussion

6.3.1. Structural and compositional investigations

The SEM and TEM micrographs (Figure 6.1a and 6.1b) show that the as-prepared Co-doped MoS_2 nanosheets are almost uniformly distributed on graphene flakes. The HRTEM image of Figure 6.1c suggests that, the catalyst is composed of nearly eight or ten layers with an interlayer distance of 0.63 nm, corresponding to the (002) plane of MoS_2 nanosheet. It also shows significant defects in MoS_2 layers due to the Co-doping. In Figure 6.1d−6.1h, the elemental distribution of Co-MoS_2/G-5 for the C, Mo, S and Co species is displayed, respectively. Figure 6.1h shows that the Co element is distributed uniformly in Co-doped MoS_2 composite, which as well confirms that the Co element is successfully doped into MoS_2.

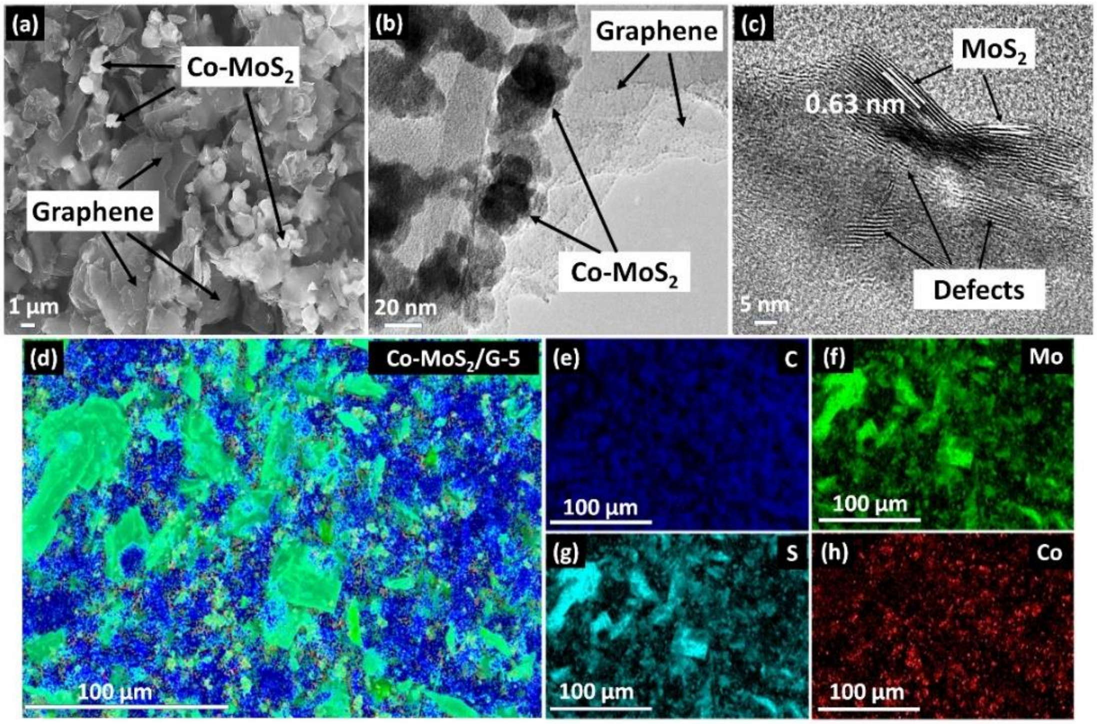

Figure 6.1. (a) SEM, (b) TEM, (c) HRTEM micrographs, and (d) EDS elemental mapping of Co-MoS_2/G-5 composite. (e−h) Elemental distributions of carbon (C), molybdenum (Mo), sulfur (S), and cobalt (Co) species, respectively.

Besides elemental distributions, EDS analysis was also performed to determine the contents of Co-MoS_2/G nanocomposites. Figure 6.2a−6.2e show the EDS results scanning on the surface of as-produced Co-MoS_2/G samples with different Co precursor amounts− 1, 3, 5, 8, and 10 mg, respectively. It illustrates that the atomic ratios of Co: Mo: S in the samples are about (0.25: 1.0: 2.25), (0.45: 1.0: 1.99), (0.31: 1.0: 1.74), (1.19: 1.0: 2.10), and (0.71: 1.0: 1.79), respectively, which further confirms the direct growth of Co-contained MoS_2 on graphene.

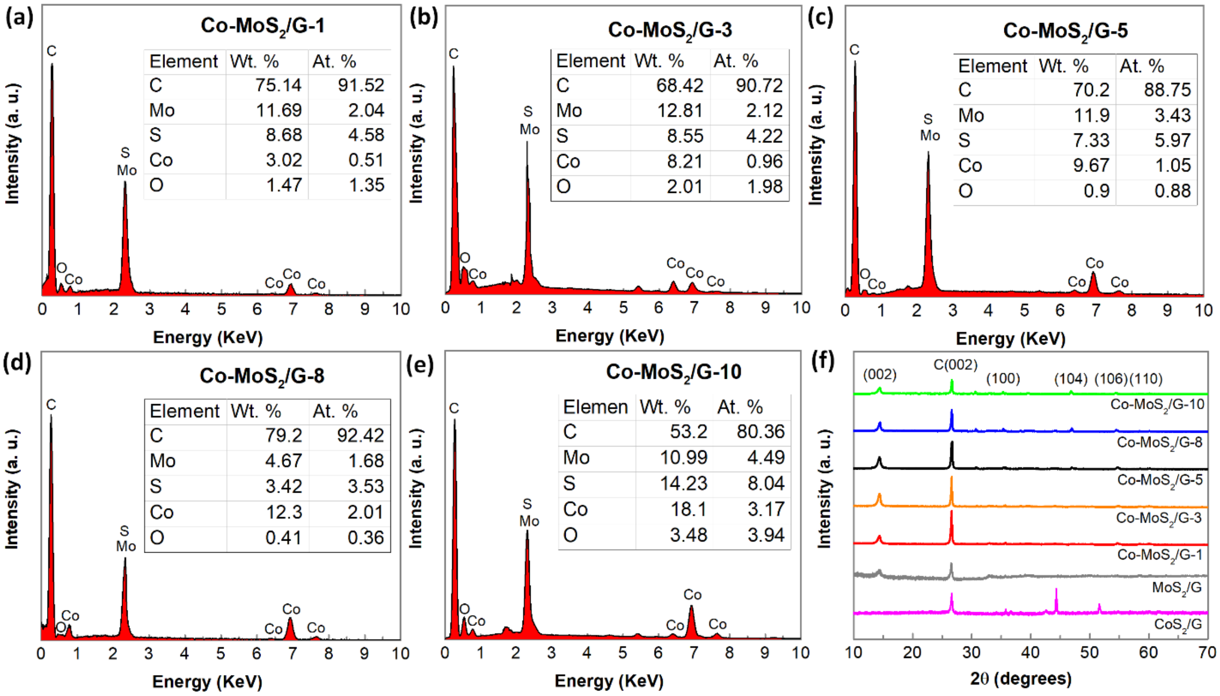

(a) Co-MoS$_2$/G-1

Element	Wt. %	At. %
C	75.14	91.52
Mo	11.69	2.04
S	8.68	4.58
Co	3.02	0.51
O	1.47	1.35

(b) Co-MoS$_2$/G-3

Element	Wt. %	At. %
C	68.42	90.72
Mo	12.81	2.12
S	8.55	4.22
Co	8.21	0.96
O	2.01	1.98

(c) Co-MoS$_2$/G-5

Element	Wt. %	At. %
C	70.2	88.75
Mo	11.9	3.43
S	7.33	5.97
Co	9.67	1.05
O	0.9	0.88

(d) Co-MoS$_2$/G-8

Element	Wt. %	At. %
C	79.2	92.42
Mo	4.67	1.68
S	3.42	3.53
Co	12.3	2.01
O	0.41	0.36

(e) Co-MoS$_2$/G-10

Elemen	Wt. %	At. %
C	53.2	80.36
Mo	10.99	4.49
S	14.23	8.04
Co	18.1	3.17
O	3.48	3.94

Figure 6.2. EDS analysis of (a) Co-MoS$_2$/G-1, (b) Co-MoS$_2$/G-3, (c) Co-MoS$_2$/G-5, (d) Co-MoS$_2$/G-8, and (e) Co-MoS$_2$/G-10. (f) XRD patterns for as-synthesized catalysts.

In addition, Figure 6.2f shows the XRD patterns of five different Co-MoS$_2$/G samples, MoS$_2$/G, and CoS$_2$/G samples. All the curves display a high intensity peak at ~26° as a reflection from carbon layers (002) of graphene. The peaks appearing in Co-MoS$_2$/G samples and MoS$_2$/G at 14.2°, 35.2°, 46.8°, 54.4°, and 58.5° are corresponding to (002), (100), (104), (106), and (110) planes, respectively, indexed to hexagonal crystalline MoS$_2$ (JCPDS card No. 37-1492).[48] The results confirm the synthesis of high purity Co-MoS$_2$/G and MoS$_2$/G composites since no impurity peaks were detected. The XRD patterns were also compared with CoS$_2$/G composite. The results indicate that Co is effectively doped into MoS$_2$ instead of forming CoS$_2$ phase, since the XRD pattern of CoS$_2$ does not match with the resultant Co-MoS$_2$/G nanocomposites.

X-ray photoelectron spectroscopy (XPS) was further employed to characterize the chemical states of as-synthesized Co-MoS$_2$/G-5 nanocomposite. As shown in survey spectrum in

Figure 6.3a, two additional peaks were found at around 781.1 eV and 798.9 eV, which are assigned to Co species.[49] It also reveals the atomic ratio of Co: Mo: S is around 0.4: 1.0: 2.4, which closely matches with the EDS result.

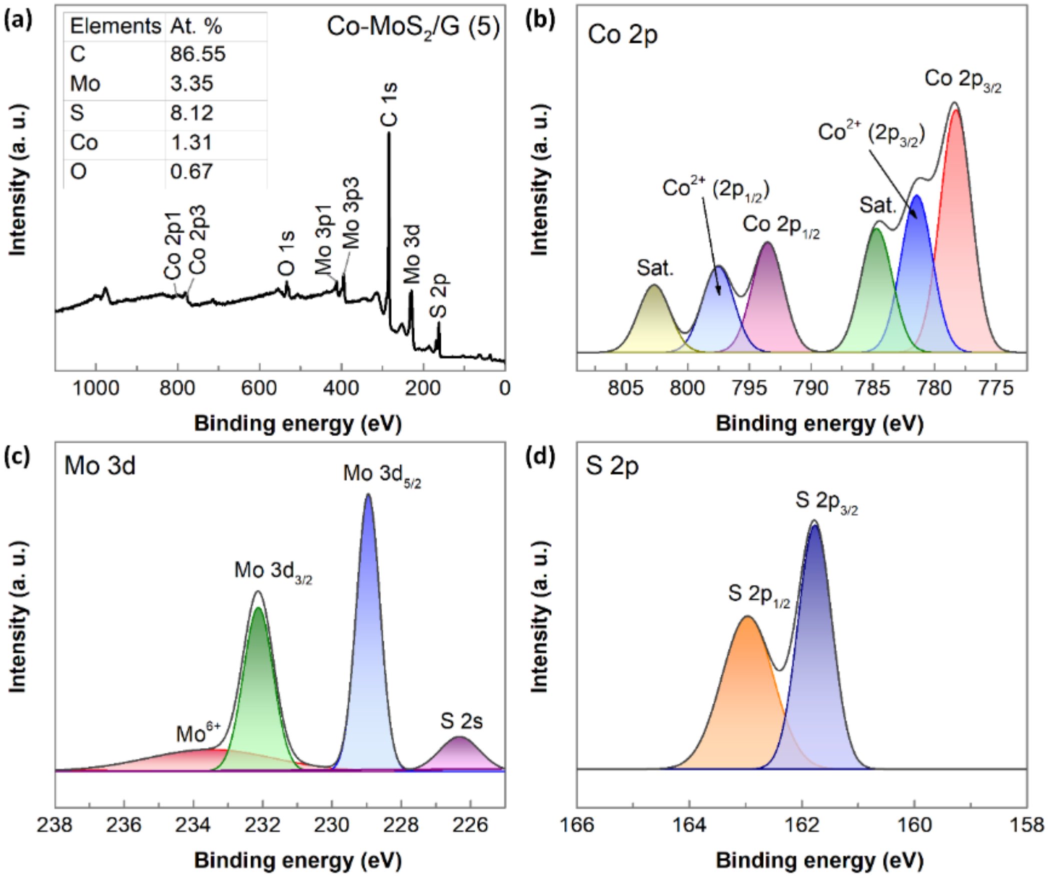

Figure 6.3. (a) XPS survey spectrum of Co-MoS2/G-5 composite. (b−d) High resolution XPS spectra for Co 2p, Mo 3d, and S 2p regions, respectively.

Figure 6.3b−6.3d demonstrate the Co 2p, Mo 3d, and S 2p XPS spectra of Co-MoS2/G-5, respectively. As shown in Figure 6.3b, the peaks appeared at 778.4 eV and 793.5 eV correspond to Co $2p_{3/2}$ and Co $2p_{1/2}$, respectively. These peaks confirm the presence of Co atom replaced the position of Mo atom from the MoS_2 lattice.[48] Whereas, the peaks at 781.4 eV and 797.5 eV belonged to Co^{2+}. The rest peaks at 784.7 eV and 802.7 eV are derived from an extended peak satellite signal.[48] In Figure 6.3c, the peaks at 228.9 eV and 232.1 eV are corresponded to Mo $3d_{5/2}$ and Mo $3d_{3/2}$, respectively, suggesting oxidation states of Mo^{4+}.[50] In Addition, a weak peak at 226.3 eV is attributed to S 2s orbital, which confirms the formation of MoS_2.[50] As shown in Figure 6.3d, The S 2p spectrum exhibits two peaks at 161.8 eV and 162.9 eV, which are assigned to the spin-orbit couple of S $2p_{3/2}$ and S $2p_{1/2}$, respectively.[49] Based on these results, it clearly shows that the Co element is effectively doped into MoS_2 lattice in the microwave-irradiated samples of Co-MoS_2/G.

6.3.2. Electrocatalytic activities of catalyst samples

To investigate the HER activities of as-prepared samples, LSVs were carried out at 2 mV s^{-1} in 0.5 M H_2SO_4 electrolyte at room temperature. Figure 6.4a displays the polarization curves of Co-MoS_2/G samples with different Co-loading (1, 3, 5, 8, and 10 mg), where Co-MoS_2/G-5 with 5 mg of Co-loading exhibits the lowest overpotential (η) of 78.1 mV to reach the current density of 10 mA cm^{-2}. The HER activity improves gradually with the increase in cobalt (Co) from 1, 3, and 5 mg for Co-MoS_2/G-1, Co-MoS_2/G-3, and Co-MoS_2/G-5 samples, respectively. However, the activity decreases for further increase in Co-loading (8 and 10 mg) for Co-MoS_2/G-8 and Co-MoS_2/G-10 samples. This may happen due to the excess amount of cobalt oxide, CoO_x (electrocatalytically less active, shown in Figure 6.4b) decomposed from $CoCO_3$ precursor or the precursor remains unreacted in the nanocomposites. Due to the best results found from Co-MoS_2/G-5 sample, it was selected to carry out the other electrochemical characterizations and comparisons. As shown in Figure 6.4b, it can be clearly observed that the bare GCE, graphene, and CoS_2/G samples do not possess any significant HER activity and the resultant Co-MoS_2/G-5 exhibits improved HER efficiency than the undoped MoS_2/G catalyst. To provide the insights into the HER mechanism, Tafel plots were derived from LSV curves by fitting the linear segments to Tafel equation (Equation 6.1): [51]

$$\eta = b \log i + a \ldots\ldots\ldots\ldots\ldots\ldots (6.1)$$

Here, η represents the overpotential, b is the Tafel slope, i is the current density and a is a constant.

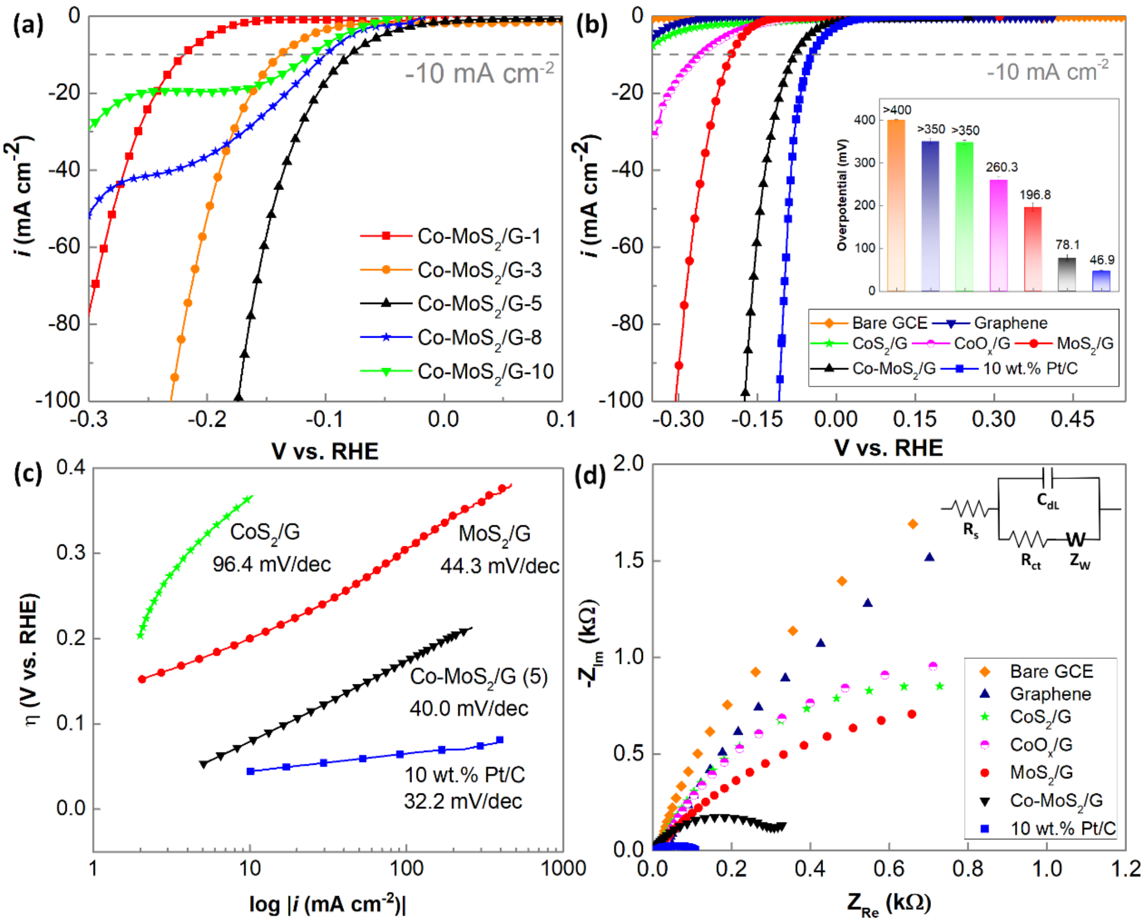

Figure 6.4. (a) LSVs for different Co-MoS_2/G samples. (b) LSVs for bare GCE, graphene, CoS_2/G, CoO_x/G, MoS_2/G, Co-MoS_2/G-5, and 10 wt.% Pt/C catalysts. [Inset: overpotentials of the subsequent catalyst samples]. (c) Tafel slopes for CoS_2/G, MoS_2/G, Co-MoS_2/G-5, and 10 wt.% Pt/C. (d) Nyquist plots at the overpotential of 150 mV vs. RHE.

According to Figure 6.4c, a Tafel slope of 40.0 mV dec^{-1} is observed for Co-MoS$_2$/G-5 catalyst within an overpotential range of 50−200 mV, which is also very close to the value of 10 wt.% Pt/C catalyst (32.2 mV dec^{-1}). It also reveals that the Volmer–Heyrovsky mechanism takes place during the hydrogen evolution on the surface of Co-MoS$_2$/G-5 catalyst.[52] For a particular electrocatalytic system, it is always preferred to achieve lower Tafel slope, which indicates faster reaction taking place. Therefore, the lower Tafel slope of Co-MoS$_2$/G-5 than the CoS$_2$/G and MoS$_2$/G samples further confirms the enhanced catalytic activity after Co incorporation into MoS$_2$/G. This improved HER activity may also be attributed to strong chemical and electronic coupling between Co-doped MoS$_2$ nanosheets and graphene network, resulting in fast electron kinetics between the catalyst and electrode surface. This hypothesis was further confirmed by EIS measurements at an overpotential of 150 mV. As shown in Figure 6.4d, in the high frequency zone, both MoS$_2$/G and Co-MoS$_2$/G-5 exhibit one capacitive semicircle, inferring that the reaction is kinetically controlled. The electrical equivalent circuit diagram (shown in top right corner) is used to model the electrode/electrolyte interface, where the C_{dL} is associated to electrical double layer capacitance and W is corresponding to Warburg impedance. Though the solution resistance (R_s) values are almost similar for all catalyst samples, but the Co-MoS$_2$/G-5 shows lower charge transfer resistance (R_{ct}) of 0.36 kΩ than other samples, except only 10 wt.% Pt/C (0.12 kΩ). Hence, much faster electron transfer is one of the key factors contributing to the superior HER kinetics for Co-MoS$_2$/G-5 catalyst. All major HER parameters are displayed in Table 6.2, measured from LSV and EIS analyses.

Table 6.2. Major electrochemical parameters of Co-MoS_2/G-5 nanocomposite, comparing with graphene, as-produced CoS_2/G, CoO_x/G, MoS_2/G samples, and 10 wt.% Pt/C catalyst.

Samples	**η at 10 mA cm^{-2} (mV vs. RHE)**	**Tafel slope (mV dec^{-1})**	**Solution resistance, R_s (Ω)**	**Charge transfer resistance, R_{ct} (kΩ)**
Bare GCE	>400.0	-	12.81	5.14
Graphene	>350.0	-	10.21	4.72
CoS_2/G	>350.0	96.4	12.10	1.38
CoO_x/G	260.3	-	11.90	1.46
MoS_2/G	196.8	44.3	11.72	1.23
Co-MoS_2/G-5	78.1	40.0	8.01	0.36
10 wt.% Pt/C	46.9	32.2	7.78	0.12

Moreover, the double-layer capacitance (C_{dl}) was measured to predict the electrochemically active surface area, by a simple cyclic voltammetry (CV) approach.[41] The CV measurements were performed within a potential range of 0.3−0.4 V *vs.* RHE as shown in Figure 6.5a−6.5d, where the currents are mainly ascribed to the charging of double layer at electrode/electrolyte interface. The measured C_{dl} values were recorded as a function of average capacitive current, $\frac{1}{2}(i_a - i_c)$ at 0.35 V vs RHE within the scan rate of 10−100 mV s^{-1} in 0.5 M H_2SO_4 electrolyte.

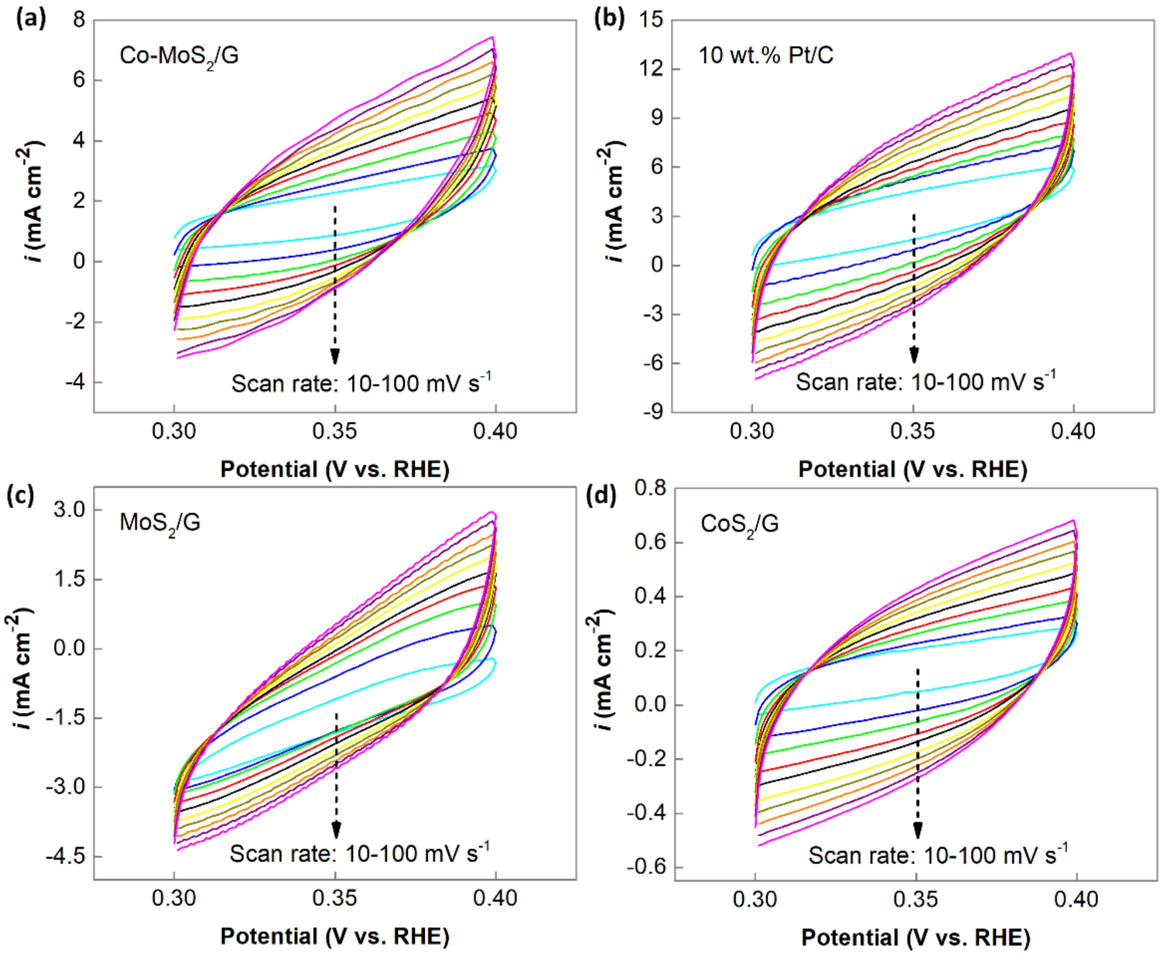

Figure 6.5. CV curves of (a) Co-MoS$_2$/G-5, (b) 10 wt.% Pt/C, (c) MoS$_2$/G, and (d) CoS$_2$/G in a potential window without faradaic reaction at the scan rates of 10−100 mVs^{-1} in 0.5 M H_2SO_4.

As displayed in Figure 6.6, the C_{dl} values of 10 wt.% Pt/C, Co-MoS$_2$/G-5, MoS$_2$/G, and CoS$_2$/G were calculated as 42.79, 22.52, 12.81, and 2.99 mF cm^{-2}, respectively, which reveals that the C_{dl} of Co-MoS$_2$/G-5 catalyst is approximately 2 times higher than the undoped MoS$_2$/G. These results clearly indicate the formation of defects due to Co-doping, which creates higher percentage of the active sites, further enhancing the HER activities.

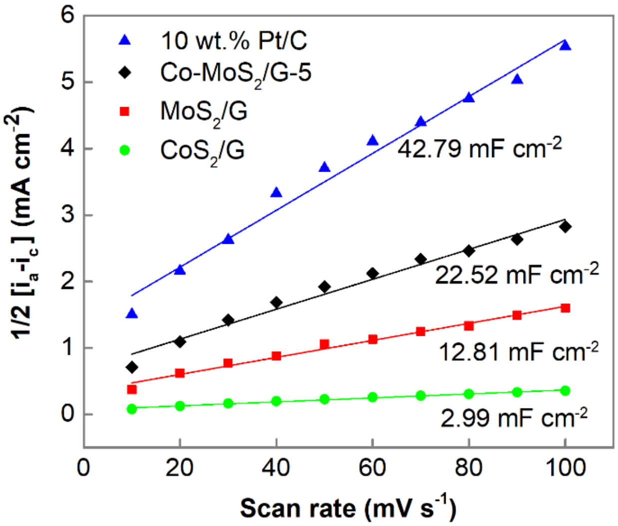

Figure 6.6. EDLC measurements for 10 wt.% Pt/C, Co-MoS$_2$/G-5, MoS$_2$/G, and CoS$_2$/G catalysts.

In addition, Figure 6.7a represents the Nyquist plots of Co-MoS$_2$/G-5 catalyst at various overpotentials of 50–200 mV. In this system, R_{ct} decreases significantly with increasing the overpotentials, from 3.96 kΩ at 50 mV to only 0.006 kΩ at 200 mV (Table 6.3). Lower R_{ct} demonstrates faster electrocatalytic activity at higher overpotential. Besides, the exchange current density (i_0) is considered as another important parameter which is generally proportional to the active surface area of catalyst materials. The i_0 can be obtained from the linearized *Butler-Volmer equation* (Equation 6.2):[43,53]

$$i_0 = \frac{RT}{nFAR_{ct}} \quad \text{……………………………………………………………………..….. (6.2)}$$

At low overpotential, the charge transfer reaction is assumed as a one-electron process (n = 1), and the surface area (A) is assumed to be the geometric area (0.0707 cm^2) of catalyst coating. Considering the overpotential at 50 mV, the i_0 of Co-MoS$_2$/G-5 is thus found to be –

$$i_0 = \frac{8.314\ Jmol^{-1}K^{-1} \times 298\ K}{1 \times 96485.33\ Cmol^{-1} \times 0.0707\ cm^2 \times 3960\ \Omega} = 0.0917 \times 10^{-3}\ A\ cm^{-2}$$

In comparison, the Nyquist plots of 10 wt.% Pt/C catalyst are shown in Figure 6.7b and based on the R_{ct} values from Table 6.3, the i_0 is calculated as 0.2115×10^{-3} A cm^{-2} at 50 mV.

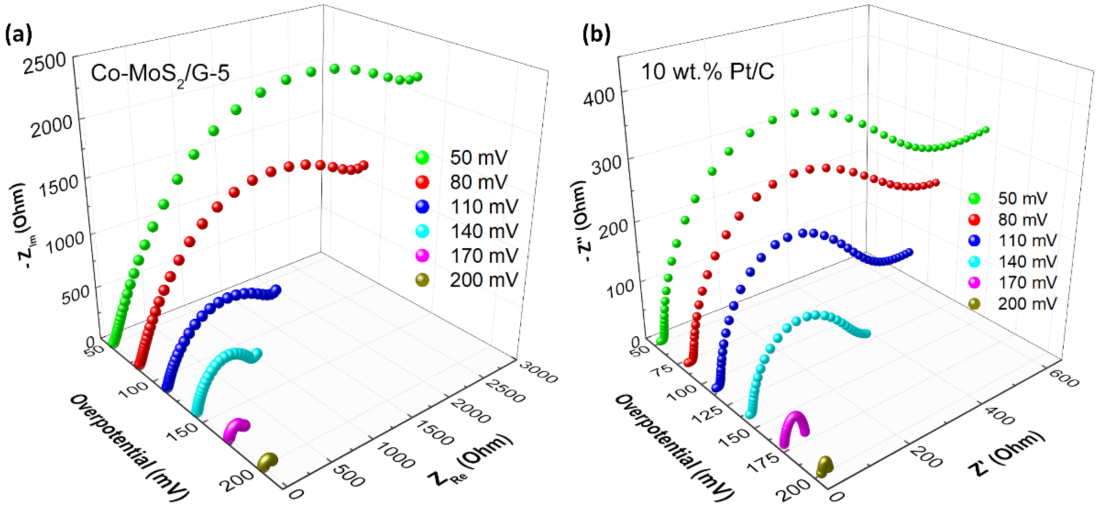

Figure 6.7. Nyquist plots showing the EIS responses of (a) Co-MoS$_2$/G-5 and (b) 10 wt.% Pt/C catalysts at various overpotentials (50−200 mV).

Table 6.3. R_s and R_{ct} values of Co-MoS$_2$/G and 10 wt.% Pt/C catalysts.

	Co-MoS$_2$/G		**10 wt.% Pt/C**	
η (mV)	**R_s (Ω)**	**R_{ct} (kΩ)**	**R_s (Ω)**	**R_{ct} (kΩ)**
50	8.845	3.960	8.003	1.717
80	8.656	2.741	7.890	1.025
110	8.412	1.910	7.901	0.698
140	8.012	0.389	7.801	0.276
170	8.001	0.115	7.718	0.021
200	7.982	0.006	7.705	0.002

Moreover, the turnover frequency (TOF) was determined for HER catalysts, which estimates the number of hydrogen molecules formed per active site of catalyst material per 1 second. If the cathodic current is considered solely designated to hydrogen evolution, TOF can be measured from the following relationship:[54,55]

$$\mathrm{TOF} = \frac{\text{No. of total hydrogen turn overs/cm}^2\ \text{geometric area}}{\text{No. of active sites/cm}^2\ \text{geometric area}} \quad \ldots\ldots\ldots\ldots\ldots\ldots\ldots\ldots\ldots\ldots\ldots \text{(6.3)}$$

Dai et al. described a simple electrochemical approach to measure the TOF values.[41] Based on their method, CV measurements (Figure 6.8) were performed for each of the catalyst samples in phosphate buffer (pH = 7) at a scan rate of 10 mV s^{-1}. Amount of charge (Q) was measured from the equation, $Q = \frac{CV\ Area}{Scan\ rate}$, and the number of active sites (n) was determined by $n = \frac{Q}{2F}$, where F is the Faraday constant. Finally, the TOF = $\frac{I}{nF} \times \frac{1}{2}$; where, I represents the current (A) at specific overpotential (η) during the LSV measurement in 0.5 M H_2SO_4.

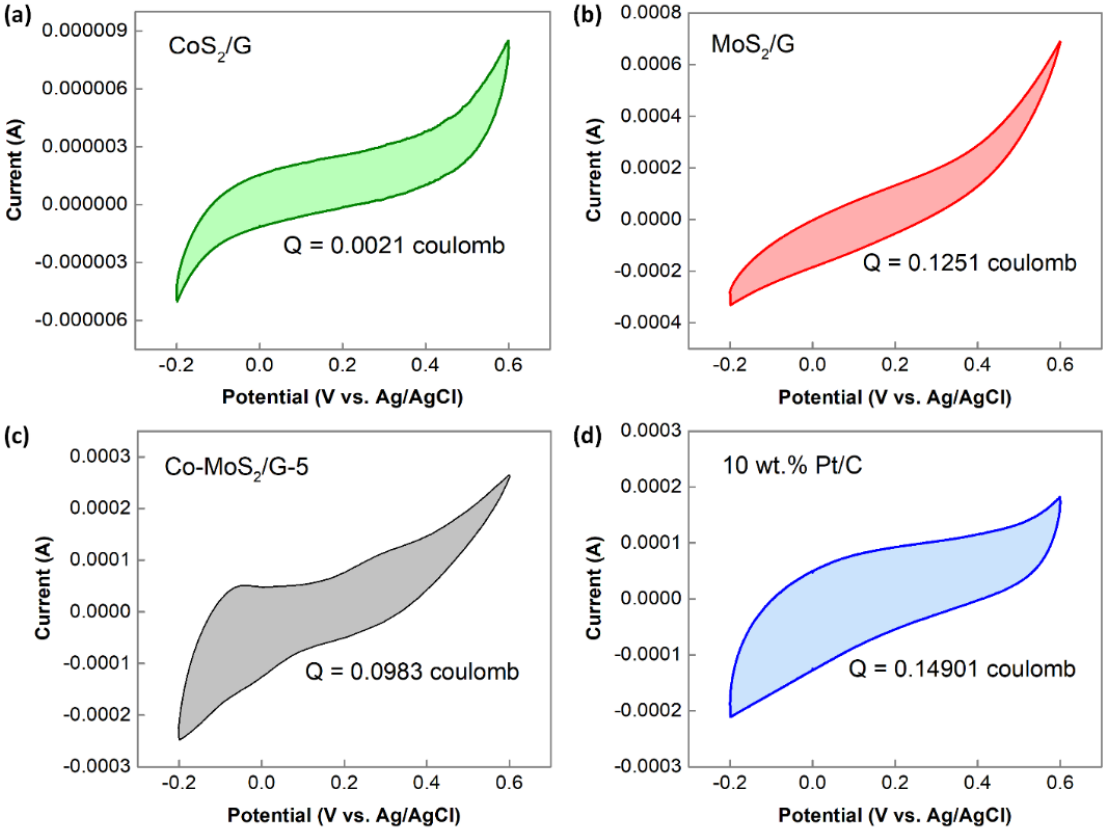

Figure 6.8. CV measurements of (a) CoS_2/G, (b) MoS_2/G, (c) Co-MoS_2/G-5, and (d) 10 wt.% Pt/C at 10 mVs^{-1} in a phosphate buffer solution.

From Figure 6.9 and Table 6.4, it can be clearly depicted that the TOF of Co-MoS_2/G-5 is higher than CoS_2/G and MoS_2/G catalysts within a wide range of overpotential (10−200 mV). Although, the TOF of 10 wt.% Pt/C catalyst is much higher than the as-produced Co-MoS_2/G-5 nanocomposite, it is still very promising and comparable with previously reported values.[41,42]

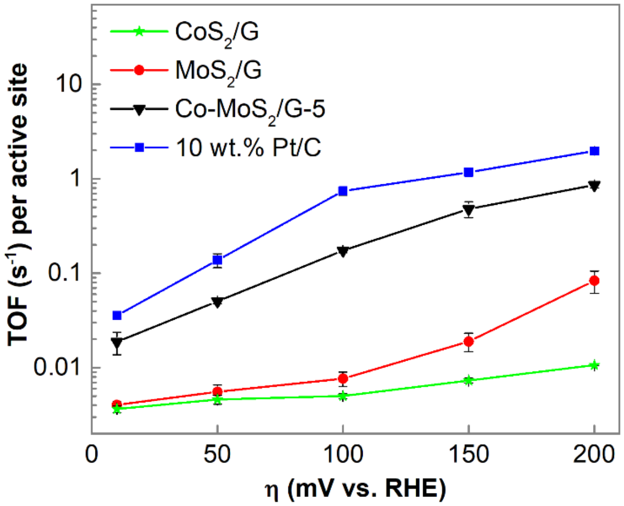

Figure 6.9. TOF measurements of catalyst samples in the overpotential range of 10−200 mV.

Table 6.4. Turn over frequencies (TOFs) of catalyst samples.

Overpotentials (mV)	**10**	**50**	**100**	**150**	**200**
	TOF (s^{-1})				
CoS_2/G	0.004	0.005	0.005	0.007	0.011
MoS_2/G	0.004	0.006	0.008	0.019	0.083
Co-MoS_2/G-5	0.019	0.051	0.174	0.481	0.858
10 wt.% Pt/C	0.035	0.138	0.743	1.174	1.976

Furthermore, the LSV tests (Figure 6.10a) were performed at a wide range of temperature from 30−120 ºC for Co-MoS_2/G-5 sample in 0.5 M H_2SO_4 electrolyte. Based on these results, the activation energy (E_a) can be measured by Arrhenius rate equation: $k = Ae^{-\frac{E_a}{RT}}$; [56] where, k is the rate of reaction, A is pre−exponential factor, R represents universal gas constant, and T is the absolute temperature. In general, the E_a is defined as the difference in electronic energy between the transition and initial states of catalyst material, which is a key factor to determine the HER efficiency.

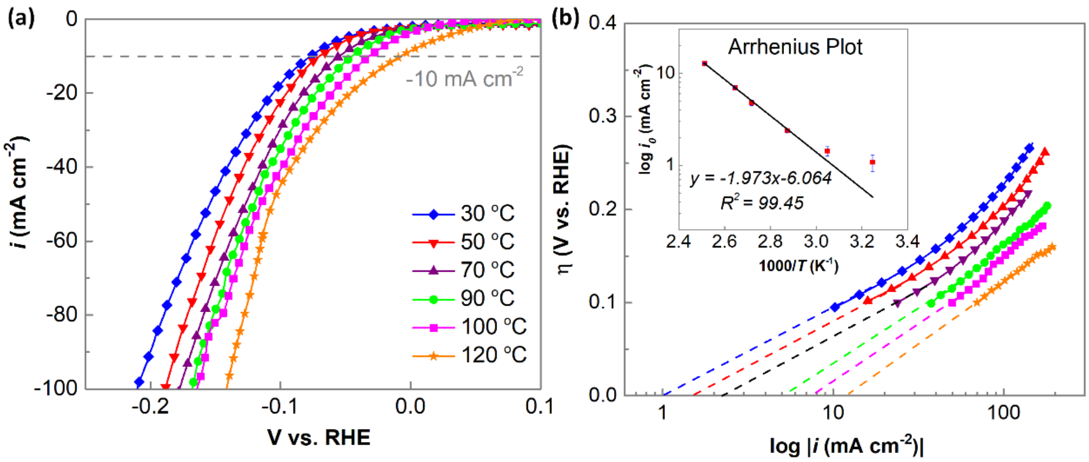

Figure 6.10. LSVs of Co-MoS$_2$/G-5 within a temperature range of 30−120 ºC. (d) Corresponding Tafel slops [Inset: Arrhenius plot].

Based on the findings in Figure 6.10a, 6.10b and Table 6.5, the HER activity improves with an increase in operating temperature by lowering the overpotentials and increasing exchange current density (i_0). The Arrhenius plot, log(i_0) *vs.* $\frac{1000}{T}$ was drawn (inset in Figure 6.10b) based on the following equation:

$$\log i_0 = logA - \frac{E_a}{2.3\ RT} \quad \ldots\ldots (6.4)$$

Where, the rate of reaction (k) is signified by the exchange current density (i_0). The activation energy (E_a) was found to be 37.73 ± 1.26 kJ mol^{-1} or around 0.4 eV for Co-MoS$_2$/G-5 sample, which is very close to the value of platinum and other noble catalysts (20.0 to 40.0 kJ mol^{-1}).[57–59] This low value of E_a also indicates that the higher HER activity of Co-MoS$_2$/G-5 catalyst was due to the higher intrinsic activity as well as the large surface area created from the defects of Co-doping.

Table 6.5. Parameters to calculate the activation energy of Co-MoS_2/G-5 catalyst.

Temperature (°C)	**η (mV vs. RHE)**	**log i_0 (mA cm^{-2})**	**Act. Energy (kJ mol^{-1})**
30	77.14	1.079	37.73 ± 1.26
50	70.06	1.428	
70	54.89	2.370	
90	45.81	4.793	
100	32.65	6.972	
120	10.49	12.779	

The electrocatalytic stability is another key factor to assess a HER catalyst and to evaluate that, 5000 cycles of CV scanning were performed at a scan rate of 50 mV s^{-1} for Co-MoS_2/G-5 catalyst in the same acidic medium of 0.5 M H_2SO_4. Figure 6.11a displays the corresponding LSV curves, which indicates a small shift of overpotential (17 mV) comparing to the initial curve at a high current density of −300 mA cm^{-2}. In addition, a continuous HER test was carried out at a constant potential of 150 mV *vs.* RHE, as shown in Figure 6.11b. The high stability of Co-MoS_2/G-5 catalyst is demonstrated by the steady current for 94 h with a small shift from −53.98 to −77.54 mA cm^{-2}. The fluctuations in this time-dependent curve may originate from damage generations in the catalyst structure caused by the continuous formation of H_2 bubbles. In addition, double-layer capacitance (C_{dl}) was again measured after 5000 cycles of continuous HER test. Based on the results from Figure 6.11c and 6.11d, it clearly demonstrates the increase in C_{dl} from 22.52 to 48.43 mF cm^{-2}, which confirms the activation of Co-MoS_2/G-5 taking place during the long run, due to increase in surface area for excessive H_2 bubbling.

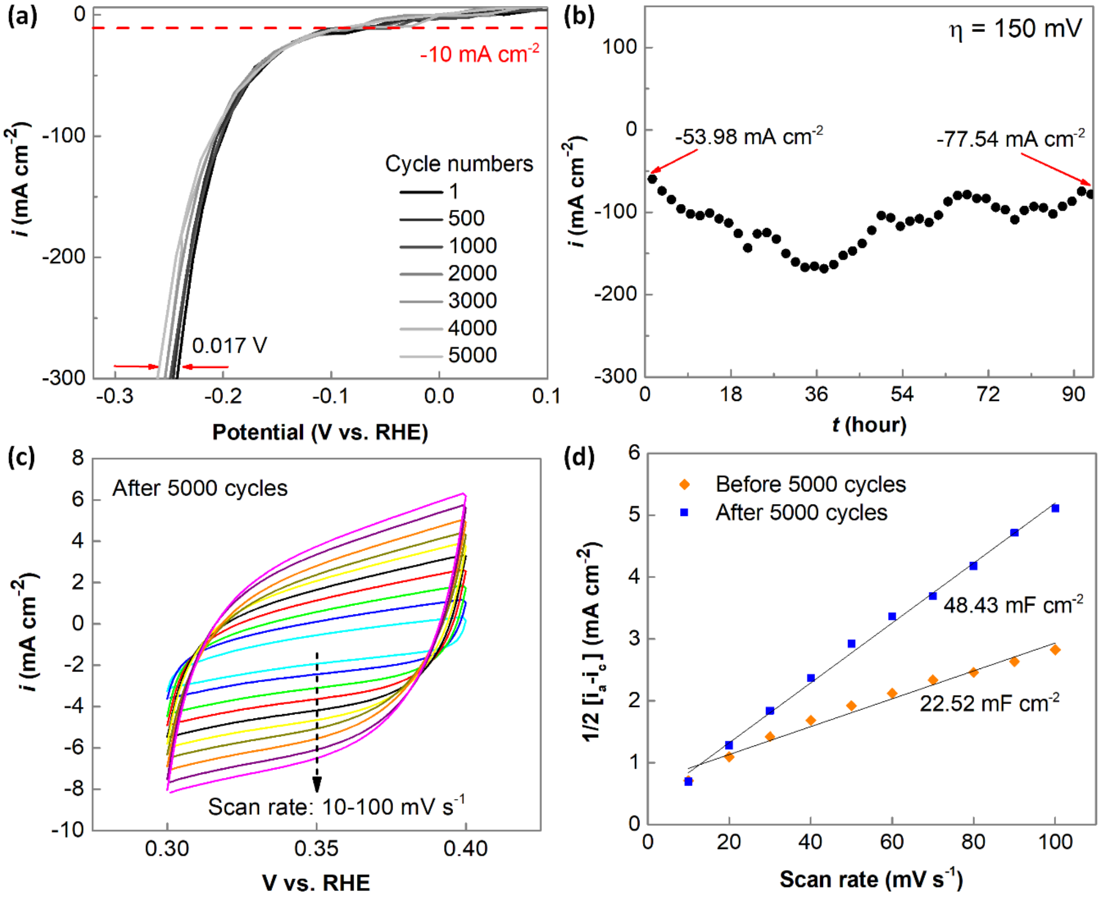

Figure 6.11. (a) Polarization curves of Co-MoS_2/G-5 at a scan rate of 50 mV s^{-1} from 1 to 5000 cycles. (b) Constant potential electrolysis test for 94 h at 150 mV *vs.* RHE. (c) CVs of Co-MoS_2/G-5 catalyst after stability test in a potential window without faradaic reaction. (d) EDLC measurements of Co-MoS_2/G-5 before and after 5000 cycles.

The Co-MoS_2/G-5 catalyst was further characterized after 5000 cycles of CV runs. As shown in Figure 6.12a and 6.12b, the EDS and XRD results confirm the existence of Co-MoS_2 nanosheets intertwined with graphene, retaining the atomic ratio of Co: Mo: S as 0.45: 1.0: 2.0, which is almost similar to the initial values. Moreover, In Figure 6.12c−6.12g, the elemental distributions are displayed for C, Mo, S and Co species, which confirms maintaining the uniform distribution of Co element in the Co-doped MoS_2 catalyst.

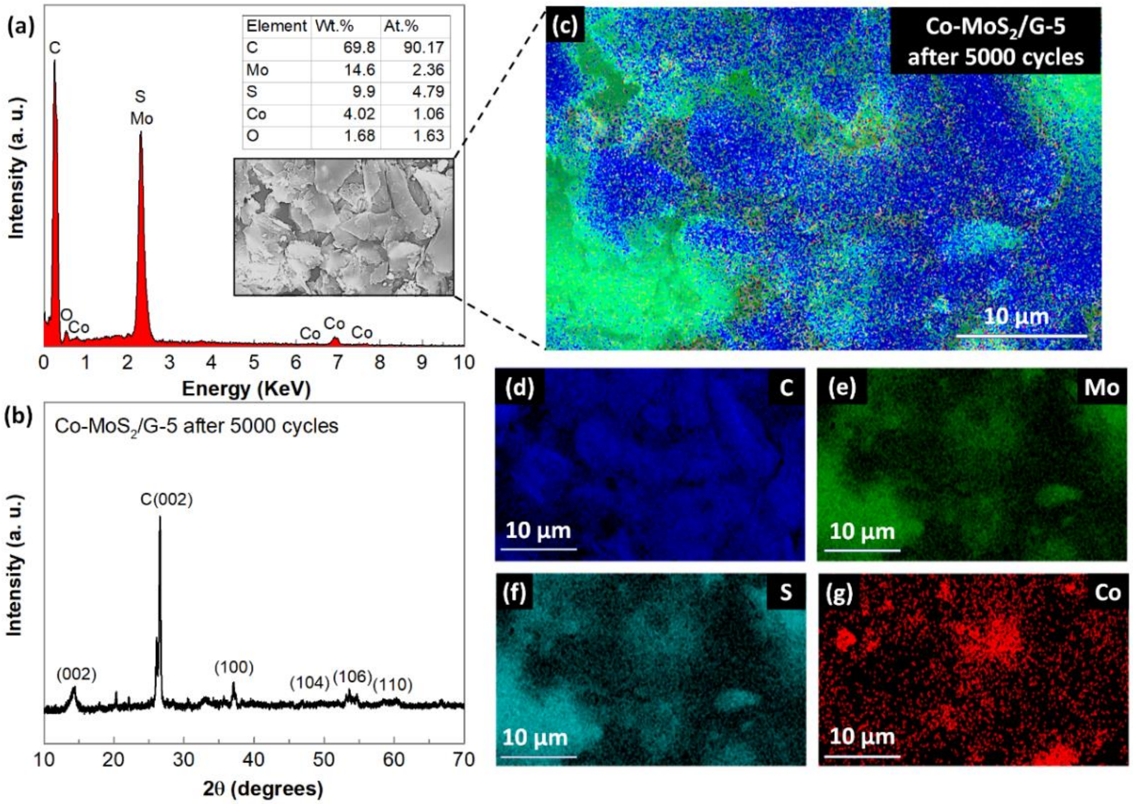

Element	Wt.%	At.%
C	69.8	90.17
Mo	14.6	2.36
S	9.9	4.79
Co	4.02	1.06
O	1.68	1.63

Figure 6.12. Physical characterizations of Co-MoS_2/G-5 catalyst after stability test: (a) EDS elemental analysis. (b) XRD patterns. (c) EDS elemental mapping. (d−g) Elemental distributions of carbon (C), molybdenum (Mo), sulfur (S), and cobalt (Co) species, respectively.

Furthermore, the present findings were compared with the previously reported results of similar Co and/or Mo-based compounds, as displayed in Table 6.6. In contrast with ultrafast and facile microwave irradiation, most of the other compounds were manufactured by various complicated approaches. Additionally, it is noticeable that the present material exhibits low overpotential and a small Tafel slope, that are better than many other similar compounds.

Table 6.6. Comparison of HER activities of the microwave-synthesized Co-MoS_2/G-5 catalyst with previously reported results for similar compounds.

Materials	**Synthesis approach**	**Electrolyte**	**Over potential at −10 mA cm^{-2} [mV vs. RHE]**	**Tafel slope [mV per decade]**	**Ref.**
Co−MoS_3 film	Electrochemical deposition	0.5 M H_2SO_4	200	43.0	[36]
CoMoS-2-C	Deposition−precipitation	0.5 M H_2SO_4	135	50.0	[41]
Co-doped MoS_2/CFP	Hydrothermal	0.5 M H_2SO_4	217	50.0	[42]
Co-MoS_2/rGO	Hydrothermal	0.5 M H_2SO_4	147	49.5	[43]
Co-doped MoS_2	CVD	0.5 M H_2SO_4	185	65.0	[49]
Co_9S_8@MoS_2/CNFs	Vapor assisted graphitization	0.5 M H_2SO_4	190	110.0	[60]
Co_9S_8/NSG-UCNT	Pyrolysis	0.5 M H_2SO_4	65	84.0	[61]
$CoMoS_4$-H	Kanatzidis' solution reaction	0.5 M H_2SO_4	170	80.0	[62]
$CoMoS_4$/sulfur-doped carbon (SDC)	Hydrothermal	0.5 M H_2SO_4	180	48.0	[63]
MoS_2-$CoMo_2S_4$/graphene	Hydrothermal	0.5 M H_2SO_4	300	42.0	[64]
CoS_x@MoS_2	Solvothermal	1.0 M KOH	146	56.5	[65]
MoS_xCo_y/TNAs	Electro-deposition	0.5 M H_2SO_4	173	42.8	[66]
$CoMoS_2$/NGO	Hydrothermal	0.5 M H_2SO_4	~110	34.1	[67]
a-MoS_x/NAC	Electro-deposition	0.5 M H_2SO_4	141	43.9	[68]
P-CoMoS/CC	Hydrothermal	1.0 M KOH	66	60.1	[69]
$CoMoS_2$/DDA	Hydrothermal	0.5 M H_2SO_4	127	124.0	[70]
N-MiMoS	Hydrothermal	1.0 M KOH	68	86.0	[71]
Phosphatized MoS_2/graphene	Hydrothermal	0.5 M H_2SO_4	187	35.0	[72]
Co-MoS_2/G	**Microwave irradiation**	**0.5 M H_2SO_4**	**78**	**40.0**	**Present study**

6.4. Summary

In summary, present study demonstrates an energy efficient, ultrafast, and reliable microwave irradiation approach to synthesize the cobalt doped molybdenum sulfide (Co-MoS_2) nanosheets uniformly distributed on graphene sheets. Among the resultant catalysts with different amount of Co-loading, the Co-MoS_2/G-5 nanocomposite with an atomic ratio of Co: Mo: S is around 0.4: 1.0: 2.4, delivers outstanding catalytic performance for hydrogen generation in acidic medium. The Co-MoS_2/G-5 catalyst reveals a low overpotential of 78.1 mV to reach 10 mA cm^{-2}, a small Tafel slope of 40.0 mV dec^{-1}, along with a high exchange current density of 0.0917 mA cm^{-2}. The resultant catalyst also demonstrates excellent stability both for 5000 cycles of CV test and 94 h constant potential test in acidic medium. These results clearly indicate that the formation of Co-Mo-S phase significantly increases the HER performance by promoting abundant defects, comparing to pure CoS_2 or pure MoS_2 phase. Moreover, the synergy of Co-MoS_2 with graphene network regulates both structural and electronic benefits, as well as the balance of active sites, and electronic conductivity. Following this simple microwave irradiation approach and the step-by-step characterization methods, other metal (Ni, Cu, Fe, Zn, etc.) doped MoS_2 catalysts can be further studied, which possess immense potential in water electrolysis devices to stimulate the hydrogen gas as a reliable future energy carrier.

6.5. References

1 J. A. Turner, *Sustain. Hydrog. Prod.*, 2016, **305**, 1–479.

2 M. Carmo, D. L. Fritz, J. Mergel and D. Stolten, *Int. J. Hydrogen Energy*, 2013, **38**, 4901–4934.

3 J. K. Norskov and C. H. Christensen, *Science (80).*, 2006, **312**, 1322–1323.

4 S. Anantharaj and S. Noda, *Small*, 2020, **16**, 1–24.

5 X. Li, X. Hao, A. Abudula and G. Guan, *J. Mater. Chem. A*, 2016, **4**, 11973–12000.

6 J. D. Benck, T. R. Hellstern, J. Kibsgaard, P. Chakthranont and T. F. Jaramillo, *ACS Catal.*, 2014, **4**, 3957–3971.

7 X. Zou and Y. Zhang, *Chem. Soc. Rev.*, 2015, **44**, 5148–5180.

8 X. Gao, J. Qi, S. Wan, W. Zhang, Q. Wang and R. Cao, *Small*, 2018, **14**, 1–9.

9 H. Sun, Z. Ma, Y. Qiu, H. Liu and G. gang Gao, Small, 2018, **14**, 1800294.

10 Q. T. Nguyen, P. D. Nguyen, D. Nguyen, Q. D. Truong, T. T. Kim Chi, T. T. D. Ung, I. Honma, N. Q. Liem and P. D. Tran, *ACS Appl. Mater. Interfaces*, 2018, **10**, 8659–8665.

11 S. Sarwar, A. Ali, Z. Liu, J. Li, S. Uprety, H. Lee, R. Wang, M. Park, M. J. Bozack, A. J. Adamczyk and X. Zhang, *J. Colloid Interface Sci.*, 2021, **581**, 847–859.

12 A. D. Handoko, K. D. Fredrickson, B. Anasori, K. W. Convey, L. R. Johnson, Y. Gogotsi, A. Vojvodic and Z. W. Seh, *ACS Appl. Energy Mater.*, 2018, **1**, 173–180.

13 S. Yuan, S. Y. Pang and J. Hao, *Appl. Phys. Rev.*, **7**, 021304 (2020).

14 S. H. Noh, J. Hwang, J. Kang, M. H. Seo, D. Choi and B. Han, *J. Mater. Chem. A*, 2018, **6**, 20005–20014.

15 L. Lin, P. Sherrell, Y. Liu, W. Lei, S. Zhang, H. Zhang, G. G. Wallace and J. Chen, *Adv. Energy Mater.*, 2020, **10**, 1903870.

16 M. Chhowalla, H. S. Shin, G. Eda, L. J. Li, K. P. Loh and H. Zhang, *Nat. Chem.*, 2013, **5**, 263–275.

17 T. F. Jaramillo, K. P. Jørgensen, J. Bonde, J. H. Nielsen, S. Horch and I. Chorkendorff, *Science (80)*, 2007, **317**, 100–102.

18 S. Xie, B. Sun, H. Sun, K. Zhan, B. Zhao, Y. Yan and B. Y. Xia, *Int. J. Hydrogen Energy*, 2019, **44**, 15009–15016.

19 Y. Li, H. Wang, L. Xie, Y. Liang, G. Hong and H. Dai, *J. Am. Chem. Soc.*, 2011, **133**, 7296–7299.

20 N. Zhang, S. Gan, T. Wu, W. Ma, D. Han and L. Niu, *ACS Appl. Mater. Interfaces*, 2015, **7**, 12193–12202.

21 H. Huang, L. Chen, C. Liu, X. Liu, S. Fang, W. Liu and Y. Liu, *J. Mater. Chem. A*, 2016, **4**, 14577–14585.

22 J. Kibsgaard, Z. Chen, B. N. Reinecke and T. F. Jaramillo, *Nat. Mater.*, 2012, **11**, 963–969.

23 L. Liu, X. Li, L. C. Xu, R. Liu and Z. Yang, *Appl. Surf. Sci.*, 2017, **396**, 138–143.

24 A. Tahira, Z. H. Ibupoto, R. Mazzaro, S. You, V. Morandi, M. M. Natile, M. Vagin and A. Vomiero, *ACS Appl. Energy Mater.*, 2019, **2**, 2053–2062.

25 X. Han, X. Tong, X. Liu, A. Chen, X. Wen, N. Yang and X. Y. Guo, *ACS Catal.*, 2018, **8**, 1828–1836.

26 V. T. Nguyen, P. A. Le, Y. C. Hsu and K. H. Wei, *ACS Appl. Mater. Interfaces*, 2020, **12**, 11533–11542.

27 A. Behranginia, M. Asadi, C. Liu, P. Yasaei, B. Kumar, P. Phillips, T. Foroozan, J. C. Waranius, K. Kim, J. Abiade, R. F. Klie, L. A. Curtiss and A. Salehi-Khojin, *Chem. Mater.*, 2016, **28**, 549–555.

28 S. Zhang, H. Yang, H. Gao, R. Cao, J. Huang and X. Xu, *ACS Appl. Mater. Interfaces*, 2017, **9**, 23635–23646.

29 Y. Liu, C. Zeng, L. Ai and J. Jiang, *Appl. Surf. Sci.*, 2019, **484**, 692–700.

30 S. H. Yu, Z. Tang, Y. Shao, H. Dai, H. Y. Wang, J. Yan, H. Pan and D. H. C. Chua, *ACS Appl. Energy Mater.*, 2019, **2**, 5799–5808.

31 J. Deng, H. Li, J. Xiao, Y. Tu, D. Deng, H. Yang, H. Tian, J. Li, P. Ren and X. Bao, *Energy Environ. Sci.*, 2015, **8**, 1594–1601.

32 R. Li, L. Yang, T. Xiong, Y. Wu, L. Cao, D. Yuan and W. Zhou, *J. Power Sources*, 2017, **356**, 133–139.

33 C. Lin, Z. Gao and J. Jin, *ChemSusChem*, 2019, **12**, 457–466.

34 M. A. Lukowski, A. S. Daniel, F. Meng, A. Forticaux, L. Li and S. Jin, *J. Am. Chem. Soc.*, 2013, **135**, 10274–10277.

35 Q. Liu, Q. Fang, W. Chu, Y. Wan, X. Li, W. Xu, M. Habib, S. Tao, Y. Zhou, D. Liu, T. Xiang, A. Khalil, X. Wu, M. Chhowalla, P. M. Ajayan and L. Song, *Chem. Mater.*, 2017, **29**, 4738–4744.

36 D. Merki, H. Vrubel, L. Rovelli, S. Fierro and X. Hu, *Chem. Sci.*, 2012, **3**, 2515–2525.

37 J. Bonde, P. G. Moses, T. F. Jaramillo, J. K. Norskov and I. Chorkendorff, *Faraday Discuss.*, 2008, **140**, 219–231.

38 Y. Rheem, S. H. Park, Y. Han, K.-H. Lee, S.-M. Choi and N. V. Myung, *J. Electrochem. Soc.*, 2019, **166**, F996–F999.

39 L. Wu, X. Xu, Y. Zhao, K. Zhang, Y. Sun, T. Wang, Y. Wang, W. Zhong and Y. Du, *Appl. Surf. Sci.*, 2017, **425**, 470–477.

40 T. Dong, X. Zhang, P. Wang, H. S. Chen and P. Yang, *Electrochim. Acta*, 2020, **338**, 135885.

41 X. Dai, K. Du, Z. Li, M. Liu, Y. Ma, H. Sun, X. Zhang and Y. Yang, *ACS Appl. Mater. Interfaces*, 2015, **7**, 27242–27253.

42 R. Bose, M. Seo, C. Y. Jung and S. C. Yi, *Electrochim. Acta*, 2018, **271**, 211–219.

43 J. Ma, A. Cai, X. Guan, K. Li, W. Peng, X. Fan, G. Zhang, F. Zhang and Y. Li, *Int. J. Hydrogen Energy*, 2020, **45**, 9583–9591.

44 X. Yin, Y. Yan, M. Miao, K. Zhan, P. Li, J. Yang, B. Zhao and B. Y. Xia, *Chem. - A Eur. J.*, 2018, **24**, 556–560.

45 J. Huang, M. Chen, X. Li, X. Zhang, L. Lin, W. Liu and Y. Liu, *Electrochim. Acta*, 2019, **300**, 235–241.

46 Y. Guo, L. Gan, C. Shang, E. Wang and J. Wang, *Adv. Funct. Mater.*, 2017, **27**, 1–7.

47 S. Sarwar, A. Nautiyal, J. Cook, Y. Yuan, J. Li, S. Uprety, R. Shahbazian-Yassar, R. Wang, M. Park, M. J. Bozack and X. Zhang, *Sci. China Mater.*, 2020, **63**, 62–74.

48 F. Zheng, N. Huang, R. Peng, Y. Ding, G. Li, Z. Xia, P. Sun, X. Sun and J. Geng, *Electrochim. Acta*, 2018, **263**, 328–337.

49 N. Huang, R. Peng, Y. Ding, S. Yan, G. Li, P. Sun, X. Sun, X. Liu and H. Yu, *J. Catal.*, 2019, **373**, 250–259.

50 Q. Wu, Y. Zhu, J. Guo, S. Wang, X. Feng and Z. Chen, *Int. J. Hydrogen Energy*, 2021, 1–10.

51 C. G. Morales-Guio, L. A. Stern and X. Hu, *Chem. Soc. Rev.*, 2014, **43**, 6555–6569.

52 W. Zhou, J. Jia, J. Lu, L. Yang, D. Hou, G. Li and S. Chen, *Nano Energy*, 2016, **28**, 29–43.

53 J. Newman and K. E. Thomas-Alyea, *Electrochemical Systems*, 2004, vol. 3.

54 D. Merki, S. Fierro, H. Vrubel and X. Hu, *Chem. Sci.*, 2011, **2**, 1262–1267.

55 J. Kibsgaard and T. F. Jaramillo, *Angew. Chemie - Int. Ed.*, 2014, **53**, 14433–14437.

56 H. Kim, J. Kim, G. H. Han, W. Guo, S. Hong, J. Park and S. H. Ahn, *J. Ind. Eng. Chem.*, 2021, **95**, 357–366.

57 C. Huff, E. Biehler, Q. Quach, J. M. Long and T. M. Abdel-Fattah, *Colloids Surfaces A Physicochem. Eng. Asp.*, 2021, **610**, 125734.

58 M. Yuan, Z. Cui, J. Yang, X. Cui, M. Tian, D. Xu, J. Ma and Z. Dong, *Int. J. Hydrogen*

Energy, 2017, **42**, 29244–29253.

59 J. Durst, C. Simon, F. Hasché and H. A. Gasteiger, *J. Electrochem. Soc.*, 2015, **162**, F190–F203.

60 H. Zhu, J. Zhang, R. Yanzhang, M. Du, Q. Wang, G. Gao, J. Wu, G. Wu, M. Zhang, B. Liu, J. Yao and X. Zhang, *Adv. Mater.*, 2015, **27**, 4752–4759.

61 M. Li, H. Zhou, W. Yang, L. Chen, Z. Huang, N. Zhang, C. Fu and Y. Kuang, *J. Mater. Chem. A*, 2017, **5**, 1014–1021.

62 L. Shao, X. Qian, X. Wang, H. Li, R. Yan and L. Hou, *Electrochim. Acta*, 2016, **213**, 236–243.

63 N. Karikalan, P. Sundaresan, S. M. Chen, R. Karthik and C. Karuppiah, *Int. J. Hydrogen Energy*, 2019, **44**, 9164–9173.

64 X. Zhang, Q. Zhang, Y. Sun and J. Guo, *Fuel*, 2016, **184**, 559–564.

65 S. Shit, S. Chhetri, S. Bolar, N. C. Murmu, W. Jang, H. Koo and T. Kuila, *ChemElectroChem*, 2019, **6**, 430–438.

66 P. Yang, B. Wang and Z. Liu, *Int. J. Hydrogen Energy*, 2018, **43**, 23109–23117.

67 X. Hou, Y. Li, L. Cheng, X. Feng, H. Zhang and S. Han, *Int. J. Hydrogen Energy*, 2019, **44**, 11664–11674.

68 L. Yang, X. Xiao, Z. Yang, Y. Cai, B. Xie, N. Zhao, X. Li, Y. Wang, M. Liu, X. Wang, G. Wang, Z. Gan, M. Meng, W. Yang, J. Zhang and J. M. Liu, *Int. J. Hydrogen Energy*, 2018, **43**, 15135–15143.

69 C. Ray, S. C. Lee, K. V. Sankar, B. Jin, J. Lee, J. H. Park and S. C. Jun, *ACS Appl. Mater. Interfaces*, 2017, **9**, 37739–37749.

70 Y. Wu, M. Zarei-Chaleshtori, B. Torres, T. Akter, C. Diaz-Moreno, G. B. Saupe, J. A. Lopez, R. R. Chianelli and D. Villagrán, *Int. J. Hydrogen Energy*, 2017, **42**, 20669–20676.

71 C. Huang, L. Yu, W. Zhang, Q. Xiao, J. Zhou, Y. Zhang, P. An, J. Zhang and Y. Yu, *Appl. Catal. B Environ.*, 2020, **276**, 119137.

72 J. Huang, M. Chen, X. Zhang, W. Liu and Y. Liu, *Int. J. Hydrogen Energy*, 2020, **45**, 4043–4053.

Chapter 7

High performance hybrid-capacitor based on $MoTe_2$/graphene through ultra-fast, facile microwave-initiated synthesis

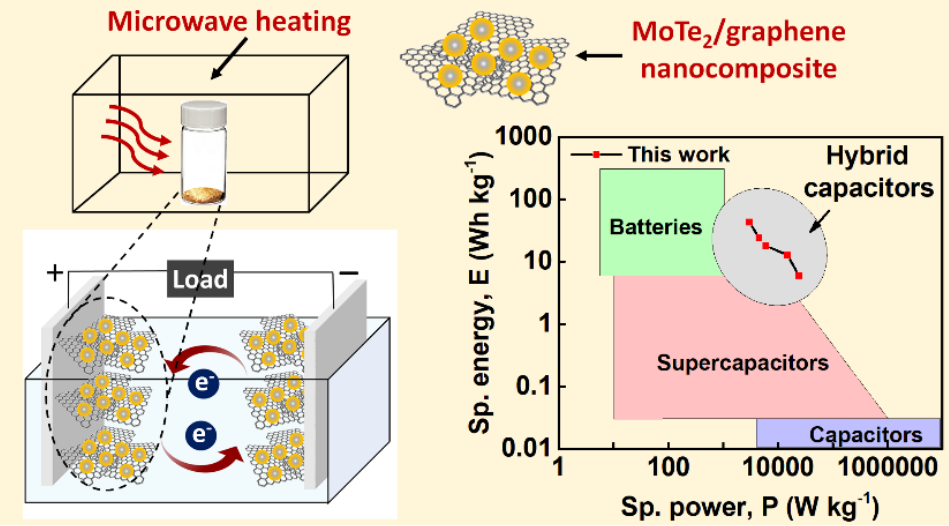

Part of this chapter has been published in Journal of Alloys and Compounds 846 (2020), 155886

Abstract

With the rapid development of world economy and an increasing use of portable electronic devices, energy storage systems are becoming more reliable on nano/micro supercapacitors. This work reports a fast and facile microwave-initiated synthesis approach of 2D-molybdenum ditelluride nanosheets on graphene substrate ($MoTe_2$/graphene), which can be used as an efficient energy storage material. The physical characterizations, such as scanning electron microscopy, transmission electron microscopy, energy-dispersive X-ray spectroscopy, and X-ray diffraction analyses substantiate the successful synthesis of $MoTe_2$/graphene nanocomposite. The electrochemical characterizations reveal their excellent supercapacitive behavior with specific capacitance of 434 ± 37.5 F g^{-1} at a current density of 1 A g^{-1} and a good cycling stability of 125% retention after 5000 cycles at 10 A g^{-1} in 1 M Na_2SO_4 aqueous solution. In addition, the symmetric $MoTe_2$/graphene//$MoTe_2$/graphene configuration displays excellent cyclic stability up to 10,000 cycles with a maximum energy density of 43.2 Wh kg^{-1} at high power density of 3000 W kg^{-1} in 1 M Na_2SO_4 electrolyte, which demonstrates the hybrid-capacitor behavior. Therefore, the microwave synthesized $MoTe_2$/graphene reveals a great potential as advanced electrode materials for energy storage devices with high electrochemical performance through one-step facile synthesis approach.

7.1. Introduction

In order to achieve a sustainable and renewable energy future successfully, it is important to develop efficient energy storage systems, especially to store the energy produced from intermittent sources such as hydro, solar and wind to utilize the energy as per necessity. Among the high-performance energy storage devices, supercapacitors (SCs) have achieved tremendous attention due to their high-power density, excellent cyclic performance, low maintenance cost, wide operational temperature range and enhanced safety.[1–3] Only drawback that restricts their potential applications is their lower energy densities. Therefore, the effort has been devoted to designing advanced electrode materials to improve SC's energy density.[2,4] In general, the energy storage mechanisms are divided into three major categories.[5] One is the non-faradaic electrical double-layer capacitor (EDLC), which stores the energy through reversible electrostatic accumulation of ions at electrode/electrolyte interface. The second type is pseudocapacitor, that depends on faradaic reaction by transferring the charges at the interface between electrode and electrolyte. Another one is the battery type, which is basically a diffusion-limited redox process relying on the kinetically limited intercalation reactions.[5] For nano-scaled materials, it is notable that the difference between pseudocapacitive charge storage and battery-like diffusion-limited intercalation is rather indeterminate.[6] Therefore, to design the high-performance supercapacitors with improved energy and power density, most research projects have been focused on developing nano-scaled electrode materials consisting of both pseudocapacitive and EDLC electrode materials by enhancing redox processes, such as redox pseudocapacitance, intercalation pseudocapacitance, as well as diffusion-limited redox process.[7,8] In this regard, nanostructured transition metal oxides, chalcogenides, and hydroxides possess pseudocapacitive behavior (owing to multiple oxidation states) with enhanced specific capacitance. However, there is a limitation in their applicability due to low electrical conductivity, aggregation in nano-sized particles and fast degradation of active electrode materials.[9–11] Recently, the nanostructured transition metal dichalcogenides (TMDs) like molybdenum sulfide (MoS_2),[12–14] molybdenum telluride ($MoTe_2$),[15,16] copper sulfide,[17] nickel sulfide,[18] tungsten selenide (WSe_2),[19] and etc. have gained much interest in energy storage applications due to their unique physicochemical properties and abundancy. The interesting 2D layered structures of TMDs provide higher surface area for charge accumulation, as well, the ion diffusion into the layers can enhance their redox properties. However, the low intrinsic conductivity, degradation by volume change and restacking of the layered interfaces yet limit the performance of TMDs for energy conversion and storage applications.[11] In contrast, carbon-based materials, such as, graphene, carbon nanotubes (CNTs), conducting polymers (CPs) exhibit non-faradaic EDLC behavior with higher conductivity, larger surface area, excellent thermal and chemical stability, and less degradation, but restricted by low specific capacitance, high hydrophobic nature and poor dispersion ability.[20] Among the carbon materials, graphene has been particularly utilized as the supporter of energy storage materials for its high specific surface area and outstanding electrical conductivity.[21–23] Hence, formation of composite can overcome this limitation by combining TMDs having a higher specific capacitance with graphene having higher cyclic stability.

In the past decade, among TMDs, MoS_2[12,24,25] and $MoSe_2$[26,27] have come forward with admirable potentials in the field of energy storage systems, whereas very few reports have emerged on $MoTe_2$ as supercapacitor even though they have better electrical properties[28], along with semi-metallic nature. Since, tellurium has a comprehensively higher electronic conductivity (2×10^2 Sm^{-1}), it is expected that the supercapacitors based on the composite of $MoTe_2$ and carbon based material can present high specific capacitance and prominent electrochemical performances by facilitating better access for electron transfer and provide lower electric series resistance (ESR).[29,30] For instance, Liu, et. al. revealed 1.5 times increment in specific capacitance of 1T′-$MoTe_2$ electrode by addition of graphene.[31,32] Karade, et.al. have designed a composite electrode with EDLC behaved multi-walled carbon nanotubes (MWCNTs) and pseudocapacitive $MoTe_2$ leading to an excellent specific capacitance of 502 F g^{-1} at 2 mV s^{-1} in liquid configuration with excellent rate capability and cyclic stability.[15] Inspired by these promising studies, we have developed a facile one step route for the fabrication of $MoTe_2$/graphene electrode, in which $MoTe_2$ nanosheets are directly grown on graphene by microwave-initiated approach. To date, most of the synthesis methods of $MoTe_2$-based materials require complex equipment setups, high energy consumption, long processing time with various safety, scalability and cost issues that could limit their range of potential applications. In this regard, microwave-initiated manufacturing can become an energy and cost-efficient approach to develop $MoTe_2$/graphene nanocomposites for supercapacitor applications. Recently, the microwave approach is a fast-growing research area, due to its advantages such as higher reaction rate, rapid volumetric heating, high selectivity, small reaction time, and increased yields of products comparing to conventional heating methods.[33,34] There are a number of microwave-initiated methods have been reported to produce TMDs and demonstrated that it can be used for the highly efficient production of nanostructured hybrid compounds.[35–38] Moreover, microwave or plasma treatment has shown several applications to produce exfoliated graphene with enhanced electrochemical properties.[39–41]

In this work, we demonstrate a direct growth of the nanocomposite of $MoTe_2$ on graphene substrate *via* microwave-initiated approach, following the similar method we employed to synthesize molybdenum disulfide (MoS_2) on graphene substrate.[42] This technique represents a clean, ultrafast (90 seconds) synthetic approach using microwave heating without any inert gas protection or intense facilities. Figure 7.1 shows the synthesis steps and supercapacitor application of the as-produced $MoTe_2$/graphene. Benefiting from the synergistic effects of pseudocapacitive behavior of $MoTe_2$ and EDLC behavior of graphene, this $MoTe_2$/graphene nanocomposite combines several advantages of higher conductivity, higher redox activity, enhanced cycling performance with an optimized electrode structure of nanosheet morphology.

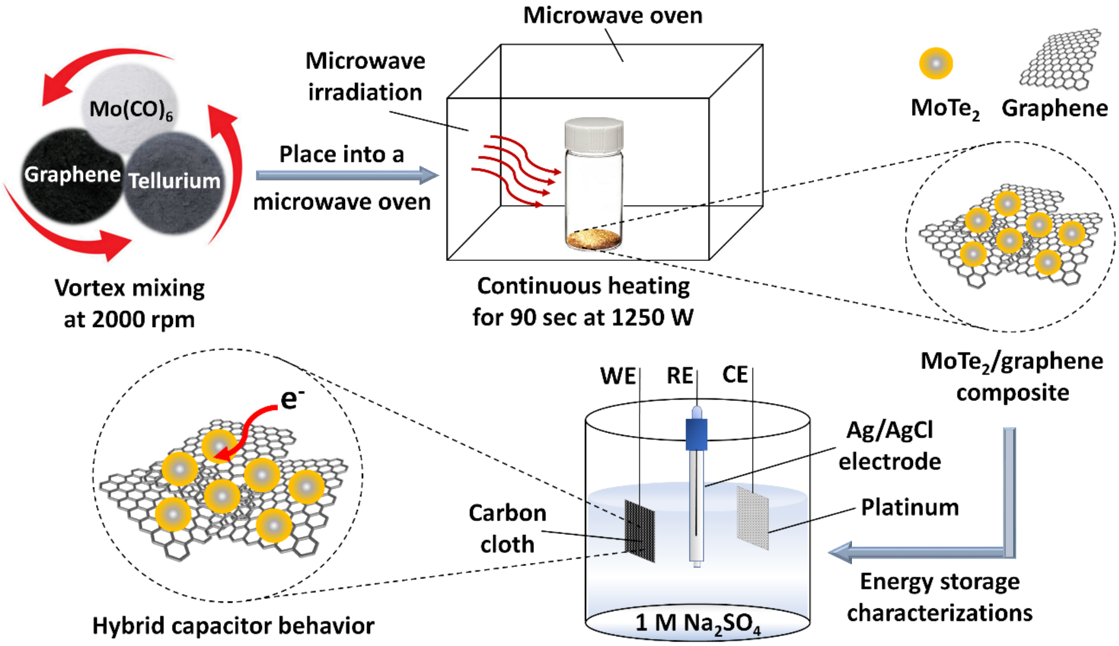

Figure 7.1. Schematic illustration of microwave-initiated synthesis of MoTe$_2$/graphene nanocomposite for supercapacitor application.

7.2. Experimental details

7.2.1. Materials and reagents

Molybdenum hexacarbonyl (Mo(CO)$_6$, 98%) was purchased from Strem Chemicals. Graphene substrate was obtained from Magnolia Ridge Inc. Tellurium (Te powder, ~325 mesh) and sodium sulfate (Na$_2$SO$_4$, anhydrous, 99%) were obtained from Alfa Aesar. Nafion (5 wt.%) was obtained from BeanTown Chemical, Inc. Nitric acid (69-70%), and acetone (CH$_3$COCH$_3$) were supplied by BDH Chemicals, VWR. All chemicals were used directly without further purification. For electrochemical characterizations, platinum (Pt) gauze (100 mesh, 99.9% metal basis) was acquired from Alfa Aesar. The silver/silver chloride (Ag/AgCl, 3 M KCl, E^0 = +0.197

V vs. RHE) reference electrode was obtained from Hach. Carbon cloth (40 cm × 40 cm) was purchased from Fuel Cell Earth LLC to be used as current collector.

7.2.2. Microwave-initiated synthesis of $MoTe_2$/graphene composites

To prepare $MoTe_2$/graphene compound, at first 10 mg of $Mo(CO)_6$, 20 mg of Te-powder and 10 mg of graphene (weight ratio = 1:2:1) were filled in a glass vial and mixed together uniformly by a speed mixer (2000 rpm). Next, this homogeneous mixture was subjected to microwave irradiation in a microwave oven (frequency 2.45 GHz, power 1250 W) for 90 seconds. Eventually, microwave heating triggers the reduction of $Mo(CO)_6$ to MoO_2 and MoO_3, then converted to $MoTe_2$ uniformly dispersed on graphene substrate, releasing other constituents in gaseous forms. During the synthesis, graphene acts as microwave susceptor to generate heat that converts precursors into $MoTe_2$, along with acting as a strong conductive supporter for $MoTe_2$ nanoparticles to prevent them from aggregation, leading to an increase in specific surface area and electrical conductivity of as-produced $MoTe_2$/graphene.

7.2.3. Material characterization techniques

To investigate the synthesis of $MoTe_2$/graphene-composite the surface morphology and chemical composition were characterized by scanning electron microscope (SEM; Apreo FE) coupled with an energy dispersive X-ray spectrometer (EDS, EDAX Instruments) with an acceleration voltage of 20 kV. The transmission electron microscopy (TEM) and high resolution TEM (HRTEM) analyses were carried out using a FEI Tecnai F20 TEM, operated at 200 kV and equipped with an EDAX EDS detector. To explore the phase and crystal structures of materials, the powder X-ray diffraction (XRD) patterns were collected on a Philips X'pert MPD diffractometer with Cu Kα radiation ($\lambda = 1.54056$ Å) at 45 kV and 40 mA. To collect the XRD data, scan speed of 0.06°/min was used over a 2θ range of 10−60°.

7.2.4. Electrochemical measurements

To test the energy storage behaviors, electrodes were prepared using carbon cloth (CC) (1 cm × 2 cm) as current collector. Prior to coat CC with $MoTe_2$/graphene composite, they were immersed in 6 M HNO_3 solution for 8h followed by washing with DI water and drying for 30 mins in a vacuum oven at 60°C to remove any of the impurities. This treated CC was coated with a homogeneous paste of individual composite and nafion (5 wt.%) with an active load of ~0.8 mg cm^{-2} and dried under vacuum for 2h at 60°C. All electrochemical studies were performed using a CH Instrument (CHI 760D) potentiostat using ‘Electrochemical Analyzer’ software (version 15.03) in a standard three-electrode setup consisting of a coated CC working electrode, silver/silver chloride (Ag/AgCl, 3 M KCl) as the reference electrode, and platinum (Pt) mesh as a counter electrode in 1 M Na_2SO_4 electrolyte. Only the stability tests were performed on Arbin Instrument (version 4.21). The electrocatalytic activities were examined by cyclic voltammograms (CVs) and galvanostatic charge-discharge (GCD) tests applying various scan rates at room temperature. Before each measurement, CV was run for 50 cycles at 10 mV s^{-1} to achieve stable condition. In addition, electrochemical impedance spectroscopic (EIS) measurements were carried out in 1 M Na_2SO_4 at open circuit potential of corresponding electrodes in the frequency range of 10^{-2} to 10^6 Hz with a single modulated AC potential of 5 mV. Afterward, the EIS spectra were fitted by the EC-Lab software. The active load of ~0.8 mg cm^{-2} was used for all the electrochemical tests to maintain better consistency of the results.

7.3. Results and discussion

7.3.1. Material characterizations

The surface morphology of $MoTe_2$/graphene composite was investigated by SEM analysis. Figure 7.2a and 7.2b demonstrate the growth of $MoTe_2$ compounds embedded on graphene flakes. The SEM images reveal the coalescing and/or overlapping of the graphene sheets, forming an interconnected conducting network, which is very important to facilitate the rapid electronic transport and to provide enough mechanical strength.

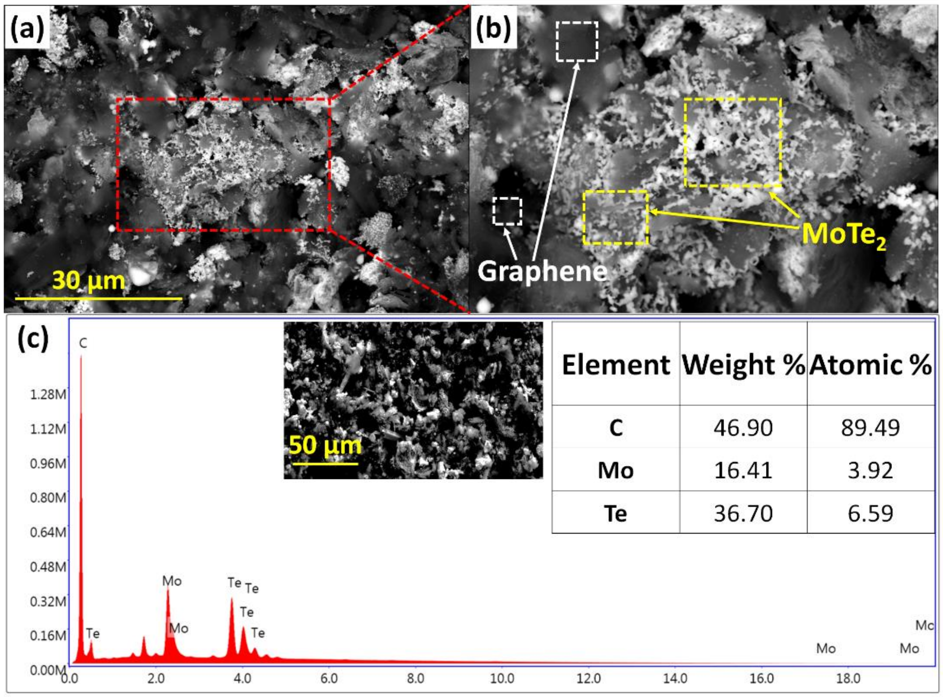

Element	Weight %	Atomic %
C	46.90	89.49
Mo	16.41	3.92
Te	36.70	6.59

Figure 7.2. (a, b) SEM images of $MoTe_2$/graphene. (c) EDS pattern of $MoTe_2$/graphene (inset table shows wt.% and at.% of carbon (C), molybdenum (Mo), and tellurium (Te) elements.

In addition, the EDS results (Figure 7.2c) exhibit that the nanosheets are primarily composed of molybdenum (Mo) and tellurium (Te) elements with a large amount (~90 at.%) of carbon (C) content due to the presence of a large amount of graphene substrate. Besides, the atomic ratio of

Mo and Te components is very close to stoichiometry (1:2), which satisfies the formula of $MoTe_2$. Furthermore, EDS elemental mapping (Figure 7.3a) was performed that shows the distribution of Mo and Te elements on graphene network. EDS results clearly illustrate the uniform distribution of $MoTe_2$ on graphene with slight agglomeration, which was beneficial for improving the electrical and ionic conductivity and enhancing the cyclic stability of $MoTe_2$ nanoparticles for the energy storage applications.

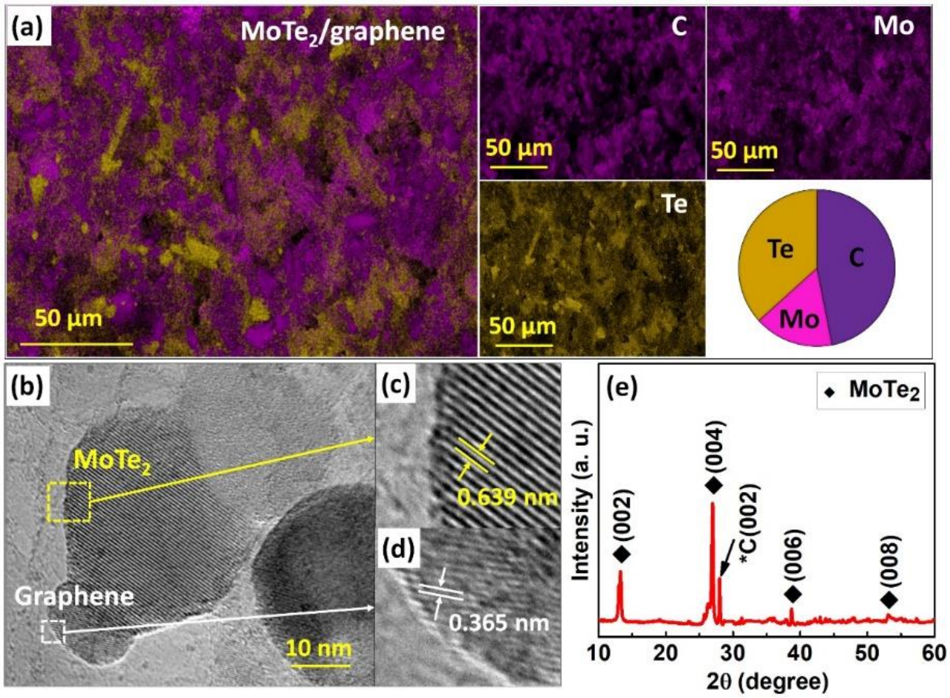

Figure 7.3. (a) EDS elemental mapping of $MoTe_2$/graphene. The violet, pink, and yellow color represents carbon (C), molybdenum (Mo), and tellurium (Te), respectively. (b) HR-TEM image of $MoTe_2$/graphene. (c, d) Interlayer spacings of $MoTe_2$ and graphene nanosheets. (e) XRD pattern of $MoTe_2$/graphene.

Additionally, TEM and HR-TEM imaging were performed to examine the microstructure and crystallinity of $MoTe_2$/graphene nanocomposite. The HR-TEM image (Figure 7.3b) prominently displays the difference between graphene and $MoTe_2$ nanosheets by their well-resolved lattice fringes with separate interplanar spacings. The $MoTe_2$ exhibits the few-layered structure with an interlayer distance of 6.39 Å (Figure 7.3c), where the graphene displays distinctive interlayer spacing of 3.65 Å (Figure 7.3d), which are similar values reported before for their corresponding (002) planes.[43–45] Moreover, to identify the formation of crystalline $MoTe_2$ nanosheets the XRD analysis was performed. Figure 7.3e displays the diffraction peaks in a range from 10^o to 60^o. The peaks appeared at 13.27^o, 26.96^o, 38.74^o, 53.09^o are corresponding to (002), (004), (006), (008) planes of $MoTe_2$, that can be indexed to the standard hexagonal 2H–$MoTe_2$ structure (JPCDS no. 15-0658).[46] Graphene displays a peak at ~27^o with high intensity as a reflection from carbon layers (002).[47] In Figure 7.3e, a few of other insignificant peaks are shown that correspond to the unreacted Te-powder (JPCDS no. 65-3370).[46]

7.3.2. Electrochemical characterizations

In order to evaluate the electrochemical properties of the $MoTe_2$/graphene and pure graphene for supercapacitor behavior, cyclic voltammetry (CV) tests were performed. Figure 7.4a shows the CV curves for all samples at a scan rate of 10 mV s^{-1} within the potential window of −0.6 to 1.4 V in 1 M Na_2SO_4 aqueous electrolyte. Since the current density for the same active load represents the capacitance at the same scan rate, apparently, the $MoTe_2$/graphene nanocomposite possesses a higher capacitance than all other samples of treated carbon cloth and pure graphene. As shown in Figure 7.4b, CV measurements at scan rates of 1 to 200 mV s^{-1} are used to explore the electrochemical properties of $MoTe_2$/graphene electrode. It clearly demonstrates that the current distribution increases with increasing scan rates, which indicates a good rate ability of $MoTe_2$/graphene in 1 M Na_2SO_4 solution.

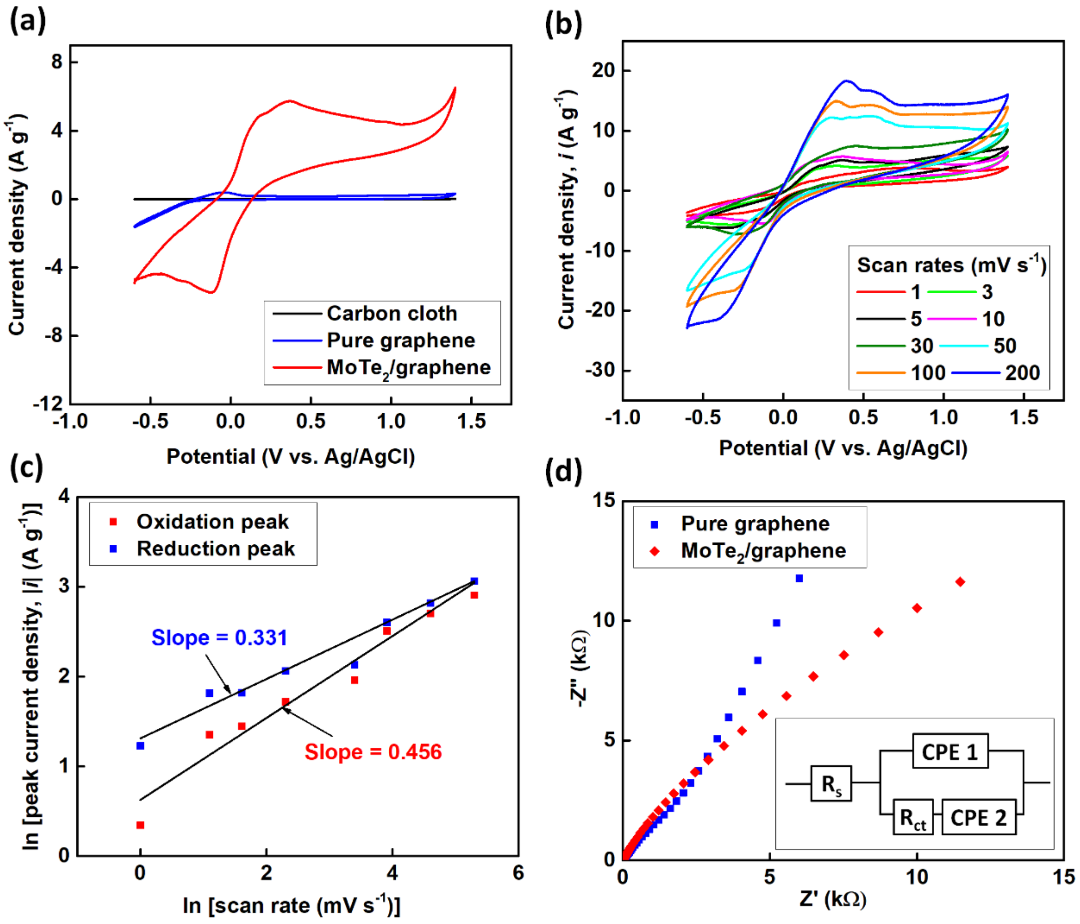

Figure 7.4. (a) The CV curves of treated carbon cloth, pure graphene, and MoTe$_2$/graphene composites within a potential window of −0.6 V to 1.4 V at 10 mV s^{-1}. (b) CV curves of MoTe$_2$/graphene at different scan rates from 1−200 mV s^{-1}. (c) Determination of the b values from the oxidation and reduction peak current densities for MoTe$_2$/graphene. (d) EIS spectra of sample electrodes, showing Nyquist impedance plots (inset: the equivalent circuit diagram).

According to Bruce Dunn and his coworkers' reports,[48,49] a series of different factors can divide the total stored charge into three parts: the capacitive contribution from double layer effect, the capacitive contribution from the charge transfer process with surface atoms (known as pseudocapacitance), and the faradaic contribution from the ion (Na$^+$) insertion/diffusion process.[50,51] These capacitive effects can be characterized by analyzing the CVs at various scan rates based on the following equation:[5,52]

$$i_p = av^b \quad \ldots\ldots\ldots\ldots\ldots\ldots\ldots\ldots\ldots\ldots\ldots\ldots \quad (7.1)$$

Here, the peak current i_p (mA cm^{-2}) obeys a power law relationship with the scan rate v (mV s^{-1}), where a and b are adjustable parameters. According to this equation, the plot of $ln\ (i_p)$ versus $ln\ (v)$ provides a slope that corresponds to the values of b. The value of b close to 1 indicates a capacitive-controlled ion storage process in the electrode, whereas, the value of b close to 0.5 suggests a diffusive-controlled process.[52] As shown in Figure 7.4c, the calculated b values of oxidation and reduction peaks are 0.456 and 0.331, respectively, suggesting a diffusion-controlled reaction (Na^+ insertion/extraction) for $MoTe_2$/graphene electrode. In addition, a couple of redox peaks are found in Figure 7.4a, indicating that the ion diffusion in $MoTe_2$/graphene nanocomposite is a reversible process. Moreover, the peak shifts of cathodic and anodic currents occur with the increase in the scan rates towards lower and higher potentials (Figure 7.4b), respectively, which may be attributed to the ohmic contributions of diffusion-controlled process.[53–55] To investigate the enhanced electrochemical performance of $MoTe_2$/graphene compared with pure graphene, EIS tests were measured at 0.35 V. Later, the Nyquist plots were fitted by an equivalent circuit shown in the inset of Figure 7.4d, and the results are listed in Table 7.1. Here, the intercepts at the real axis in the high frequency range represent the electrolyte resistance (R_s).[56–58] The values of R_s for $MoTe_2$/graphene and pure graphene are 9.48 and 19.78 Ω, respectively. Noticeably, the $MoTe_2$/graphene electrode reveals the smaller R_s value, indicating the high ionic and electrical conductivity and good contact between $MoTe_2$/graphene and carbon cloth current collector,[59] which is beneficial for improving the ion transport rate during the charge/discharge process. This reduced R_s value for $MoTe_2$/graphene composite than pure graphene could be achieved because of the reduction of graphene during microwave irradiation, thus improving the ion/charge transport properties. In addition, R_{ct} refers to charge transfer resistance, which is associated with the process at the electrolyte/electrode interface. The fitted results display lower R_{ct} of 12.18 Ω for $MoTe_2$/graphene than graphene, which could be attributed to facilitate Na^+ ion diffusion into the composite materials. The enhanced electrochemical property arises because of the synergistic effect of $MoTe_2$ and graphene with the increased electrical conductivity, specific surface area and the wettability of the electrode material. Furthermore, the straight line at low frequency represents the mass transfer of Na^+ ions into the electrode materials.[60]

Table 7.1. EIS parameters of $MoTe_2$/graphene and pure graphene electrodes based on the corresponding fitted Nyquist plots.

Samples	**R_s (ohm)**	**R_{ct} (ohm)**	**CPE 1 ($F\ s^{-1}$)**	**CPE 2 ($F\ s^{-1}$)**
$MoTe_2$/graphene	9.48	12.18	0.094×10^{-3}	0.65×10^{-3}
Pure graphene	19.78	10.04×10^{3}	0.260×10^{-3}	0.186×10^{-3}

To further characterize the energy storage behaviors, Figure 7.5a illustrates GCD performance of treated carbon cloth, pure graphene, and $MoTe_2$/graphene electrodes within the potential of −0.6 to 1.4 V vs Ag/AgCl at a current density of 1 A g^{-1}. GCD curves reveal the highest discharge time for $MoTe_2$/graphene composite, comparing to other sample electrodes. Based on the previously mentioned three possible ways for reaction kinetics during charge-discharge,[61] the possible ways for present study are shown below:

(1) Non-faradaic due to double-layer formation:

i) $MoTe_2$ surface + $Na^+ + e^- \rightarrow$ ($Na–MoTe_2$) surface

(2) Faradic charge transfers due to pseudocapacitive behavior:

ii) $MoTe_2 + Na^+ + e^- \leftrightarrow Na - MoTe_2$

(3) Na^+ ion diffusion due to intercalation pseudocapacitance:[29,62]

iii) $MoTe_2 + xNa^+ + xe^- \rightarrow Na_xMoTe_2$

iv) $Na_xMoTe_2 + xe^- \rightarrow Mo + Na_2Te$

v) $Mo + Na_2Te \rightarrow MoTe_2 + Na^+ + xe^-$

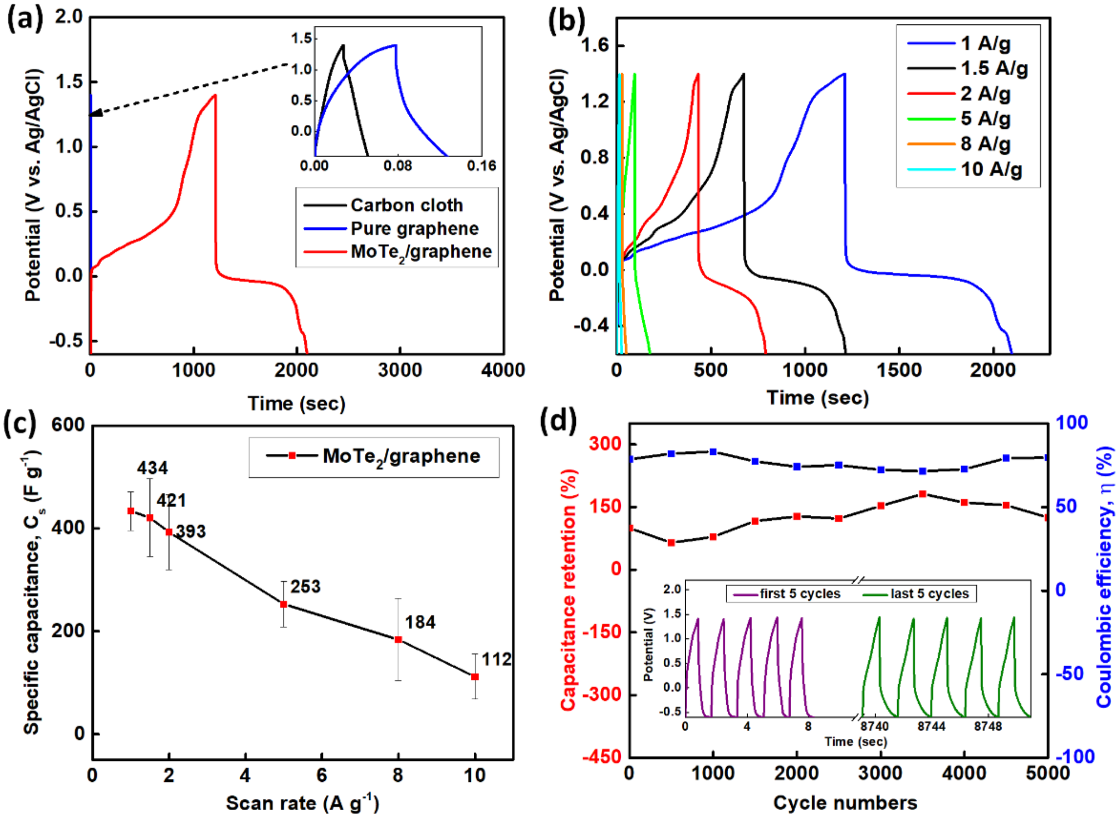

Figure 7.5. (a) GCD curves for carbon cloth, pure graphene, and $MoTe_2$/graphene composites at a current density of 1 A g^{-1}. (b) GCD profile of $MoTe_2$/graphene at different current densities of 1−10 A g^{-1}. (c) Plotting of capacitance versus current densities (1−10 A g^{-1}). (d) Corresponding cycling performance for 5000 cycles at 10 A g^{-1} and coulombic efficiencies.

In addition, the GCD curves at different current densities (1, 1.5, 2, 5, 8 and 10 A g^{-1}) for $MoTe_2$/graphene electrode are exhibited in Figure 7.5b, where the discharge time decreases with respect to increasing the current density, designating better rate potential of the electrode material. The remarkable electrochemical properties of $MoTe_2$/graphene were further emphasized by rate capability tests, where the specific capacitance (C_s) and coulombic efficiency (η) were calculated according to the following relationships (Equations 7.2 and 7.3):[63]

Specific capacitance, $C_s = \frac{2I \int V dt}{m(\Delta V)^2}$ …………………………………….………..……..... (7.2)

Coulombic efficiency, $\eta = \frac{\Delta t_d}{\Delta t_c} \times 100\%$ ……………………………...……..……….. (7.3)

Where, *I* is the discharge current in ampere (A), *ΔV* is the potential window in volt (V), *Δt* is the discharge time in sec (s), *m* is the mass of active material in gram (g), and Δt_c and Δt_d are charging and discharging times in sec (s), respectively. As shown in Figure 7.5c, the specific capacitance of $MoTe_2$/graphene electrode is 434 F g^{-1} at 1 A g^{-1}, while from CV curves specific capacitance is calculated as 1755 F g^{-1} (Figure 7.6) at a scan rate of 1 mV s^{-1}. At the low current density, the diffusion of ions

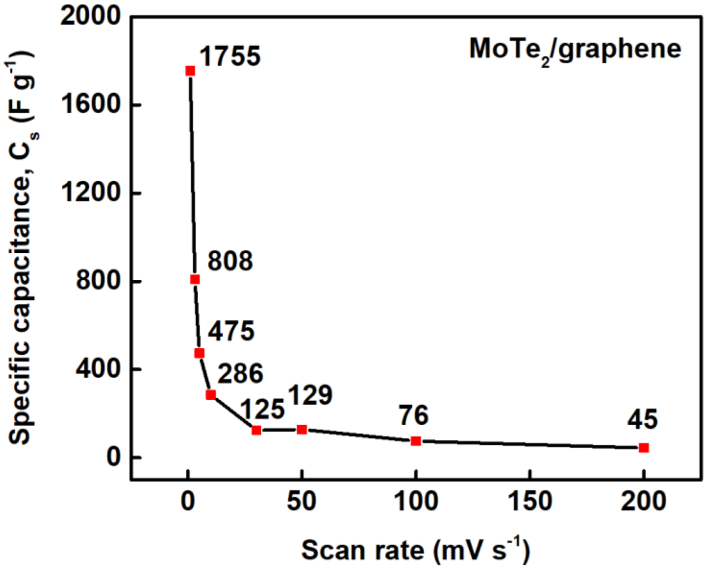

Figure 7.6. Plotting of specific capacitance versus scan rates (1−200 mV s^{-1}) for $MoTe_2$/graphene electrode from cyclic voltammogram (CV) analysis.

from the electrolyte can gain access to almost all available sites of the electrode, leading to a complete insertion reaction. However, with the increase of current densities (Figure 7.5c) or scan rates (Figure 7.6), capacitance declines due to the lack of enough time for the charges to migrate into electrode materials. This decrease in capacitance can also be associated with the inevitably irreversible loss of Na^+ ions for the formation of the electrode-electrolyte interface layer. Furthermore, the electrochemical stability of the $MoTe_2$/graphene nanocomposite was investigated at a current density of 10 A g^{-1} in 1 M Na_2SO_4 aqueous solution (Figure 7.5d). It shows that the initial capacitance (112.58 F g^{-1}) of the $MoTe_2$/graphene electrode increases to 140.74 F g^{-1} after 5000 cycles, which reveals that the electrode retains about 125% of the initial capacitance. This increase in specific capacitance can be attributed to the Na^+ ion intercalation taking place inside material structures, that associates to the increased specific surface area as well as charge storage capacities. It can be also observed that the $MoTe_2$/graphene composite electrode exhibits very good coulombic efficiencies of ~80% (Figure 7.5d) during the stability test.

To confirm the presence of intercalation pseudocapacitance due to Na^+ ion diffusion, further study has been conducted. Based on previous reports, current density at a fixed potential in CV curves can be expressed as follows, to differentiate the effect of capacitance quantitatively *via* the scan rates:[49,64]

$$i = k_1 v + k_2 v^{0.5} \quad \ldots\ldots\ldots\ldots\ldots\ldots\ldots\ldots \text{(7.4)}$$

$$\frac{i}{v^{0.5}} = k_1 v^{0.5} + k_2 \quad \ldots\ldots\ldots\ldots\ldots\ldots\ldots\ldots \text{(7.5)}$$

Where, v is the scan rate (mV s^{-1}), $k_1 v$ and $k_2 v^{0.5}$ correspond to the current contributions of capacitive effects and the diffusion-controlled ion insertion processes, respectively. It is thus possible to distinguish the fraction of the current arising from Na^+ ion diffusion and that from capacitive processes at specific potentials by determining k_1 and k_2 values. Based on equation 5, by plotting $\frac{i}{v^{0.5}}$ versus $v^{0.5}$, k_1 and k_2 were determined from the slope and the y-intercept at specific potentials, which are displayed in Figure 7.7a and 7.7b.

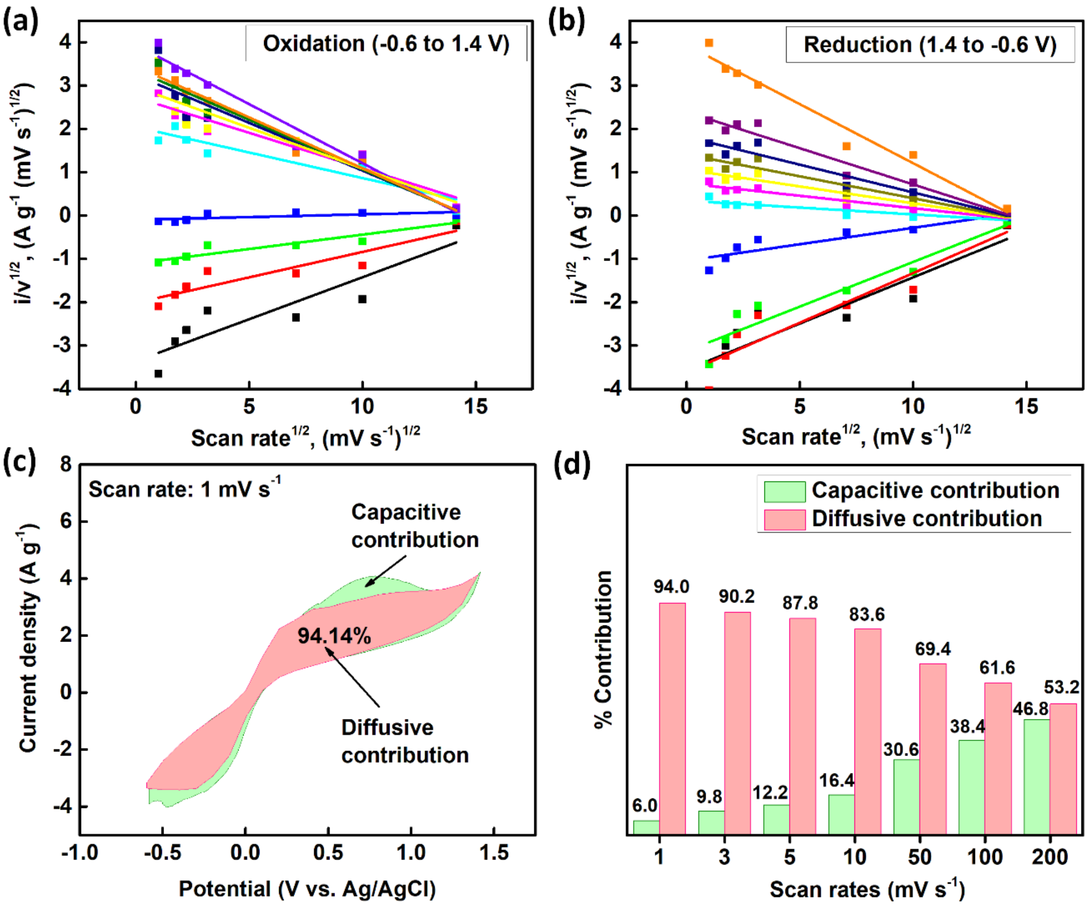

Figure 7.7. Linear fitting of $i/v^{1/2}$ *vs.* $v^{1/2}$ in (a) oxidation range (–0.6 to 1.4 V) and (b) reduction range (1.4 to –0.6 V) of $MoTe_2$/graphene with varying scan rates (1−200 mV s^{-1}) in 1 M Na_2SO_4 solution. (c) Capacitive (green region) and diffusive contributions (pink region) at 1 mV s^{-1}. (d) Capacitive and diffusive contributions at various scan rates (1−200 mV s^{-1}).

Afterward, the capacitance contributions were calculated according to Equation 7.4. As displayed in Figure 7.7c, the diffusive mechanism contributes approximately 94% of the total capacitance for MoTe$_2$/graphene at 1 mV s^{-1}. Moreover, with the increase in scan rates (1−200 mV s^{-1}), ions cannot get enough time to intercalate inside the material structures, therefore the diffusive contribution decreases and capacitive contribution increases (Figure 7.7d).

The physicochemical characterizations after running for 5000 GCD cycles are presented in Figure 7.8, where the EDS and XRD results (Figure 7.8a and 7.8b) confirm the existence of MoTe$_2$ nanosheets on graphene substrate, maintaining the atomic ratio of molybdenum (Mo) and tellurium (Te) close to 1:2. Figure 7.8c exhibits the excellent adhesion of MoTe$_2$/graphene coating on carbon cloth, even after 5000 cycles.

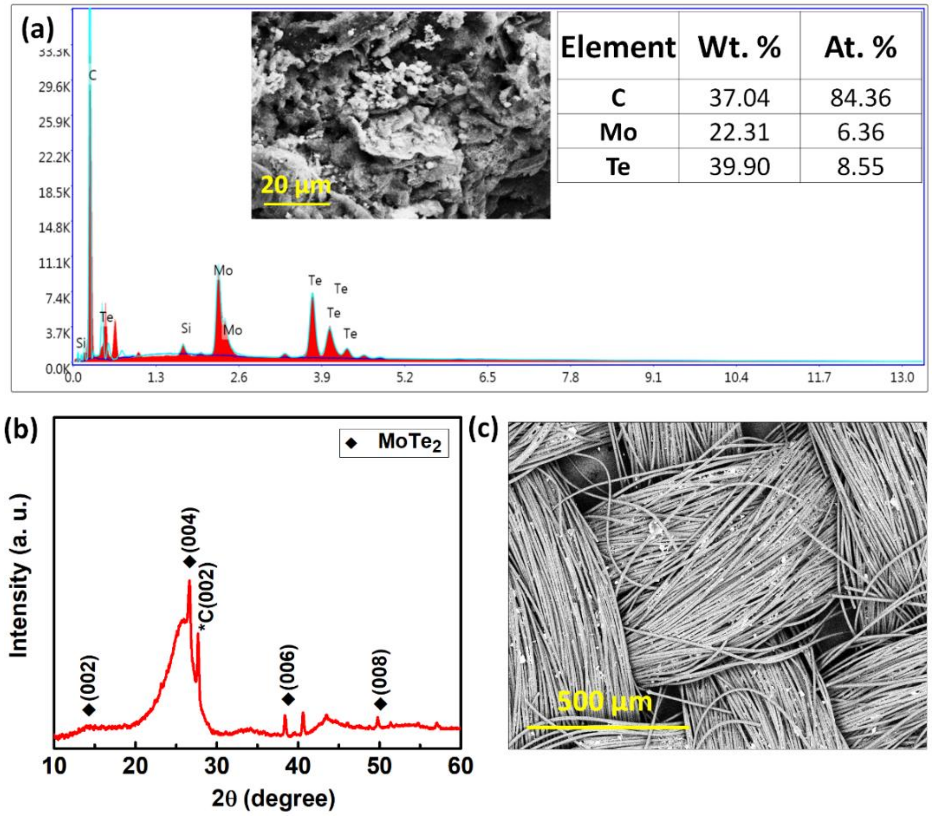

Element	Wt. %	At. %
C	37.04	84.36
Mo	22.31	6.36
Te	39.90	8.55

Figure 7.8. Material characterizations of MoTe$_2$/graphene after the cycling performance for 5000 cycles: (a) EDS pattern of MoTe$_2$/graphene nanocomposite (inset table shows weight% and atomic% of carbon (C), molybdenum (Mo), and tellurium (Te) elements. (b) SEM image of MoTe$_2$/graphene-coated carbon cloth. (c) XRD pattern of MoTe$_2$/graphene.

To explore further the supercapacitor behaviors of $MoTe_2$/graphene, the aqueous symmetric configuration of $MoTe_2$/graphene//$MoTe_2$/graphene was fabricated in 1 M Na_2SO_4 electrolyte, as shown in Figure 7.9a.

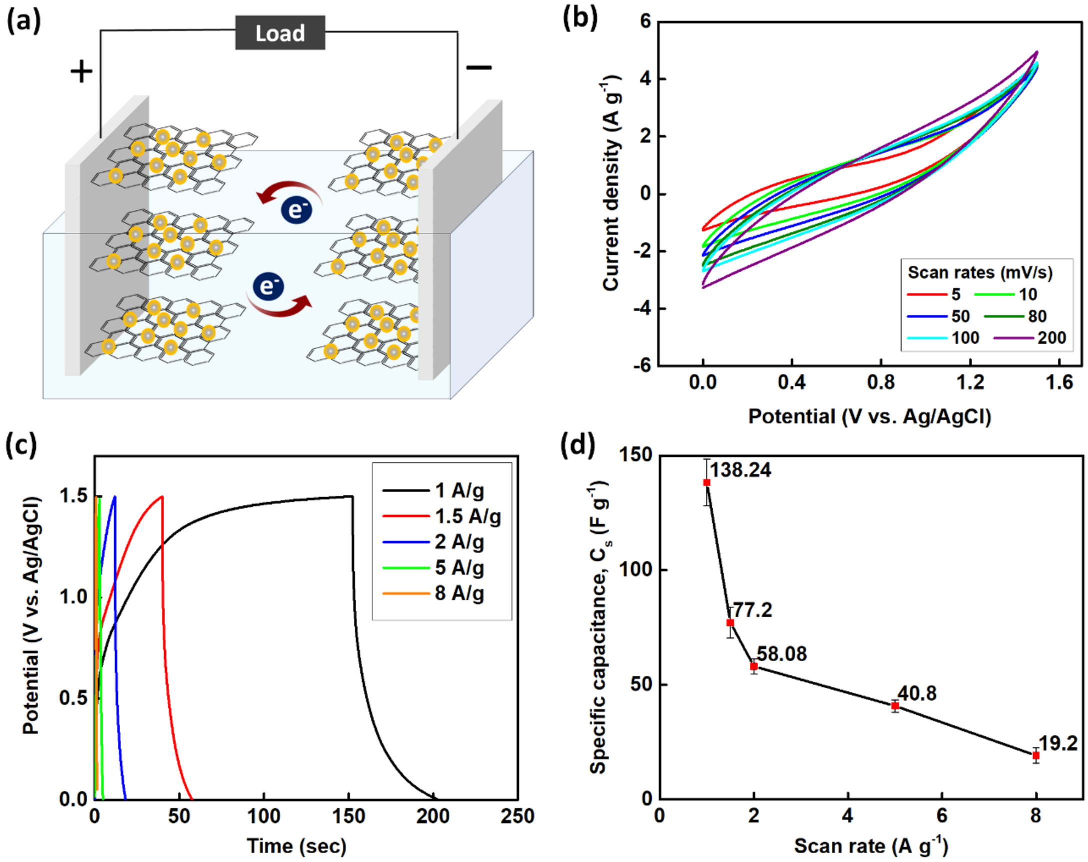

Figure 7.9. (a) Schematic of the symmetric $MoTe_2$/graphene//$MoTe_2$/graphene configuration in 1 M Na_2SO_4 electrolyte. (b) CV profiles at different scan rates within a potential window of 0 to 1.5 V vs. Ag/AgCl. (c) GCD curves at different current densities (1−8 A g^{-1}). (d) Plotting of capacitance versus current densities (1−8 A g^{-1}).

The cell was tested by CV over a wide range of scan rates from 5 to 200 mV s^{-1} (Figure 7.9b) within a potential range of 0 to 1.5 V. The specific capacitance values were calculated from GCD profiles and are presented in Figure 7.9c and 7.9d. The specific capacitance of the symmetric $MoTe_2$/graphene//$MoTe_2$/graphene configuration is found 138 F g^{-1} at a current density of 1 A g^{-1}, based on the total mass of the active materials in the two electrodes by applying the following Equation 7.6:

$$\text{Specific capacitance, } C_s = \frac{4I\int V dt}{m(\Delta V)^2} \quad \ldots\ldots\ldots\ldots \quad (7.6)$$

Additionally, the Ragone plot, relating the specific energy to the specific power is an efficient way to evaluate the supercapacitive performance of electrode material. The energy density (E, Wh kg^{-1}) and power density (P, W kg^{-1}) of an electrode can be calculated using the following Equations 7.7 and 7.8:[63]

$$\text{Energy density, } E = \frac{1}{2}\frac{C(\Delta V)^2}{3.6} \quad \ldots\ldots\ldots\ldots \quad (7.7)$$

$$\text{Power density, } P = \frac{E \times 3600}{t} \quad \ldots\ldots\ldots\ldots \quad (7.8)$$

Where, C is the specific capacitance in F g^{-1}, ΔV is the potential window in volt (V), and t is the discharge time in second (s).

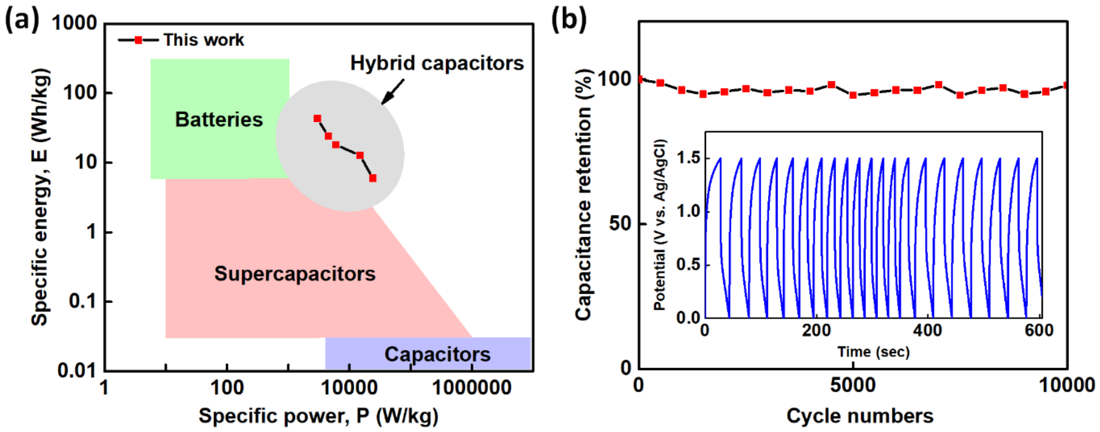

Figure 7.10. (a) Ragone plot of specific energy vs. specific power. (b) Cycling performance for 10,000 cycles at the current density of 10 A g^{-1} (inset shows a section of GCD curves).

As shown in Figure 7.10a and Table 7.2, for the symmetric supercapacitor configuration of $MoTe_2$/graphene//$MoTe_2$/graphene, energy density reaches 43.2 Wh kg^{-1} at a power density of 3,000 W kg^{-1}, and still remains 6 Wh kg^{-1} at a power density of 24,000 W kg^{-1}, which exhibits a large power density range that can be obtained while maintaining a good energy density.

Table 7.2. Supercapacitor parameters of symmetric $MoTe_2$/graphene//$MoTe_2$/graphene configuration in 1 M Na_2SO_4 electrolyte.

Current density, ***I*** **(A g^{-1})**	**Specific capacitance, C_s (F g^{-1})**	**Energy density,** ***E*** **(Wh kg^{-1})**	**Power density,** ***P*** **(W kg^{-1})**
1	138.2	43.2	3000
1.5	77.2	24.1	4500
2	58.1	18.2	6000
5	40.8	12.8	15000
8	19.2	6.0	24000

These results clearly illustrate that the $MoTe_2$/graphene composite possesses excellent hybrid capacitor properties for energy storage application, combining the battery and supercapacitor energy storage behaviors. Furthermore, the cycling life, as one of the most essential requirements in practical applications, has been tested at a constant current density of 10 A g^{-1} for 10,000 cycles. As shown in Figure 7.10b, 98% of the initial capacitance is still retained even after 10,000 cycles, indicating a good long-term stability of the aqueous symmetric $MoTe_2$/graphene//$MoTe_2$/graphene hybrid-capacitor. A comparison of specific capacitance of the resultant $MoTe_2$/graphene is presented with the previous literature values in Table 7.3.

Table 7.3. A comparison of microwave-synthesized $MoTe_2$/graphene with other TMD-based composites from the published energy storage reports.

Material	**Synthesis method**	**Electrolyte**	**Specific capacitance**	**Energy density (Wh kg^{-1})**	**Power density (W kg^{-1})**	**% Retention (No. of cycles)**	**Ref.**
MWCNT/ $MoTe_2$	SILAR	1M NaOH	502 Fg^{-1} at 2 mVs^{-1}	18.51	410	81% at 100 mVs^{-1} (5000)	15
$MoTe_2$/ FLG	direct heating, ball milling	Li-ion battery	596.5 mAh g^{-1} at 0.1 Ag^{-1}	-	-	99% at 0.5 A g^{-1} (400)	16
M-MoS_2-PANi	exfoliation, chemical oxidative polymerization	3M KOH	510 Fg^{-1} at 1 Ag^{-1}	-	-	80% at 10 A g^{-1} (2500)	24
MoS_2/ CNT	Hydrothermal	1M Na_2SO_4	74.05 Fg^{-1} at 2 Ag^{-1}	-	-	81% at 2 A g^{-1} (1000)	25
$MoSe_2$/ MWCNTs	‘dip & dry’ followed by chemical bath deposition	0.5M H_2SO_4	232 Fg^{-1} at 1.4 Ag^{-1}	7.41	681	93% at 100 mVs^{-1} (1000)	26
1T' $MoTe_2$	colloidal chemical synthesis	2M KOH	1393 Fg^{-1} at 1 Ag^{-1}	56.4	800	98% at 50 A g^{-1} (1000)	31
NiTe	Hydrothermal	3M KOH	804 Fg^{-1} at 1 Ag^{-1}	33.6	807.1	91% at 5 A g^{-1} (1000)	65
$MoTe_2$/ graphene	**microwave heating**	**1 M Na_2SO_4**	**434 Fg^{-1} at 1 Ag^{-1}, 1755 Fg^{-1} at 1 mVs^{-1}**	**43.2**	**3000**	**125% at 10 A g^{-1} (5000)**	**This work**

The superior electrochemical performance of the $MoTe_2$/graphene composite can be ascribed to the combined effect of the excellent electrical conductivity of the graphene sheets, good contact between $MoTe_2$ and graphene sheets, as well as the facilitated transfer of electrolyte ions and charges through the nanostructures of the hybrid materials. This clearly shows the promising energy storage behavior of $MoTe_2$/graphene composite for potential practical applications, considering the simplest synthesis approach *via* microwave-initiated irradiation.

7.4. Summary

In summary, we have synthesized $MoTe_2$ nanosheets uniformly dispersed on graphene substrate by microwave-initiated heating method and have explored their supercapacitor applications in energy storage systems. The physicochemical characterizations (i. e. SEM, TEM, EDS, and XRD) verified that the as-produced $MoTe_2$ nanosheets were well anchored on graphene substrate, revealing the effectiveness of our ultra-fast (90 sec) synthesis method. Along with being the microwave absorber, graphene provides a stable support, higher electrical conductivity and the large specific surface area for the growth of $MoTe_2$ nanosheets, facilitating both the electronic and ionic transports along with improving the mechanical strength during charge/discharge cycling stability tests. The resultant $MoTe_2$/graphene composite showed excellent supercapacitor behavior with enhanced cycling performance. The aqueous symmetric $MoTe_2$/graphene//$MoTe_2$/graphene configuration behaves as hybrid capacitors, which is capable to fill the gap between high-energy density batteries and high-power density supercapacitors by their fast charge-discharge performance and excellent electrochemical stabilities. Moreover, the microwave-initiated synthesis is an environmentally benign and simple method, capable for extending to large-scale, economic production that makes the as-produced $MoTe_2$/graphene an attractive low-cost electrode material with high performance and promising stability for energy storage supercapacitor devices.

7.5. References

1 D. Qi, Y. Liu, Z. Liu, L. Zhang and X. Chen, *Adv. Mater.*, 2017, **29**, 1–19.

2 G. Wang, L. Zhang and J. Zhang, *Chem. Soc. Rev.*, 2012, **41**, 797–828.

3 J. R. Miller and P. Simon, *Science (80)*, 2008, **321**, 651–652.

4 Q. Lu, J. G. Chen and J. Q. Xiao, *Angew. Chemie - Int. Ed.*, 2013, **52**, 1882–1889.

5 F. Guo, N. Gupta and X. Teng, *Supercapacitors - Theor. Pract. Solut.*, 2018.

6 T. Brezesinski, J. Wang, S. H. Tolbert and B. Dunn, *J. Sol-Gel Sci. Technol.*, 2011, **57**, 330–335.

7 S. Bose, T. Kuila, A. K. Mishra, R. Rajasekar, N. H. Kim and J. H. Lee, *J. Mater. Chem.*, 2012, **22**, 767–784.

8 J. Li and F. Gao, *J. Power Sources*, 2009, **194**, 1184–1193.

9 T. Cottineau, M. Toupin, T. Delahaye, T. Brousse and D. Bélanger, *Appl. Phys. A Mater. Sci. Process.*, 2006, **82**, 599–606.

10 R. R. Salunkhe, Y. V. Kaneti and Y. Yamauchi, *ACS Nano*, 2017, **11**, 5293–5308.

11 M. A. Bissett, S. D. Worrall, I. A. Kinloch and R. A. W. Dryfe, *Electrochim. Acta*, 2016, **201**, 30–37.

12 R. Thangappan, S. Kalaiselvam, A. Elayaperumal, R. Jayavel, M. Arivanandhan, R. Karthikeyan and Y. Hayakawa, *Dalt. Trans.*, 2016, **45**, 2637–2646.

13 B. Xie, Y. Chen, M. Yu, T. Sun, L. Lu, T. Xie, Y. Zhang and Y. Wu, *Carbon N. Y.*, 2016, **99**, 35–42.

14 M. S. Javed, S. Dai, M. Wang, D. Guo, L. Chen, X. Wang, C. Hu and Y. Xi, *J. Power Sources*, 2015, **285**, 63–69.

15 S. S. Karade and B. R. Sankapal, *ACS Sustain. Chem. Eng.*, 2018, **6**, 15072–15082.

16 N. Ma, X. Y. Jiang, L. Zhang, X. S. Wang, Y. L. Cao and X. Z. Zhang, *Small*, 2018, **14**, 1–8.

17 Y. K. Hsu, Y. C. Chen and Y. G. Lin, *Electrochim. Acta*, 2014, **139**, 401–407.

18 A. Wang, H. Wang, S. Zhang, C. Mao, J. Song, H. Niu, B. Jin and Y. Tian, *Appl. Surf. Sci.*, 2013, **282**, 704–708.

19 C. V. V. M. Gopi, A. E. Reddy, J. S. Bak, I. H. Cho and H. J. Kim, *Mater. Lett.*, 2018, **223**, 57–60.

20 S. Iqbal, H. Khatoon, A. Hussain Pandit and S. Ahmad, *Mater. Sci. Energy Technol.*, 2019, **2**, 417–428.

21 Y. Bin Tan and J. M. Lee, *J. Mater. Chem. A*, 2013, **1**, 14814–14843.

22 Z. Hu, K. Ma, W. Tian, F. Wang, H. Zhang, J. He, K. Deng, Y. X. Zhang, H. Yue and J. Ji, *Appl. Surf. Sci.*, 2020, **508**, 144777.

23 Y. Zhu, X. Lv, L. Zhang, X. Guo, D. Liu, J. Chen and J. Ji, *Electrochim. Acta*, 2016, **215**, 247–252.

24 S. A. Ansari, H. Fouad, S. G. Ansari, M. P. Sk and M. H. Cho, *J. Colloid Interface Sci.*, 2017, **504**, 276–282.

25 M. Chen, Y. Dai, J. Wang, Q. Wang, Y. Wang, X. Cheng and X. Yan, *J. Alloys Compd.*, 2017, **696**, 900–906.

26 S. S. Karade and B. R. Sankapal, *J. Electroanal. Chem.*, 2017, **802**, 131–138.

27 J. Jia, J. Wu, J. Dong, Y. Tu, Z. Lan, L. Fan and Y. Wei, *IEEE J. Photovoltaics*, 2016, **6**, 1196–1202.

28 A. Kumar and P. K. Ahluwalia, *Eur. Phys. J. B*, 2012, **85**, 18–22.

29 M. R. Panda, A. Raj K, A. Ghosh, A. Kumar, D. Muthuraj, S. Sau, W. Yu, Y. Zhang, A. K. Sinha, M. Weyland, Q. Bao and S. Mitra, *Nano Energy*, 2019, **64**, 103951.

30 Y. Liu, J. Wang, Y. Xu, Y. Zhu, D. Bigio and C. Wang, *J. Mater. Chem. A*, 2014, **2**, 12201–12207.

31 M. Liu, Z. Wang, J. Liu, G. Wei, J. Du, Y. Li, C. An and J. Zhang, *J. Mater. Chem. A*, 2017, **5**, 1035–1042.

32 M. Liu, X. Wang, Z. Huang, P. Guo and Z. Wang, *Mater. Lett.*, 2017, **206**, 229–232.

33 X. Zhang and Z. Liu, *Nanoscale*, 2012, **4**, 707–714.

34 Z. Liu, L. Zhang, S. Poyraz, J. Smith, V. Kushvaha, H. Tippur and X. Y. Zhang, *Rsc Adv.*, 2014, **4**, 9308–9313.

35 Z. Liu, L. Zhang, R. Wang, S. Poyraz, J. Cook, M. J. Bozack, S. Das, X. Zhang and L. Hu, *Sci. Rep.*, **6**, 22503 (2016).

36 Y. Jiang and Y.-J. Zhu, *J. Phys. Chem. B*, 2005, **109**, 4361–4364.

37 X. Yang, Y. Tian, S. Sarwar, M. Zhang, H. Zhang, J. Luo and X. Zhang, *Electrochim. Acta*, **311** (2019) 230−243.

38 S. Anantharaj, J. Kennedy and S. Kundu, *ACS Appl. Mater. Interfaces*, 2017, **9**, 8714–8728.

39 Y. Zhu, S. Murali, M. D. Stoller, A. Velamakanni, R. D. Piner and R. S. Ruoff, *Carbon N. Y.*, 2010, **48**, 2118–2122.

40 D. Wang, R. Dai, X. Zhang, L. Liu, H. Zhuang, Y. Lu, Y. Wang, Y. Liao and Q. Nian, *Carbon N. Y.*, 2020, **161**, 880–891.

41 Y. Wang, F. Yu, M. Zhu, C. Ma, D. Zhao, C. Wang, A. Zhou, B. Dai, J. Ji and X. Guo, *J. Mater. Chem. A*, 2018, **6**, 2011–2017.

42 S. Sarwar, A. Nautiyal, J. Cook, Y. Yuan, J. Li, S. Uprety, R. Shahbazian-yassar, R. Wang, M. Park, M. J. Bozack and X. Zhang, *Sci. CHINA Mater.*, 2019, 1–13.

43 A. Roy, H. C. P. Movva, B. Satpati, K. Kim, R. Dey, A. Rai, T. Pramanik, S. Guchhait, E. Tutuc and S. K. Banerjee, *ACS Appl. Mater. Interfaces*, 2016, **8**, 7396–7402.

44 Y. Sun, Y. Wang, D. Sun, B. R. Carvalho, C. G. Read, C. H. Lee, Z. Lin, K. Fujisawa, J. A. Robinson, V. H. Crespi, M. Terrones and R. E. Schaak, *Angew. Chemie - Int. Ed.*, 2016, **55**, 2830–2834.

45 T. K. Gupta, B. P. Singh, V. N. Singh, S. Teotia, A. P. Singh, I. Elizabeth, S. R. Dhakate, S. K. Dhawan and R. B. Mathur, *J. Mater. Chem. A*, 2014, **2**, 4256–4263.

46 Z. Wang, W. Wang, Y. Yang, W. Li, L. Feng, J. Zhang, L. Wu and G. Zeng, *Int. J. Photoenergy*, 2014, 1–6.

47 M. Khan, A. Bin Yousaf, M. Chen, C. Wei, X. Wu, N. Huang, Z. Qi and L. Li, *Nano Res.*, 2016, **9**, 837–848.

48 T. Brezesinski, J. Wang, J. Polleux, B. Dunn and S. H. Tolbert, 2009, 1802–1809.

49 J. Wang, J. Polleux, J. Lim and B. Dunn, *J. Phys. Chem. C*, 2007, **111**, 14925–14931.

50 W. G. Pell, B. E. Conway, W. A. Adams and J. De Oliveira, *J. Power Sources*, 1999, **80**, 134–141.

51 B. E. Conway, *Electrochim. Acta*, 1993, **38**, 1249–1258.

52 J. Kang, Q. Su, H. Feng, P. Huang, G. Du and B. Xu, *Electrochim. Acta*, 2019, **301**, 29–38.

53 R. Sun, Q. Wei, J. Sheng, C. Shi, Q. An, S. Liu and L. Mai, *Nano Energy*, 2017, **35**, 396–404.

54 A. Vlad, N. Singh, J. Rolland, S. Melinte, P. M. Ajayan and J. F. Gohy, *Sci. Rep.*, 2014, **4**, 1–7.

55 G. Alarcón-Angeles, B. Pérez-López, M. Palomar-Pardave, M. T. Ramírez-Silva, S. Alegret and A. Merkoçi, *Carbon N. Y.*, 2008, **46**, 898–906.

56 K. Zhou, W. Zhou, L. Yang, J. Lu, S. Cheng, W. Mai, Z. Tang, L. Li and S. Chen, *Adv. Funct. Mater.*, 2015, **25**, 7530–7538.

57 S. Li, J. Chen, M. Cui, G. Cai, J. Wang, P. Cui, X. Gong and P. S. Lee, *Small*, 2017, **13**,

1–9.

58 S. Li, X. Cao, C. N. Schmidt, Q. Xu, E. Uchaker, Y. Pei and G. Cao, *J. Mater. Chem. A*, 2016, **4**, 4242–4251.

59 X. Chen, M. Cheng, D. Chen and R. Wang, *ACS Appl. Mater. Interfaces*, 2016, **8**, 3892–3900.

60 V. A. Agubra, L. Zuniga, D. De La Garza, L. Gallegos, M. Pokhrel and M. Alcoutlabi, *Solid State Ionics*, 2016, **286**, 72–82.

61 N. R. Chodankar, G. S. Gund, D. P. Dubal and C. D. Lokhande, *RSC Adv.*, 2014, **4**, 61503–61513.

62 Y. Wang, Y. Song and Y. Xia, *Chem. Soc. Rev.*, 2016, **45**, 5925–5950.

63 B. Pandit, D. P. Dubal and B. R. Sankapal, *Electrochim. Acta*, 2017, **242**, 382–389.

64 A. J. Bard, L. R. Faulkner, *ELECTROCHEMICAL METHODS Fundamentals and Applications*, 1944.

65 P. Zhou, L. Fan, J. Wu, C. Gong, J. Zhang and Y. Tu, *J. Alloys Compd.*, 2016, **685**, 384–390.

Chapter 8

Future research and conclusion

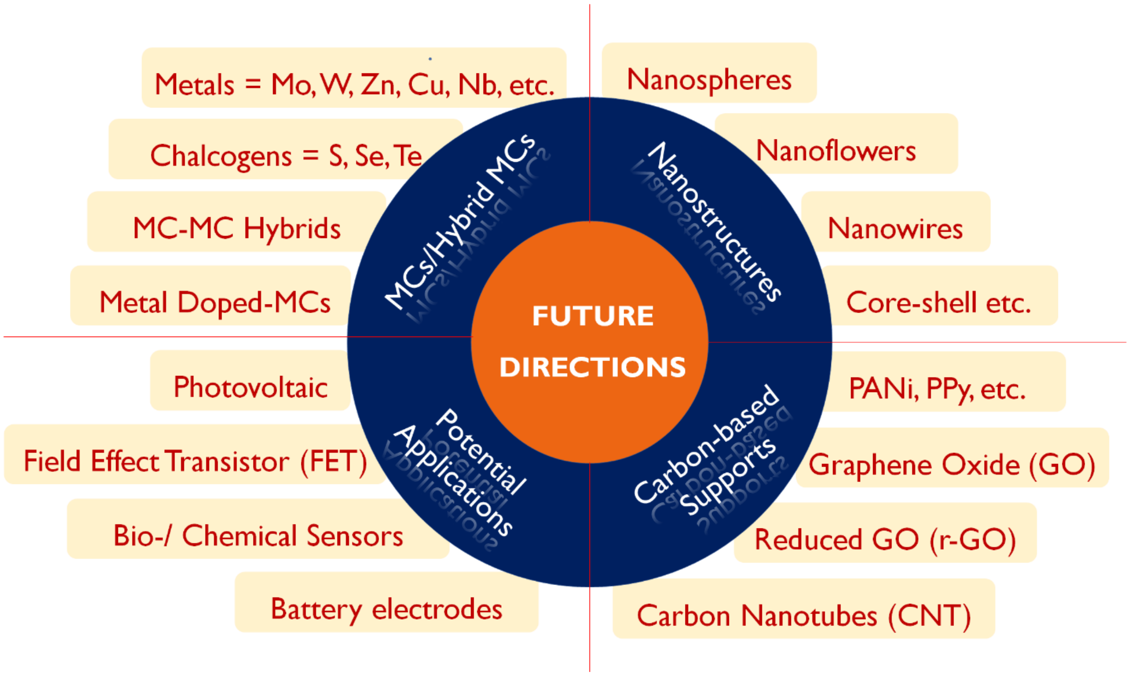

This chapter describes the possible future works to advance the present research.

8.1. Future directions

For the future development of this research, it is very important to understand the mechanisms behind the electrocatalytic activities and energy storage behaviors of metal chalcogenides (MCs) with graphene nanocomposites. The appealing features of these materials do not solely depend on the intrinsic properties of the constructing components but also on the method of intelligent construction, hybridization, and the synergy of these nanomaterials. In this regard, microwave-initiated synthesis approach ought to be performed to construct nanocomposites in a highly controlled manner, with improved physicochemical and electrochemical properties of final products. Based on the outcomes of this research, the future work can focus on four diverse directions: (i) exploring other combinations of MCs and their hybrids, such as WS_2, WSe_2, VS_2, $CoSe_2$, $CoTe_2$, etc.; (ii) synthesizing a variety of nanostructures (nanosheets, nanotubes, nanoflowers, etc.) of MCs; (iii) growing MCs on a series of different carbon-based supports like, carbon nanotubes (CNTs), conducting polymers (PANi, PPy, etc.), reduced graphene oxide (rGO) and observing the effects on electrochemical (EChem) activities; (iv) employing MC-based nanocomposites for other potential applications, such as photovoltaic, thermoelectric/magnetic devices, chemical/biological sensors, electrocatalytic activity towards oxygen reduction reaction (ORR), battery electrodes and so on. Scalability can also be a great focus for the future research to commercializing these nanocomposites in the practical world of industries through microwave-initiated synthesis approach.

8.1.1. Exploring other MCs and their hybrid compounds

Metal chalcogenides (MCs), including metal sulfides (MS_x), metal selenides (MSe_x) and metal tellurides (MTe_x), have attracted tremendous attention for various functional applications due to their unique physicochemical properties (e.g., high electrical conductivity, good thermal stability, earth abundancy, etc.).[1–3] Although, in the MC family, molybdenum disulfide (MoS_2) has been subjected to the most intensive research, recently, it has been demonstrated that, akin to MoS_2, the electronic structures of other MCs (such as WS_2, WSe_2, and $MoSe_2$) and their electrical transport, optical and optoelectronic properties are strongly influenced by the number of layers, microstructures, routes of synthesis, and electrical contacts.[4] Currently, various strategies, such as controlled heteroatom doping, engineering nanostructures, and hybridization with conductive frameworks, etc., have been carried out to improve the intrinsic properties of MC-based compounds. The recent research has progressed to develop several of MCs (e.g., MS_x or MSe_x or MTe_x; M = Fe, Co, Ni, Sn, Mo, W, V, Sb, Mn, Zn, Cu, Nb, Ti, Ta, Bi or a mixture of metals) for electrocatalysis and supercapacitor/battery applications.[5–10] The basic crystal structures of the 2D MCs are illustrated in Figure 8.1a and the possible MC compounds based on the position of the metal are shown in the periodic table (Figure 8.1b).[11]

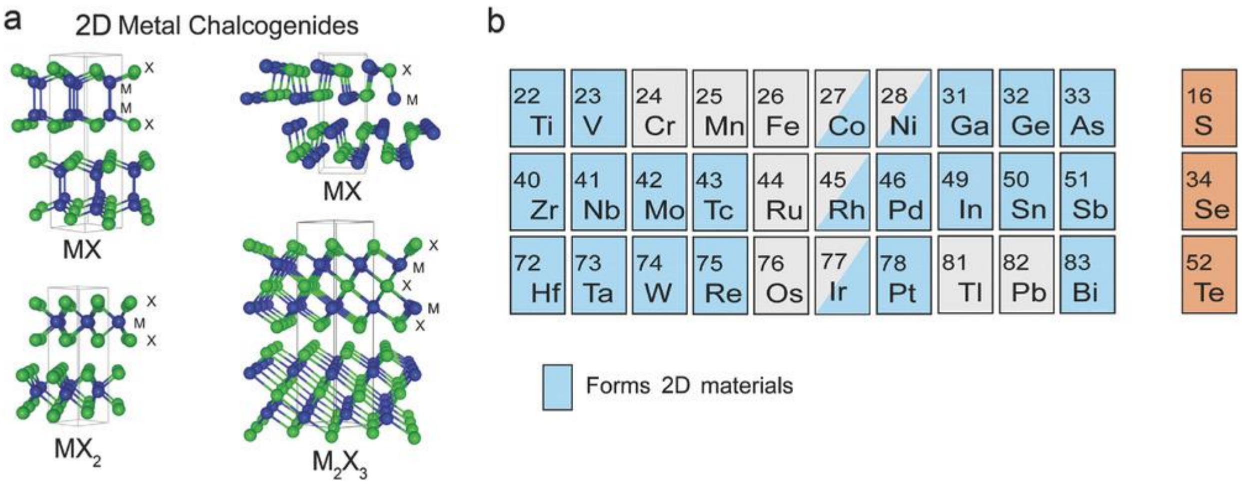

Figure 8.1. (a) Schematic description of various MC crystal structures in MX, MX_2, and M_2X_3 type stoichiometries. (b) Known layer structured 2D MCs, organized based on the metal elements involved.[11]

The 2D metal monochalcogenides (MX, e.g., GaS, InS, GaSe, GeS, SnS, SnSe, GaTe, FeSe) mostly correspond to group IIIA or IVA metals.[4] In addition, the elements from group IIIB-VIII and IVA can be used to form 2D metal dichalcogenides (MX_2, e.g., MoS_2, WSe_2, $MoTe_2$, GeS_2, $SnSe_2$, etc.). Furthermore, MX_3 and M_2X_3 are two types of 2D metal trichalcogenides with different stoichiometric proportions. The metal component of MX_3 (e.g., TiS_3, $ZrSe_3$, $HfSe_3$, $NbSe_3$, etc.) is usually from group IVB or group VB.[4] M_2X_3 possesses various crystal structures with different arrangements of atoms in a layer and stacking configurations. Moreover, introducing noble metals (Pt, Au, Ru, Pd, etc.) to hybridize with single-phased MC nanomaterials is highly estimated to bring enhanced or unique useful properties for electrochemical applications. In recent years, many noble metal−modified MC nanostructures have been prepared by different methods.[12–14] Furthermore, the intense research on modifying MCs with MCs has an extended history. The created MC–MC nanostructures usually exhibit multifunctionalities, enhanced intrinsic properties, and revolutionary new properties. For instance, hybrid MoFeNiS and MoFeNiS/rGO catalysts were prepared by the one-step hydrothermal method for HER by M Askari et al.[15] By modulating the components of alloys based on 2D MCs, such as $Mo_xW_{1-x}S_2$ and $SnS_{2x}Se_{2-2x}$, a controllable bandgap covering a continuous region of the spectrum can be realized.[16] In contrast to other 2D MCs, ReX_2 and $WMoTe_2$ are special distorted 1T crystal phases, and significant differences exist in the different orientations in the layer planes of their crystal structures.[17] There are many such examples of single–component MCs, noble metal–MC hybrids, and MC–MC hybrids. The energy–efficient microwave–initiated synthesis can be a promising way to explore these other combinations of metal chalcogenides with their enhanced properties.

8.1.2. Synthesis of different nanostructures of metal chalcogenides (MCs)

Through different synthesis approaches, metal chalcogenides (MCs) have been synthesized with different types of nanostructures, such as nanoparticles, nanosheets, nanowires, nanofibers, nanotubes, quantum dots, nanoribbons, nanobelts, nanocapsules, and so on, considering their different morphologies, orientations, and characteristics. To date, the microwave-initiated irradiation has been applied to prepare various MC nanomaterials.[18–24] Alonso-Vante et al.[18] and Amini et al.[21] reported the synthesis of carbon-supported Co_3S_4, $CoSe_2$, and CoSe nanoparticles with small sizes and narrow distributions within 3–5 min by microwave stimulation. The group of Ramanath reported a rapid and scalable (gram-a-minute) microwave-irradiated solvothermal synthesis of sulfurized Sb_2Se_3 nanowires and nanotubes.[25] The authors have discovered that, the diameter and length of these 1D nanostructures can be controlled by tuning the microwave dose (= microwave power × time). Moreover, the increasing nanotube content can be resulted with the increase in microwave dose, that is 7–10% for 60 s, 15–17% for 90 s, and 62–65% for 120 s syntheses, respectively (Figure 8.2).[25] A similar morphology control process was demonstrated by EI-Shall and co-workers in their microwave synthesis of semiconductor nanorods and nanowires.[26] They have demonstrated that by simply varying the microwave radiation times from 30–60 s to 1–2 min to >3 min, the stepwise formation of the ZnS and ZnSe nanowires from small spherical nuclei to short aligned rods to long assemblies of nanowires was observed. Moreover, Wang et al.[27] has prepared MoS_x@CNT hybrids having the shape of caterpilliar with core-shell structure by a facile solvothermal strategy. This protocol helped to enrich the ultrathin MoS_x nanosheets with basal edges and unsaturated S atoms on its entire surface, eventually increasing the density of active sites along with resulting superior HER activity and stability. Xiang et al.[28] synthesized flower-like MoS_2

layers assembled on graphene foam (GF) via microwave irradiation, by dipping GF into a sealed glass tube containing a solution of $Na_2MoO_4 \cdot 2H_2O$ and thioacetamide, under microwave condition of 180 ºC for 12 h.

Based on these previous studies, it can be clearly seen that the microwave-initiated synthesis can be successfully employed to generate different nanostructures of MC-based nanomaterials, MC nanocomposites, and MC hybrid materials. By adjusting the reaction precursors, experimental conditions and microwave parameters, a variety of nanostructures can be developed through this facile microwave-irradiation approach.

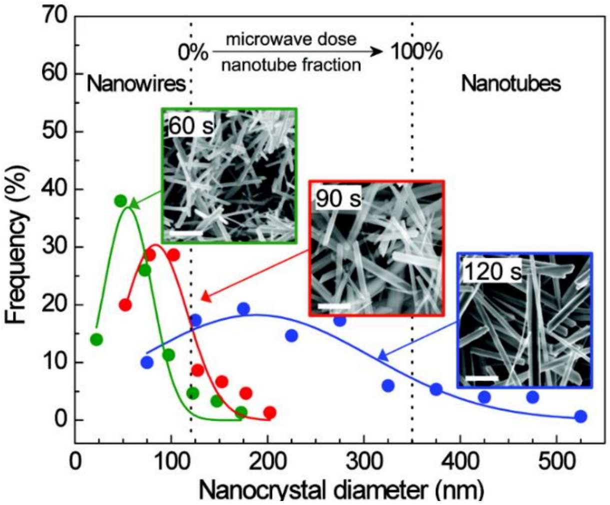

Figure 8.2. Size distribution graphs with SEM insets (scale bars = 1 mm) of the Sb_2Se_3 nanocrystals.

8.1.3. Employing other different carbon-based supports

The hybridization of 2D MCs with a highly conductive supporting material has been one of the fascinating routes to generate new functional hybrid materials that can overcome the issues with restacking, low electrical conductivity, and poor electrical contact, as well as boost MC activities for real advanced applications. Taking these factors into account, many efforts have coupled 2D MCs with various carbon-based supporting materials to expose more active sites and facilitate the charge transfer ability.[27–33] Carbon materials especially activated carbon, graphene, reduced graphene oxide (r-GO), carbon nanotubes (CNTs), carbon nanodots, fullerenes, carbon nanospheres, etc. have been intensively studied as substrates to host MC nanomaterials for electrochemical applications.[34–37] Figure 8.3 displays a few of the examples where different carbon-based supports have been employed to synthesize MC-based hybrid materials.

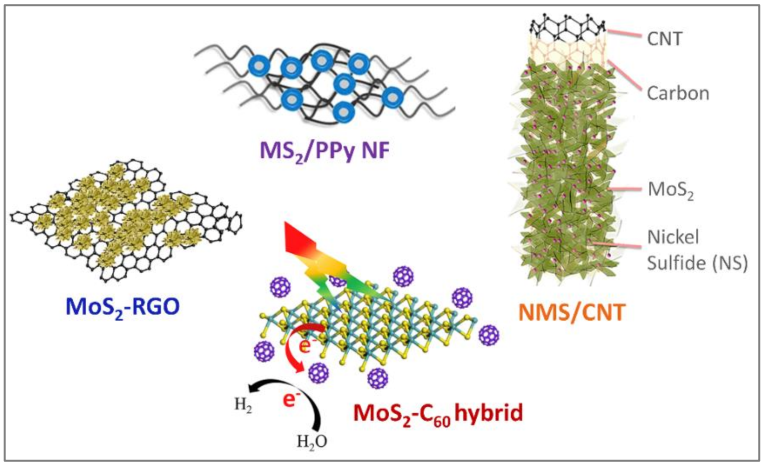

Figure 8.3. Metal chalcogenides on different carbon-based supports: Polypyrrole nanofiber (PPy NF), reduced graphene oxide (RGO), carbon nanotube (CNT) and fullerene (C_{60}).[22,38–40]

Additionally, the conducting polymers (CPs), like polyaniline (PANi), polypyrrole (PPy), polythiophene (PTh) and Poly(3,4-ethylenedioxythiophene) (PEDOT) have attracted great interests in electrocatalytic, energy storage, sensors, and electrochromic devices since the discovery in 1960.[41–44] They have high conductivity and excellent capacitive properties, which could be beneficial for better electrocatalytic and energy storage applications. Among the CPs, PANi generates most attention because it has the highest specific capacitance due to multi-redox reactions, better thermal stability, good electronic properties, easy synthesis, and low cost for its infinite abundance.[41,45,46] Therefore, the CPs can be prominently used as a support for MCs or hybrid MC nanomaterials.

8.1.4. Other potential applications of MC-based compounds

MC-based nanomaterials and nanocomposites have considered attractive for diverse applications, which are inspired by their exceptional physicochemical properties, including large surface area, high mechanical properties, electrostatic efficiency, good semiconducting ability, high catalytic activity, optical transparency, sensor sensitivity, high chemical stability, low cost, and easy synthesis.[29,47,48] Therefore, there has recently been rapid increase in research on 2D MCs for various application fields, such as batteries, supercapacitors, electrocatalysts, transistors, optical displays, solar cells, and sensors.[4,5,29,47,49] A few of the examples are displayed in Figure 8.4.

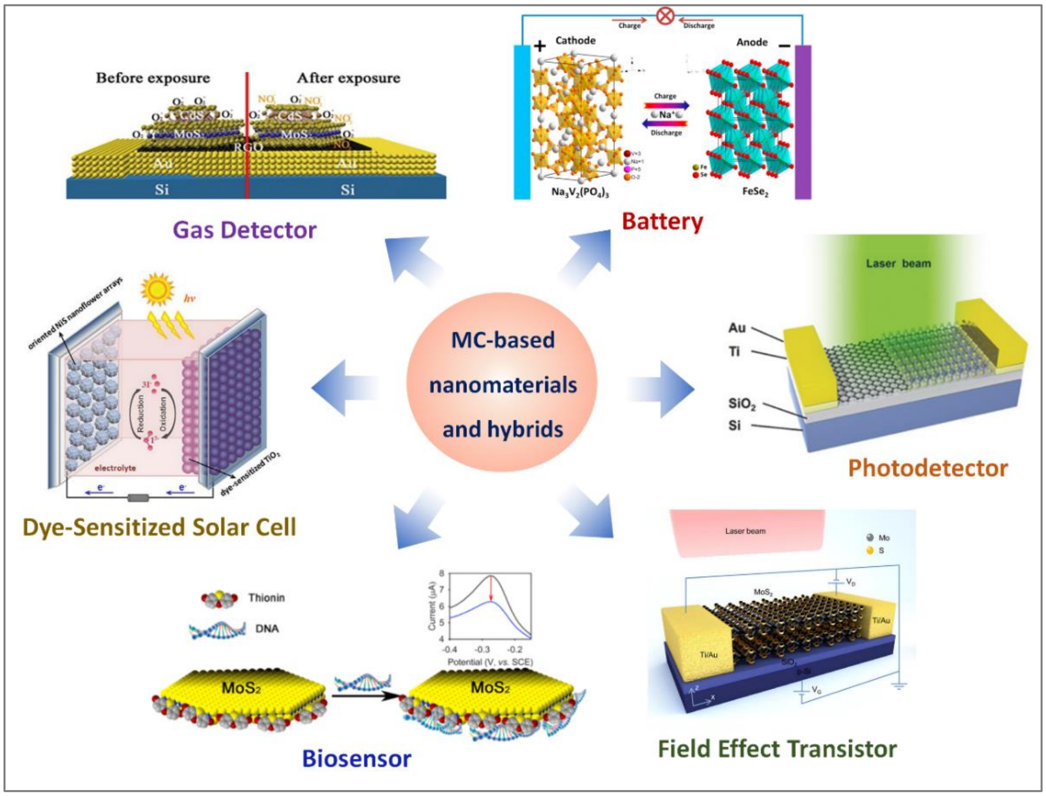

Figure 8.4. Applications of 2D MCs for transistors, solar cells, gas detectors, batteries, photodetectors, and biosensors.[50–55]

8.1.4.1. Electrochemical sensor applications

The huge demand for developing highly sensitive, selective, low power consuming, reliable and portable sensors have stimulated extensive research on new sensing materials based on MCs. The high surface to volume ratio in MCs offers huge potential for the detection of large amounts of target analysts per unit area as well as rapid response and recovery with low power consumptions for various sensing applications including gas, chemical, small molecules, methyl parathion, dopamine, glucose, DNA, and RNA biosensors.[50,56–59] Moreover, the recent demonstration of scalable synthesis of MCs has shown the potential to fabricate cost-effective, reliable sensors.

8.1.4.2. Dye-sensitized solar cells

Dye-sensitized solar cells (DSSCs) have been widely studied, due to their low cost, simple fabrication strategy, and great photovoltaic conversion efficiency.[60] Platinum (Pt) is the most common catalyst with high electrocatalytic activity; however, its high-cost leads to a critical barrier to produce cost-effective devices for commercialization purpose.[60,61] Recent development of MCs, carbon supported−MCs and MC−hybrids is a promising route for discovering suitable materials to apply for DSSCs, in requirement of high yield and reduced cost.[51,62–64] Generally, the power conversion efficiency of DSSCs based on MCs as counter electrode are not high enough for real application to date. Therefore, the development of novel MC-based hybrids by modified methods to produce unique morphologies and structures, or heteroatom doping process is expected to further improve the efficiency of devices in future.

8.1.4.3. Batteries

Rechargeable batteries, such as lithium-ion batteries (LIBs), sodium-ion batteries (SIBs), potassium-ion batteries (PIBs) are the basic power sources for our everyday actions, due to their high energy density and long-term cyclic stability. To fabricate efficient devices, rapid and stable insertion/extraction process of ions is the crucial requirement of high−performance energy storage materials. The stability of electrode structure during the insertion/extraction process of ions is also a key factor to prolong the cycle life of batteries. Considering this, MC layers have been considered as an ideal candidate. The major issue for real applications of MCs is insufficient cyclic stability.[30,47] Therefore, integration of MCs with highly conductive graphene nanosheets has been one of the promising options to remarkably increase the porosity, specific surface area, and physicochemical properties of the obtained material, due to the compatibility of their structure and morphology, thus promoting the corresponding electrochemical performances, in term of activity and stability. Recently, studies of the hierarchical 2D and 3D sheet-like structures of MC-based hybrids have been extensively developed as superior electrode materials in LIBs, SIBs, and PIBs.[65–70] To further enhance the capacity of electrode materials through improvement of the surface area and the number of exposed active sites, as well as reduce the restacking and aggregation phenomenon, the growth of vertical sheet-like structures of MCs on graphene surface has been of interest.[71–73] In addition, the development of 3D architectures of 2D-MC/graphene is also a promising route to gain maximum benefit from their structure.[52,74–77] Recently, the aerogels of MC-based hybrids have been also considered as ideal candidates for battery applications.[78–80] These materials possess excellent conductivity for improving the charge transfer ability, and large surface area for MCs assembly, preventing mechanical peeling off and the restacking of MCs during operation, and enhancing wettability for effective ion diffusion, as well as good contact area between electrolyte and catalysts.

8.1.4.4. OER/ORR electrocatalysts for fuel cell

During the past decade, fuel cells have attracted much attention, due to their easy conversion from chemical energy to electric energy with high power density. The Pt based electrocatalysts have been extensively employed for fuel cell applications; however, the high cost, high toxicity, and low stability are critical factors limiting their applications. Therefore, the development of novel nanomaterials for fuel cell is still a high requirement to date. Although the cathode catalyst still represents a considerable portion of the total system cost, the real bottleneck of water electrolysis process corresponds to the anodic oxygen evolution reaction (OER) and oxygen reduction reaction (ORR). The construction of nanostructured MCs and their hybrids as electrocatalysts has recently been considered a potential route to discover suitable catalyst materials for fuel cells.[81–85] Generally, the hybrids based on MCs and graphene could produce good response towards ORR; however, their performance has so far remained significantly lower than that of the commercial Pt/C electrode. Therefore, development of novel synthesis approaches or doping process has recently demonstrated to be necessary to create nanostructured carbon supported−MC hybrids with superior active sites, conductivity, and oxygen absorption ability, thereby promising enhanced behaviors.

8.1.4.5. Thin film transistors (TFTs)

Electronic devices using the charge of electrons to process or store information are a vitally important part of modern information technology. They also serve as the basis for other applications. The strategy of continuous miniaturization of devices has been developed in recent decades to enhance the properties of traditional semiconductors, such as silicon-based devices. However, this strategy will be terminated when the size of devices approaches the atomic dimension. The scaling limits of conventional silicon-based technology over the last decades suggest that atomically thin semiconductors such as MCs might be applicable for future generation large-scale electronics,[86,87] provided manufacturing and integration challenges can be resolved. Several articles have reviewed breakthroughs and perceived applications of 2D materials. Different types of basic electronic devices and applications for 2D metal chalcogenides are the FETs, p–n junctions, tunneling devices, and Schottky junctions, etc. Recently, the flexible electronics, particularly 2D thin film transistors (TFTs) has emerged, which is the core device required for many flexible technology device concepts, much like the conventional FET.[88–94]

8.1.4.6. Optoelectronic devices

Emerging MCs present excellent performance for optoelectronic applications. In contrast with graphene, the abundant band structures of 2D MCs provide a reliable foundation for optoelectronic applications. Their spatial restriction to an ultrathin atomic-scale plane provides optoelectronic properties distinct from those of conventional bulk materials. Moreover, the outstanding ability to form van der Waals heterojunctions provides the possibility to extend the optoelectronic applications. Some remarkable optoelectronic applications are in photodetectors, light-emitting devices, etc.[4,91,93]

8.2. Conclusion and perspectives

The huge energy requirement and fossil-fuel induced environmental pollution create an enormous challenge for scientists to develop clean and sustainable technologies to provide abundant energy in an economically viable way. Energy conversion and storage (ECS) devices such as fuel cells, water electrolysis cells, solar cells, Li-ion batteries, supercapacitors, etc. have the capability to power the energy demanding areas that range from portable electronics to transportation and even stationary power plants. Nevertheless, the real application of ECS devices will depend critically on synthesizing new functional materials with the merits of low cost, high efficiency, and outstanding properties. In present research, several projects have been described to develop the microwave-irradiation as a general synthesis approach to produce metal chalcogenides (MCs) on graphene networks. Nanomaterials with specific morphologies have always been attracted for their unique physical and chemical properties. The controlled microwave-initiated synthesis approach can provide a direct and facile method to obtain the desired morphologies in MC-based nanocomposites materials. Present research also includes the detailed investigation on sustainable energy-related applications of the resultant MC/graphene nanocomposites. The obtained results from the projects indicate that the microwave-irradiation approach is a promising method to synthesize MC-based compounds on graphene. This synthesis approach is very simple, energy and time efficient, and is suitable for continuous synthesis of large quantities of desired products. This method is expected to be applied for synthesizing many other combinations and nanostructures of MC-based nanomaterials or hybrids on a huge range of carbon-based supports such as graphene, conducting polymers, carbon nanotubes etc. In this work, the physicochemical (SEM, TEM, EDS, XRD, XPS, Raman, BET) and electrochemical characterizations (CV, LSV, EIS, GCD, etc.) have been performed to confirm the formation of MC/graphene nanocomposites and their intrinsic properties for energy applications, respectively. The obtained data from several experiments confirm the electrocatalytic activities of as-produced MC-based nanocomposites towards hydrogen evolution reaction (HER) and their characteristics as super-capacitive energy storage materials. These results thus provide new opportunities for the development of renewable and economic hydrogen production technologies and a high promise for future electrochemical energy storage applications. In addition, due to the unique properties of MC/graphene hybrids, their applications should be considered in some other novel fields, such as batteries, photovoltaics, biomedicine, drug delivery, tissue engineering, sensors, transistors, and optoelectronic applications. Also, the technological integration and construction strategies to build complete MC-based electrochemical devices are necessary requirements in future studies.

8.3. References

1 S. Chandrasekaran, L. Yao, L. Deng, C. Bowen, Y. Zhang, S. Chen, Z. Lin, F. Peng and P. Zhang, *Chem. Soc. Rev.*, 2019, **48**, 4178–4280.

2 M. Luo, H. Yu, F. Hu, T. Liu, X. Cheng, R. Zheng, Y. Bai, M. Shui and J. Shu, *Chem. Eng. J.*, 2020, **380**, 122557.

3 D. Jamwal and S. K. Mehta, *ChemistrySelect*, 2019, **4**, 1943–1963.

4 Y. Cui, Z. Zhou, T. Li, K. Wang, J. Li and Z. Wei, *Adv. Funct. Mater.*, 2019, **29**, 1–33.

5 Y. Zhang, Q. Zhou, J. Zhu, Q. Yan, S. X. Dou and W. Sun, *Adv. Funct. Mater.*, 2017, **27**, 1–34.

6 J. Ni, X. Bi, Y. Jiang, L. Li and J. Lu, *Nano Energy*, 2017, **34**, 356–366.

7 Y. Liu, Z. Che, X. Lu, X. Zhou, M. Han, J. Bao and Z. Dai, *Nanoscale Adv.*, 2020, **2**, 583–604.

8 H. Tao, Q. Fan, T. Ma, S. Liu, H. Gysling, J. Texter, F. Guo and Z. Sun, *Prog. Mater. Sci.*, 2020, **111**, 100637.

9 J. Huang, Z. Wei, J. Liao, W. Ni, C. Wang and J. Ma, *J. Energy Chem.*, 2019, **33**, 100–124.

10 S. Li, X. Hao, A. Abudula and G. Guan, *J. Mater. Chem. A*, 2019, **7**, 18674–18707.

11 A. Giri, G. Park, H. Yang, M. Pal, J. Kwak and U. Jeong, *Adv. Mater.*, 2018, **30**, 1–19.

12 E. Er and N. Erk, *Microchim. Acta*, **187**, 223 (2020).

13 Y. Zhang, M. L. Snedaker, C. S. Birkel, S. Mubeen, X. Ji, Y. Shi, D. Liu, X. Liu, M. Moskovits and G. D. Stucky, *Nano Lett.*, 2012, **12**, 1075–1080.

14 K. Jiang, B. Liu, M. Luo, S. Ning, M. Peng, Y. Zhao, Y. R. Lu, T. S. Chan, F. M. F. de Groot and Y. Tan, *Nat. Commun.*, 2019, **10**, 1–9.

15 M. B. Askari, P. Salarizadeh, S. M. Rozati and M. Seifi, *Polyhedron*, 2019, **162**, 201–206.

16 Y. Wang, L. Huang, B. Li, J. Shang, C. Xia, C. Fan, H. X. Deng, Z. Wei and J. Li, *J. Mater. Chem. C*, 2017, **5**, 84–90.

17 C. Gong, Y. Zhang, W. Chen, J. Chu, T. Lei, J. Pu, L. Dai, C. Wu, Y. Cheng, T. Zhai, L. Li and J. Xiong, *Adv. Sci.*, 2017, **4**, 1700231.

18 Y. Feng, T. He and N. Alonso-Vante, *Chem. Mater.*, 2008, **20**, 26–28.

19 S. Poyraz, J. Cook, Z. Liu, L. Zhang, A. Nautiyal, B. Hohmann, S. Klamt and X. Zhang, *J. Mater. Sci.*, **53**, 12178–12189 (2018).

20 J. Liu and D. Xue, *J. Mater. Chem.*, 2011, **21**, 223–228.

21 P. Nekooi, M. Akbari and M. K. Amini, *Renew. Energy*, 2010, **35**, 6392–6398.

22 Z. Liu, L. Zhang, R. Wang, S. Poyraz, J. Cook, M. J. Bozack, S. Das, X. Zhang and L. Hu, *Sci. Rep.*, 2016, **6**, 1–8.

23 N. Liu, X. Wang, W. Xu, H. Hu, J. Liang and J. Qiu, *Fuel*, 2014, **119**, 163–169.

24 S. Anantharaj, J. Kennedy and S. Kundu, *ACS Appl. Mater. Interfaces*, 2017, **9**, 8714–8728.

25 R. J. Mehta, C. Karthik, W. Jiang, B. Singh, Y. Shi, R. W. Siegel, T. Borca-Tasciuc and G. Ramanath, *Nano Lett.*, 2010, **10**, 4417–4422.

26 A. B. Panda, G. Glaspell and M. S. El-Shall, *J. Am. Chem. Soc.*, 2006, **128**, 2790–2791.

27 X. Wang, Y. Zheng, J. Yuan, J. Shen, L. Niu and A. jun Wang, *Electrochim. Acta*, 2017, **235**, 422–428.

28 J. Xiang, D. Dong, F. Wen, J. Zhao, X. Zhang, L. Wang and Z. Liu, *J. Alloys Compd.*, 2016, **660**, 11–16.

29 M. Y. Li, C. H. Chen, Y. Shi and L. J. Li, *Mater. Today*, 2016, **19**, 322–335.

30 K. Leng, Z. Chen, X. Zhao, W. Tang, B. Tian, C. T. Nai, W. Zhou and K. P. Loh, *ACS Nano*, 2016, **10**, 9208–9215.

31 H. Yuan, L. Kong, T. Li and Q. Zhang, *Chinese Chem. Lett.*, 2017, **28**, 2180–2194.

32 Muhammad Yousaf, Asif Mahmood, Yunsong Wang, Yijun Chen, Zhimin Ma and Ray P. S. Han, *J. Electr. Eng.*, 2016, **4**, 58–74.

33 X. Zhang, A. Selkirk, S. Zhang, J. Huang, Y. Li, Y. Xie, N. Dong, Y. Cui, L. Zhang, W. J. Blau and J. Wang, *Chem. - A Eur. J.*, 2017, **23**, 3321–3327.

34 S. K. Park, G. D. Park, D. Ko, Y. C. Kang and Y. Piao, *Chem. Eng. J.*, 2017, **315**, 355–363.

35 J. Zhu, Z. Chen, L. Jia, Y. Lu, X. Wei, X. Wang, W. D. Wu, N. Han, Y. Li and Z. Wu, *Nano Res.*, 2019, **12**, 2250–2258.

36 X. Zhang, Q. Zhang, Y. Sun, P. Zhang, X. Gao, W. Zhang and J. Guo, *Electrochim. Acta*, 2016, **189**, 224–230.

37 X. Huang, L. Yang, S. Hao, B. Zheng, L. Yan, F. Qu, A. M. Asiri and X. Sun, *Inorg. Chem. Front.*, 2017, **4**, 537–540.

38 C. Chen, Y. He, G. Xiao, Y. Xia, H. Li and Z. He, *Appl. Surf. Sci.*, 2018, **444**, 511–521.

39 X. Yang, L. Zhao and J. Lian, *J. Power Sources*, 2017, **343**, 373–382.

40 J. Guan, J. Wu, D. Jiang, X. Zhu, R. Guan, X. Lei, P. Du, H. Zeng and S. Yang, *Int. J. Hydrogen Energy*, 2018, **43**, 8698–8706.

41 S. Bhadra, D. Khastgir, N. K. Singha and J. H. Lee, *Prog. Polym. Sci.*, 2009, **34**, 783–810.

42 X. Jia, Y. Ge, L. Shao, C. Wang and G. G. Wallace, *ACS Sustain. Chem. Eng.*, 2019, **7**, 14321–14340.

43 B. S. Dakshayini, K. R. Reddy, A. Mishra, N. P. Shetti, S. J. Malode, S. Basu, S. Naveen and A. V. Raghu, *Microchem. J.*, 2019, **147**, 7–24.

44 A. U. Agobi, L. HITLER, T. O. Magu and P. M. Dass, *J. Chem. Rev.*, 2019, **1**, 19–34.

45 N. Shoaie, M. Daneshpour, M. Azimzadeh, S. Mahshid, S. M. Khoshfetrat, F.

Jahanpeyma, A. Gholaminejad, K. Omidfar and M. Foruzandeh, *Microchim. Acta*, **186**, 465 (2019).

46 S. Cho, J. S. Lee and H. Joo, *Polymers*, 2019, ***11***(12), 1965.

47 W. Choi, N. Choudhary, G. H. Han, J. Park, D. Akinwande and Y. H. Lee, *Mater. Today*, 2017, **20**, 116–130.

48 X. Huang, Z. Zeng and H. Zhang, *Chem. Soc. Rev.*, 2013, **42**, 1934–1946.

49 X. Li and H. Zhu, *J. Mater.*, 2015, **1**, 33–44.

50 S. Kumar, V. Pavelyev, P. Mishra, N. Tripathi, P. Sharma and F. Calle, *Mater. Sci. Semicond. Process.*, 2020, **107**, 104865.

51 Y. Li, H. X. Zhang, F. T. Liu, X. F. Dong, X. Li and C. W. Wang, *Superlattices Microstruct.*, 2019, **125**, 66–71.

52 H. Fan, H. Yu, Y. Zhang, J. Guo, Z. Wang, H. Wang, N. Zhao, Y. Zheng, C. Du, Z. Dai, Q. Yan and J. Xu, *Energy Storage Mater.*, 2018, **10**, 48–55.

53 H. M. Li, D. Y. Lee, M. S. Choi, D. Qu, X. Liu, C. H. Ra and W. J. Yoo, *Sci. Rep.*, 2014, **4**, 1–7.

54 Y. H. Wang, K. J. Huang and X. Wu, *Biosens. Bioelectron.*, 2017, **97**, 305–316.

55 W. Deng, Y. Chen, C. You, B. Liu, Y. Yang, G. Shen, S. Li, L. Sun, Y. Zhang and H. Yan, *Adv. Electron. Mater.*, 2018, **4**, 1–8.

56 Q. Yan, L. Gao, J. Tang and H. Liu, *J. Semicond.*, 2019, **40**, 111604.

57 M. Sakthivel, R. Sukanya, S. M. Chen, K. Pandi and K. C. Ho, *Renew. Energy*, 2019, **138**, 139–151.

58 P. Karthick Kannan, P. Shankar, C. Blackman and C. H. Chung, *Adv. Mater.*, 2019, **1803432**, 1–27.

59 D. Wang, Q. Li, Z. Xing and X. Yang, *Talanta*, 2018, **178**, 905–909.

60 J. Gong, K. Sumathy, Q. Qiao and Z. Zhou, *Renew. Sustain. Energy Rev.*, 2017, **68**, 234–246.

61 M. Yu, X. Wu, J. Zhang, Y. Meng, Y. Ma, J. Liu and S. Li, *Electrochim. Acta*, 2017, **258**, 485–494.

62 S. Li, H. Min, F. Xu, L. Tong, J. Chen, C. Zhu and L. Sun, *RSC Adv.*, 2016, **6**, 34546–34552.

63 E. Bi, H. Chen, X. Yang, F. Ye, M. Yin and L. Han, *Sci. Rep.*, 2015, **5**, 1–10.

64 J. Balamurugan, S. G. Peera, M. Guo, T. T. Nguyen, N. H. Kim and J. H. Lee, *J. Mater. Chem. A*, 2017, **5**, 17896–17908.

65 Z. Yu, J. Ye, W. Chen, S. Xu and F. Huang, *Carbon N. Y.*, 2017, **114**, 125–133.

66 S. K. Srivastava, B. Kartick, S. Choudhury and M. Stamm, *Mater. Chem. Phys.*, 2016, **183**, 383–391.

67 Y. Liu, W. Wang, Y. Wang and X. Peng, *Nano Energy*, 2014, **7**, 25–32.

68 J. Zhou, Y. Liu, S. Zhang, T. Zhou and Z. Guo, *InfoMat*, 2020, **2**, 437–465.

69 H. Tan, Y. Feng, X. Rui, Y. Yu and S. Huang, *Small Methods*, 2020, **4**, 1–46.

70 S. Dai, L. Wang, M. Cao, Z. Zhong, Y. Shen and M. Wang, *Mater. Today Energy*, 2019, **12**, 114–128.

71 Z. Luo, J. Zhou, L. Wang, G. Fang, A. Pan and S. Liang, *J. Mater. Chem. A*, 2016, **4**, 15302–15308.

72 Y. Teng, H. Zhao, Z. Zhang, L. Zhao, Y. Zhang, Z. Li, Q. Xia, Z. Du and K. Świerczek, *Carbon N. Y.*, 2017, **119**, 91–100.

73 Y. Guo, Y. Zhang, Y. Wang, D. Zhang, Y. Lu, R. Luo, Y. Wang, X. Liu, J. K. Kim and Y. Luo, *Electrochim. Acta*, 2019, **296**, 989–998.

74 S. Yuan, S. Wang, L. Li, Y. H. Zhu, X. B. Zhang and J. M. Yan, *ACS Appl. Mater.*

Interfaces, 2016, **8**, 9178–9184.

75 X. Cao, Y. Shi, W. Shi, X. Rui, Q. Yan, J. Kong and H. Zhang, *Small*, 2013, **9**, 3433–3438.

76 W. Miao, Y. Zhang, H. Li, Z. Zhang, L. Li, Z. Yu and W. Zhang, *J. Mater. Chem. A*, 2019, **7**, 5504–5512.

77 L. Zhang, W. Fan, W. W. Tjiu and T. Liu, *RSC Adv.*, 2015, **5**, 34777–34787.

78 Y. Pan, X. Cheng, M. Gao, Y. Fu, J. Feng, L. Gong, H. Ahmed, H. Zhang and V. S. Battaglia, *ACS Appl. Mater. Interfaces*, 2020, **12**, 33621–33630.

79 L. Jiang, B. Lin, X. Li, X. Song, H. Xia, L. Li and H. Zeng, *ACS Appl. Mater. Interfaces*, 2016, **8**, 2680–2687.

80 E. Barrios, D. Fox, Y. Yee, L. Sip, R. Catarata, J. E. Calderon, N. Azim, S. Afrin, Z. Zhang and L. Zhai, *Polymers (Basel).*, 2019, **11**, 1–41.

81 J. Guo, Y. Shi, X. Bai, X. Wang and T. Ma, *J. Mater. Chem. A*, 2015, **3**, 24397–24404.

82 S. Xin, Z. Liu, L. Ma, Y. Sun, C. Xiao, F. Li and Y. Du, *Nano Res.*, 2016, **9**, 3795–3811.

83 Z. P. Wu, X. F. Lu, S. Q. Zang and X. W. Lou, *Adv. Funct. Mater.*, 2020, **30**, 1–20.

84 Y. Zuo, Y. Liu, J. Li, R. Du, X. Han, T. Zhang, J. Arbiol, N. J. Divins, J. Llorca, N. Guijarro, K. Sivula and A. Cabot, *Chem. Mater.*, 2019, **31**, 7732–7743.

85 J. Zhang, B. Jiang, J. Zhang, R. Li, N. Zhang, R. Liu, J. Li, D. Zhang and R. Zhang, *Mater. Lett.*, 2019, **235**, 53–56.

86 G. Kim and H. S. Shin, *Nanoscale*, 2020, **12**, 5286–5292.

87 S. Liu, A. Granados Del Águila, X. Liu, Y. Zhu, Y. Han, A. Chaturvedi, P. Gong, H. Yu, H. Zhang, W. Yao and Q. Xiong, *ACS Nano*, 2020, **14**, 9873–9883.

88 C. H. Chu, H. C. Lin, C. H. Yeh, Z. Y. Liang, M. Y. Chou and P. W. Chiu, *ACS Nano*, 2019, **13**, 8146–8154.

89 T. K. Paul and Q. D. M. Khosru, *AIP Adv.*, **10**, 045226 (2020).

90 S. P. Madhusudanan, K. Mohanta and S. K. Batabyal, *J. Solid State Electrochem.*, 2019, **23**, 1307–1314.

91 W. Y. Lee, S. Ha, H. Lee, J. H. Bae, B. Jang, H. J. Kwon, Y. Yun, S. Lee and J. Jang, *Adv. Opt. Mater.*, 2019, **7**, 2–8.

92 W. S. Lee, Y. G. Kang, H. K. Woo, J. Ahn, H. Kim, D. Kim, S. Jeon, M. J. Han, J. H. Choi and S. J. Oh, *Chem. Mater.*, 2019, **31**, 9389–9399.

93 F. Wang, Y. Zhang, Y. Gao, P. Luo, J. Su, W. Han, K. Liu, H. Li and T. Zhai, *Small*, 2019, **15**, 1–18.

94 R. J. Chang, Y. Sheng, T. Chen, N. Mkhize, Y. Lu, H. Bhaskaran and J. H. Warner, *ACS Appl. Nano Mater.*, 2019, **2**, 4222–4231.